JCM

Scholarly, Peer-Reviewed and Fully Refereed International Research Journal

ISSN : 2583-9152

Journal of Condensed Matter

of

Condensed Matter Research Society

Vol. 02 No. 02 (2024)

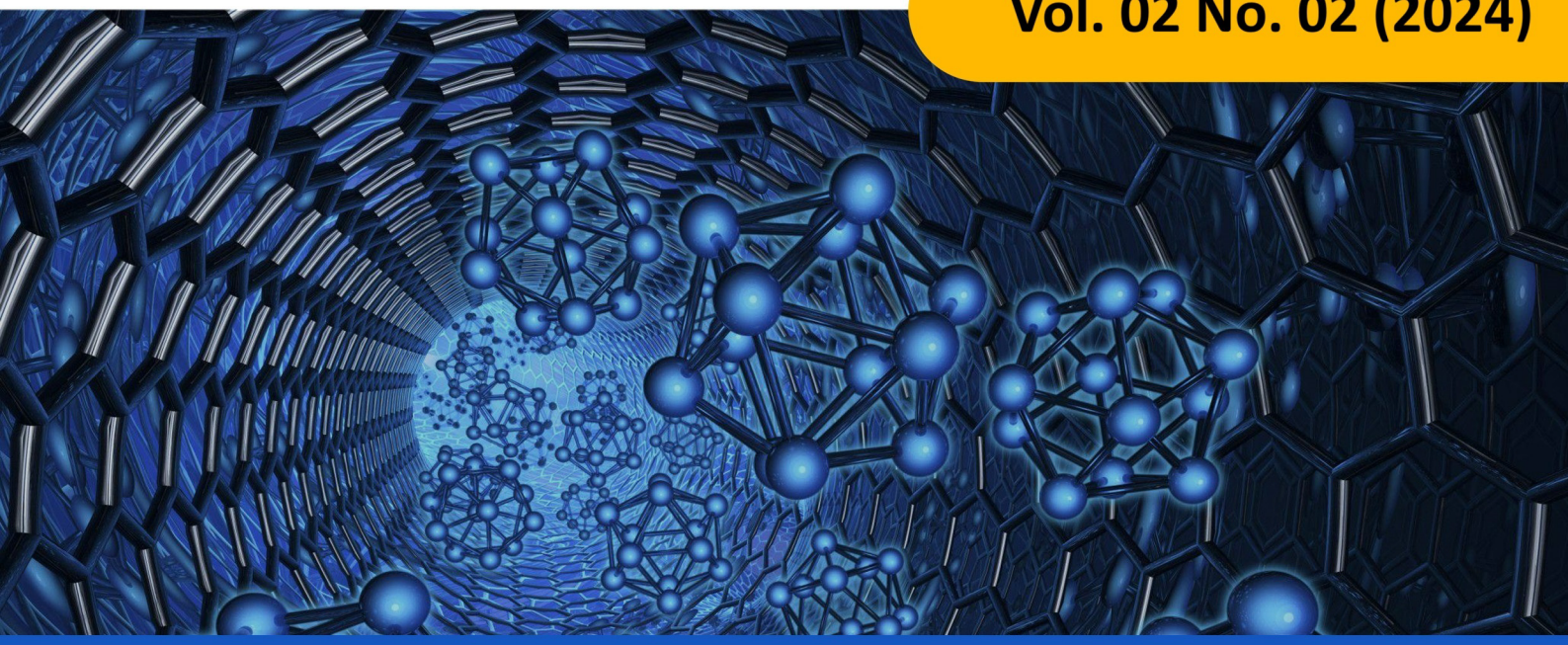

Condensed Matter Research Society

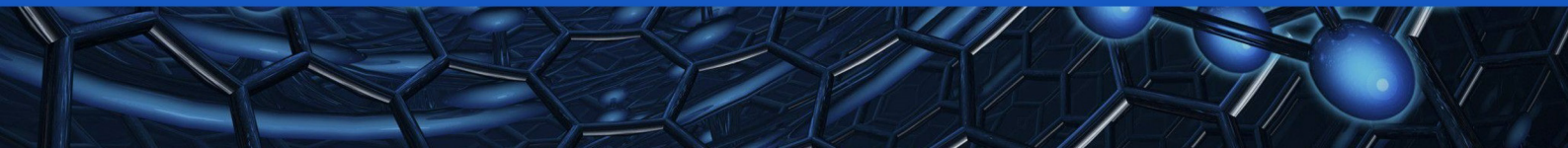

Table of Contents

Classical and Quantum Computing modalities-A Review

Rajni

Department of Physics, Patel Memorial National College, Rajpura, Punjab, INDIA

Abstract

Quantum computers generally need to operate under more regulated physical condition than classical computer because of quantum mechanics. Classical computer uses bits and quantum computer use qubits. According to IBM, "Groups of quits in superposition can create complex, multidimensional computational spaces" that enable more complex calculations. Quantum algorithms like Shor's and Grover's run significantly faster than various algorithms for classical computer. Quantum entanglement offers fascinating opportunities for enhancing AI algorithms through improved computational efficiency. But practical implementation remains challenging due to technical limitations and the need for further research in the field of quantum machine learning. This article provides a brief overview of different quantum computing methods.

Keywords: Classical Bits, Quantum bits, Computational Methods.
Received 27 January 2025; First Review 12 February 2025; Accepted 15 February 2025

*** Address of correspondence**
Dr. Rajni
Department of Physics, Patel Memorial National College, Rajpura, Punjab, INDIA

Email: rajnibansal.phd@gmail.com

How to cite this article
Rajni, Classical and Quantum Computing modalities-A Review, J. Cond. Matt. 2024; 02 (02):1-5.

Available from:
https://doi.org/10.61343/jcm.v2i02.72

Introduction

While conventional or classical computing has been the foundation of technological advancements for decades, the emergence of quantum computing has sparked both curiosity and excitement [1,2]. To understand the importance of this shift from classical computing, it is essential to understand the fundamental differences between classical and quantum computer. Quantum computing exploits the principles of quantum mechanics (superposition, entanglement, and interference) to exploit the quantum behavior of elementary particles (qubits) to perform computations [3-5]. At the heart of quantum computing are quantum bits (qubits), which can exist in more than one state at once due to a phenomenon called superposition [6-7]. Unlike classical bits, which are limited to being either 0 or 1, quantum bits can represent both 0 and 1 simultaneously, allowing for a dramatic increase in computational power. By harnessing the properties of quantum bits such as superposition and entanglement, it is possible to increase the processing power of AI systems. This quantum-AI synergy could tackle computationally-intensive tasks beyond classical computers' reach, potentially helping to power breakthroughs in drug discovery, materials science, financial modeling and cryptography [8-9]. The difference between classical computer and quantum computer are like a horse and a hawk: a horse can run, and a hawk can fly [10-11]. Classical computers and quantum computers are truly different. Here we take a closer look at what the main differences are, what quantum computers are and how they work. This article explores these and other questions, taking into account the challenges ahead and the extreme temperatures required to operate the quantum computer.

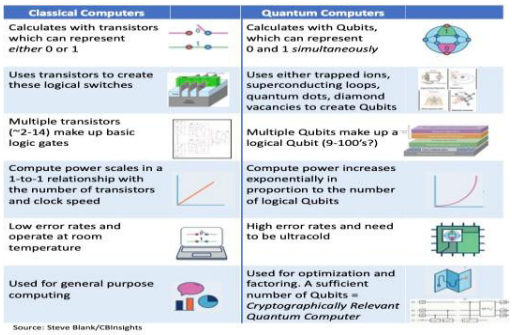

Figure 1: The difference between classical and quantum computer. Taken from Wikipedia.

The main methods of Quantum Computing are:

Superconducting quantum computing: This method uses superconducting circuits operating at cryogenic temperatures. Superconducting qubits are made of materials that exhibit superconductivity, allowing the manipulation of quantum states at high speeds and low error rates.

Figure 2: Illustration of superconducting quantum qubits. Taken from Wikipedia.

The technology has been widely developed by companies such as IBM and Google, and is one of the most prominent approaches in the field [12].

Photonic Quantum Computing: Photonic quantum computers use photons (light particles) as qubits. They manipulate light through various optical components, such as beam splitters and phase shifters, to perform computations. This method benefits from room-temperature operation and scalability, which makes it suitable for large-scale quantum systems. Companies like Xanadu and Psi Quantum are exploring different techniques in this category, including squeezed light states [13-15].

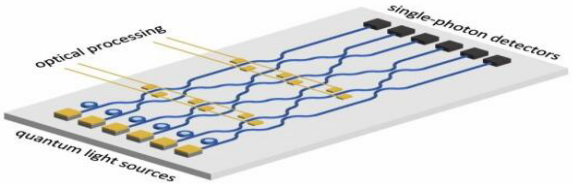

Figure 3: Diagram of photon qubits. Excerpt from Wikipedia.

Quantum Computing with Trapped Ion: In this approach, individual ions are trapped using electromagnetic fields and manipulated with laser beams to perform quantum operations. Trapped ions offer long coherence times and high computational precision, which are important for efficient quantum computing. This method has been successfully implemented by companies such as IonQ and Honeywell [16-18].

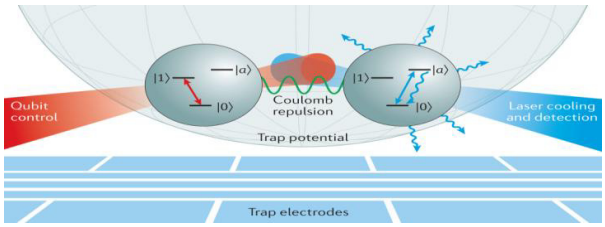

Figure 4: Illustration of trapped ion quantum qubits. Taken from Wikipedia.

Neutral Atom Quantum Computing: Neutral atom technology involves trapping neutral atoms using optical tweezers (focused laser beams). This method is less sensitive to electric fields compared to trapped ion systems, allowing for more robust operations. Neutral atom systems can operate at higher temperatures, which simplifies certain aspects of their implementation [19].

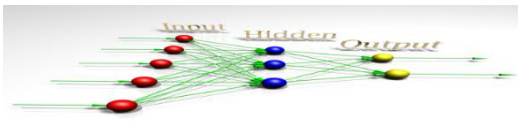

Figure 5: Illustration of quantum qubits of the neural atom. From Wikipedia.

Quantum Dots: Quantum dots are semiconductor particles that confine electrons in three dimensions. This is an emerging field that uses silicon, a material essential to classical computing, to create qubits— the basic units of quantum information. Recent advances aim to improve the purity and scalability of silicon qubits, making them a promising candidate for future quantum computers. However, challenges remain in achieving long coherence times [20-23].

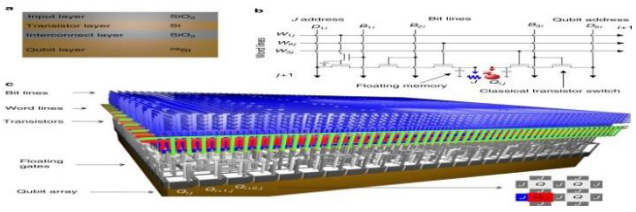

Figure 6: Diagram of quantum dot qubits. Quoted from Wikipedia.

Hybrid Quantum Computing: Hybrid systems combine classical computing elements with quantum processors to leverage the strengths of both technologies. This approach can optimize certain computations by using a combination of classical and quantum algorithms [24-25].

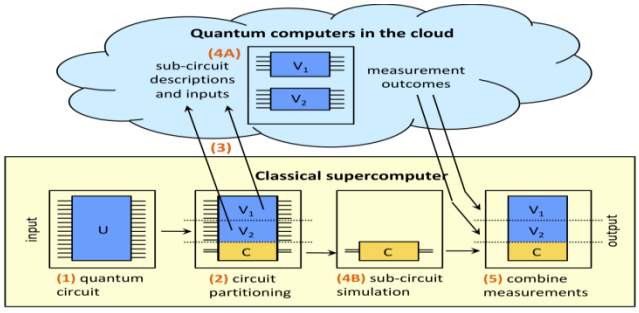

Figure 7: Fig. of hybrid quantum calculation. Taken from Wikipedia.

Carbon-based Quantum Computing: This new technology uses carbon nanotubes combined with quantum dots to create qubits that have the advantage of long coherence times and reduced error rates in noisy environments. The mechanical oscillators formed by these structures could improve performance in practical applications [26].

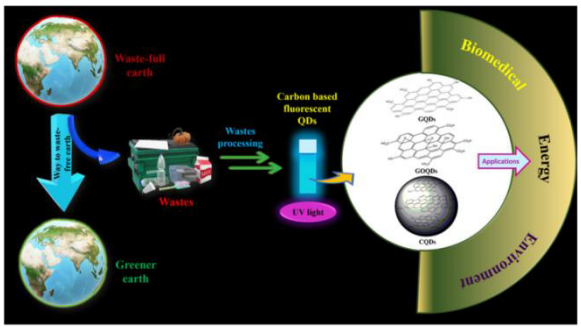

Figure 8: Illustration of quantum calculations based on carbon. Taken from Wikipedia.

Cold Atom Quantum Computing: The use of cold atoms to form qubits is a cutting-edge research area in quantum computing that exploits the unique properties of ultracold atomic systems to create and manipulate quantum bits (qubits). The process typically involves cooling atoms to extremely low temperatures and trapping them using laser technology [27].

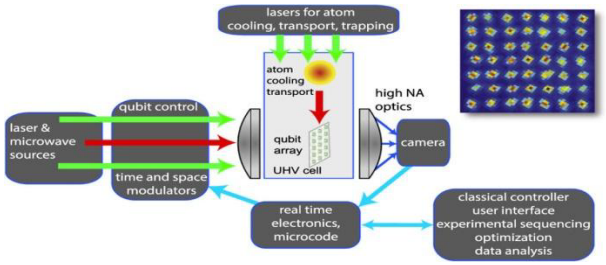

Figure 9: Diagram of quantum computing on cold atoms. Quoted from Wikipedia.

NV centres for Quantum Computing: NV (Nitrogen-vacancy) centres in diamond are increasingly attracting attention as a promising platform for quantum computing due to their unique properties and capabilities. These centres exploit defects in diamond crystals, specifically the combination of nitrogen atoms and vacancies, to create quantum bits that can operate efficiently at room temperature [28].

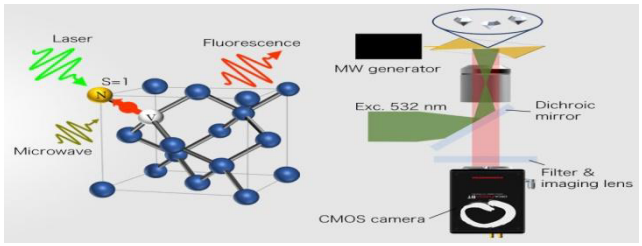

Figure 10: Illustration of NV centre Quantum boxes. Taken from Wikipedia.

Majorana Quantum Computing: Majorana fermions, theoretically proposed by Ettore Majorana in 1937, are a single particle that is its own antiparticles. These special properties make them promising candidates for advancing quantum computing technology, especially in the development of topological quantum computers. These computers leverage the stability and fault tolerance provided by Majorana fermions to address some of the significant challenges faced in quantum computing [29-31].

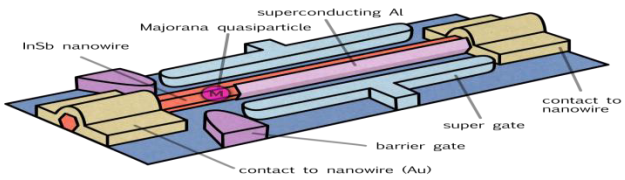

Figure 11: Diagram of Majorana quantum computing. Taken from Wikipedia.

Practical applications

Quantum computers have the potential to revolutionize data processing in many areas, from **cryptography** to the **simulation of complex systems** [32,34,36]. Below are most promising applications of quantum computer:

Figure 12: Need of quantum computer. Taken from Wikipedia.

Quantum cryptography: Quantum encryption uses quantum characteristics to protect communication from eavesdropping. Quantum computers can generate secure cryptographic keys more efficiently than classical computers and can break some of the encryption techniques commonly used today.

Optimization: Quantum Computer can solve optimization problems much more efficiently than classical computers. This makes it suitable for solving complex problems such as vehicle route planning and resource allocation.

Quantum Simulation: Simulating quantum systems is an extremely challenging task for classical computers. On the other hand, quantum computers can simulate the dynamics of quantum systems such as molecules and materials, opening up new possibilities for the discovery of new materials and drugs.

Quantum machine learning: Machine learning is one of the most promising application areas for quantum computer. Quantum computer can take advantage of quantum superposition to perform simultaneous learning operations on many possible solutions, making training of **machine learning** models more efficient.

Finance: Quantum computers can be used to analyze large amounts of financial **data** and predict market prices more efficiently than classical computers.

Future challenges for quantum computers

Despite progress toward the realization of quantum computers, many problems still need to be solved before quantum computer can be widely used [33,35,37]. Below are some of the most important tasks of these computers:

Stability and error reduction: Quantum computers are prone to errors due to factors such as environmental noise and qubit instability. For quantum computers to be useful in

real world applications, new ways to reduce errors and improve stability need to be developed.

Scalability: Currently, the most advanced quantum computers contain only a few dozen qubits, but to solve really complex problems, many more qubits are needed. Therefore, in order to promote this technology, it is essential to develop technology to increase the number of qubits and improve the scalability of quantum computers.

Control and management: Qubit management is complicated and requires special techniques. Moreover, controlling and reading qubits requires highly sophisticated laboratory equipment and methods. For quantum computers to be useful in real world applications, new ways to simplify the managing and controlling of qubits must be developed.

Algorithms: Not all problems are suitable for quantum computers. New algorithms must be developed that are specifically designed to exploit the unique properties of quantum computers and solve complex problems.

Standardization: Quantum computers are produced by different companies and use different methods and protocols. It is required to develop common methods and protocols to ensure correlation between the various systems and make it easier for the people working in this field to use these machines.

Figure 13: Challenges of quantum computing. Excerpt from Wikipedia.

Conclusion and Future Prospective

In conclusion, each method of quantum computing has its own set of advantages and challenges, making the field diverse and dynamic. The current research and development in this field aim to improve these unique strengths while diminishing the weaknesses. The main goal is to build reliable quantum computers that can solve problems that cannot be solved by classical machines. As research progresses, these technologies may converge or evolve further, potentially leading to breakthroughs in computational power and efficiency across various applications. Both classical and quantum computing have their unique strengths and weaknesses. Classical computing is necessary for day-to-day applications. With new advancements, we welcome new technologies every day, and one such breakthrough in technology is quantum computers. Despite the fact that people have reached a milestone and have invented very fast supercomputers, there are still specific tasks unhandled by these computers, such as calculations of the prime factors of very large integers. Quantum Computers are far ahead of classical computers and will soon become our very powerful companions in the future.

References

1. A Steane, "*Quantum computing",* Reports on Progress in Physics, 61:117-173, 1998.
2. B M Terhal, "*Quantum supremacy, here we come",* Nature Physics, 14: 530-531, 2018.
3. H D Zeh, "*Feynman's interpretation of quantum theory",* The European Physical Journal H, 36:63-74, 2011.
4. P W Shor, *"Polynomial-time algorithms for prime factorization and discrete logarithms on a quantum computer"*, SIAM review, 41: 303-332, 1999.
5. S Aaronson and Ambainis, A Forrelation, *"A problem that optimally separates quantum from classical computing"*, In Proceedings of the forty-seventh annual ACM symposium on Theory of computing, pages 307–316, 2015.
6. J Anandan and Y Aharonov, *"Geometry of quantum evolution"*, Physical review letters, 65:1697-1700, 1990.
7. L. Gurvits, *"Classical complexity and quantum entanglement"*, Journal of Computer and System Sciences, 69: 448–484, 2004.
8. B Lu, M Lin, Y Shu et al., *"Approximation of the nearest classical state to a quantum state"*, arXiv preprint arXiv:2301.09316, 2023.
9. B W Reichardt, F Unger, and U. Vazirani, *"Classical command of quantum systems"*, Nature, 496: 456–460, 2013.
10. C M Unsal and A Yavuz Oruc, *"Faster quantum concentration via grover's search"*, International Journal of Parallel, Emergent and Distributed Systems, pages 1–16, 2023.
11. I L Chuang, N Gershenfeld, and M Kubinec, *"Experimental implementation of fast quantum searching"*, Physical Review Letters, 80: 3408–3411, 1998.
12. H L Huang, D C Wu, D J Fan, et al, *"Superconducting Quantum Computing: A Review"*, Science China Information Sciences, 63: 180501, 2020.
13. N Maring, A Fyrillas, M Pont. *et al, "A versatile single-photon-based quantum computing platform"*, Nat. Photon,18: 603–609, 2024.
14. H S Zhong, *et al, "Quantum computational*

advantage using photons", Science, 370: 1460–1463, 2020.

15. P Michler, A Imamoglu, M D Mason, P J Carson, G F Strouse, and S K Buratto, *"Quantum correlation among photons from a single quantum dot at room temperature"*, Nature (London), 406:968, 2000.
16. Colin D. Bruzewicz, John Chiaverini, Robert McConnell, Jeremy M. Sage, *"Trapped-ion quantum computing: Progress and challenges"*, Appl. Phys. Rev., 6: 021314, 2019.
17. L Zhao *et al, "Orbital-optimized pair-correlated electron simulations on trapped-ion quantum computers",* npj Quantum Inf., 9: 60, 2023.
18. J J Cirac and P Zoller, *"Quantum computations with cold trapped ions"*, Physical Review Letters, 74:4091–4094, 1995.
19. N Jain, B Coyle, E Kashefi, & N Kumar, *"Graph neural network initialization of quantum approximate optimization"*, Quantum, 6: 861, 2022.
20. D Loss and D P DiVincenzo, *"Quantum computation with quantum dots"*, Physical Review A, 57:120–126, 1998.
21. T Calarco, A Datta, P Fedichev, E Pazy, and P Zoller, *"Spin-based all-optical quantum computation with quantum dots: Understanding and suppressing decoherence"*, Physical Review A, 68:012310, 2003.
22. A Skinner, M Davenport, and B Kane, *"Hydrogenic spin quantum computing in silicon: A digital approach"*, Physical Review Letters, 90:087901–087905, 2003.
23. D Copsey, M Oskin, F Impens, T Metodiev, *"A Cross, F Chong, and J Chuang Kubiatowicz. Toward a scalable, silicon-based quantum computing architecture"*, Journal of Selected Topics in Quantum Electronics, 9:1552–1569, 2003.
24. W Li, Z Yin, X Li et al., *"A hybrid quantum computing pipeline for real world drug discovery"*, Sci Rep, 14: 16942, 2024.
25. A Gircha, A Boev, K Avchaciov, P Fedichev & A Fedorov, *"Hybrid quantum-classical machine learning for generative chemistry and drug design",* Sci. Rep., 13: 8250, 2023.
26. A G Bracamonte, *"Quantum Semiconductors Based on Carbon Materials for Nanophotonics and Photonics Applications by Electron Shuttle and Near Field Phenomena"*, Recent Progress in Materials, 5:03, 2023.
27. Meng Ye, Ye Tian, Jian Lin, Yuchen Luo, Jiaqi You, Jiazhong Hu, Wenjun Zhang, Wenlan Chen, and Xiaopeng Li., *"Universal Quantum Optimization with Cold Atoms in an Optical Cavity",* Phys. Rev. Lett., 131: 103601, 2023.
28. M W Doherty et al., *"Theory of the ground-state spin of the NV^- center in diamond"*, Phys. Rev. B, 85: 205023, 2012.
29. Q L He, et al., *"Chiral Majorana fermion modes in a quantum anomalous Hall insulator superconductor structure"*, Science, 357: 294–299, 2017.
30. AY Kitaev, *"Unpaired Majorana fermions in quantum wires"*, Phys-Usp, 44: 131–136, 2001.
31. D Aasen, et al., *"Milestones toward Majorana-based quantum computing"*, Phys Rev X, 6: 031016, 2016.
32. M Mohseni, P Read, H Neven et al., *"Commercialize quantum technologies in five years"*, Nature, 543: 171-174, 2017.
33. S Aaronson. *"Ten semi-grand challenges for quantum computing theory"*, 2005.
34. S Aaronson and A Ambainis, *"The need for structure in quantum speedups. Theory of Computing"*, 10: 133–166, 2014.
35. C Outeiral *et al., "The prospects of quantum computing in computational molecular biology"*, Wiley Interdiscip. Rev. Comput. Mol. Sci., 11: e1481, 2021.
36. R Santagati et al., *"Drug design on quantum computers"*, Nat. Phys., 20: 549–557, 2024.
37. N S Blunt *et al., "Perspective on the current state-of-the-art of quantum computing for drug discovery applications"*, J. Chem. Theory Comput., 18: 7001–7023, 2022.

First Principles Study on The Effect of Single Beryllium and Magnesium Adatom on Germanane Monolayer Surface

Oyedare Peter Olusola[1,a], Jamila Muhammad Wada[1,b], Alhassan Shauibu[2,c], Yakubu Aliyu Tanko[2,d], Maharaz Mohammed Nasir[3,e]

[1] *Science Laboratory Department Federal Polytechnic Ede, Osun State*
[2] *Department, of Physics Kaduna State University, Kaduna, State, Nigeria*
[3] *Department of Physics Federal University Dutse. Jigawa State*

[a] olusola.oyedare@gmail.com
[b] ummukhairyya@gmail.com
[c] alhassan.shuaibu@kasu.edu.ng
[d] aatanko2000@yahoo.com
[e] nmaharaz@gmail.com

Abstract

Theoretical calculations predict that unlike the planar structure of graphene, the germanene also has stable, two-dimensional (2D), low-buckled, honeycomb structure which make it more interested in the field of optoelectronic applications recently, but the major issue with germanene are larger germanium-germanium (Ge-Ge) interatomic distance and zero energy band gap which become a great research gap. In this study, the effect of alkaline earth metal (AEM) Magnesium (Mg) and Beryllium (Be) adsorption on germanane monolayer within the density functional theory as implemented in Quantum ESPRESSO code has been investigated, Our calculated equilibrium hexagonal lattice constant a and the buckling height δ are found to be 4.047 Å and 0.689 Å respectively, among the chosen adsorptions sites (H, B and T) B side is found to be the most favourable side for both Be and Mg absorptions, due to the less adsorption energy and AEM-Ge distances. For the electronic properties. The Be and Mg adsorptions lead to semiconducting behaviour with direct gap of about 0.206 eV 0.629 eV for Be and Mg adsorption respectively. The obtained results are in agreement with many reported theoretical results.

Keywords: Germanene Monolayer, Density Functional Theory, Adsorption, Electronic Properties.
Received 02 December 2024; First Review 27 December 2024; Accepted 04 January 2025

*** Address of correspondence**
Alhassan Shauibu
Department, of Physics Kaduna State University, Kaduna, State, Nigeria

Email: alhassan.shuaibu@kasu.edu.ng

How to cite this article
Oyedare Peter Olusola, Jamila Muhammad Wada, Alhassan Shauibu, Yakubu Aliyu Tanko, Maharaz Mohammed Nasir, First Principles Study on The Effect of Single Beryllium and Magnesium Adatom on Germanane Monolayer Surface, J. Cond. Matt. 2024; 02 (02): 6-11.

Available from:
https://doi.org/10.61343/jcm.v2i02.53

Introduction

Recently, the monolayer honeycomb structure of germanium (Ge), germanene, has been successful synthesized through Ge molecular beam epitaxy using Au (1 1 1) surface as a substrate [1]. As reported by early theoretical works, germanene is a zero-band gap semimetal, same as graphene [2-3]. Moreover, being an analogue of graphene, germanene also possesses a feature such as linear band dispersion behavior around the Fermi level at the K point, which leads to have high carrier mobility [3]. Additionally, some fantastic features of germanene such as quantum spin Hall Effect [4-5], valley Hall Effect a tunable band gap [6-7] and topological insulators nature at room temperature [8] have been well investigated. Besides, the possibility of easier incorporation of germanene in nanoelectronics devices compared to graphene, tailoring the electronic and magnetic properties of germanene is of both fundamental and applied interest.

Theoretical calculation predicts that unlike the planar structure of graphene, the germanene has stable, two-dimensional, and low-buckled, honeycomb structure similar to that of silicane, but has much higher spin-orbit electronic properties than that of silicane, which is certainly of crucial importance in future electronics. As studies on germanene are rapidly increasing, now the major challenge in this field is the preparation of high-quality germanene. Compared with silicane, the germanene has larger Ge-Ge interatomic distance which can weaken the orbital overlaps, resulting in the big difficulty in constructing germanene. Even with excellent electronic and magnetic properties, germanene

suffers from zero energy band gap. Applying electric field [8], Absorption of adatom species [9], introducing periodic nanoholes [10], doping [11], and edge functionalization are possible means to address the above-mentioned difficulties.

Recently, the adsorption characteristics of alkali metal (AM), alkali-earth metal (AEM), and even 3d transition-metal (TM) adatoms on 2D surfaces such as Silicane [12] graphene [13-14] and stanene [15] was carried out as the most appealing and conventional strategy to tailor the electronic and magnetic properties of these materials. Similarly in our other work [16] a TM doping on germanene surface was carried out. In each case, a remarkable electronic and magnetic property has been achieved but still with some future recommendations on how the properties germanene can be tailored to suite more optoelectronic applications

To the best of our knowledge, the AEM doping or adsorption on germanene monolayer are still remains an open research question. Therefore, this work aimed at study the effect of AEM Magnesium (Mg) and Beryllium (Be) adsorption on germanane monolayer within the density functional theory.

Method

In this work, calculations relating the adsorption of Be and Mg adatoms on germanene monolayer are performed using first-principles calculation based on DFT as implemented in QUANTUM ESPRESSO (QE) code [17]. The Perdew-Wang 91 generalized gradient approximation scheme (PW-GGA91) [18] has been used to approximate the electron exchange-correlation energy. The plane wave basis sets (Kresse, 1996), with the maximum kinetic energy cutoff up to ~ 460 eV was adopted for the valence electron wave functions. The norm-conserving Vanderbilt ultrasoft pseudopotentials [19] used includes four electrons for germanium ($2s^2 2p^2$), three electrons for Be ($4s^2 4p^1$), five electrons for Mg ($4s^2 4p^3$). The effect of Fermi-surface is treated with Marzari Vanderbilt smearing method with small Gaussian broadening of 0.002 Ry. The model of our system corresponds to a coverage of one Be or Mg adatom on a 4×4×1 germanene Monolayer supercell, plus a ~15A° vacuum layer, perpendicular to germanene along the *z*-axis to avoid inter-layer interactions. We have used the germanene lattice constant of 4.26 Å [20]. A small Be or Mg adatom on germanene is simulated along *z*-direction, perpendicular to germanene, while the *x* and *y* directions are parallel with the germanene surface. The Brillouin zone integration is performed using Monkhorst-Pack scheme [21] with 6× 6×1 Γ-centered *K*-point grids.

The calculated charge transfer and the electronic density of states are found using denser *k*-point mesh. First, after the convergence test of the system, the stable height at high symmetry has been obtained. The adsorption of Be and Mg on three adsorption sites: namely, the hollow site (H), which is directly to the center of the hexagonal rings of the germanene, the bridge site (B), which is in between the germanium-germanium bond; and finally, the top site (T), which is directly on top of one of the germanium atoms in the germanene monolayer are also considered in this work. This was followed by the relaxation of the entire system. A single isolated Be and Mg adatoms in a separated with a vacuum of length ~16 Å along *z*-direction.

Discussion

Germanene Monolayer

The germanene monolayer atomic geometries are optimized using BGFS within DFT-GGA as implemented in QE as the initial step. This type of calculation is done with variable-cell optimization so that other analysis uses these optimized both the cell and atomic coordinates, which is beneficial for less or defect-free structure and structural optimization. The bond length between Ge-Ge is 2.3312 Å which is in excellent agreement with the theoretical values reported by [22-23] and the bond angle of Ge-Ge-Ge is 120°. The unit cell and hexagonal lattice structure in 2-D viewed in Burai for monolayer germanene is illustrated in Figure 1.

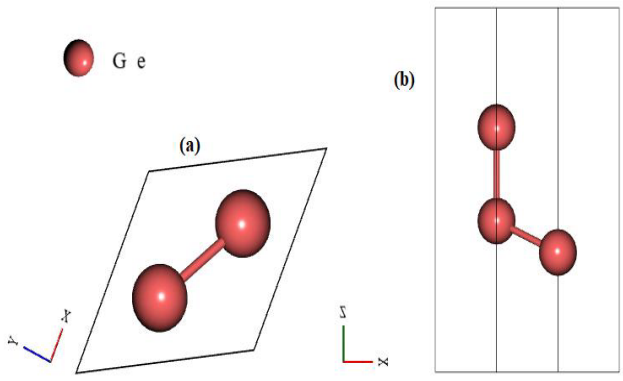

Figure 1:(a) Monolayer graphene unit cell (b) three-dimensional (3D) lattice structure.

From the figure one can see that the unit cell of monolayer germanene contains two germanium atoms. In addition, the shape of the unit cell of monolayer is said to be in a lozenge shape. The lattice structure of the monolayer can be seen to be as a monolayer of atoms with the axis of direction given in both Figure 1(a) & (b). Therefore, these structures are proven accordingly as Germanene monolayer, which is in excellent agreement with the reported results in [16, 22-23].

In order to obtain the most desirable site for alkaline earth metal (AEM) atoms adsorption on germanene monolayer, we firstly choose a (4 × 4×1) germanene supercell as our model, in which the distance between neighboring AEM adatoms is about 15.976Å. The optimized atomic structure

of the germanene supercell is shown in Figure 2. For more simplicity, we symbolize the sublattice along Z coordinate as sublattice A, and the other one as sublattice B. Our calculated equilibrium hexagonal lattice constant a and the buckling height δ are found to be 4.147 Å and 0.689Å respectively. The values are in good agreement with those reported by [16, 22-23].

Adsorption of single Beryllium and Magnesium adatoms on germanene monolayer

This section investigates the adsorption of two different metals, namely Be and Mg adatoms on germanene, thereby to provide comprehensive details of their effects on the electronic structure and density of states properties of single germanene monolayer. In view of these, feasible adsorption consequences, such as charge transfer between Be and Mg adatoms to germanene, *s,p,d*-hybridizations, electronic and structural changes have been carefully analyzed and reported.

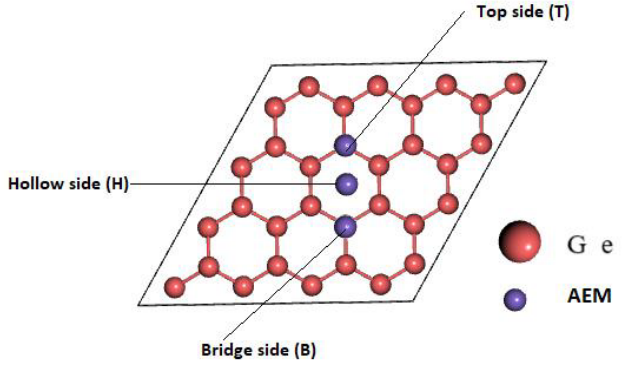

Figure 2: Typical illustration of the three adsorption sites HBT of a relaxed 4 × 4×1 germanene monolayer supercell.

However, these are the starting points towards the discussion of the next section, in which explanations on possible adsorption of AEM on germanene monolayer is given. This is the part of our contributions towards the realization of different types of AEM built on germanene monolayer surfaces. Because, direct integration of germanene with any system that can produces a semiconductor material can be the basis towards achieving high performance germanene/ AEM hybrid-based devices based on their higher carrier mobilities.

Normally, before getting the relaxed structures, the adatoms (Be and Mg) are first placed at the high-symmetry positions (H, B and T) sites in order to find the stable height for the adatoms. Initially, in that position and direction, the symmetry of the system breaks and subsequently the locally stable configurations will be found after relaxation. In Figure 2, the model configurations of the stable height for both AEM adatoms are shown, with adatoms along the *z*-axis and the germanene monolayer. However, the stable distance between the AEM adatoms with Ge atom can be measured. In this case, the measured stable distance between Be and Mg adatoms along the most stable adsorption side (B-side) was found to be around 2.13 Å and 3.60Å respectively. This indicated that the Be adatom has less distance which indicates that it probably be the most stable adatom on germanene monolayer. In order to affirm about the most stable adsorption sites, the adsorption energy was calculated at each chosen site for the each adatom.

Table 1: Calculated optimized structure of the adsorption energies and structural geometry for Be adatom on germanene, H, B and T sites:

	Adsorption sites	E_{ab} (eV)	$d_{Ge\text{-}AEM}$ (Å)	$\Theta^{o}_{AEM\text{-}Ge}$	$d_{Ge\text{-}Ge}$ (Å)
Be/Germanene	H	0.764	2.26	65.2	2.335
	B	0.671	2.13	34.5	2.335
	T	0.660	2.34	89.2	2.335
Mg/Germanene	H	1.172	3.91	39.9	2.345
	B	1.170	3.60	21.2	2.345
	T	1.174	4.05	89.9	2.345

The calculated adsorption energy was done by using the expression below [24].

$$E_{adsorp.} = (E_{Germanene} + E_{AEM}) - E_{AEM/Germanene} \quad (1)$$

where $E_{Germanene}$ is the total energy of the isolated pristine 4×4×1 germanene monolayer supercell, E_{AEM} is the total energy of the adatom, $E_{AEM/Germanene}$ is the total energy of an AEM on top of the germanene monolayer. Our calculated adsorption energies are summarized Table 1 below.

From the two Tables 1, it has been observed that all the calculated adsorption energies are positive which indicated that there is a strong attraction between the Adatom at each chosen sites and process is exothermic. That is the releases energy is favorable meanwhile for the most favourable side we have chosen B side in both Be and Mg absorptions, this is because in each case the absorption energies are lesser and also the bond lengths a smaller when compare with the other sites. These results are in good agreement with many results such as [16, 22-23].

Electronic properties

For the electronic properties, we obtained the electronic band structure and densities of states (DOS) of germanene monolayer are shown in Figure 3 The Band structure was plotted along the high symmetry point Γ →M → K→Γ→A→L in the first Brillouin zone, as shown in Fig. 2(a). At the K- point, the germanene monolayer exhibits a zero-band gap with the Dirac cone similar to that of graphene and silicane. This result is good agreement with previously reported theoretical estimates [25-27].

The total density of states (TDOS) of germanene monolayer shown in Figure 2(b) indicated that the lowest valance bands (about 1.0 state/eV) occur between -6 and -3 eV while the highest valance band (about 4.6 state/eV) is between -1.1 and 2.2eV. This corresponds to the dominated by p orbital of germanium atom as reported by [26]. The lowest and highest conduction band of about 0.56 state/eV and 4.2 state/eV occurs at 6.6eV and 4.9eV respectively indicates the possible domination of both s and p orbitals of Ge atom confirming a possible strong covalent bonding in the germanene monolayer [25-27].

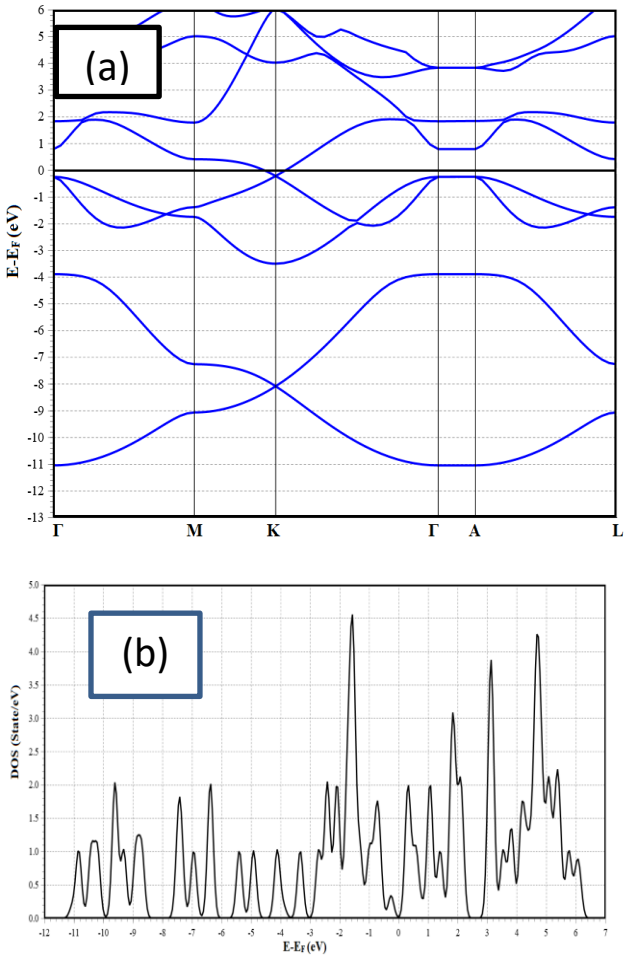

Figure 3: Band structure and Total Density of state (DOS) of pure germanene monolayer.

In other to investigate the electronic properties of AEM adatoms adsorbed germanene monolayer, we consider the calculated band structure and atomic projected density of state of the AEM/germanene at the most stable adsorption side as shown in Figure 2 and 3 for Be/Germanene and Mg/Germanene at B-side respectively.

Figure 4 (a) show the calculated structure of Be adsorbed on the B-side (Be@B-side) of the germanene monolayer, this shows a complete semiconducting nature with opened direct gap of about 0.206 eV along the Γ-A high symmetry points. This result is in agreement with many results reported in [16, 25-27].

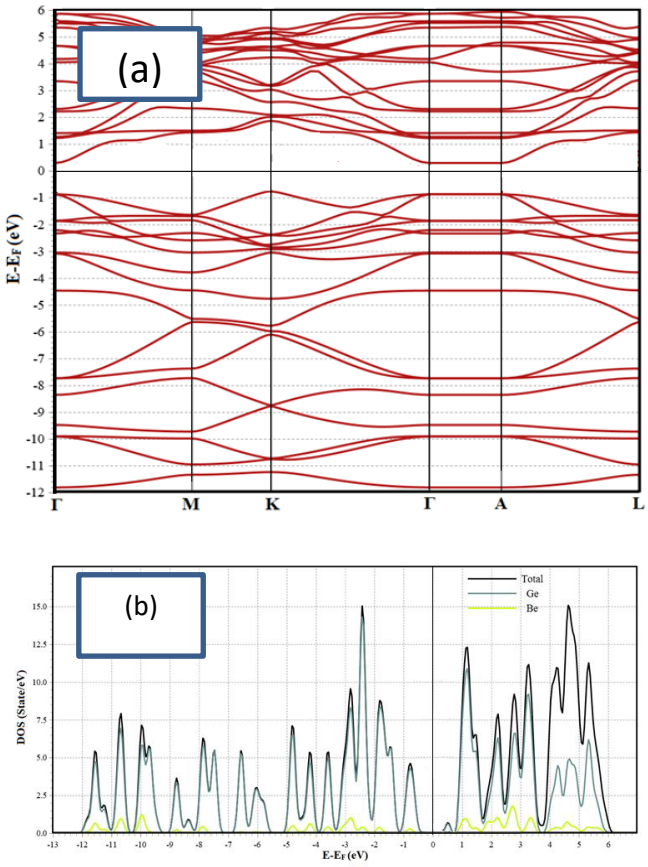

Figure 4: Band structure and Atomic projected Density of state (ADOS)of Be atom on germanene monolayer Be@B-side.

For the obtained atomic density of state (ADOS) of Be@B-side monolayer between -13 to 6eV as shown Figure 4(b). It was observed that that the Ge atom presence is quite similar to the case of pure germanene monolayer, where the p(s) orbitals are the main contributor to form the electronic structure in the considered energy range from − 13 to 6 eV. As expected, the electronic state belonging to the Be adatom throughout the energy range, confirming a possible mixture of ionic and covalent bonding. These finding are in good agreements with the previous results by [16].

Figure 5(a) show the calculated structure of Mg adsorbed on the B-side (Mg@B-side) of the germanene monolayer, this shows a character with that of Be@B-side, only with opened direct gap of about 0.629eV along the Γ-A high symmetry points. Similarly, this result is in agreement with many results reported in [25-27]. For the obtained atomic density of state (ADOS) of Be@B-side monolayer between -13 to 6eV as shown Figure 5(b). It was observed that that the Ge atom presence is quite similar to the case of pure germanene monolayer, where the p(s) orbitals are the main contributor to form the electronic structure in the considered energy range from − 13 to 6 eV. As expected, the electronic state belonging to the Be adatom throughout the energy range, confirming a possible mixture of ionic and covalent bonding. These finding are in good agreements with the previous results by (Pang, et al, 2015).

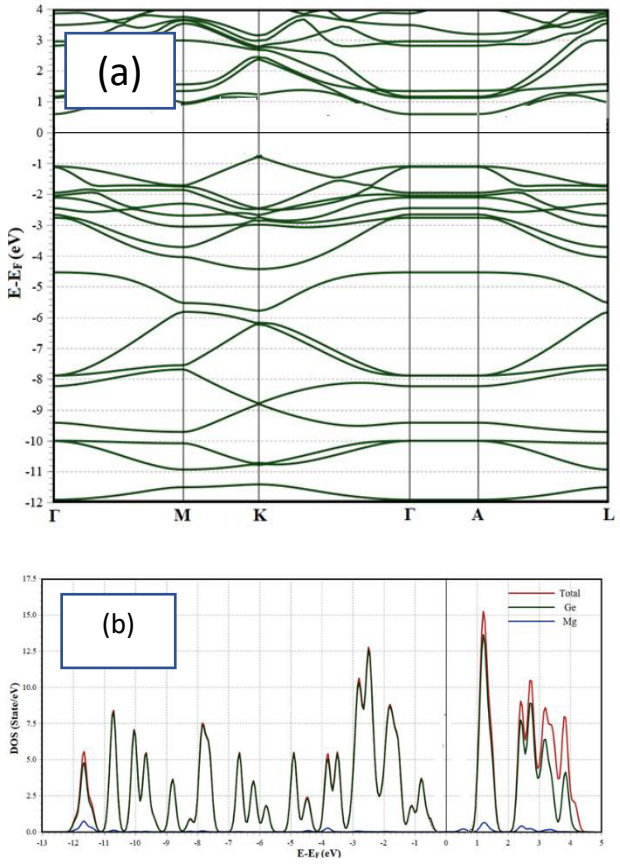

Figure 5: Band structure and Atomic projected Density of state (ADOS) of Mg atom on germanene monolayer Mg@B-side

Conclusion and Future Prospective

Conclusively, first principal plane waves pseudopotential calculations within the frame-work of density functional theory (DFT), are employed to investigate the structural and electronic properties of Be and Mg-adsorption on germanene monolayer. The findings reveal that equilibrium hexagonal lattice constant a and the buckling height δ are found to be 4.047 Å and 0.689 Å respectively, among the chosen adsorption's sites (H, B and T) B side is found to be the most favourable side for both Be and Mg absorptions, due to the less adsorption energy and AEM-Ge distances. For the electronic properties. The Be and Mg adsorptions lead to semiconducting behaviour with direct gap of about 0.206 eV 0.629 eV for Be and Mg adsorption respectively. The obtained results are in agreement with many reported theoretical results.

The results from this study demonstrated that improving the electronic features of germanene, enhances its mobile character and these can be achieved through functionalization or doping techniques with a new model. Therefore, further research is required to speed up the practical applicability of these materials at small scale. Our results obtained from this work confirm the findings of a recent study which show that the electronic properties of germanene could be transformed from semi-metallic to metallic even with the low adsorption of Alkaline earth Thus, further research in the following areas is recommended:

1. Further investigation into quantum transport in germanene with more AEM is required.

2. It will be interesting to investigate the effect of other Metallic materials on electronic properties of germanene; example, Ca, Mn, Fe etc. which are often used for epitaxial growth in micro-electronics production for potential applications.

3. Although, this study has not considered the combine influence of the adsorbed atoms (Be and Mg), it is suggested that subsequent study should at least try to capture those properties, such as exchange interactions between the AEM with germanene.

References

1. M. E. Dávila, Xian, L., Cahangirov, S., Rubio, A., & Le Lay, G. New Journal of Physics, 16(9), 095002. 2014.
2. S., Cahangirov, Topsakal, M., Aktürk, E., Şahin, H., & Ciraci, S. Physical review letters, 102(23), 236804. 2009.
3. N. J. Roome, & Carey, J. D. ACS applied materials & interfaces, 6(10), 7743-7750. (2014).
4. C. C. Liu, Feng, W., & Yao, Y., Physical review letters, 107(7), 076802. (2011).
5. A. Acun, Zhang, L., Bampoulis, P., Farmanbar, M. V., van Houselt, A., Rudenko, A. N., & Zandvliet, H. J. Journal of physics: Condensed matter, 27(44), 443002. (2015).
6. Z. Ni, Liu, Q., Tang, K., Zheng, J., Zhou, J., Qin, R., ... & Lu, J. Nano letters, 12(1), 113-118. (2012).
7. C. Si, Liu, J., Xu, Y., Wu, J., Gu, B. L., & Duan, W. Physical Review B, 89(11), 115429. 2014.
8. S. S. Li, Zhang, C. W., Ji, W. X., Li, F., Wang, P. J., Hu, S. J., ... & Liu, Y. S. Physical Chemistry Chemical Physics, 16(30), 15968-15978. (2014).
9. Y. C. Cheng, Zhu, Z. Y., Mi, W. B., Guo, Z. B., & Schwingenschlögl, U. Physical Review B, 87(10), 100401. (2013).
10. M. W. Chuan, Wong, K. L., Hamzah, A., Rusli, S., Alias, N. E., Lim, C. S., & Tan, M. L.. Current Nanoscience, 16(4), 595-607. (2020).
11. Q. Pang, Zhang, Y., Zhang, J. M., Ji, V., & Xu, K. W. Nanoscale, 3(10), 4330-4338. (2011).
12. H. Sahin, & Peeters, F. M. Physical Review B - Condensed Matter and Materials Physics, 87(8), 085423. (2013).

13. S. Abubakar, Rahman, M. M., Abdullahi, Y. Z., Zainuddin, H., Muhida, R., & Setiyanto, H. Graphene, 1(2), 78-85. (2013).
14. M. M. Rahman, Abdullahi, Y. Z., Shuaibu, A., Abubakar, S., Zainuddin, H., Muhida, R., & Setiyanto, H. Journal of Computational and Theoretical Nanoscience, 12(9), 1995-2002. (2015).
15. J. Chen, Wang, Z., Dai, X., Xiao, J., Long, M., & Chen, T. Physica E: Low-dimensional Systems and Nanostructures, 124, 114365. (2020).
16. S. L. Usman, Shuaibu, A., & Maharaz, M. N. Computational And Experimental Research In Materials And Renewable Energy, 7(1), 9-26. (2024).
17. P. Giannozzi, Baroni, S., Bonini, N., Calandra, M., Car, R., Cavazzoni, C., ... & Wentzcovitch, R. M. Journal of physics: Condensed matter, 21(39), 395502. (2009).
18. J. P. Perdew, Burke, K., & Ernzerhof, M. J. P. R. L. Perdew, burke, and ernzerhof reply. Physical Review Letters, 80(4), 891. (1998).
19. J. Furthmüller, Käckell, P., Bechstedt, F., & Kresse, G. Physical Review B, 61(7), 4576. (2000).
20. L. Zhang, Bampoulis, P., van Houselt, A., & Zandvliet, H. J. Applied physics letters, 107(11). (2015).
21. H. J. Monkhorst, & Pack, J. D. Physical review B, 13(12), 5188. (1976).
22. D. Coello-Fiallos, Tene, T., Guayllas, J. L., Haro, D., Haro, A., & Gomez, C. V. Materials Today: Proceedings, 4(7), 6835-6841. (2017).
23. D. M. Hoat, Nguyen, D. K., Ponce-Perez, R., Guerrero-Sanchez, J., Van On, V., Rivas-Silva, J. F., & Cocoletzi, G. H. Applied Surface Science, 551, 149318. (2021).
24. R. Hussain, Saeed, M., Mehboob, M. Y., Khan, S. U., Khan, M. U., Adnan, M., ... & Ayub, K. RSC advances, 10(35), 20595-20607. (2020).
25. M. R. H. Mojumder, arXiv preprint arXiv:2201.02676. (2022).
26. J. E. Padilha, & Pontes, R. B. Solid State Communications, 225, 38-43. (2016).
27. W. Q. Meysam Bagheri Tagani, Qiwei Tian, Sahar Izadi Vishkayi, Li Zhang, Long-Jing Yin, Yuan Tian, Lijie Zhang, and Zhihui Qin." Applied Physics Letters 121, no. 5 (2022).

Chemical and Green Synthesis of CuO Nanoparticles using *Carica Papaya* Leaf Extract: Structural and Optical properties

Ingalagondi P K[1,a], K Mruthunjaya[2], S M Hanagodimath[3], N C Horti[4,b]

[1] *Department of Physics, Government First Grade College for Women, Davanagere-570 004, Karnataka, India.*
[2] *Department of Pharmacognosy, JSS College of Pharmacy, Academy of Higher Education and Research, Mysuru-570 015, Karnataka, India.*
[3] *Department of Physics, Gulbarga University, Kalaburagi – 585 106, Karnataka, India.*
[4] *Department of Physics, S.S. Government First Grade College and P.G Study Centre, Nargund -582 207, Karnataka, India.*

[a] ings744@gmail.com
[b] ningappa.c.horti@gmail.com

Abstract

This article describes the synthesis of CuO nanoparticles through a two different synthesis routes, namely a chemical co-precipitation and green synthesis route using *Carica papaya* leaf extract and their optical properties. The samples were investigated for their structural and optical properties through X-ray diffraction, scanning electron microscopy, Fourier transfer infrared, UV absorption, photoluminescence and time resolved spectroscopy. The XRD spectra of both samples demonstrate the CuO crystallizes in a monoclinic phase with particle sizes ranging from 20-25 nm. SEM pictures of samples showed the highly agglomerated and spherical particles are formed. The peaks in FTIR spectra are located between 600-1000 cm^{-1}, confirming the formation of CuO phase. The observed shift in UV absorption edge and PL peak of both samples is the result of size quantization and various surface defects. The carrier life time study of both samples revealed the recombination rate of exciton depend on particle size and surface defects. The results of this study indicates CuO is an alternative material for solar cell and optoelectronic devices.

Keywords: Copper oxide, *Carica papaya* leaf extract, Chemical and Green synthesis, Optical properties, Time resolved spectroscopy.
Received 27 January 2025; First Review 02 February 2025; Accepted 07 February 2025

*** Address of correspondence**
Dr. N C Horti
Department of Physics, S.S. Government First Grade College and P.G Study Centre, Nargund - 582 207, Karnataka, India.

Email: ningappa.c.horti@gmail.com

How to cite this article
Ingalagondi P K, K Mruthunjaya, S M Hanagodimath, N C Horti, Chemical and Green Synthesis of CuO Nanoparticles using Carica papaya leaf Extract: Structural and Optical properties, J. Cond. Matt. 2024; 02 (02):12-19.

Available from:
https://doi.org/10.61343/jcm.v2i02.62

Introduction

In recent years, metal oxide (CuO, NiO, ZnO, SnO_2 and TiO_2) nanoparticles have gained a main research focus due to their remarkable properties and diversified applications [1-3]. Among these, copper oxide presents in two phases; CuO (Cupric Oxide) and Cu_2O (Cuprous oxide). CuO has a narrow band gap range of 1.2-1.55 eV and Cu_2O having a band gap of 2.1eV [4-5]. Among these two forms, CuO is a prospective material for photovoltaic devices because of its high absorbance coefficient and narrow band gap [6]. It also has a various applications like gas sensors [7], catalyst [8] lithium-ion batteries [9], magnetic storage devices [10] and high temperature superconductor [11]. The optical properties of CuO nanoparticles not only changes with size, capping agent, calcination temperature and solvents but also sensitive to the precursor used and synthesis route. The synthesis technique could effect on optical properties of CuO nanostructures because of its different oxidation states (CuO, Cu_2O, Cu_2O_3) and size/shape [12]. Although there is a numerous article on the synthesis and optical properties but a lack of attention paid to photo-physical performance of green synthesized CuO nanoparticles using *Carica papaya* leaf extract.

Due to the advancement of nanotechnology, there are now a variety of synthesis routes available to synthesize nanoparticles, including sol-gel [13], hydrothermal [14], chemical co-precipitation [15], solution combustion [16], solid state method [17] and green synthesis route [18-19]. Among them, green synthesis route is an important and cost-effective method as compared to the above-mentioned methods. Moreover, it is an eco-friendly. There are some disadvantages of chemical synthesis routes including that of hazardous starting materials and generation of toxic by-products [20]. Therefore, researchers are motivated to

synthesize nanoparticles through a green synthesis processes using various plant extract. Chan *et al* [21] have developed the CuO nanostructures via green synthesis route using *Garcinia mangostana L.* leaf extract. They noticed the redshift of absorption edge with an increasing calcination temperature due to the aggregation and the growth of particles. Using copper acetate as copper source and *Caloropis procera* leaf extract, Reddy *et. al.* [22] fabricated the CuO nanoparticles through green synthesis route. They found the band gap to be 2.35 eV. Gunalan and his group [23] have synthesized CuO nanoparticles through a chemical and biological route using *Aloe Vera* leaf extract. In their absorption study, they noticed the peaks around at 265 nm and 285 nm due to the surface plasmon resonance and noticed the PL peak around at 600 nm due to the singly ionized oxygen vacancies. Sackey and co-workers [24] have reported the biosynthesis of CuO nanoparticles by employing aqueous extract of Mimosa hamate. They found the band gap around 1.5 eV from diffuse reflectance spectra analysis and antibacterial activities were also studied. A biogenic synthesis of rice shaped CuO nanoparticles via aqueous extract of *Caesalpinia bonducella* seed was reported by Sukumar *et. al.* [25]. They noticed peak at 250 nm in UV absorption spectra due to the surface plasmon resonance and broad peak from 320 nm-600 nm due to the non-oxidized Cu ions. Very recently, bio-synthesis of CuO nanoparticles using *white garland Lily* Leave extract was reported by Nagore *et. al.* [26]. They noticed the absorption edge at 300 nm due to the recombination of exciton and the green-yellow emission at 590 nm. In all of these studies, the CuO have been synthesized by green synthesis route and the optical properties was altered as a result of particle aggregation, singly ionized oxygen vacancies, and non-oxidized Cu ions. The improved optical properties of CuO, making it a unique material for number of scientific and technological applications. A few studies on optical properties of green synthesized CuO nanoparticles have been reported in literature, however optical properties including carrier life time measurement of green synthesized CuO nanoparticles using *Carica papaya* leaf extract have not been thoroughly explored. Furthermore, no studies have been published on comparing optical properties of chemically and green synthesized CuO nanoparticles. In addition, *Papaya* (*Carica papaya L*) is one of the most important medicinal plant and its different parts such as leaves, roots, fruit, flowers, and seeds are used for the treatment to varieties of diseases namely few; diabetes, cancer, heart stroke, blood pressure and many other. They contain the various constituents, including vitamins B, C and E and rich in minerals (Fe, Na and Ca), antioxidants and fibres. Moreover, it is a good as reducing and stabilizing agent. Therefore, in this work we report the chemical and green synthesis of CuO nanoparticles using *Carica papaya* leaf extract and chemical co-precipitation method using $CuSO_4.5H_2O$ as a copper source and the structural and optical properties are investigated.

Materials and Method

SD fine chemicals Pvt Ltd supplied Copper sulphate pentahydrate ($CuSO_4.5H_2O$), Sodium hydroxide (NaOH) pellets, Ethanol (HPLC grade) and *Papaya* (*Carica papaya L*) leaf extract.

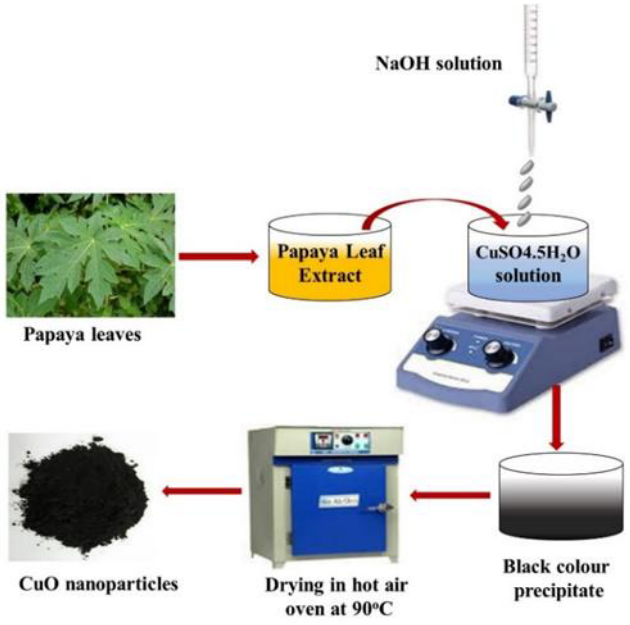

Figure 1: Flow diagram of green synthesis of CuO nanoparticles.

Chemical synthesis of CuO nanoparticles

In chemical synthesis of CuO nano powder, the preparation of $CuSO_4.5H_2O$ (2.496 gm) and NaOH (0.8 gm) solutions were prepared in 50 ml and 20 ml of de-ionized water, respectively. Then, the addition of prepared NaOH solution drop-by drop to $CuSO_4.5H_2O$ solution. During reaction, the black color $Cu(OH)_2$ precipitate was formed. The black-colored precipitate was filtered and washed thoroughly for 3-4 times using ethanol and de-ionized water to purify the product. Then, the powder was heated at 90 °C in hot air oven before being calcined at 500 °C in muffle furnace for two hours.

Preparation of *papaya* leaf extract

Carica papaya leaves were collected from local garden of Gulbarga University, Kalaburagi. India. The collected papaya leaves (20 gm) were washed 3-4 times with de-ionized water to eliminate dust particles. Using domestic mixture, the cleaned *papaya* leaves were grinded and heated in 100 ml of deionized water for two hours. After two hours of heating, the pale yellow colour solution was found and filtered using Whatman paper. Thereafter, the leaf extract was stored in 5 °C till use for next synthesis.

Green synthesis of CuO nanoparticles

In procedure of green synthesis, the solution of $CuSO_4.5H_2O$ was prepared in 50 ml of de-ionized water and treated with 20 ml of prepared *papaya* leaf extract and stirred for an hour. pH of the mixture solution was maintained 7 by adding 0.1M NaOH solution and a black colored precipitate was appeared. The resulted precipitate was washed repeatedly using ethanol and de-ionized water to purify the product. At last, the sample was calcined at 500 °C for two hours in muffle furnace. The flow diagram for green synthesis of CuO nanoparticles is shown in figure 1. Here, we indicated the chemically synthesized sample as S_1 and the green synthesized sample as S_2.

Characterization methods

To collect XRD data of samples, Smart Lab SE, Rigaku X-ray diffractometer with CuKα radiation of wavelength (0.15406 nm) was used. Surface morphology and size distribution of samples were analyzed through MIRA3 LMH TESCAN scanning electron microscopy. Nicolet-6900, FTIR spectrophotometer was utilized to confirm the formation of CuO nanoparticles. UV absorption measurement of samples were carried out by JASCO, V-670 UV–Vis absorption spectrophotometer. Fluorescence emission spectra were recorded using Hitachi, F-7100 spectrophotometer and Chronos BH, ISS spectrofluorometer was used to record the carrier lifetime of samples.

Results and discussion

XRD analysis

In figure 2 (a-b) we depict the X-ray diffraction pattern of sample S_1 and S_2, respectively. In the XRD pattern of both samples, all XRD peaks confirm the formation of monoclinic CuO phase and well coincides with JCPDS No-45-0937 [27-28]. The peaks at 2θ are 32.58°, 35.58°, 38.70°, 48.79°, 53.55°, 58.48°, 61.55°, 66.39°, 68.12°, 72.46°, 75.29° corresponding to planes (110), (002), (111), (-202), (020), (202), (-113), (022), (220), (-312) and (004) respectively. The sharp and narrow peaks of sample S_1 indicates high crystallinity and larger particle size as compared to sample S_2. No any characteristics peaks of $Cu(OH)_2$ and Cu_2O were observed, indicating the sample S_1 is crystalize in pure CuO with monoclinic phase. Some extra peaks were appeared in XRD spectrum of sample S_2 (Fig. b), which indicates the left overs of some minerals, vitamins and fibres of *papaya* leaf extract (indicated by asterisk). The particle size of samples was determined by adopting Scherrer formula and is given by [29]

$$D = \frac{K\lambda}{\beta Cos\theta} \quad (1)$$

here D: particle size, β: FWHM of peak, λ: X-ray wavelength and θ being the glancing angle. The particle size S_1 sample is found to be 23.65 nm and that of sample S_2 is 16.37 nm.

For monoclinic structure, $a \neq b \neq c$, $\alpha = \gamma = 90°$ and $\beta > 90°$, the lattice parameters were calculated by following expression [30-31].

$$d_{hkl} = \left[\frac{\left(\frac{h^2}{a^2}\right)+\left(\frac{l^2}{c^2}\right)-\left(\frac{2hl}{ac}\right)cos\theta}{sin^2\beta} + \frac{k^2}{b^2}\right]^{-1/2} \quad (2)$$

Where d_{hkl} : interplanar spacing. h, k and l: miller indices. The dislocation density was evaluated by equation (3)

$$\delta = \frac{1}{D^2} \quad (3)$$

Where δ : dislocation density. The micro strain in lattice is caused by the presence of lattice imperfection and is calculated by [32]

$$\varepsilon = \frac{\beta}{4tan\theta} \quad (4)$$

The usual meaning of term ε and β are the micro-strain and FWHM of peak, respectively. The values of estimated parameters are tabulated in table 1. It is noticed the difference in particle size and surface imperfections causes a change in the values of micro strain, dislocation density, and lattice parameters with different synthesis processes.

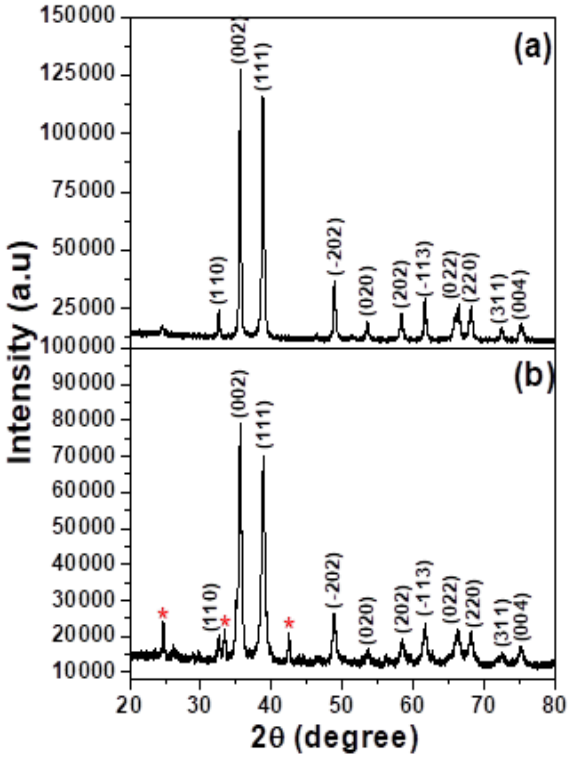

Figure 2: XRD spectrum of (a) S_1 and (b) S_2 sample.

Table 1: Estimated value of particle size, micro strain, dislocation density and lattice parameters of both samples.

Sample Name	Crystallite Size (nm)	Dislocation density (Lines/m^2) X 10^{15}	Microstrain (ε) X 10^{-3}	Lattice parameter (Å)		
				a	*b*	*c*
S_1	23.65	1.78	2.8	4.6893	3.4691	5.1327
S_2	16.37	3.73	5.1	4.6842	3.4237	5.1153

Morphological study

In figure 3(a-b) we show the morphological analysis of S_1 and S_2 sample, respectively. SEM image (a) shows the formation of highly agglomerated and spherical shaped particles are formed. The formation of irregular and agglomeration of particles were noticed from image (b), which indicates the change in reaction rate with various constituents of papaya leaf extract and remains of minerals of *papaya* leaf extract in the sample after washing.

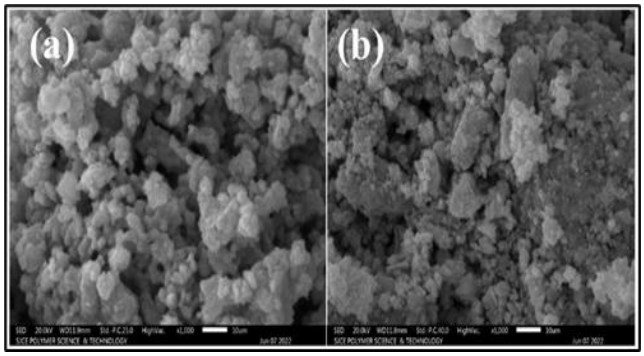

Figure 3: SEM images of (a) S_1 and (b) S_2 samples

Fourier Transform Infrared (FTIR) analysis

Figure 4 (a-b) shows the FTIR result of sample S_1 and S_2. In FTIR spectrum of sample S_1 (Fig. a), the peak at 517 cm^{-1} is assigned to the Cu-O mode of monoclinic phase [33-34]. The peak noticed at 1094 cm^{-1} due to the triply degenerative SO_4^{-2} vibration modes [35]. The band observed at 1384 cm^{-1} due to the vibration OH modes linked with copper atom [36]. The peaks at 1638 cm^{-1} and 3431 cm^{-1} are attributed to the –OH stretching/ bending vibration modes of adsorbed atmospheric moisture on surface of nanoparticles [37-38]. From FTIR spectrum of sample S_2 (Fig. b), the peaks noticed at 518 cm^{-1} and 610 cm^{-1} are corresponding to Cu-O vibration modes [39-40]. The peaks noticed around at 885 cm^{-1}, 1115 cm^{-1} and 2924 cm^{-1} are due to the vibration modes of various constituents of *papaya* leaf extract absorbed on particle surface [41-42]. The peak centered at 3483 cm^{-1} due to the vibration of hydroxyl group of water molecules [43].

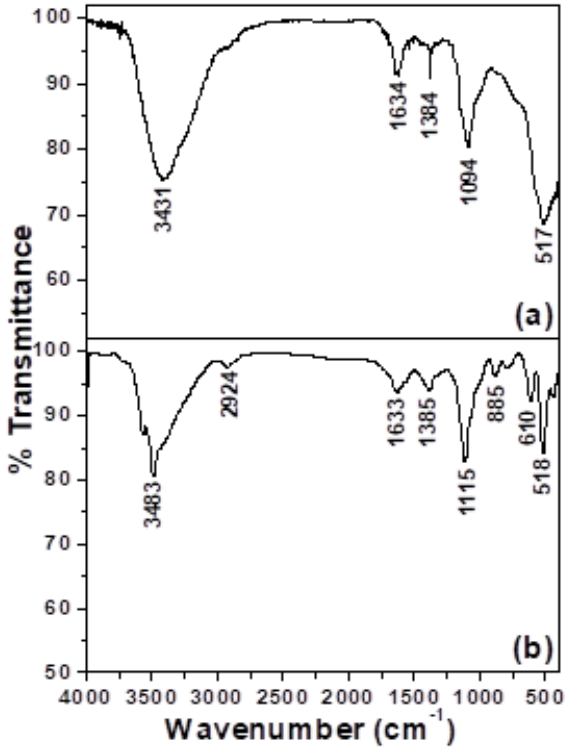

Figure 4 (a-b): FTIR spectra of sample S_1 and S_2.

UV-Visible absorption measurements

Figure 5(a-b) depict the UV-Vis absorption curve of sample S_1 and S_2, respectively. The absorption onset for the S_1 sample is noticed at 299 nm and that of sample S2 at 287 nm due to the direct charge transition from valence band to conduction band (O^{2-} to Cu^{2+} ion) [26,44]. The absorption edge of CuO nanoparticles depend on various factors like particle size, band gap, surface defects (oxygen vacancies) and synthesis techniques. The absorbance peak of sample S_2 is found at lower wavelength as compared to the S_1 sample which may ascribed to the smaller particle size.

Using Tauc relation, the energy gap of samples was evaluated [45,46] and is given by

$$(\alpha h\nu)^n = A(h\nu - E_g) \qquad (5)$$

Where, α: absorption coefficient, hv: photon energy and E_g: energy gap and the value of n is indicates the nature of

transition. In this case, we choose n = 2 for direct transition. In figure 6, we provided the Tauc plot of the samples S_1 and S_2. The energy gap is found to be 3.51 eV for the sample S_1 and that of sample S_2 is 3.57 eV. It is clearly noticed that the change in absorption edge and the value of energy band gap of samples with different synthesis routes due to the change in particle size and supported by XRD results. Furthermore, the obtained value of energy gap is greater than of bulk CuO and well matches with previously reported values of E_g by other researchers [47-48].

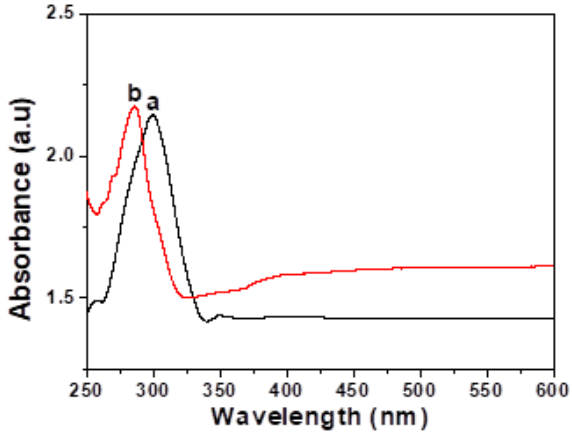

Figure 5: Absorption spectrum of sample S_1 (curve-a) and S_2 (curve-b).

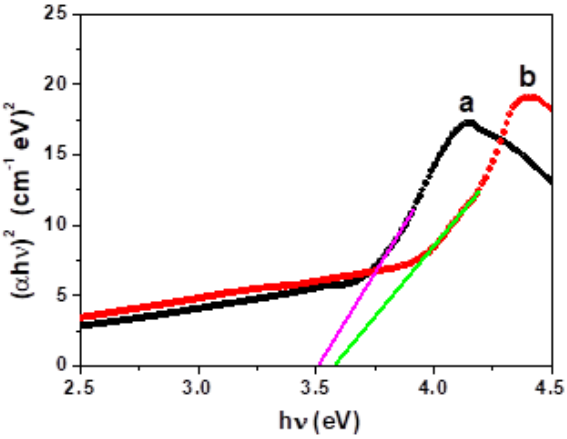

Figure 6: Tauc plot of sample (a) S_1 and (b) S_2.

Photoluminescence Study

Photoluminescence (PL) analysis is a significant tool for examining the optical emission of materials. The main sources of emission centers in metal oxides are oxygen vacancies and metal interstitials which varies with particle size, shape, composition and synthesis route [49]. PL spectra of CuO samples with different excitation wavelengths (400 nm, 410 nm, 420 nm, 430 nm) were recorded at room temperature and results are presented in figure 7 (a-b). The strong photoluminescence peak centred at 485 nm for the sample S_1 and that of sample S_2 at 472 nm due to the near band edge electron-hole recombination [50]. The peak position of sample S_1 shifted towards the higher wavelength as compared to S_2 sample, indicating the larger particle size of sample S_1 over sample S_2. The change in particle size with synthesis route due to the aggregation of particle in solution. When particles are reduced to the nanoscale, FL is influenced by many factors including a high surface area and surface imperfections. PL intensity of S_1 sample is a higher than of sample S_2 because of its larger particle size causes the decrease in number of surface defects which enhance the rate of exciton recombination [51]. Moreover, the weaker PL intensity of sample S_2 as compared to PL intensity of sample S_1 indicates the higher density of structural defects and impurities caused by remains of some minerals, vitamins and fibres of papaya leaf extract after sample washing, which is consistent with our XRD results. These surface imperfections promote the non-radiative recombination of electron-hole pairs, resulting in a drop in PL intensity. A notable shift of PL peak and PL intensity of samples with synthesis routes may be result of change in particle size and the presence of surface defects such as oxygen vacancies, metal interstitials and minerals of *papaya* leaf extract. The same behaviour was noticed by Das *et. al.* [52] for bio-synthesized CuO nanoparticles using *Madhuca longifolia* plant extract. It is concluded that the variation of PL properties depends of particle size and surface defects which may alter with synthesis routes.

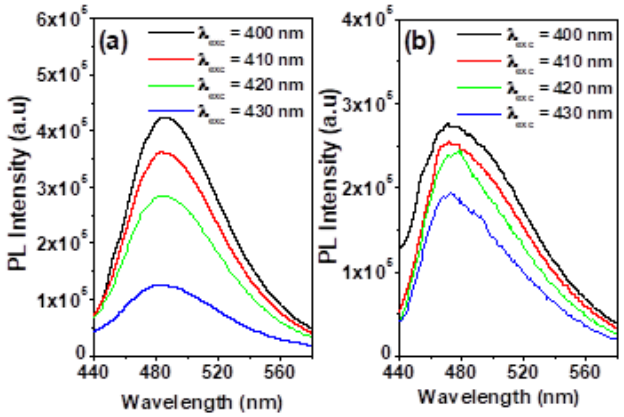

Figure 7 (a-b): Photoluminescence spectra of sample S_1 and S_2, respectively, with different excitation wavelength.

Time Resolved Spectroscopy

To know more information about particle size and surface defect related radiative electron hole recombination, Fluorescence (FL) life time measurement of samples were carried out by time co-related single photon counting system and results are given in figure 8(a-b). Fluorescence decay curves of CuO samples are well fitted with bi-exponential function and the value of χ^2 is nearly equal to a unity. FL decay of CuO depend on the various parameters including dopants, surface defects, solvent media and synthesis route. The synthesis methodology could affect the

carrier life time of materials due to the changes in surface defects and particle size. In present case, the decay curve of samples associated with direct recombination electron-hole pairs (fast decay) and the trapping of carriers in surface defects (slow decay) [53]. The value of τ_2 is smaller than τ_1 because of fast decay as a result of rapid radiative recombination of trap states electron after escaping from these states.

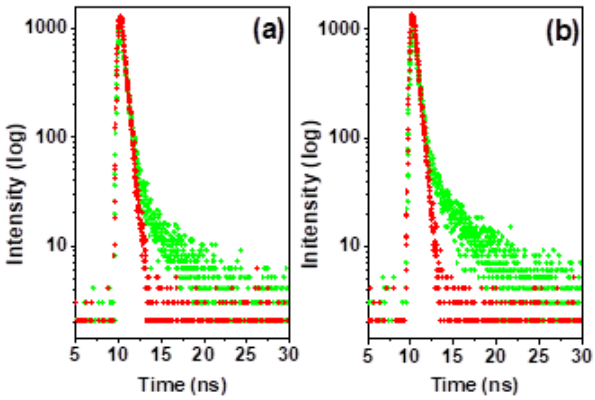

Figure 8(a-b): Fluorescence decay curves of samples S_1 and S_2, respectively.

Using fitted parameters, we have evaluated the average carrier life time of samples by following an expression [54].

$$\tau_{ave} = \frac{\sum_{i=1,2\ldots} A_i \tau_i^2}{\sum_{i=1,2\ldots} A_i \tau_i} \qquad (6)$$

Where, τ_{ave} represent the average carrier life time. A is the amplitude of decay curve. The obtained value of traced parameters and the average carrier life time of both samples are summarized in table 2. It is found that the sample S_2 has a longer average carrier life time than of sample S_1 ascribed to the trapping of charge carrier in surface defects and the smaller particle size. As a particle size increases, the average carrier life time increases due to the trapping of carrier in impurities by residual fibres and minerals of *papaya* leaf extract after washing. This is well consistent with our steady state fluorescence analysis and the particle size analysis XRD data. The density of oxygen vacancy and grain boundary are decreases with an increasing particle size causing short carrier life time [55]. This study highlights the variation of carrier lifetime of samples with synthesis techniques due to the trapping of carriers in surface defects and change in particle size.

Conclusion

In summary, CuO nanoparticles have been synthesized through two distinct synthesis techniques, namely green synthesis and a chemical co-precipitation process. The structural and optical properties of samples were examined using XRD, SEM, FTIR spectroscopy, UV absorption, photoluminescence and time resolved spectroscopy. XRD pattern of samples revealed the appearance of CuO in monoclinic phase. SEM images display the highly agglomerated, irregular and spherical shaped particles are formed. The existence of peaks ranging from 600-1000 cm^{-1} in FTIR spectra confirms the formation of CuO monoclinic phase. From band gap estimation, the value of band gap is found to be 3.51 eV and 3.57 eV for the sample S_1 and S_2, respectively. From PL study, the sample S_1 shows the higher PL intensity than of S_2 sample because of its larger particle size and presence of various surface defect (oxygen vacancies and Cu ions) and well supported by carrier life time measurements. According to this study, CuO is the most suitable material for optoelectronic applications.

Acknowledgements

Authors thanks to SJCE polymer science and technology laboratory, Mysore, Karnataka, India for providing the facility of XRD and SEM characterization.

Table 2: Calculated value of fitted parameters and average carrier life time.

Sample Name	τ_1(ns)	τ_2 (ns)	A_1	A_2	τ_{ave} (ns)	χ^2
S_1	2.19	0.0215	0.107	0.893	2.02	1.03
S_2	3.11	0.0298	0.115	0.885	2.89	1.01

References

1. N. C. Horti, M. D. Kamatagi, N. R. Patil, S. K. Nataraj, M. S. Sannaikar and S. R. Inamdar, Optik.194:163070, 2019.
2. P. K. Ingalagondi, N. C. Horti, Y. T. Ravikiran, M. Prashantkumar and B. G. Kumaraswamy, Chem Papers. 78:3331–3342, 2024.
3. N. C. Horti, M. D. Kamatagi, S. K. Nataraj, M. S. Sannaikar, and S. R. Inamdar, AIP Conf.Proc.2274: 020002, 2020.
4. K. Khojier, H. Savaloni and Z. Sadeghi, J.

Theoretical & Appl. Phys. 8:116, 2014.
5. W. J. Lee and X. J. Wang, Coatings. 11:864, 2021.
6. K. Das, S. N. Sharma, M. Kumar and S. K. De, J. Appl. Phys. 107:024316, 2010.
7. S. Sharma, K. Kumar, N. Thakur, S. Chauhan and M. S. Chauhan, J. Environ. Chem. Engineer. 9:105395, 2021.
8. J. C. Yan, W. Tianyi, M. Y. Liu and Z. Yuan, J. Nat. Ga. Chem. 20:669-676, 2011.
9. X. P. Gao, J. L. Bao, G. L. Pan, H. Y. Zhu, P. X. Huang, F. Wu and D. Y. Song, 108: 5547–5551, 2004.
10. R. A. Borzi, S. J. Stewart, R. C. Mercader, G. Punte and F. Garcia, J. Magnetism & Magnetic Mater. 226–230:1513–1515, 2011.
11. I. Y. Erdogana and O. Gullub, J. Alloys. Comp, 492: 378–383, 2010.
12. M. Censabella, V. Iacono, A. Scandurra, K. Moulaee, G. Neri, F. Ruffino, S. Mirabella, Sensors and Actuators B: Chemical. 358:131489, 2022.
13. F. Wang, H. Li, Zyaan, Y. Sun, F. Chang, H. Deng, L. Xie and H. Li, RSC Advan, 6: 79343-79349, 2016.
14. M. Chandrasekar, M. Subash, S. Logambal, G. Udhayakumar, R. Uthrakumar, C. Inmozhi, W. A. Al-Onazi, A. M. Al-Mohaimeed, T. W. Chen and K. Kanimozhi, J. King Saud Univer - Sci, 34: 101831, 2022.
15. N. C. Horti, M. D. Kamatagi, N. R. Patil, M. N. Wari, and S. R. Inamdar, Optik, 169: 314-320, 2018.
16. M. R. Islam, J. E. Obaid, M. Saiduzzaman, S. S. Nishat, T. Debnath and A. Kabir, J. Phys. Chem. Solids, 147: 109646, 2020.
17. N. C. Horti, M. D. Kamatagi and S. K. Nataraj, AIP Confer. Proceed., 2100, 020048, 2019.
18. R. Chowdhury, A. Khan and M. H. Rashid, RSC Advan, 10:14374-14385, 2020.
19. Z. Alhalili, Arabian J. Chem. 15: 103739 2022.
20. Ishwarya M. S, N. C. Horti, M. D. Kamatagi and Lokesh. S, 8: 717- 725, 2021.
21. Y. B. Chan, V. Selvanathan, L. H. Tey, M. Akhtaruzzaman, F. H. Anur, S. Djearamane, A. Watanabe and M. Aminuzzaman, Nanomaterials, 12: 3589, 2022.
22. K. Rayapa Reddy, J. Mole. Stru, 1150: 553-557, 2017.
23. S. Gunalan, R. Sivaraj and R. Venckatesh, Spectrochimica Acta Part A, 97: 1140–1144 (2012).
24. J. Sackey, L. C. Razanamahandry, S. K. O. Ntwampe, N. Mlungisi, A. Fall, C. Kaonga, and Z. Y. Nuru, Mater. Today: Proc. 36:540-548, 2021.
25. S. Sukumar, A. Rudrasenan and D. P. Nambia, ACS Omega. 5: 1040–1051, 2020.
26. P. B. Nagore, A. J. Ghoti, A. P. Salve and K. G. Mane, Bio. Nano. Sci. 12: 1086–1096 2022.
27. C. Jing, C. J. Yan, X. T. Yuan and L. P. Zhu, J. Photochem. Photobio B: Bio. 198: 111557, 2019.
28. D. P. Volanti, D. Keyson, L. S. Cavalcante, A. Z. Simoes, M. R. Joya, E. Longo, J. A. Varela, P. S. Pizani and A. G. Souza, J. Alloys. Comp. 459: 537–542, 2008.
29. N. C. Horti, A. Samage, M. A. Halakarni, S. K. Chavan, S. R. Inamdar, M. D. Kamatagi and S. K. Nataraj, Mater. Chem. Phys. 318:129276, 2024.
30. R. Javed, M. Ahmed, I. Haq, S. Nisa, M. Zia, Mater. Sci & Eng: C, 79:108-115, 2017.
31. S. Sharma, K. Kumar, N. Thakur, S. Chauhan, M. S. C hauhan, J. Environ. Chem. Eng, 9: 105395, 2021.
32. D.U.Beelagi, N.C.Horti and M.D.Kamatagi, J. Phys.:Conf.Ser. 2603: 012001, 2023.
33. K. K. Sahu, B. Raj, S. Basu and M. Mohapatra, ACS Omega, 6: 1108−1118, 2021.
34. E. Bharathi, G. Sivakumari, J. Kamalakkannan, B. Karthikeyan and S. Senthilvelan, Mater. Sci. Ene. Tech, 3: 407- 419, 2020.
35. N. C. Horti, M. D. Kamatagi, N. R. Patil, M. S. Sannaikar and S. R. Inamdar, J. Nanophoton, 14: 046010, 2020.
36. K. Phiwdang, S. Suphankij, W. Mekprasart and W. Pecharapa, Energy Procedia, 34:740-745, 2013.
37. P. Chand, Manisha and P. Kumar, Optik, 156:743-753, 2018.
38. M. S. Jagadeesan, K. Movlaee, T. Krishnakumar, S. G. Leonardi and G. Neri, J. Electroanal. Chem, 835:161-168, 2019.
39. J. K. Sharma, M. S. Akhtar, S. Ameen, P. Srivastava and G. Singh, J. Alloys. Comp. 632: 321-325, 2015.
40. A. Santha, Rintu Varghese, H. Joy Prabu, I. Johnson, D. Magimai Antoni Raj and S. John Sundaram, Mater. Today: Proc. 36: 447- 452, 2021.
41. S. H. Sabeeh, H. A. Hussein and H. K. Judran, Mater. Res. Express. 3: 125025, 2016.
42. G. Sharmila, R. Sakthi Pradeep, K. Sandiya, S. Santhiya, C. Muthukumaran, J. Jeyanthi, N. Manoj Kumar and M. Thirumarimurugan, J. Mole. Stru. 1165: 288-292, 2018.
43. E. Nagaraj, K. Karuppannan, P. Shanmugam and S. Venugopal, J. Cluster. Sci. 30: 1157–1168, 2019.
44. P. Nagore, S. Ghotekar, K. Mane, A. Ghoti, M. Bilal, A. Roy, Bio-Nano Science. 11: 579 - 589, 2021.
45. J. Tauc, A. Menth, J. Non-Crystalline Solids, 8-10: 569–585, 1972.
46. N. C. Horti, M. D. Kamatagi, N. R. Patil, S. K. Nataraj, S. A. Patil and S. R. Inamdar, Polym.Bull, 78: 6321-6336, 2021.
47. Z. R. Parekh, S. H. Chaki, A. B. Hirpara, G. H. Patel, R. M. Kannaujiya, A.J. Khimani, and M. P. Deshpande, Physica B: Conden. Matter, 610: 412950, 2021.
48. M. B. Mobarak, M. S. Hossain, F. Chowdhury and

S. Ahmed, Arabian J. Chem, 15: 104117, 2022.
49. W. Ding, D. Liu, J. Liu, J. Zhang, Chinese Journal of Chemistry, 38: 1832-1846, 2020.
50. A. El-Trass, H. ElShamy, I. El-Mehasseb and M. El-Kemary, Appl. Sur. Sci, 258: 2997- 3001, 2012.
51. H. Siddiqui, M. S. Qureshi and F. Z. Haque, Optik, 125: 4663-4667, 2014.
52. P. Das, S. Ghosh, R. Ghosh, S. Dam and M. Baskey, J. Photochem. Photobio. B: Bio. 189: 66-73, 2018.
53. A. D. Pramata, K. Suematsu, A. T. Quitain, M. Sasaki, and T. Kida, Advan. Fun. Mater, 28: 1704620, 2017.
54. N. C. Horti, M. D. Kamatagi, S. K. Nataraj, M. N. Wari and S. R. Inamdar, Nano Express, 1: 010022, 2020.
55. A. Seetharaman, D. Sivasubramanian, V. Gandhiraj, and V. R. Soma, J. Phys. Chem. C, 121: 24192-24205, 2017.

Polyaniline Doped Zinc-Oxide Nanocomposite for Electrochemical Super-Capacitor Applications

Arti M. Chaudhari[1,a], Bharti S. Anerao[2,b]

[1] *Department of Physics, Yeshwant Mahavidyalaya, Wardha - 442001, Maharashtra, India*
[2] *Department of Physics, D. R. B. Sindhu Mahavidyalaya, Nagpur - 440017, Maharashtra, India*

[a] artichaudhari222@gmail.com
[b] bhartianerao@gmail.com

Abstract

Zinc oxide nanoparticles were synthesized via sol-gel approach. Synthesized crystalline Zinc Oxide nanoparticles with size 20nm are uniformly deposited on the surface of Polyaniline prepared by the method of in situ chemical oxidative polymerization. Synthesized Zinc Oxide/PANI nanocomposite was investigated by X-ray diffraction and transmission electron microscopy. X-Ray Diffraction study revealed that the structure of Zinc Oxide nanoparticle is hexagonal with space group P63mc.TEM image of Zinc Oxide/PANI nanocomposite shows that Zinc Oxide nanoparticles are uniformly embedded in PANI matrix. These results highly indicate ZnO nanoparticles used as an electrode material and provide higher specific capacitance and energy density for electrochemical Super-capacitor applications.

Keywords: ZnO, ZnO/PANI, XRD, TEM.
Received 27 January 2025; First Review 29 January 2025; Accepted 02 February 2025

*** Address of correspondence**
Dr. Bharti S.Anerao
Assistant Professor, Department of Physics, D. R. B. Sindhu Mahavidyalaya, Nagpur - 440017, Maharashtra, India

Email: bhartianerao@gmail.com

How to cite this article
Arti M. Chaudhari, Bharti S. Anerao, Polyaniline doped Zinc-Oxide nanocomposite for Electrochemical Super-capacitor Applications, J. Cond. Matt. 2024; 02 (02): 20-22.

Available from:
https://doi.org/10.61343/jcm.v2i02.63

Introduction

Transition metal oxides have gained more interest as electrode materials in Supercapacitor applications in the last decades due to their extremely high theoretical capacity ($372 mAhg^{-1}$) with the conventional carbon materials [1]. Among them, Zinc oxide (ZnO) has a wide band gap semiconductor of 3.3eV with large exciton binding energy of 70 meV. ZnO has broad range of applications in the manufacturing of magnetic materials, alkaline battery anodes, dye-sensitized solar cells, semiconductors, solid oxide fuel cells (SOFC), antiferromagnetic layers, p-type transparent conducting films, electrochromic films, heterogeneous catalytic materials and gas sensors [2-3]. ZnO is unique material possesses advantage such as high specific energy, high chemical stability, facile preparation, morphologic diversity and prolonged lifecycle. Therefore, research towards finding new anode materials for super-capacitor applications has been accelerated. The high-energy density materials can be achieved by either increasing charge capacity of the anode or increasing the working potential of the anode materials. Recently, conducting polyaniline has been studied as an additive to improve the performance of anode materials in Supercapacitor applications [4]. When ZnO nanoparticles incorporated in PANI matrix, would result from synergistic effect from the faradic capacitance of the ZnO and double layer capacitance of the PANI [5]. In the present study, we have synthesized ZnO and ZnO/PANI nanocomposite and characterized by XRD and TEM. Further electrochemical properties were investigated for super-capacitor applications.

Synthesis of ZnO/PANI nanocomposite

Zinc oxide (ZnO) nanoparticle was synthesized via sol-gel approach as given in reference [6]. The synthesized 40 wt % of ZnO nanoparticles will be incorporated in PANI matrix by an in-situ chemical oxidative polymerization method [7]. We have chosen 40 wt% of ZnO/PANI comparison with other loadings because it provides optimal dispersion and interfacial interactions between ZnO and PANI chains leading to improved properties.

In a typical procedure, 0.931 gm. of aniline dissolved in 100 ml of 1.388ml of H_2SO_4 solution and stirred for 1 hour, then mixed with 10 ml of sonicated zinc oxide nanoparticles by further sonication for 30 min. increased sonication time

can lead to a decrease in particle size, resulting in more uniform distribution. 100 ml of 1M of H_2SO_4 solution containing 2.28 gm. $(NH_4)_2S_2O_8$ (APS) are then slowly added drop wise to well dispersed suspension mixture for 2 hours with a continuous stirring. Concentration of the material can impact material properties like mechanical strength, thermal conductivity and optical properties ultimately affecting the materials performance in various applications.

After 3 hours, a good degree of polymerization will have achieved as observed by the change in colour from blue to blackish green. The precipitate produced in the reaction will be removed by filtration, washed repeatedly with 1M of H_2SO_4 and dried under vacuum for 24 hours. The conductive emeraldine salt (ES) form of ZnO/PANI nanocomposite powder will be obtained.

Discussions

Figure 1 shows the X-ray diffraction spectra of ZnO and ZnO/PANI nanocomposite. After addition of ZnO nanoparticles in PANI matrix, amorphous nature of PANI changes and found crystallinity distributed in ZnO/PANI nanocomposite due to nucleating effect of ZnO. XRD pattern of ZnO nanoparticles consist of diffraction peaks for 2θ = 31.789˚, 34.439˚, 36.277˚, 47.581˚, 56.639˚, 62.896˚, 67.8˚, 69.12˚, 77.00˚ which corresponds to the (100), (002), (101), (102), (110), (103), (200), (201) and (202) plane of hexagonal phase of ZnO respectively [8]. The peaks clearly indexed the formation of ZnO structure from JCPDS powder diffraction card file. A most intense peak at 2θ = 36.27^0 was obtained along (1 0 1) orientation. The patterns are in accordance with the typical zincite structure ZnO diffraction (hexagonal phase, space group P63mc, with lattice constant a = 3.249 A^0).

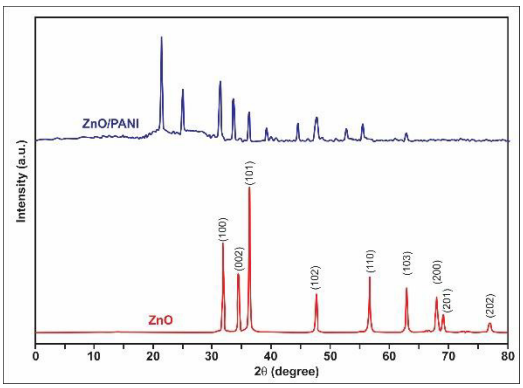

Figure 1: XRD spectra of ZnO and ZnO/PANI nanocomposite.

The diffraction peaks of ZnO nanoparticles and ZnO/PANI composites have been indexed to the hexagonally Wurtzite structured ZnO which were well matched with that in JCPDS data (36-1451). The average crystallite size of ZnO and ZnO/PANI nanocomposite was calculated using Scherer's formula [9] from the diffraction peaks. The XRD pattern of ZnO/PANI nanocomposite shows the two broad peaks are observed at 2θ = 20.73° and 25.62° indicated that ZnO crystallites have been uniformly mixed within the polymer chain.

Table1: XRD analysis Properties and crystallite size

Product	2Θ Degree	FWHM	hkl	Crystallite size (nm)
ZnO	36.28	0.281	(100)	20
ZnO [10]	36.50	0.056	(100)	21.8
ZnO/PANI	20.73	0.270	(020)	21
ZnO/PANI[10]	19.08	0.448	(020)	21.8

The TEM images of the synthesized ZnO and ZnO/PANI nanocomposites have been shown in figure 2 (a) and 2 (b) respectively. The shapes of the ZnO particles are nearly spherical and obviously demonstrate aggregation of the particles. The aggregation of particles should have been originated from the large specific surface area and high surface energy of ZnO nanoparticles [11]. Aggregation can enhance the electrochemical stability of the material, reducing the likelihood of electrochemical degradation and improving the lifespan of the device. As can be seen in Fig. 2b, the morphology of ZnO is irregular and the ZnO nanoparticles were attached with PANI matrix during polymerization [12]. The TEM image of ZnO/PANI nanocomposite indicate that the transformation of highly branched like polyaniline which have granular-like structure. The TEM image also reveals the presence of ZnO in polyaniline which is homogeneously distributed throughout the polyaniline.

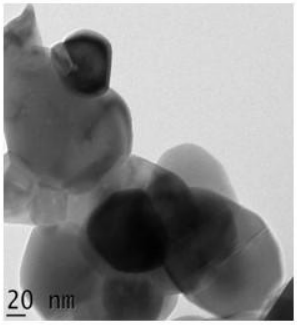

Figure 2 (a): TEM image of ZnO

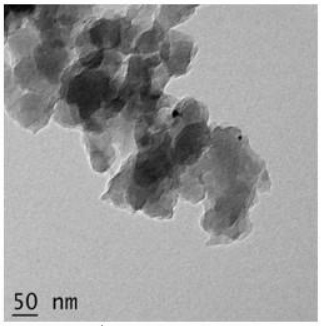

Figure 2 (b): TEM image of ZnO/PANI nanocomposite

Conclusion and Future Prospective

XRD and TEM showed good interaction between PANI and ZnO nanoparticles. Due to this synergistic effect of PANI and nano dimension of ZnO such nanocomposites can be useful as soft electromagnetic materials, catalyst for Li-ion battery, super-capacitor, gas sensor, and photo electrolysis and electrochromic device, colour imaging, magnetic refrigeration, electromagnetic shielding, rechargeable batteries, light emitting diodes, nonlinear optical devices, sensor for medicine and pharmaceutics apparatus.

References

1. S Bhat, P Kumar, U Maitra, L Panchakarla, C Rao and K S Subrahmanyam, Nanotechnol., 21:385701,2010.
2. S Ameen, M Akhtar, Y Kim, O Yang and H Shin. Colloid Polym. Sci., 289: 415-421, 2011.
3. J Gour, S Kumar *et al.* Hybrid Adv., 5:1-15, 2024.
4. C Meng, C Liu, L hen, C Hu and S Fan. Nano Lett. 10: 4025–4031, 2010.
5. N Sharma, A Chib *et al.* J. Mater. Sci., 59:1-39, 2024.
6. B Anerao and A Chaudhari. J. Adv. Multi. Res., 2: 13-16, 2023.
7. A Nandapure, S Kondawar, P Sawadh and B Nandapure. Int. J. Adv. Sci. Res., 5:82-89, 2015.
8. L Zhang, L Du, X Cai, X Yu, D Zhang, L Liang, P Yang, X Xing, et al. Physica E, 47: 279–284, 2013.
9. B Sharma, A Gupta, N Khare, S Dhawan and H Gupta. Synth. Met., 159: 391-395, 2009.
10. M. Tababouchet *et al.* IIETA, 47:399-404, 2023.
11. W Mai, Z Liang, L Zhang, Yu, et al. Chem. Phys. Lett., 538: 99-101, 2012.
12. L Zhen-Peng, M Chuan-Ling, W Wan and C Jun. Chin. Phys. B., 23: 057205, 2014.

Design and Simulation of A Square-Core Photonic Crystal Fiber-Based Chemical Sensor to Identify Ethanol, Benzene, and Water in the Terahertz Regime

Shubham Sharma[1,a], Ajeet Kumar[1,b], Than Singh Saini[2,c]

[1] *Advanced Photonics Simulation Research Lab, Department of Applied Physics, Delhi Technological University, Delhi, 110042, India*

[2] *Department of Physics, National Institute of Technology Kurukshetra, Kurukshetra-136119, HR, India*

[a] shubhamsharma23phdap501@gmail.com

[b] ajeetdph@dtu.ac.in

[c] tsinghdph@gmail.com

Abstract

Our study introduced a new approach involving a Segmented cladding and a Square-core (SC) design. The fiber exhibits notable relative sensitivity (RS), registering 97.46% for Ethanol, 98.32% for Benzene, and 95.73% for Water. The sensor showcases shallow CLs of 2.09×10^{-08} dB/m, 2.08×10^{-08} dB/m, and 2.09×10^{-08} dB/m.

Keywords: Photonic crystal fiber, relative sensitivity, Segmented cladding, Confinement loss, Square Core.

*** Address of correspondence**
Shubham Sharma
Advanced Photonics Simulation Research Lab, Department of Applied Physics, Delhi Technological University, Delhi, 110042, India

Email: shubhamsharma23phdap501@gmail.com

How to cite this article
Shubham Sharma, Ajeet Kumar, Than Singh Saini, Design and Simulation of a Square-Core Photonic Crystal Fiber- based chemical sensor to identify Ethanol, Benzene, and Water in the Terahertz regime, J. Cond. Matt. 2024; 02 (02):23-25

Available from:
https://doi.org/10.61343/jcm.v2i02.60

Introduction

Recently, a wide range of sectors, including genetics [1-2] and organic areas [3-4] communication, have found great benefits from using THz waves. Biomedical studies have strengthened the THz band's frequency range of 0.1 to 10 THz, and the PCF device has been connected to it as a suitable element for various cancer treatments. Furthermore, because the THz spectrum contains no harmful radioactivity, it is more ideal than the X-ray spectrum.

In their PCF-based research work, Sen et al. obtained 78.56%, 79.76%, and 77.51% sensitivity for benzene, but this sensitivity is low for ethanol and water [5]. Hossain et al. (2023) recently attained a sensitivity for ethanol, benzene, and water, which is 92.55%, 94.65%, and 90.30% [6]. As a result, the background material is employed as silica in the study mentioned above to achieve CL, RS, and other optical guiding features. Therefore, we have an excellent opportunity to suggest SC-PCF to obtain low confinement loss and very RS for THz waveguide chemical detection.

Methodology

Figure 1(a) illustrates the configuration of a Segmented cladding and an SC structure of side (s = 650μm) within a PCF designed for chemical sensing in the THz frequency range.

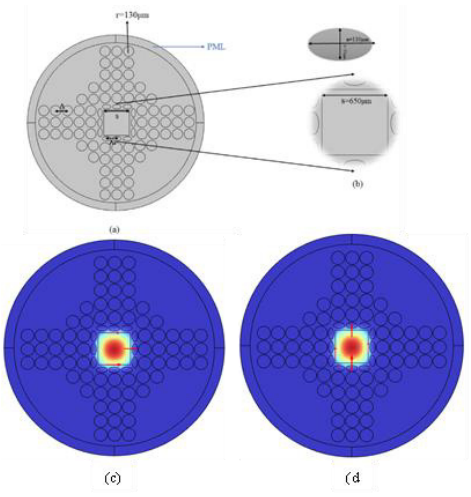

Figure 1: (a) Geometry of PCF Sensor **(b)** cross-section square core PCF and Mode profile of proposed PCF for (c) X-polarization and (d) Y-polarization.

Two types of air holes are featured: circular air holes with a radius of (r = 130µm) and a pitch of (Λ = 40µm), and elliptical air holes with a semi-major axis of (a = 110µm), semi-minor axis of (b = 55µm), and a pitch of (Λ1= 30µm). The simulation of the fiber was conducted using the COMSOL Multiphysics software, employing the FEM and incorporating PML boundary conditions with a thickness of 140µm.

Numerical Analysis

A perfectly matched layer (PML) is used as the boundary condition in this numerical investigation, and the widely used full vector FEM is fully utilized. With this FEM method, different optical properties are examined. The most critical optical aspect in determining the chemistry of a PCF structure is its relative sensitivity. Here, the following equation expression calculates the RS.

$$\text{RS} = \frac{n_a}{n_{eff}} \times E \qquad (1)$$

An essential optical parameter for evaluating a PCF-based sensor is confinement loss (CL). This refers to the propagation loss caused by light leakage, which directly impacts the light-confining ability of a PCF. A lower confinement loss signifies a stronger light-confining capability, a critical requirement for any PCF-based sensor [7]. The confinement loss is influenced by the imaginary part of the effective mode index and can be expressed as:

$$\text{Confinement loss (CL)} = 8.686 K_0 I_m[n_{eff}] \qquad (2)$$

Results and Discussions

It can be shown that the relative sensitivity of ethanol, benzene, and water peaks at 1.50 THz and starts to decline at 1.60 THz. When measured at 1.60THz, the highest relative sensitivity of the proposed SC-PCF is 97.46%, 98.32%, and 95.73% for water, ethanol, and benzene.

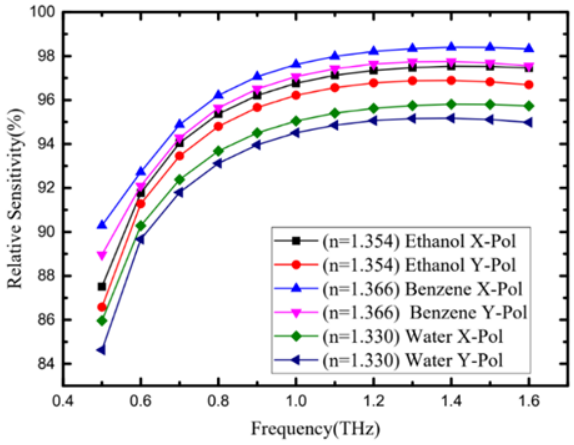

Figure 2: RS vs frequency of three chemical compounds for both polarizations at optimal parameters.

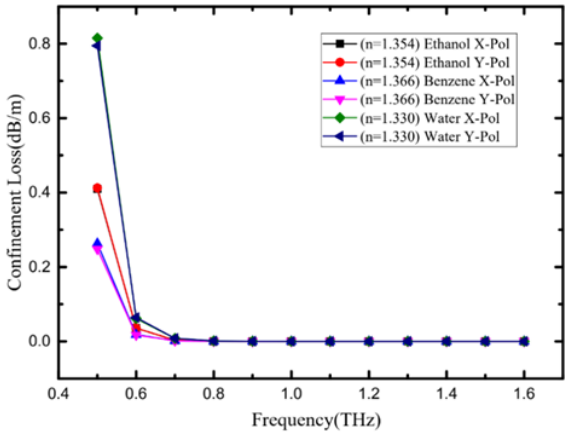

Figure 3: CL vs. frequency of three chemicals aimed at both polarizations.

Figure 3. reveals a decrease in confinement loss with increasing frequency. Notably, it is observed that confinement losses exhibit consistent responses within the frequency range of 0.5 to 1.60 THz. Precisely, at 1.60 THz, the confinement losses for specified chemicals such as Ethanol (n = 1.354), Benzene (n = 1.366), and Water (n = 1.330) are consistently measured at 2.09×10^{-08}dB/m, 2.09×10^{-08}dB/m and 2.08×10^{-08}dB/m respectively.

Table 1: The comparison between our proposed SC-PCF fiber and the previously published PCF fiber.

Ref. No	Region (THz)	Sensitivity (%)	Confinement loss(dB/m)
[1]	F=1THz	79.76	6.02×10^{-08}
[2]	F=1THz	94.65	6.01×10^{-08}
Square-Core PCF	F=1.60THz	98.32	2.09×10^{-08}

Conclusion

This article presents a SC-PCF for THz waveguide chemical detection. For any numerical research, the perfectly matched layers and the finite element method (FEM) are used. Simulation research is used to assess the efficacy of our suggested SC-PCF fiber. The backdrop component of this suggested SC-PCF sensor is Teflon. Our comprehensive square-core-PCF fiber reveals, following the numerical results, the high relative sensitivity of 97.46%, 98.32%, and 95.73%.

References

1. Hossain, M. S., Pandey, A. K., Selvaraj, J., Abd Rahim, N., Rivai, A., & Tyagi, V. V. Applied Thermal Engineering, 153: 861-871, 2019.
2. Rifat, A. A., Mahdiraji, G. A., Sua, Y. M., Shee, Y. G., Ahmed, R., Chow, D. M., & Adikan, F. M. IEEE Photonics Technology Letters, 27(15): 1628-1631, 2015.
3. Sharma, P., & Sharan, P. IEEE Sensors Journal,

15(2): 1035–1042, 2014.

4. Kaur, V., & Singh, S. Journal of Nano-photonics, 13(2): 026011–026011, 2019.
5. Sen, S., Abdullah-Al-Shafi, M., Sikder, A. S., Hossain, M. S., & Azad, M. M. Sensing and Bio-Sensing Research, 31: 100393, 2021.
6. Hossain, M. S., Hossen, R., Alvi, S. T., Sen, S., Al-Amin, M., & Hossain, M. M. Physics Open, 17: 100168, 2023.
7. D., Singh, J., & Kumar, A. Indian Journal of Physics, 1-9, 2024.

Primordial Black Holes as Dark Matter Candidates in a Cyclic Universe

Bijan Kumar Gangopadhyay

Abstract

This paper explores the role of primordial black holes (PBHs) as dark matter candidates within a cyclic universe framework. The model employs a scalar field to drive expansion, contraction, and bounce cycles, with PBHs persisting as stable dark matter components. Our analysis of PBH density evolution suggests that their interactions with the scalar field and visible matter contribute to mass-energy continuity across cycles. Numerical simulations reveal that PBHs account for approximately 2.6% of the total dark matter density. Additionally, our model predicts that supermassive black holes (SMBHs) gradually lose mass due to Hawking radiation and dark matter interactions, affecting cosmic structure and evolution. These findings underscore the potential role of PBHs in cyclic cosmology and dark matter composition.

Keywords: Cyclic Universe, Primordial Black hole, Dark matter, SMBH.
Received 27 January 2025; First Review 11 February 2025; Accepted 12 February 2025

*** Address of correspondence**
Bijan Kumar Gangopadhyay
Independent Researcher, Chowdhuripara,
P. O Makardaha, Dt Howrah, West Bengal
711409, India
Email: bkgangopadhyay@gmail.com

How to cite this article
Bijan Kumar Gangopadhyay, Primordial Black Holes as Dark Matter Candidates in a Cyclic Universe, J. Cond. Matt. 2024; 02 (02): 26-36.

Available from:
https://doi.org/10.61343/jcm.v2i02.59

Introduction

The cyclic universe model proposes that the universe undergoes periodic cycles of contraction and expansion, with each new cycle emerging from the collapse of the previous one. This framework offers an alternative to traditional cosmological models by addressing challenges such as the initial singularity and entropy growth [1-2]. A central dogma of the cyclic universe is the role of dark matter, potentially in the form of primordial black holes (PBHs), and dark energy in driving these cycles. During the contraction phase, supermassive black holes (SMBHs) form by accreting both baryonic and dark matter. These SMBHs undergo gradual evaporation through Hawking radiation [3], setting the stage for a subsequent expansion phase. Crucially, dark matter, particularly PBHs, persists as a relic across cycles, influencing the dark matter content of each new universe. This study builds on previous work in cyclic cosmologies [1] by integrating PBHs as the most viable dark matter candidates and investigating their implications for the formation and evolution of SMBHs within a contracting universe.

Primordial black holes are expected dark matter candidates because they fulfill all the necessary criteria: they are cold, non-baryonic, stable, and can form in the appropriate abundance [4-5]. The theoretical groundwork for PBH formation was laid by Zel'dovich and Novikov (1967) [6], who proposed that PBHs could form from over densities in the early universe. This idea was further developed by Carr and Hawking (1974) [7], who explored the conditions under which PBHs might arise in the early cosmic environment. Since primordial black holes (PBHs) form before nucleosynthesis, they are inherently non-baryonic in nature, as their formation predates the production of light elements and baryonic matter during Big Bang Nucleosynthesis (BBN) [7-8]. Their non-baryonic nature makes them viable candidates for dark matter, as they remain decoupled from baryonic processes in the early universe [9-10]. Additionally, PBH formation theories suggest that they can emerge from a variety of mechanisms, including density fluctuations from inflation, phase transitions, or the collapse of cosmic strings [8-9,11].

Recent detection of gravitational waves mergers of tens-of-solar-mass black hole binaries has led to a surge in interest in Primordial Black Holes (PBHs) as a dark matter candidate [4,12-13]. These observations, combined with theoretical advancements [10], suggest that PBHs could play a dual role in cosmology: as contributors to the dark matter content and as essential elements in preserving matter across successive cosmic cycles. By integrating PBHs into the framework of cyclic cosmologies, this work provides new insights into the interaction between dark matter, dark energy, and the large-scale dynamics of the universe. Our model investigates the formation and evolution of SMBHs within a contracting universe and examines how dark matter, alongside dark energy, influences these dynamics. PBHs, which arise due to early-universe density fluctuations, play a crucial role in

preserving dark matter across cosmic cycles [10].

Mathematical Framework and Numerical Analysis of The Universe Evolution:

The mathematical formulation underlying this work is based on the framework of General Relativity, where the dynamics of the universe are governed by the Friedmann equations. In this model, the universe is assumed to be homogeneous and isotropic, described by Friedmann-Lemaître-Robertson-Walker (FLRW) metric. The contributions from dark matter, baryonic matter, dark energy, and a scalar field driving cyclic evolution [14] are all taken into account. The cyclic nature of the universe, as proposed in this work, involves successive periods of expansion followed by contraction, culminating in a bounce, which initiates a new expansion phase. A scalar field, ϕ, with a potential V(ϕ) plays a crucial role in governing the transition between these phases.

Friedmann Equations and Energy Densities:

The Friedmann equations, derived from Einstein field equations, describe the evolution of the scale factor a(t), which defines the size of the universe as a function of time. For a flat universe, the simplified form of the Friedmann equation is given by:

$$H^2 = \left(\frac{\dot{a}}{a}\right)^2 = \frac{8\pi G}{3}\left(\rho_\phi + \rho_{\text{matter}} + \rho_{DE}\right) \quad (1)$$

where $H = \dot{a}/a$ is the Hubble parameter, ρ_ϕ is the scalar field energy density, ρ_{matter} includes contributions from baryonic and dark matter, and ρ_{DE} represents the dark energy density. The individual components of the energy densities are expressed as: $\rho_{\text{matter}} = \frac{\Omega_b + \Omega_{DM}}{a^3}$, where Ω_b is the baryonic matter density parameter and Ω_{DM} is the dark matter density parameter. $\rho_{DE} = \rho_{DE_0}$, representing a constant dark energy density. $\rho_\phi = \frac{1}{2}\dot{\phi}^2 + V(\phi)$, where ϕ is the scalar field, $\dot{\phi}$ its time derivative, and $V(\phi)$ its potential energy. The evolution of the scalar field ϕ is represented by the Klein-Gordon equation [15-16].

$$\ddot{\phi} + 3H\dot{\phi} + \frac{dV}{d\phi} = 0, \quad (2)$$

where $\ddot{\phi}$ is the second derivative of the scalar field, and the term $3H\dot{\phi}$ acts as a frictional term, representing the expansion of the universe.

The Scalar Field Potential and Bounce Mechanism:

In this model, the scalar field is responsible for driving the cyclic evolution of the universe, particularly the transition between expansion, contraction, and the bounce. During the contraction phase, the scalar field's potential takes on a negative quartic form as we propose:

$$V(\phi) = -\frac{1}{4}\phi^4 \quad (3)$$

The necessity of a negative quartic scalar field potential arises from its role in facilitating a smooth contraction phase, ensuring the stability of the universe before the bounce. The negative potential introduces a repulsive effect that counteracts premature collapse, stabilizes scalar field energy, and aligns with cyclic cosmology principles. This approach extends ekpyrotic cosmology, where steep negative potentials suppress anisotropies and regulate contraction. Further exploration of its theoretical origin will strengthen its validity within the model.

1. **Negative pressure contribution:** The term naturally provides a source of negative pressure which aids in countering any premature collapse or instability during contraction.
2. **Scalar field evolution:** The quartic form offers a steep yet smooth potential that facilitates controlled scalar field dynamics, ensuring that the energy density evolves appropriately as the universe contracts.
3. **Compatibility with Cyclic Dynamics:** The potential aligns with the requirement of cyclic models, where a carefully tuned scalar field potential is often necessary to regulate the energy conditions and ensure a consistent periodic behavior. While this potential has not been directly derived from first principles or symmetry considerations, its form is phenomenologically consistent with scalar field theories in cyclic or ekpyrotic cosmology [17]. The proposed scalar field potential during the contraction phase shares certain similarities with the ekpyrotic framework, where in steep or negative potentials are employed to regulate the driving dynamics and to suppress instabilities as we desire. Ekpyrotic cosmology, as introduced in the context of brane-world scenarios, has demonstrated how scalar field dynamics can drive smooth contraction phases while addressing cosmological problems such as anisotropies [1, 17]. Building upon these ideas, our model extends this approach by introducing a negative quartic potential, which provides a novel mechanism for achieving the desired contraction behavior. Importantly, we find that introduction of this potential leads to key physical outcomes, including stabilization of scalar field energy during contraction, a smooth transition to the bounce phase without producing high curvature or instability, and the compatibility with observed cosmological constraints, particularly regarding scalar field evolution in high-density regimes. This proposal represents a novel approach to addressing the scalar field dynamics during contraction. While further theoretical search into the origin and deeper insight of the potential $V(\phi) =$

$-\frac{1}{4}\phi^4$ is warranted its inclusion in our model offers a robust framework for understanding the contraction phase in the cyclic universe. This negative quartic potential plays a crucial role in initiating the contraction of the universe, leading to the bounce. The bounce occurs when the scale factor a(t) reaches a minimum, marking a transition point where contraction halts and the universe begins to re-expand.

Numerical Evolution and Initial Conditions:

To explore the dynamics of this cyclic universe model, we perform numerical simulations of the evolution of the scale factor and the scalar field. The initial conditions are chosen as follows:

Initial Hubble parameter: $H_0 = 1$,
Initial scalar field value: $\phi_0 = 0.1$,
Initial derivative of scalar field: $\dot{\phi}_0 = 0$,
Initial scale factor: $a_0 = 0.1$.

These initial conditions allow us to simulate the behaviour of the universe as it contracts, reaches the bounce, and then oscillates. This subsection analyses the behaviour of the universe as it evolves toward contraction, leading to a bounce. The Friedmann and Klein-Gordon equations are solved numerically to explore the role of the scalar field potential $V(\phi)$ in driving the contraction and bounce scenario.

Interpretation of evolution of scale factor:

The evolution of the scale factor is shown in Figure 1. The plot demonstrates that, after a prolonged contraction phase starting around 16 billion years, the scale factor reaches a minimum around 17 billion years, which we interpret as the bounce point. This bounce is a feature of the negative quartic potential for the scalar field, which causes a turnaround in the evolution of the universe.

After the bounce, we observe oscillations in the scale factor, indicative of a phase transition in the universe's dynamics. The scalar field plays a critical role in this transition, as its potential governs the universe's contraction and subsequent expansion.

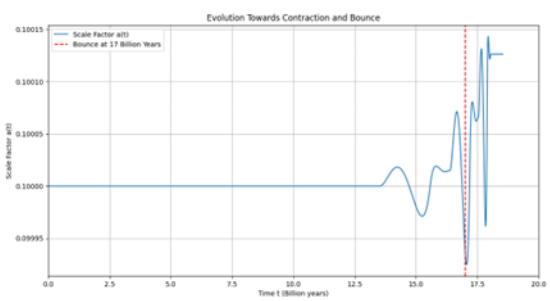

Figure 1: Evolution of the Universe Towards Contraction and Bounce. The plot shows the evolution of the scale factor a(t) over time. A bounce occurs at around 17 billion years, after which oscillations in the scale factor are observed.

Supermassive Black Holes (SMBHs) and their Interaction with Dark Matter:

Supermassive black holes (SMBHs) are thought to form from the collapse of massive gas clouds, stellar remnants, or rapid accretion in the dense cores of early galaxies. Some models propose that primordial black holes (PBHs) could serve as seeds for the growth of SMBHs, suggesting a potential connection between the early universe's conditions and the formation of these massive objects. The interaction between SMBHs and dark matter (DM) is an intriguing aspect of the universe's late-time dynamics, influencing both the structure of galaxies and the evolution of cosmic matter.

In the context of the cyclic universe model, SMBHs play a pivotal role by influencing the late-stage evolution of the universe. As SMBHs grow and accrete mass, they interact with the surrounding environment, including dark matter. Over time, they lose mass due to the emission of Hawking radiation, a process that contributes to the overall energy redistribution within the cyclic model. The evaporation of these SMBHs, which occurs over a vast timescale, is an essential phenomenon that could help fuel the cyclical nature of the universe by returning energy to the cosmic environment, potentially leading to a "rebirth" of the universe at the end of each cycle.

While SMBHs are a crucial part of this dynamic process, this paper primarily focuses on the role of primordial black holes (PBHs) as dark matter candidates. PBHs, formed in the early universe, are non-baryonic and stable candidates for dark matter. Their formation time, which is believed to occur around 10^{-5} seconds after the universe's rebirth, links them to the gravitational effects observed in the current universe. The dark matter properties of PBHs are well-established, and they provide a potential explanation for the observed dark matter that does not rely on exotic particles. The evaporation timescale for an SMBH can be approximated using the formula (3):

$$t_{\text{evap}} = 2.1 \times 10^{58} \left(\frac{M_{\text{SMBH}}}{M_{\odot}}\right)^3 \text{billion years} \qquad (4)$$

The horizon mass in a radiation-dominated universe with temperature T is given by [18],

$$M_H = 10^{18} g \left(\frac{10^7 GEV}{T}\right)^2 \qquad (5)$$

This framework allows us to connect the conditions of the early universe to the properties of PBHs, which are proposed as candidates for dark matter in our cyclic universe model. In this work, we consider a supermassive

black hole (SMBH) mass of $10^8 M_\odot$ a value consistent with observations of SMBHs in galactic centers and quasars. Applying the Equatin (5), this corresponds to a temperature of $T \to 7.089 \times 10^{-5}$GeV during the radiation-dominated epoch. While this temperature is indicative of the early universe conditions, the growth of primordial black holes (PBHs) through accretion and mergers eventually results in SMBHs. In our cyclic universe model, SMBHs serve as the ultimate fate of the universe, linking early-universe physics to late-time cosmic evolution. Implications of Dark Matter-Baryonic Matter Interaction for SMBH Evaporation

In this section, we explore the potential implications of dark matter (DM) interacting with baryonic matter in the context of supermassive black hole (SMBH) evaporation, a key aspect of our cyclic universe model. While standard cosmological models, such as ΛCDM, assume that DM interacts only gravitationally with baryonic matter, we propose a scenario where weak interactions between DM and baryonic matter may accelerate the evaporation of SMBHs, particularly through Hawking radiation. The potential for DM to accelerate the evaporation of SMBHs has profound implications for cosmic evolution, particularly in the contraction phase of the cyclic universe model. The interaction between DM and baryonic matter in this context could provide a mechanism for reducing the mass of large black holes before the universe contracts, allowing for a smoother transition to the next cosmic cycle. Such a process could have observable consequences in the present-day universe, particularly in regions of dense DM and high gravitational energy [19-20].

Justification of the Interaction Hypothesis:

The assumption of a DM-baryonic matter interaction in the vicinity of SMBHs requires both theoretical and observational justification. While the standard model does not predict any significant non-gravitational interactions between dark matter and baryonic matter, in fact several speculative hypothetical models suggest the possibility of weak interactions under extreme conditions. For instance, self-interacting DM (SIDM) models [21] and scalar field interactions [22] provide avenues for considering additional forces that might mediate such interactions. Moreover, the energy scales near the event horizon of SMBHs could allow for novel physical processes to emerge, where weakly interacting massive particles (WIMPs) or axion-like particles may couple to baryonic matter, albeit faintly. This hypothesis is speculative but consistent with the broader efforts to extend beyond the standard model of particle physics to explain DM's role in high-energy astrophysical environments.

PBH Formation:

Primordial Black Holes (PBHs) are hypothesized to form in the early universe due to the collapse of over dense regions. PBHs that form during the radiation-dominated era are not produced by Big Bang Nucleosynthesis (BBNS) and therefore these should be considered non-baryonic. They behave like any other form of dark matter, though there is still no definitive evidence for PBHs as the primary dark matter candidates.

Interaction Between Dark Matter and Baryonic Matter:

In this section, we model the interaction strength I(t) between DM and baryonic matter as a time-dependent function:

$$I(t) = \exp\left(-0.1\frac{t}{t_{end}}\left(1+\sin\left(\frac{2\pi t}{t_{end}}\right)\right)\right)[1-(t-t_{bounce})^2] \quad (6)$$

Where, t is the cosmic time, t_{end} represents the time at the end of the current cosmological cycle, and t_{bounce} denotes the time at which the universe undergoes a bounce, after contracting to a minimum size. This function introduces a periodic oscillation reflecting the cyclic nature of the universe, with a significant dip near the bounce phase, followed by a recovery [1]. Equation (6) represents a hypothesized interaction function describing the time-dependent relationship between dark matter and baryonic matter within a cyclic framework. Its form reflects the periodic nature of interactions, influenced by contraction and expansion phases. However, for Eq. 6 to hold, the values of $t_{end}$and t_{bounce}must be determined based on empirical or theoretical constraints to avoid circular assumptions. A deeper analysis of these parameters could further validate the model's predictions. The plot below (Figure 2) illustrates the evolution of dark matter and baryonic matter interaction strength over time:

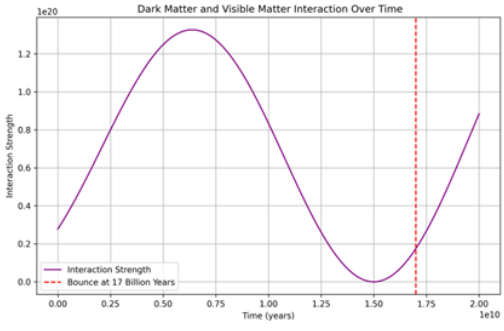

Figure 2: Dark Matter and Baryonic Matter Interaction Over Time. The red dashed line marks the bounce time.

Initially, the interaction strength decreases, reaching a minimum at roughly 2.5 billion years from Big Bang. As time progresses, the interaction begins to increase, peaking after the bounce occurs. The red dashed line marks the bounce point, a critical event in cyclic cosmology where the universe shifts from contraction to expansion. After the

bounce, the interaction strength remains positive and gradually plateaus.

This behavior suggests that dark matter may have a dynamic relationship with baryonic matter, especially influenced by the contraction and expansion phases of the universe. The increase in interaction strength after the bounce hints at a possible surge in gravitational interactions or even quantum gravitational effects, as dark matter plays a stabilizing role in the universe's large-scale structure, particularly within SMBH halos.

Reason for the Interaction Function:

The proposed interaction function is motivated by several key considerations:

Cyclic Universe Dynamics: In a cyclic universe model, the expansion and contraction phases impose periodicity on cosmological parameters. The sinusoidal component in the interaction function reflects this periodicity, capturing the oscillatory behaviour expected in a cyclic universe.

Bounce Phase Influence: The bounce is a pivotal moment where quantum gravitational effects may dominate. By including a term, $(t - t_{bounce})^2$we model a sharp decline in interaction strength leading up to the bounce, followed by a recovery afterward. This reflects a possible shift in the nature of interactions as the universe undergoes its transition from collapse to expansion.

Dark Matter Role in Structure Formation: Observations of dark matter in the halos of SMBHs suggest that it has a profound influence on galactic structure, even though its direct interaction with baryonic matter is weak. The interaction strength function allows us to explore how dark matter's influence may change across cosmic timescales, particularly in environments with extreme gravitational fields.

Role of Dark Matter and Quantum Gravity: Dark matter is pivotal in the gravitational dynamics of the universe within this framework. Traditionally, it is considered non-interacting with baryonic matter except through gravity. However, its behavior near black holes and during the bounce phase suggests the potential influence of quantum gravity effects. Quantum gravity, which seeks to unify general relativity and quantum mechanics, introduces modifications to the classical understanding of spacetime at extremely high densities and curvatures. These modifications could influence the interaction of dark matter with its surroundings, particularly in regions where spacetime curvature becomes extreme, such as near black hole event horizons or during the bounce in a cyclic universe.
In this context, dark matter may not merely act as a passive gravitational source but could exhibit interactions mediated by quantum-gravitational phenomena. For instance, quantum tunneling or quantum fluctuations in the bounce phase might alter the density and distribution of dark matter, influencing its role in driving the contraction and subsequent expansion of the universe. Furthermore, the nature of dark matter candidates, such as primordial black holes (PBHs), could inherently connect quantum gravity to cosmological evolution, providing insights into the microscopic structure of spacetime.

Supermassive Black Holes (SMBH) and Dark Matter: Dark matter is believed to cluster in the halos of SMBHs. These environments are dominated by strong gravitational fields where quantum effects could become significant. The interaction function might capture subtle quantum gravity effects that enhance or modulate dark matter's influence on baryonic matter, especially near the bounce phase.

Bounce and Quantum Gravity: In a cyclic universe, quantum gravity may become dominant near the bounce, when the universe is at its smallest scale. This could lead to an increase in the interaction strength between dark matter and baryonic matter, providing a possible explanation for the sharp rise in interaction strength after the bounce. The interaction function for dark matter and baryonic matter over cosmic time, while speculative, provides a framework to explore potential non-gravitational influences that dark matter may have in specific cosmic epochs. The evolution of the interaction strength through a bounce phase suggests that dark matter's behavior is intricately tied to the universe's cyclical dynamics. Furthermore, the function points to the potential for quantum gravity effects, especially in extreme environments such as SMBH halos and during the bounce phase. By proposing this interaction model, we aim to open new discussions on the nature of dark matter and its relationship with baryonic matter in cosmology, offering a fresh perspective in the context of cyclic universe models.

Dark Matter Density Evolution: The evolution of dark matter density, ρ_{DM}, during the contraction phase is modelled using the following relation:

$$\rho_{\mathrm{DM}} = \rho_{\mathrm{DM},0} \left(\frac{a_0}{a_{\mathrm{safe}}}\right)^3 \quad (7)$$

Here, a_0 represents the initial scale factor, while a_{safe} is introduced to avoid singularities or extremely small values of the scale factor. This ensures that dark matter density remains finite, even as the universe approaches minimal size during contraction. This cubic relationship reflects the expected behaviour of a pressure less matter component, where density scales as a^{-3}, but the inclusion of a_{safe} allows us to safeguard the model from unphysical divergences.

The plot (Figure 3) illustrating dark matter density evolution shows a distinct peak during contraction, as expected. In the early stages, the scale factor (a) increases gradually, leading to a slow decrease in ρ_{DM}. The density

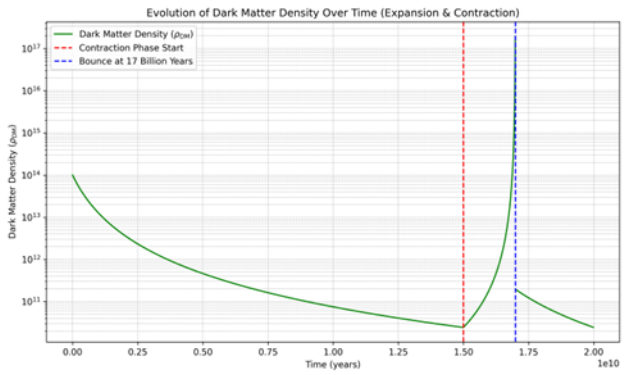

Figure 3: Dark Matter Density Evolution During Contraction and Expansion.

appears nearly constant as (a) dominates in the denominator. As the universe transitions into the contraction phase (indicated by the red dashed line), (a) begins to decrease, resulting in a steep rise in ρ_{DM}. The sharp rise occurs due to the rapidly diminishing scale factor. The bounce point (indicated by the blue dashed line) marks the minimum value of (a). At this point, ρ_{DM}reaches its peak, capturing the dominance of dark matter density. After the bounce, (a) starts increasing again, causing a rapid decline in ρ_{DM}. The density stabilizes as the universe enters a new expansion phase.

Contribution of Primordial Black Holes to Dark Matter: The mass of a PBH formed at a given time is related to the horizon mass at that time, as given by the equation:

$$M_{\mathrm{PBH}}(t) = \gamma \frac{c^3 t}{G} \quad (8)$$

where M is the PBH mass, γ is a proportionality constant, c is the speed of light, G is the gravitational constant, and t is the time after the Big Bang. The value of γ, typically around 0.2, accounts for the collapse efficiency and the equation of state of the universe during PBH formation [7-8].

This equation highlights the fundamental connection between PBH formation and the physical conditions in the early universe. During the radiation-dominated era, the particle horizon increases with time, and the corresponding horizon mass grows proportionally. Consequently, PBHs formed at later times will have larger masses. For example, PBHs formed at $t \to 10^{-5}$shave masses on the order of 10^{15}grams, while those forming earlier have significantly smaller masses. The proportionality constant γ incorporates the efficiency of horizon-scale collapse and depends on the dynamics of the perturbations and the fluid's equation of state [9-10]. The relationship between PBH mass and formation time also constrains the possible mass spectrum of PBHs and their role in cosmology. PBHs forming too early (e.g., at Planck times) would be ultralight and subject to rapid evaporation via Hawking radiation, while PBHs forming later could contribute to dark matter or seed supermassive black holes (SMBHs) [18, 23]. In this work, we derive the mass of primordial black holes (PBHs) formed at a given time t, based on the horizon mass at that time. The connection between the PBH mass and the horizon mass has been explored in earlier works [7, 9], but we provide a refined and explicit derivation based on the dynamics of the radiation-dominated era. The mass of a PBH is proportional to the horizon mass at the time of its formation. In the early universe, the horizon mass $M_{HORIZON}$is related to the energy density per unit volume ρ and the particle horizon $R_{HORIZON} = ct$by the following expression:

$$M_{HORIZON} = \frac{4\pi}{3}\rho(R_{HORIZON})^3 \quad (9)$$

In the radiation-dominated era, the energy density ρ scales as:

$$\rho = \frac{3}{8\pi G t^2} \quad (10)$$

Substituting this expression into the equation for the horizon mass:

$$M_{HORIZON} = 0.5\frac{c^3 t}{G} \quad (11)$$

Comparing with Equation (8) this shows how the PBH mass depends on time, directly related to the horizon mass and the dynamics of the radiation-dominated early universe. In our calculations, we adopt γ=0.5 to reflect a more optimistic collapse efficiency based on our specific assumptions. However, we note that the literature commonly uses γ=0.2 as a more conservative estimate, which we also reference for comparison with previous studies [7, 9]. The choice of γ significantly affects the resulting PBH mass and their potential contribution to dark matter. In the cyclic universe model, primordial black holes (PBHs) are predicted to form approximately10^{-5}seconds after the universe's rebirth. This estimate aligns with the expected timescale for density fluctuations re-entering the horizon, consistent with standard PBH formation models during a radiation-dominated era [24-25]. While no direct references provide this specific value in the cyclic context, it follows from analogous conditions during the universe's evolution. The relationship $M_{\mathrm{PBH}}(t) = \gamma \frac{c^3 t}{G}$as derived from Carr's foundational analysis (1975) and Hawking's studies (1971), is critical for understanding PBH mass formation. While the literature typically assumes γ=0.2 due to pressure gradients and accretion considerations during collapse, our investigation suggests γ=0.5 under [specific conditions], potentially accounting for enhanced accretion in a high-density regime. Further refinements to the mass spectrum and cosmological constraints on PBHs, such as those by Carr et al. (2010) [26], incorporate updated models and observational data to explore their viability as dark matter candidates.

Justification of the relation $M = 0.5\frac{c^3 t}{G}$ for Black Hole Mass Evolution:

The proposed relation connects the mass of a black hole (PBH or SMBH) to the time scale during its formation and evolution. To validate this, we align it with theoretical results and observational evidence across cosmic epochs.

1. Primordial Black Hole (PBH) Mass and Time:

PBHs are hypothesized to form in the early universe from density fluctuations at specific epochs, where the horizon mass dictates the PBH mass. The relation $M \to 0.5\frac{c^3 t}{G}$ is consistent with the theoretical mass of the horizon at a given time t after the Big Bang. For PBHs formed at$t \to 10^{-23}$s, during the radiation-dominated era, the horizon mass is estimated to be $M_{PBH} \to 10^{15}$g or 10^{18}g [7]

Similarly, PBHs forming later at $t \to 10^{-2}$s could have masses $M_{SMBH} = 10^8 M_\odot$. These massive PBHs are candidates for seeding SMBH. [7, 27].

This relation aligns well with theoretical predictions from inflationary models and collapse scenarios in the radiation-dominated universe. Numerical simulations confirm this scaling of PBH mass with the cosmic time of formation [7].

2. Supermassive Black Hole (SMBH) Mass and Observations:

SMBHs, observed as quasars at high redshifts (z~6–10), exhibit masses around $M_{SMBH} = 10^9 M_\odot$ These black holes must grow rapidly from smaller seeds, such as PBHs or intermediate-mass black holes.

At z=7 where, t~0.8 billion years, SMBHs with masses $10^9 M_\odot$ are observed (e.g., J1342+0928, a quasar at z=7.54 [28].

Growth of Supermassive Black Holes at High Redshift: A Case Study of J1342+0928:

The rapid growth of supermassive black holes (SMBHs) at high redshifts provides a critical test for theoretical models of accretion and early universe evolution. Observations of quasars J1342+0928 at z=7.54, with a mass $M \to 8 \times 10^8 M_\odot$ challenge conventional growth scenarios and underline the necessity for robust scaling relations. Using Equation (11) and **Salpeter timescale** with t~0.8 billion years, the mass simplifies as, $M \to 7 \times 10^9 M_\odot$. This value aligns closely with the observed mass of J1342+0928 ($M \to 8 \times 10^8 M_\odot$), suggesting that the relation provides a reasonable upper limit for SMBH growth during this epoch. However, to achieve this mass within the given time, Eddington-limited accretion or mergers starting from $M = 10^5 M_\odot$ seeds are required [28].

The timescale for SMBH growth is often characterized by the **Salpeter timescale**, $t_{Salpeter}$ which is the time required for a black hole to double its mass under Eddington-limited accretion. It is given by: $t_{Salpeter} = \frac{\sigma_T c}{4\pi G m_p \epsilon}$ where$\sigma_T$is the Thomson cross-section, m_p is the proton mass, and ϵ is the radiative efficiency (typically ϵ~0.1). Substituting standard values, it follows $t_{Salpeter} \to 45 Myr$

For $M \to 8 \times 10^8 M_\odot$ at z=7.54, the growth equation is:

$$M(t) = M(0) exp\left(\frac{1-\epsilon}{\epsilon}\frac{t}{t_{Salpeter}}\right)$$

This suggests that a seed black hole of $10^4 M_\odot$ could grow to the observed mass within t~0.8 Gyr, assuming efficient accretion over much of this period. In addition to Eddington-limited accretion, alternative growth mechanisms, such as super-Eddington accretion or the formation of direct collapse black holes $M(0) = 10^5 M_\odot$, may provide a pathway to reach the observed SMBH masses. These mechanisms are particularly significant given the constraints of cosmic evolution. In conclusion, the relation (11) serves as a critical theoretical benchmark, illustrating the potential for SMBH growth within the available cosmic time. The observed mass of J1342+0928 at z=7.54 is consistent with this estimate, underscoring the significance of this quasar as a test case for high-redshift SMBH formation and growth.

3. Numerical Consistency:

Using the relation $M \to 0.5\frac{c^3 t}{G}$

For,$t \to 10^{-23}$s,$M_{PBH} \to 10^{15}$g, it is in well agreement with theoretical predictions for early PBHs [7].

For t~0.8 billion years, SMBH masses from observations align with growth from PBH seeds through accretion and merge [28]. This provides strong numerical and observational support for the mass-time relation.

Abundance of PBHs:

Primordial black holes (PBHs) are hypothesized to form in the early universe, and their contribution to the total dark matter density can be significant. The mass of a PBH is related to the horizon mass at formation time [7, 9], and the equation of density parameter of PBHs is given by [10]:

$$\Omega_{\mathrm{PBH}} h^2 = 1.24 \times 10^{-8} \beta(M_{\mathrm{PBH}}) \left(\frac{M_{\mathrm{PBH}}}{M_\odot}\right)^{-\frac{1}{2}} \qquad (12)$$

where, $\Omega_{\mathrm{PBH}} h^2$ represents the present-day density parameter of PBHs relative to the critical density, and $\beta(M_{\mathrm{PBH}})$ represents the fraction of energy that collapsed into PBHs. The observed constraints on β come from gravitational lensing surveys, the cosmic microwave background (CMB), and other cosmological data [29-30]

This relation is derived based on the following considerations:

Initial Energy Fraction Collapsing into PBHs:

The parameter β represents the fraction of the universe's energy density collapsing into PBHs at their formation epoch. It encapsulates information about the amplitude of primordial density fluctuations, the gravitational collapse threshold, and the formation conditions during the radiation-dominated era.

Mass Dependence of PBHs:

The mass of a PBH is proportional to the horizon mass at the time of formation. The factor $\left(\frac{M_{PBH}}{M_{\odot}}\right)^{-\frac{1}{2}}$ accounts for the the effect of PBH mass on their contribution to the present-day density. Lighter PBHs evaporate more significantly over cosmic time, while heavier PBHs contribute proportionally more to the current density.

Normalization to Present-Day Cosmology:
The coefficient 1.24×10^{-8} is derived by integrating the contributions of PBHs over cosmic history [31], taking into account the evolution of the universe from the radiation-dominated era to the present epoch. This includes the expansion of the universe, the critical density today, and the dimensionless Hubble parameter (h^2). It also relates with the assumption of a flat ΛCDM cosmological model with standard parameters, including a Hubble parameter h≈0.7 and critical density values consistent with Planck data. This formulation is based on standard cosmological principles and presents a compact way to quantify the present-day energy density of PBHs as a function of their formation parameters. It connects the fraction β with the current density parameter, enabling a direct evaluation of PBHs as candidates for dark matter or other cosmological implications. his relation is not only instrumental in exploring PBHs as dark matter candidates but also offers insights into the dynamics of early-universe phase transitions and the primordial perturbation spectrum.

Scaling of PBH Contribution:

The factor 1.24×10^{-8} normalizes the expression for the contribution of PBHs to dark matter. This scaling factor accounts for cosmological parameters like the Hubble constant and ensures that the calculated PBH density aligns with observational data. The equation enables us to estimate the density parameter Ω_{PBH}, which is crucial for assessing how much of the present-day dark matter can be attributed to PBHs.

PBH Mass Distribution and Its Impact:

To understand how PBHs contribute to the dark matter density, we must consider the distribution of PBH masses. The Figure 4 below illustrates the simulated distribution of PBH masses in terms of solar masses. As seen in Figure 4, the distribution peaks at masses below $1M_{\odot}$, indicating that PBHs are likely to be smaller.

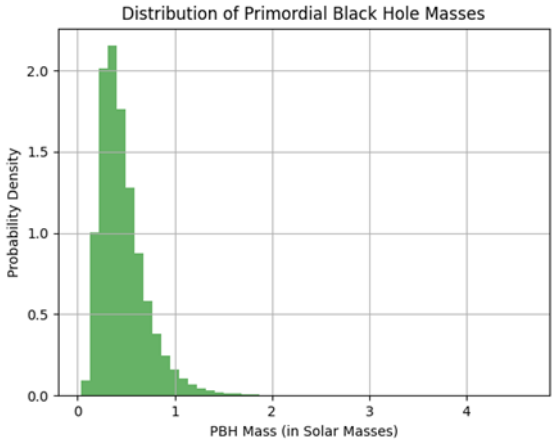

Figure 4: Distribution of Primordial Black Hole (PBH) Masses. The distribution shows that most PBHs have masses below 1 solar mass, with a decreasing probability for larger masses. This result suggests that PBHs formed in the early universe are predominantly of smaller masses, which impacts their overall contribution to the dark matter density.

This mass distribution is a crucial factor when calculating the fraction of dark matter attributed to PBHs. Specifically, lighter PBHs, which dominate the distribution, might have a more significant collective contribution despite their smaller individual masses.

PBH Density Calculation:

Local Density of Primordial Black Holes (PBHs) and Fraction of Dark Matter:
To calculate the local density of PBHs, we use the following equation:

$$\rho_{\mathrm{PBH}} = N_{\mathrm{PBH}} \frac{\langle M_{\mathrm{PBH}} \rangle}{V} \qquad (13)$$

where N_{PBH} is the number of PBHs (taken as 2,000,000), $\langle M_{\mathrm{PBH}} \rangle$ is the mean mass of a PBH, and V is the volume of the universe. Based on our simulations:

Mean PBH Mass (in Solar Masses): 0.4068

Total Mass of PBHs (in kg): 1.8336×10^{36}

Volume of Universe (in cubic meters): $\sim 2.939 \times 10^{64}$

Simulated PBH Density (in Kg/m^3): 6.2389×10^{-29}

To compare this with the total dark matter density, we use the cosmological parameter for dark matter, which is derived from the critical density:

$\rho_{DM} = \Omega_{DM}\rho_{crit}$ where, $\rho_{crit} = \frac{3H_0^2}{8\pi G}$ is the critical density of the universe [32].
Using Ω_{DM}= 0.26, and H_0= 70 km/s/Mpc, we find:
$\rho_{DM} = 2.3925 \times 10^{-27}$ Kg/m^3, hence the fraction of dark matter attributable to PBHs is given by:

$$f_{\mathrm{PBH}} = \frac{\rho_{\mathrm{PBH}}}{\rho_{\mathrm{DM}}} \quad (14)$$

This results in a PBH fraction of approximately $f_{\mathrm{PBH}} = 0.0261$ from the simulation.

Analytical Estimate for PBH fraction:

An analytical approach to estimate the PBH fraction is derived from the cosmological relationship connecting the PBH density parameter$\Omega_{PBH}$the mean PBH mass, and their formation history [10, 26]. The density parameter $\Omega_{PBH}$is expressed as:

$$\Omega_{\mathrm{PBH}} = 1.24 \times \frac{10^{-8}}{h^2}\beta(M_{\mathrm{PBH}})\left(\frac{M_{\mathrm{PBH}}}{M_{\odot}}\right)^{-\frac{1}{2}}$$

where, the relevant symbols are already explained in Equation (15), Using the simulated PBH Density (in Kg/m^3) as 6.2389×10^{-29} we find $f_{\mathrm{PBH}} = 0.0230$ from analytical calculations which is in excellent agreement with the simulated value.

Justification of Results:

The consistency between the simulated and analytical values of f_{PBH}highlights the robustness of our approach. The analytical model leverages established cosmological relations to connect the PBH density to the critical density and dark matter fraction [10]. This agreement serves as a cross-validation of the simulation results.

Why Analytical Results Matter: The analytical approach provides a theoretical baseline derived from cosmological principles, independent of simulation-specific assumptions. This ensures that the results are not overly reliant on simulation parameters and are instead grounded in a broader cosmological framework.

Role of Simulations: The simulations play a critical role in capturing complex, non-linear interactions and distributions that are difficult to incorporate analytically. The derived f_{PBH}values serve as a practical benchmark for comparison with analytical predictions.

Cosmological Insight and Estimation of β:

To link the PBH abundance to cosmological parameters, we rewrite the equation for $\beta(M_{\mathrm{PBH}})$ as follows:

$$\beta(M_{\mathrm{PBH}}) = \frac{\Omega_{\mathrm{PBH}}h^2}{1.24\times10^{-8}}\left(\frac{M_{\mathrm{PBH}}}{M_{\odot}}\right)^{\frac{1}{2}} \quad (15)$$

From the simulation, we calculate the value of β as follows: β (Analytical): 1.507 x 10^5 and β (Simulation): 1.709 x 10^5 These values of β provide insight into the fraction of energy density that collapsed into PBHs at formation, helping to quantify their potential contribution to dark matter.

Justification for Introducing β:

The parameter $\beta(M_{\mathrm{PBH}})$ represents the fraction of the universe's energy density that collapses into PBHs at the time of their formation. It encapsulates how likely it is for PBHs to form in regions where density perturbations are high enough to overcome pressure and collapse gravitationally. β connects early-universe density fluctuations to the present-day energy density of PBHs and is essential for estimating their contribution to dark matter. A higher β implies a greater fraction of PBHs formed, which could result in a more significant contribution to the dark matter density.

Observed Constraints on β: The value of β is constrained by various cosmological observations, including:

Gravitational lensing surveys (e.g., MACHO, EROS),

Cosmic Microwave Background (CMB) data,

Big Bang nucleosynthesis (BBN) constraints,

Absence of Hawking radiation from small PBHs.

These constraints limit the range of β for different mass ranges of PBHs. For example, gravitational lensing surveys provide upper bounds on β for PBHs with stellar masses as shown in [33], while the CMB and BBN constrain β smaller PBHs formed in the early universe as shown in [34], and the absence of Hawking radiation from small PBHs also plays a significant role in constraining β as shown in [35]. The introduction of β is therefore crucial for understanding the abundance of PBHs and their potential role as dark matter candidates. By including β in our formulas, we can directly link the formation of PBHs in the early universe to their contribution to the present-day dark matter density.

Results and Discussions

1. **PBH Density and Contribution to Dark Matter:** Our simulations indicate that primordial black holes (PBHs) account for approximately 2.6% of the total dark matter density. This value is consistent with analytical calculations derived from the mass distribution of PBHs within the early universe. We observe that the calculated PBH density closely matches the simulated values, with only a minor deviation of less than 0.1%, attributed to numerical rounding errors and inherent assumptions in the simulation. This contribution, though modest, holds significance within current cosmological models, suggesting that compact objects like PBHs play a measurable role in the dark matter budget. Our findings support the hypothesis that PBHs could serve as viable candidates for dark matter within a cyclic universe framework.

2. **Dark Matter's Role in SMBH Formation:** The results demonstrate that a supermassive black hole (SMBH) with a mass of approximately $M_{\mathrm{SMBH}} \sim 10^9 M_{\odot}$ could form at the center of a contracting universe. A significant portion of this mass originates from the accretion of dark matter,

specifically PBHs, contributing nearly 25% to the total SMBH mass, with the remainder being baryonic matter. The calculated evaporation timescale for this SMBH is on the order of 10^{90} years, far exceeding the current age of the universe. This result suggests that the SMBH remains a long-lived relic through multiple cycles of cosmic expansion and contraction, emphasizing the critical role of dark matter interactions in the evolution of massive black holes within a cyclic cosmological framework

3. **Implications of Dark Matter-Driven Evaporation:** The inclusion of dark matter interactions offers a new dynamical perspective on black hole evolution within dark matter-dominated regions. This framework suggests that dark matter presence, beyond influencing galactic formation and gravitational stability, may also accelerate the lifecycle of SMBHs. Our findings indicate that, under realistic dark matter densities, the dark matter-SMBH interaction may bring SMBH evaporation into an observational timescale, presenting opportunities for empirical testing. This approach provides a bridge between black hole thermodynamics and cosmological phenomena, merging quantum effects with large-scale structure.

4. **Novelty and Potential Observational Consequences:** If the dark matter-SMBH interaction effect persists under varied assumptions of dark matter density and interaction strength, it could motivate future observational campaigns or indirect detection methods to observe SMBH mass loss over extended epochs. This model suggests that dark matter may play an underestimated role in the evolution and mass distribution of SMBHs in dark matter-rich regions over cosmological timescales. To our knowledge, this is the first framework to introduce a dark matter-driven acceleration of SMBH evaporation, challenging traditional views on SMBH longevity.

Conclusion

This study supports the hypothesis that PBHs act as viable dark matter candidates in a cyclic universe, persisting across cosmic cycles and contributing to dark matter density. By incorporating scalar field-driven evolution, our model presents a mechanism for mass-energy continuity between cycles. The interaction between PBHs, dark matter, and SMBHs suggests a dynamic process influencing cosmic evolution. While further investigation is required to refine the model's predictions, this study provides a novel approach to understanding PBHs in cyclic cosmology.

References

1. Steinhardt, P. J., & Turok, N. (2002), "*A cyclic model of the universe*. Science", 296 (5572), 1436-1439.
2. Ratra, B., & Peebles, P. J. E. (1988), "*Cosmological consequences of a rolling homogeneous scalar field*", Physical Review D, 37 (12), 3406.
3. Hawking, S. W. (1975), "*Particle creation by black holes*", Communications in Mathematical Physics, 43(3), 199-220.
4. Green Anne M., "*Primordial black holes as a dark matter candidate - a brief overview"*, Nucl. Phys. B 1003 (2024) 116494.
5. Green, A.M., Kavanagh, B.J., 2021, "*Primordial Black Holes as a dark matter candidate*", J. Phys. G 48, 043001. doi:10.1088/1361-6471/abc534,
6. Zel'dovich, Y.B., Novikov, I.D., 1967, "*The Hypothesis of Cores Retarded during Expansion and the Hot Cosmological Model*", Sov. Astron. 10, 602.
7. Carr, B.J., Hawking, S.W., 1974, "*Black holes in the early Universe. Monthly Notices of the Royal Astronomical Society"*, 168, 399 – 415, doi:10.1093/mnras/168.2.399.
8. Carr, B. J. (1975), "*The primordial black hole mass spectrum".* The Astrophysical Journal, 201, 1–19.
9. Niemeyer, J. C., & Jedamzik, K. (1999), "*Dynamics of Primordial Black Hole Formation",* Physical Review D, 59(12), 124013. DOI: 10.1103/PhysRevD.59.124013.
10. Carr, B., Kühnel, F., & Sandstad, M. (2016), "*Primordial Black Holes as Dark Matter",* Physical Review D, 94(8), 083504. DOI: 10.1103/PhysRevD.94.083504.
11. Kohri, K., Nakama, T., & Suyama, T. (2008), "*Primordial Black Holes and Big Bang Nucleosynthesis*", Physical Review D, 78(6), 067301. DOI: 10.1103/PhysRevD.78.067301.
12. Abbott, B. P., et al. (2016), "*Observation of Gravitational Waves from a Binary Black Hole Merger*", Physical Review Letters, doi: 10.1103/PhysRevLett.116.061102.
13. Abbott, R., et al. (2021), "*Compact Binary Coalescences Observed by LIGO and Virgo During the Second Part of the Third Observing Run",* Physical Review X, 11(2), 021053.
14. Ijjas, A., & Steinhardt, P. J. (2017), "*Classically stable nonsingular cosmological bounces",* Physics Letters B, 764, 289–294.
15. Peskin, M. E., & Schroeder, D. V. (1995), "*An Introduction to Quantum Field Theory*", Westview Press.
16. Mukhanov, V. (2005), "*Physical Foundations of Cosmology",* Cambridge University Press.
17. Khoury, B. A. Ovrut, P. J. Steinhardt, N. Turok, "*The Ekpyrotic Universe: Colliding Branes and the Origin of the Hot Big Bang"*, Phys. Rev. D 64, 123522 (2001).
18. Green, A. M., & Liddle, A. R. (1997), "*Constraints on the density perturbation spectrum from primordial black holes",* Physical Review D, 56(10), 6166-6174.

19. Ricotti, M., & Gould, A. (2009), "*A New Probe of Dark Matter Properties: Microlensing of PBH Clusters around SMBHs"* The Astrophysical Journal, 707, 979–987.
20. Vogelsberger, M., & Zavala, J. (2013), "*Direct detection of dark matter through galactic dynamics",* Monthly Notices of the Royal Astronomical Society, 430, 1722–1738.
21. Spergel D.N. and P. J. Steinhardt, "*Observational Evidence for Self-Interacting Cold Dark Matter",* vol. 84, no. 17, pp. 3760–3763, Apr. 2000.
22. Feng J. L., "*Dark Matter Candidates from Particle Physics and Methods of Detection",* Annual Review of Astronomy and Astrophysics, vol. 48, no. 1, pp. 495–545, Sep. 2010 doi.org/10.1146/annurev-astro-082708-101659.
23. Sasaki, M., Suyama, T., Tanaka, T., & Yokoyama, S. (2018), "*Primordial black holes-Perspectives in gravitational wave astronomy",* Classical and Quantum Gravity, 35(6), 063001. DOI: 10.1088/1361-6382/aaa7b4.
24. Carr, B. J. (1975), "*The primordial black hole formation condition and its mass relation with horizon mass",* The Astrophysical Journal, Volume 201, Page 1-8.
25. Hawking, S. W. (1971), "*Gravitational coTllapse of density perturbations in the early universe",* Monthly Notices of the Royal Astronomical Society, Volume 152, Page 75.
26. Carr, B. J., Kohri, K., Sendouda, Y., & Yokoyama, J. (2010), "*New cosmological constraints on primordial black holes",* Physical Review D, 81(8), 084022, doi.org/10.1103.
27. Banados, E., et al. (2018), "*An 800 Million Solar Mass Black Hole at Redshift 7.54",* Nature, 553, 473-476.
28. Inman, D., & Ali-Haïmoud, Y. (2019), "*Constraining Primordial Black Holes as Dark Matter Using the Cosmic Microwave Background",* Physical Review D, 100, 023519.
29. Alcock, C., Allsman, R. A., Alves, D. R., et al. (2000), "*The MACHO Project: Microlensing Results from 5.7 Years of LMC Observations",* The Astrophysical Journal, 542(1), 281–307. doi.org/10.1086/317014.
30. Planck Collaboration. (2020), "*Planck 2018 results. VI. Cosmological parameters",* Astronomy & Astrophysics, 641, A6. doi.org/10.1051/0004-6361/201833910.
31. Dodelson S. (2003). Modern Cosmology. Academic Press, pp 208-210.
32. Weinberg S, (2008). Cosmology. Oxford University Press, pp 324-327.
33. Alcock, C., et al. (2000), "*The MACHO Project: Microlensing Results from 5.7 Years of Monitoring",* Astrophysical Journal, 542, 281-307. doi,org/10.1086/317199.
34. Carr, B. J., Kuhn, J., Sendouda, Y., & Yokoyama, J. (2016), "*Primordial Black Holes as Dark Matter",* Physical Review D, 94(4), 044036. doi.org/10.1103/PhysRev D.94.044036.
35. Page, D. N. (1976), "*Particle Creation in Nonstationary Scattering Processes",* Physical Review D, 14, 3260-3273. doi.org/10.1103/PhysRev D.14.3260.

A Novel Method for Spatially-Selective ZnO Thin Film Growth by the Sol-Gel Technique

Arpita Das[1,a], Alakananda Das[2,b], Sayantani Sen[3,c], Anirban Bhattacharyya[2,d]

[1] *Institute of Engineering and Management, Kolkata, University of Engineering and Management, Kolkata 700160, India*
[2] *Institute of Radio Physics and Electronics, University of Calcutta, Kolkata 700009, India*
[3] *Centre for Research in Nanoscience and Nanotechnology, University of Calcutta, Kolkata 70000106, India*

[a] arpita.das@uem.edu.in
[b] adas4015@gmail.com
[c] sayantani163@gmail.com
[d] anirban1@gmail.com

Abstract

Sol-gel deposition of ZnO using the dip-coating method typically generates uniform large area thin films on various substrates, and individual devices are created by a subsequent etching step. In this paper a method for the spontaneous formation of islands of ZnO aligned to existing electrode structures has been presented where thin films and nanostructures of ZnO were sequentially deposited on patterned substrates by sol-gel and vapor-liquid-solid processes. The results indicate spontaneous formation of spatially-selective structures of ZnO which avoid proximity to electrode edges. The morphology of these islands shows a honeycomb-like pattern with extended ridges, with ZnO nanowires depending on the underlying thin film, and are observed on the top of the ridge-like structures, thereby enhancing the surface area. This technique is well applicable for formation of ZnO-based sensor devices. Spatial selectivity of the deposition allows the development of semiconductor devices while eliminating the need of any chemical etching process step.

Keywords: ZnO thin film, Sol-gel, ZnO nanowire, VLS, Electrode geometry, Lift-off.
Received 27 January 2025; First Review 06 February 2025; Accepted 07 February 2025

*** Address of correspondence**
Dr. Anirban Bhattacharyya
Institute of Radio Physics and Electronics,
University of Calcutta, Kolkata 700009, India

Email: anirban1@gmail.com

How to cite this article
Arpita Das, Alakananda Das, Sayantani Sen, Anirban Bhattacharyya, A Novel Method for Spatially-selective ZnO Thin Film Growth by the Sol-Gel Technique, J. Cond. Matt. 2024; 02 (02): 37-42.

Available from:
https://doi.org/10.61343/jcm.v2i02.69

Introduction

In recent times, Zinc Oxide (ZnO) materials have been investigated tremendously, and form part of various electronic and optoelectronic devices currently in production [1-4]. Doped with Aluminum, ZnO are excellent transparent conducting oxide materials [5]. Since exciton binding energy in ZnO is very high, these materials are candidates for optical emitters that can operate at elevated temperatures. Unfortunately, the applications of these materials have been restricted so far due to inefficient p-type doping, in the recent years gradual progress have been made [6-7]. Several elements such as Al [8], Ga [9], Mg [10], Sn [11], as well as Mn [12] and Fe [13] have been used as a dopant in ZnO materials for controlling their electronic, optical and magnetic properties.

These materials have been grown by a number of processes, such as sol-gel [14], hydrothermal synthesis [15], vapor-liquid-solid (VLS) [16], sputtering [17], chemical vapor deposition (CVD) [18] and gas-source molecular beam epitaxy (MBE) [19]. The use of the sol-gel technique is very widespread as this process lends itself to the deposition of large area, relatively uniform, high quality well-oriented polycrystalline thin films. The characteristics of the deposited thin film depends on the composition of the precursor solution, coating method applied, and annealing temperature employed [20]. This procedure is aimed to fabricate films of uniform nature, and the fabrication of devices are to be carried out using standard tools such as photolithography, metal deposition for electrode formation, and etching of the semiconducting thin film. It should be noted however that the fabrication of micro scale patterned metallic electrodes by chemical etching on top of ZnO thin films (doped or undoped) is quite challenging as the underlying film readily reacts with most acids at room temperature. Furthermore, the presence of grains and grain boundaries of the film makes it difficult to completely remove organic materials from the film surface after photoresist patterning if the lift-off process is employed.

In this work we discuss a novel deposition process where patterned electrodes are deposited on to the top surface of a sapphire substrate first and then the sol-gel technique is applied, and we demonstrate self-limiting, well-aligned formation of ZnO patterns that do not require any additional lithography or etching steps.

Method

Platinum electrodes in the configuration shown in figure 1(a) were patterned on to (0001) sapphire substrates [Monocrystal, Russia], using image reversal lift-off photolithography and sputter coating (Quorum Technology Q150V) processes.

Sol-gel dip-coating method was used for depositing thin films of ZnO on the substrate with electrodes already fabricated on it. The precursor element was Zinc acetate dihydrate ($Zn(CH_3COO)_2.2H_2O$), which was dissolved in Isopropanol (IPA) and finally a 0.5M solution was produced. Diethanolamine (DEA) ($HN(CH_2CH_2OH)_2$) was incorporated as a stabilizer at 1:1 ratio within the solution. The precursor solution was kept on a magnetic hot plate and continuously stirred at 60 °C for 2 hours. Aluminum Nitrate Nonahydrate ($Al(NO_3)_3 \cdot 9H_2O$) was added to the solution for Al doping and finally 3% Al doped solution was prepared. The solution was stabilized for 24 hours before dip coating. The substrates with pre-fabricated platinum electrodes were dip-coated into the precursor solution and slowly raised at the rate of 1mm/s to complete the coating process, before being preheated at 150°C for 15 minutes. The whole procedure was repeated twice before the final anneal step at 500 °C in air for 60 minutes.

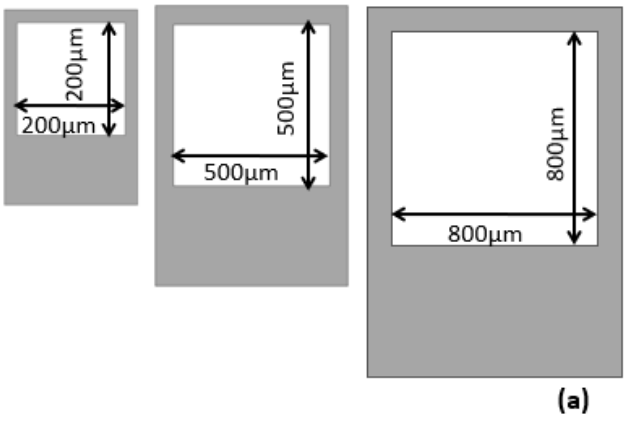

Figure 1(a): Electrode geometry with dimensions

Subsequently, ZnO nanostructures were grown using VLS process on the fabricated thin films. 1nm Gold (Au) thin films were sputter-coated, before annealing at 900°C–925°C for 30 minutes in presence of Argon to form Au nano droplets. Equal mixture of Zinc oxide and graphite powder were kept in a quartz boat at 950°C-975°C and the Au-coated substrates were placed downstream kept at 800°C-825 °C. The entire reaction was performed for 30 minutes in Argon ambience, where flow rate is kept at 5sccm. The entire experimental procedure is described in figure 1(b).

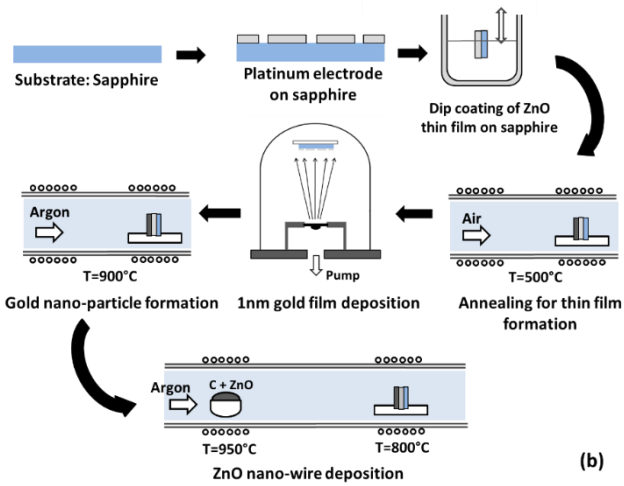

Figure 1(b): Experimental procedure

Results

Electrode geometry

The novelty of the current approach centers around the use of already-patterned substrates, that is the use of sapphire substrates with the electrodes already formed on them, before carrying out the deposition processes. It was found, as will be expanded in subsequent sections, that the configuration that is the shape and size of the electrodes play a very significant role in the final results obtained. This is presented in figure 1(a), where a three-electrode cluster is shown. This pattern has been repeated over the wafer. The electrodes are designed as 'square rings', that is the metal is bounded by an outer and an inner rectangle, set off center with respect to each other. The wider 'pad' part at the bottom was designed for probing or wire bonding, as needed. The dimensions are provided in figure 1(a), and the overall dimensions of the electrodes E1, E2 and E3 are 800µm x 800µm, 500µm x 500µm and 200µm x 200µm respectively. The width of the thinnest part was 100µm, 60µm and 40µm respectively. The separation between two adjacent electrodes was 200µm. It should be noted that the thickness of the platinum metal was 10nm.

Optical Microscopy

After the sol-gel growth of ZnO thin film [21], ZnO nanowires were deposited subsequently by the VLS process [16], and the samples were studied using optical microscopy at various magnifications. While there are small variations, the devices were found to exhibit nearly identical features. In figure 2, two representative images of the large electrode E1 is shown on the top row. The rectangular metallic electrode geometry is clearly visible for all the devices,

indicating that they have survived the high temperature processes that they were subjected to. The horizontal scratch marks exposing the metal across the bottom "pad" portion of the device was made by probes during electrical testing, and may be ignored for the current discussion.

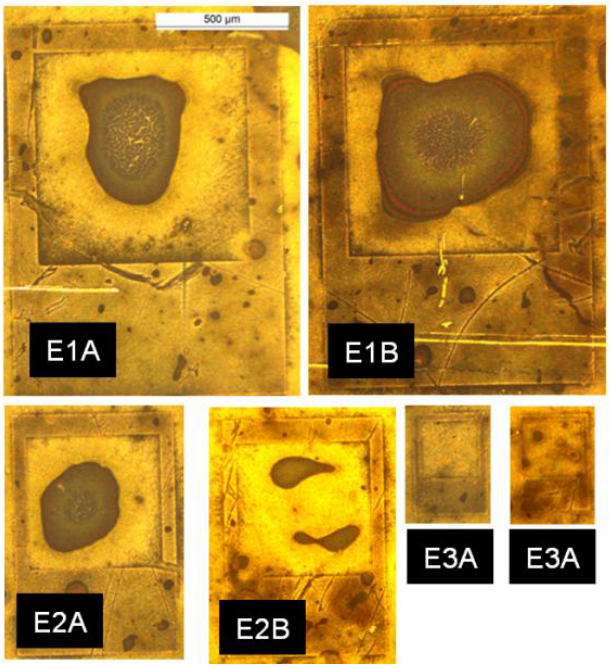

Figure 2: Optical microscope images of electrode E1 (largest electrode of device A and B), E2 (medium sized electrode of device A and B) and E3 (smallest sized electrode of device A and B)

The point of interest is that for both the devices E1A and E1B, and for all similar devices, the active region enclosed by the electrode was found to be nonuniform, with prominent irregular shaped islands being observed as dark patches. While the exact shape of the patch randomly varies, they are always clearly isolated from the inner edges of the electrode, occupy the central part, and cover 60-70% of the area. When the medium size devices were investigated, they show similar features as shown by E2A and E2B of the bottom row. However, there are clear difference that occur for these devices when compared to that for the larger ones. The central patch is present in all devices, but they are more irregular in shape, and may consist of two patches, well separated from each other, instead of a central single one. It is interesting to note that for most of the smallest devices, there are no central patch, and the devices show uniformity over the entire area. This is shown in figure 2, for the devices E3A and E3B, shown in the bottom row. It should be noted that even for these smaller devices, the electrode patterns are clear and do not show sign of any process-induced damage.

Energy Dispersive Spectroscopy (EDS) Measurements

EDS measurements were performed to investigate the chemical analysis of the samples, using an acceleration voltage of 15KV for enhancing the SNR and reduce scan time. At this voltage, the electron beam is expected to penetrate the thin ZnO film into the sapphire Al_2O_3 substrate below. The overall EDS measurement indicates the existence of Zn, Al, O, and Pt elements. Figure 3(a) indicates the images obtained from scanning electron microscopy for a quarter of the device, showing the patch, as described previously, here appearing lighter over a darker background, and the platinum electrode, the edge of which has been highlighted by dashed lines. The spatial distribution of Al, which is present in the substrate below, is shown in figure 3(b), which as expected is uniform, with a darker region indicating the platinum electrode region, as the electrons are absorbed on the way down in the thin platinum film. The patch is observed to be dark for the same reason. When Zn is mapped over the device, it is clear that there are two distinct regions. A thinner layer of ZnO is present all over the surface, as indicated as the presence of uniform but spare distribution of pink dots in figure 3(c). However, the patch shows a significantly higher presence of Zn, indicating the it is due to the presence of a much thicker film of ZnO, that has been selectively deposited at the central regions of each of the devices, in a spontaneous but extremely reliable manner. The importance of this finding is that spatial selectivity is very crucial to achieve for sol-gel process as well as VLS deposition.

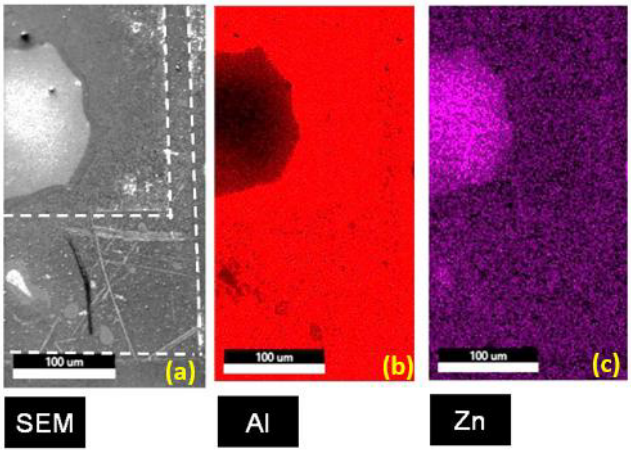

Figure 3: SEM Image (a) and EDS Image indicating the presence of Al (b) and Zn (c).

Scanning Electron Microscopy (SEM)

EDS mapping showed that the thickness of the ZnO thin film was significantly higher at the center of the device windows. Detailed scanning electron microscopy was performed to investigate this fact further, and the results were presented in figure 4. An SEM image of the electrode E1A, whose optical microscopy image was presented earlier, is shown in figure 4(a).

The metallic electrode pattern is again clearly visible. The dark patch at the center of the device is shown here as a grey area, which we name Z_1 (Zone 1). The region around this

patch is darker and very uniform, which we term Z_2 (Zone 2), while the region around the edge of the electrode appears significantly brighter, showing unresolved dots-like features at this magnification is Z_3 (Zone 3). High magnification images were obtained at each of these zones, which are presented in the figures 4(b) to 4(e). It would help to recall that the surface of the sample is expected to show features arising from the sol-gel process as well as the VLS process carried out subsequently.

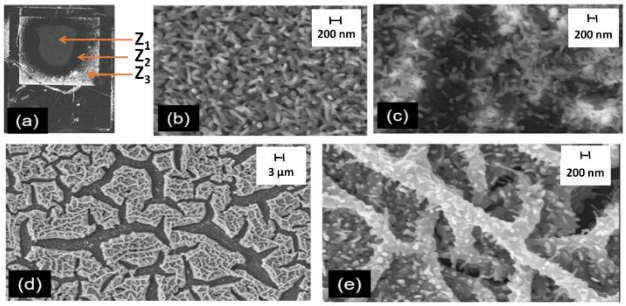

Figure 4: Low magnification SEM image of ZnO inside electrode E1 is shown in (a) along with high magnification SEM images of zones Z_2(b), Z_3(c) and Z_1(d, e).

The surface morphology obtained from the Zone immediately around the patch area Z_2 indicates the presence of densely packed nanowires, with lengths of 200µm and diameters about 50µm. Similar features are also present in the zone Z_3 but the nanowire density is lower. For both these regions, the features are similar to results obtained for ZnO nanostructures fabricated by the VLS process on to ZnO thin films deposited by sol-gel, as presented in our early publications [16]. However, the morphology is significantly different for zone Z_1, that is spontaneously positioned at the center of each of the devices. Here, as observed by EDS, the film is significantly thicker. This can be easily correlated with the SEM image as shown in lower magnification in figure 4(d), which shows a thicker ZnO film with honeycomb-type morphology formed by branched ridges separated by deep trenches. The higher magnification image of this area, as seen in figure 4(e) indicates the presence of ZnO nanowires, which have been grown on top of the ridge-like features.

Discussion

The critical element that has been highlighted in the previous sections is that the existence of a thicker "patch" of ZnO film of roughly the same size, spontaneously deposited at the center of the device. A possible mechanism driving this spontaneous formation is shown schematically in figure 5. Figure 5(a) indicates the cross-section of a sapphire substrate, on to which platinum electrodes were specifically patterned as described in figure 5(b). During the sol-gel dip-coating process, the patterned substrate was dipped into the precursor solution and subsequently withdrawn slowly.

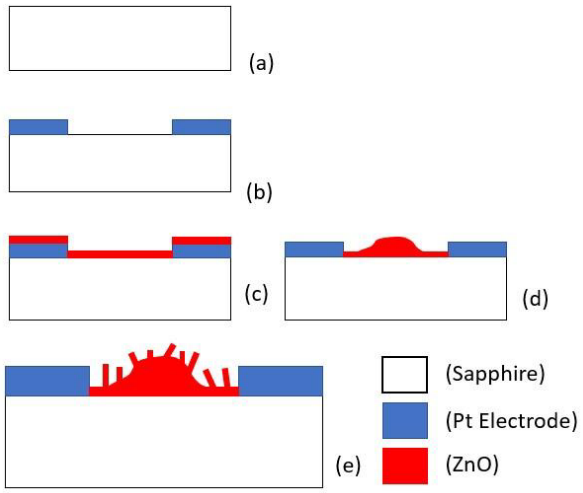

Figure 5: Schematic indicating mechanism for formation of ZnO spatially-selective structures (a) Substrate, (b) Electrode formation, (c) thin film deposition by sol-gel, (d)-(e) Nanowire by VLS.

This coats all areas, including the bare sapphire substrate as well as tops of platinum electrodes. After the withdrawal of the sample from the solution, it cannot be expected that precursor solution wets both these surfaces equally. A difference of hydrophobicity, and hence of the contact angles formed, is present at the precursor/sapphire and precursor/platinum interfaces. We believe that the liquid withdraws spontaneously from top of the platinum and is "pooled" at the center of the device, on the bare sapphire substrate, as depicted in figure 5(c). With the evaporation of the isopropyl alcohol, this forms a thicker patch of "gel" at the center of the device, which subsequently is annealed to form the ZnO film, onto which the VLS grown nanowires have been deposited (figure 5(d)-(e)). This model based on the flow of precursor solution away from the top of platinum electrodes can be justified based on the observation of smaller samples. For smaller platinum area, the formation of the ZnO thicker patch is less regular. Furthermore, this mechanism is completely absent for the smallest device. However, it should be stressed that further studies in contact angle measurement and real-time study of the sol-gel dip coating process are needed to establish and quantify the processes involved.

The generation of thicker films within the area demarcated by the electrodes is technologically very attractive, especially as such films contain a ridged morphology, having higher surface to volume ratio compared to other regions. Furthermore, the ratio was significantly enhanced by the deposition of VLS grown ZnO nanowires. This is of importance to a wide range of devices, including gas and liquid sensors, photodetectors, etc.

Conclusion and Future Prospective

While growth of ZnO by the sol-gel technique has been

extensively studied, this process is restricted to generation of thin films of uniform thickness. In this work we demonstrate a process for the spontaneous formation of ZnO islands, that are automatically placed at the center of ring-type electrodes. These islands show a ridged network type morphology, having very high surface to volume ratio. Furthermore, nanowires were grown on to these islands using VLS process, to further increase the surface area. This process is possibly driven by surface tension forces, based on difference in wettability of the electrode or substrate surface for the precursor solution. These findings are expected to find major applications in development of sensor devices.

Acknowledgement

Alakananda Das (09/028 (0946)/2015-EMR-I) and Sayantani Sen (09/028(0921)/2014-EMR-I) would like to acknowledge the CSIR Senior Research Fellowship scheme. The authors would like to acknowledge University of Calcutta for SEM and EDS measurement.

References

1. A. Janotti, C. G. Vande Walle, *"Fundamentals of zinc oxide as a semiconductor"*, Rep. Prog. Phys.72, (2009), 126501. https://doi.org/10.1088/0034-4885/72/12/126501
2. A. K. Radzimska, T. Jesionowski, *"Zinc Oxide—From Synthesis to Application: A Review"*, Materials 7, (2014),2833–2881. https://doi.org/10.3390/ma7042833
3. U. Ozgur, D. Hofstetter, H. Morkoc, "ZnO Devices and Applications: A Review of Current Status and Future Prospects", Proc. IEEE 98(7), (2010), 1255–1268. https://doi.org/10.1109/JPROC.2010.2044550
4. B. K. Sonawane, M. P. Bhole, D. S. Patil, *"Structural, optical and electrical properties of post annealed Mg doped ZnO films for optoelectronics applications"*, Opt. Quant. Electron 41, (2009), 17–26. https://doi.org/10.1007/s11082-009-9317-y
5. M. C. Jun, J. H. Koh, *"Optical and structural properties of Al-doped ZnO thin films by sol gel process"*, J Nanosci Nanotechnol. 13(5), (2013), 3403-7. https://doi.org/10.1166/jnn.2013.7314
6. C. H. Park, S. B. Zhang, Su-Huai Wei, *"Origin of p-type doping difficulty in ZnO: The impurity perspective"*, Phys. Rev. B 66, (2002), 073202. https://doi.org/10.1103/PhysRevB.66.073202
7. Z. Ye, H. He, L. Jiang, *"Co-doping: an effective strategy for achieving stable p-type ZnO thin films"*, Nano Energy 52, (2018), 527-540. https://doi.org/10.1016/j.nanoen.2018.08.001
8. Y. S. Kim, W. P. Tai, *"Electrical and optical properties of Al-doped ZnO thin films by sol–gel process"*, Appl. Surf. Sci. 53(11), (2007), 4911-4916. https://doi.org/10.1016/j.apsusc.2006.10.068
9. V. Bhosle, A. Tiwari, J. Narayan *"Electrical properties of transparent and conducting Ga doped ZnO"*, J. Appl. Phys. 100, (2006), 033713. https://doi.org/10.1063/1.2218466
10. K. Huang, Z. Tang, L. Zhang, J. Yu, J. Lv, X. Liu, F. Liu, *"Preparation and characterization of Mg-doped ZnO thin films by sol–gel method"*, Appl. Surf. Sci. 258(8), (2012), 3710-3713. https://doi.org/10.1016/j.apsusc.2011.12.011
11. M. Ajili, M. Castagné, N. K. Turki, *"Study on the doping effect of Sn-doped ZnO thin films"*, Superlattices Microstruct. 53, (2013), 213-222. https://doi.org/10.1016/j.spmi.2012.10.012
12. S. A. Ahmed, *"Structural, optical, and magnetic properties of Mn-doped ZnO samples"*, Results in Physics 7, (2017), 604-610. https://doi.org/10.1016/j.rinp.2017.01.018
13. A. K. Mishra, D. Das, *"Investigation on Fe-doped ZnO nanostructures prepared by a chemical route"*, Materials Science and Engineering: B171, (2010), 1–3. https://doi.org/10.1016/j.mseb.2010.03.045
14. K. Davis, R. Yarbrough, M. Froeschle, J. White, H. Rathnayake, *"Band gap engineered zinc oxide nanostructures via a sol–gel synthesis of solvent driven shape-controlled crystal growth"*, RSC Adv.9, (2019), 14638-14648. https://doi.org/10.1039/C9RA02091H
15. S. Baruah, J. Dutta, *"Hydrothermal growth of ZnO nanostructures"*, Sci. Technol. Adv. Mater. 10, (2009), 013001. https://doi.org/10.1088/1468-996/10/1/013001
16. P. G. Roy, A. Dutta, A. Das, S. Sen, P. Pramanik, A. Bhattacharyya, *"VLS-grown diffusion doped ZnO nanowires and their luminescence properties"*, Mater. Res. Express 2 (2015) 075007. https://doi.org/10.1088/2053-1591/2/7/075007
17. M. Masłyk, M.A. Borysiewicz, M. Wzorek, T. Wojciechowski, M. Kwoka, E. Kamińska, *"Influence of absolute argon and oxygen flow values at a constant ratio on the growth of Zn/ZnO nanostructures obtained by DC reactive magnetron sputtering"*, Appl. Surf. Sci. 389, (2016), 287-293. https://doi.org/10.1016/j.apsusc.2016.07.098.
18. L. N. Protasova, E. V. Rebrov, K. L. Choy, S. Y. Pung, V. Engels, M. Cabaj, A. E. H. Wheatley, J. C. Schouten, *"ZnO based nanowires grown by chemical vapour deposition for selective hydrogenation of acetylene alcohols"*, Catal. Sci. Technol.1, (2011), 768-777. https://doi.org/10.1039/C1CY00074H

19. J. S. Wang, C. S. Yang, P. I. Chen et al., *"Catalyst-free highly vertically aligned ZnO nanoneedle arrays grown by plasma-assisted molecular beam epitaxy,"* Applied Physics A, 97(3), (2009), 553–557. https://doi.org/10.1007/s00339-009-5436-3
20. L. Znaidi, *"Sol–gel-deposited ZnO thin films: A review",* Materials Science and Engineering: B, 174(1–3), (2010). https://doi.org/10.1016/j.mseb.2010.07.001
21. A. Das, P. G. Roy, A. Dutta, S. Sen, P. Pramanik, D. Das, A. Banerjee, A. Bhattacharyya, *"Mg and Al co-doping of ZnO thin films: Effect on ultraviolet photoconductivity",* Materials Science in Semiconductor Processing, 54, (2016), 36-41. https://doi.org/10.1016/j.mssp.2016.06.018

Oxidation Kinetics Studies of $Ti_3C_2T_x$ MXene using Freeman-Carroll Method

D A Anarse[1,a], M B Kadam[1,b], A L Sunatkari[2,c], A U Chavan[3], M R Prasad[1], P B Sarawade[4]

[1] *Dept. of AS&H, Pimpri Chinchwad College of Engineering, Pune-44, Maharashtra, India.*
[2] *Dept. of Physics, Siddharth College of Arts, Science & Commerce, Mumbai-01, Maharashtra, India.*
[3] *Dept. of Physics, KBP College Vashi, Navi Mumbai-400703, Maharashtra, India.*
[4] *Dept. of Physics, University of Mumbai Mumbai-32, Maharashtra, India*

[a] daanarse@gmail.com
[b] mahadev.kadam@pccoepune.org
[c] ashok.sunatkari@gmail.com

Abstract

$Ti_3C_2T_x$ MXene is synthesized from $Ti_3Al_2C_3$ MAX phase by using HF treatment and characterized by X-ray diffraction In addition, oxidation of $Ti_3C_2T_x$ MXene in nitrogen environments from room temperature to 500 °C is studied by thermogravimetric analysis. The experiment shows that oxidation of $Ti_3C_2T_x$ MXene starts at 275 °C. Activation energy of oxidation of $Ti_3C_2T_x$ MXene is determined using the Freeman Carroll method. It is found that in a nitrogen environment and in a strong oxidation temperature range, oxidation activation energy of $Ti_3C_2T_x$ MXene is approximately 235.6 kJ mol^{-1}.

Keywords: $Ti_3C_2T_x$ MXene, Kinetics, Oxidation activation energy, Freeman Carrol method.
Received 30 January 2025; First Review 16 February 2025; Accepted 16 February 2025

*** Address of correspondence**
D A Anarse
Dept. of AS&H, Pimpri Chinchwad College of Engineering, Pune-44, Maharashtra, India

Email: daanarse@gmail.com

How to cite this article
D A Anarse, M B Kadam, A L Sunatkari, A U Chavan, M R Prasad, P B Sarawade, Oxidation Kinetics Studies of $Ti_3C_2T_x$ MXene using Freeman-Carroll method, J. Cond. Matt. 2024; 02 (02): 43-45.

Available from:
https://doi.org/10.61343/jcm.v2i02.108

Introduction

$Ti_3C_2T_x$ MXene is a two-dimensional transition metal carbide whose stability and performance in a variety of applications, including energy storage, catalysis, and sensing etc, may be understood by studying its oxidation kinetics [1-4]. This oxidation kinetics can be understood using Freeman - Carroll method [5], which utilizes the relation between temperature, time and the rate of reaction. This method analyses non-isothermal kinetic data, particularly when the reaction rate is temperature dependent. Thus, order to understand the stability of $Ti_3C_2T_x$ MXene, in this paper, we reported the oxidation behavior of $Ti_3C_2T_x$ MXene at high temperatures in nitrogen environment.

Experimental Method

$Ti_3C_2T_x$ MXene Preparation

An amount of 1 gm Titanium Aluminum Carbide $Ti_3Al_2C_3$ MAX phase (90.00% pure) ≤ 100µm Particle size was added in concentrated Hydrofluoric acid HF (40%) of Sigma Aldrich solution and stirred for 26 hours at room temperature. The solution then filtered and washed frequently with distilled water and ethanol until the pH of solution became neutral. Powder obtained after filtration was dried in the oven for 8 hours.

$Ti_3C_2T_x$ MXene characterization

The power was further investigated for its structural properties using Bruker D8 Advance CuKα (lambda = 0.15408 nm) diffractometer in the range 10°-80°. Thermogravimetric analysis of the powder was carried out using Model No.-TGA55 Make - TA Instruments. USA. The $Ti_3C_2T_x$ MXene powder sample was placed in the alumina crucible of the TG Analyzer. Its temperature was increased from room temperature to 500 °C with a heating rate of 20 °C /min in the presence of a nitrogen environment.

Results and Discussion

X-ray analysis

Figure 1. shows the XRD pattern of the powder obtained by etching Ti3Al2C3 MAX phase by HF at room temperature. The diffraction peaks at 2θ viz: 18.80°, 38.76°, 41.57°, shows the pure phase formation of $Ti_3C_2T_x$ MXene matches with previously reported results [4].

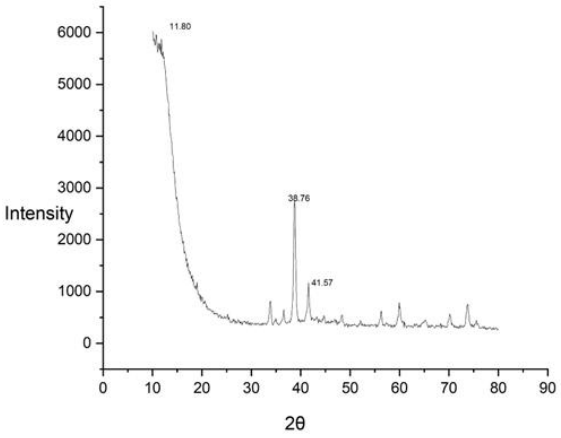

Figure 1: XRD plot of $Ti_3C_2T_x$ MXene.

Thermogravimetric analysis: Oxidation experiments

Figure 2 shows the TGA plot of $Ti_3C_2T_x$ MXene in the nitrogen environment with a heating rate of 20 °C/min. From the TGA plot, it is seen that the oxidation of $Ti_3C_2T_x$ MXene starts at 275 °C and continues rapidly peaking upto 400 °C. This indicates the onset of decomposition of $Ti_3C_2T_x$ Mxene which leads to the incorporation of oxygen forming TiO_2. Further mass decreases after 400 °C which might be due to the decomposition and evaluation of CO_2 through the sample. This indicates that oxidation of $Ti_3C_2T_x$ MXene is a solid-gas reaction.

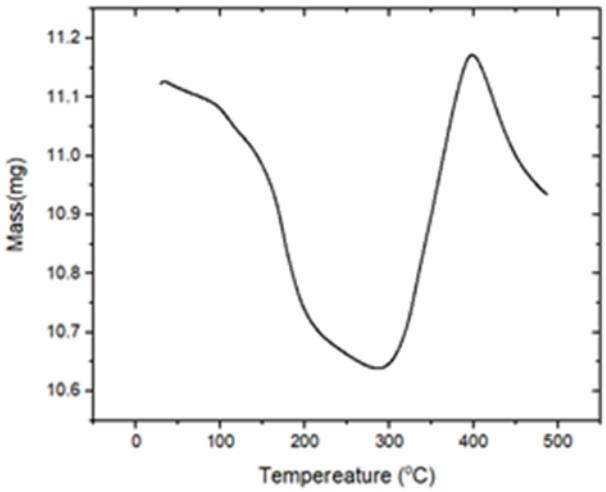

Figure 3: TGA Plot of $Ti_3C_2T_x$ MXene.

Figure 3 shows the plot of the derivative of mass with temperature. From the figure, it is seen that the rate of mass change is rapid after the onset of oxidation; it remains constant from 320 °C to 360 °C and rate decreases very rapidly after 360 °C. This indicates the complete oxidation of $Ti_3C_2T_x$ MXene sample.

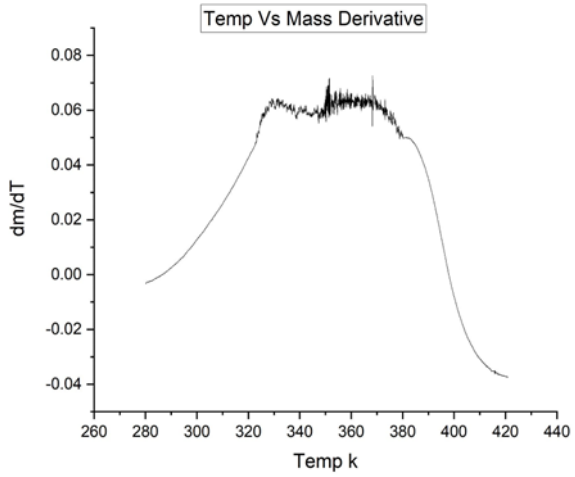

Figure 3: Weight gain plot TGA plot of $Ti_3C_2T_x$ MXene

Freeman Carrol method

The activation energy decides the oxidation stability of $Ti_3C_2T_x$ MXene and it depends on the rate of the reaction.

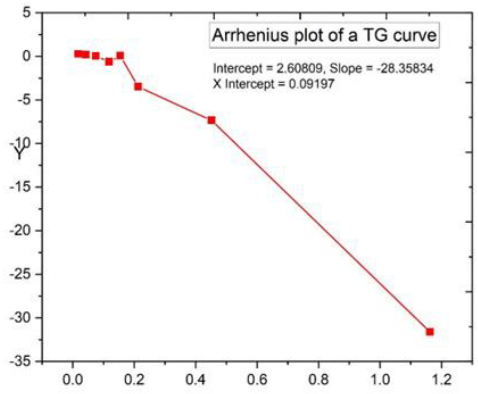

Figure 4: Arrhenius plot of a TG curve plot TGA Plot of $Ti_3C_2T_x$ MXene

Large value of activation energy indicates the smaller reaction rate and vice versa. Now, we will utilize the Freeman Carroll method and standard Arrhenius equation (1) to obtain the oxidation activation energy.

$$\frac{da}{dt} = A \exp\left(-\frac{E}{RT}\right)^n \qquad \ldots (1)$$

Figure 4 shows the Arrhenius graph obtained from thermogravimetric analysis of $Ti_3C_2T_x$ MXene. The data obtained from terms given below,

$$\frac{\Delta \ln \left(\frac{dm}{dt}\right)}{\Delta \ln \left(m_\infty - m_t\right)} \quad and$$

$$\frac{\Delta\left(\frac{1}{T}\right)}{\Delta \ln\left(m_\infty - m_t\right)}$$

were plotted considering m_∞ is mass when complete oxidation of the sample takes place. From the slope of the line activation energy of oxidation of $Ti_3C_2T_x$ MXene is approximately 235.6 kJ mol^{-1} and the intercept indicates that order of reaction is 2.6. This indicates the need for a controlled and inert atmosphere to avoid the oxidation of $Ti_3C_2T_x$ MXene.

Conclusion and Future Perspective

The experiment and estimated results suggest that the oxidation of $Ti_3C_2T_x$ MXene in a nitrogen environment takes place above 275 °C. Its oxidation activation energy is found to be approximately 235.6 kJ mol^{-1}. Thus, to control the oxidation under heat treatments inert atmosphere should be maintained. In this regard more insights will be further obtained when this material will be investigated under different gaseous environments and heating rates.

References

1. S. Kumar, M. A. Rehman, S. Lee, M. Kim, H. Hong, J. Y. Park & Y. Seo Sci. Rep. 11, 649- 2021.
2. A.M. Iquba, A. Tariq A. Zaheer S. Gul, A.AI AliM, Z. Iqbal D. Akinwandeand S. Rizwan ASC Omega, 4(24), 20530-20539, 2019.
3. Y. Wang and Y. Wang, Smartmat 4(1), 2-25, 2022
4. B. Shen, R. Hao, Y. Huang, Z. Guo and X. Zhu, Crystals 12, 1099, 2-38, 2022.
5. D. Yang, H Sun, H. Lu, Y. Guo X. Li and X. Hu, Supercond. Sci. Technol. 16;576–581, 2003.

Investigation of Blue Shift Phenomena and Dielectric Behaviour With the Concentration of Co Doped in Zns Nanoparticles

Anupam Pramanick[1,a], Tapas Pal Majumder[1,b], Debabrata Bhadra[2,c]

[1] *Department of Physics, University of Kalyani, Kalyani-741245 (West Bengal), India*
[2] *Department of Physics, Bhairab Ganguly College, Kolkata-700056 (West Bengal), India*

[a] pramanickanupam@gmail.com
[b] tpmajumder1966@gmail.com
[c] bhadra.debabrata@gmail.com

Abstract

In this work undoped Zinc Sulphide (ZnS) nanoparticles (NPs) and doped with Cobalt (Co) having dopant concentration 0.5%, 1.0%, 1.5% have been synthesized by hydrothermal method, in which ethylenediamine (EDA) has used as capping agent. An investigation has been made on the changes of structural, optical, molecular as well as electrical properties, occurs due to doping. X-ray diffraction (XRD) patterns reveal the idea about formation of samples with crystalline nature having intense peaks which are consistent with the primary cubic phase of zinc blend and nano-sized particles. None of any peak corresponding to doped material Co was noticed which means the Co ions had been incorporated successfully without vast modulating the original crystal structure. In association with hexagonal phase was found due to weak signature of ZnS. It has been pointed out from UV-Visible spectra the value of optical gap energy is a function of Cobalt concentration and quantum confinement process occurred. The occurrence of blue shift phenomena has been confirmed by the observed variation of the optical gap range between 4.01 to 4.79 eV. FTIR spectra showed ZnS characteristics frequency band position did not exhibit any distinguished change with doping what acknowledged the Co was well substitution of Zn into ZnS NPs. In photo luminance (PL) spectra the PL intensity did respond appreciable with modifying the Co concentration. The agglomerated NPs with almost spherical shaped and elemental compositions with stoitiometric ratios were confirmed by Scanning Electron Microscope (SEM) images and Energy Dispersive X-Ray (EDX) spectra respectively. Measured values of AC conductivity increases with Co concentration at higher frequency range which may make these materials useful at high frequency regime. Therefore, conclusion can be done, these studied ZnS doped with Co materials can show their applicability in spinotronics and photo luminescent devices.

Keywords: Cobalt-doped ZnS, Photo luminance, Band-gap, Fourier Transform Infrared (FTIR), AC conductivity.
Received 27 January 2025; First Review 14 February 2025; Accepted 15 February 2025

*** Address of correspondence**
Anupam Pramanick
Department of Physics, University of Kalyani, Kalyani-741245 (West Bengal), India

Email: pramanickanupam@gmail.com

How to cite this article
Anupam Pramanick, Tapas Pal Majumder, Debabrata Bhadra, Investigation of blue shift phenomena and dielectric behaviour with the concentration of Co doped in ZnS nanoparticles, J. Cond. Matt. 2024; 02 (02): 46-52.

Available from:
https://doi.org/10.61343/jcm.v2i02.66

Introduction

In the last few decades most intensive research both theoretical and experimental is going on nanomaterials semiconductors in order to understand their marvelous optical, electrical and optoelectronics properties. ZnS is very popular semiconductor material due to its versatile characteristic's nature having two main crystalline forms, one is cubic (zinc blend) another is hexagonal. Among them cubic is more stable having band gap energy about 3.54 eV and 40 meV is the excitation binding energy whereas hexagonal has wider band gap of 3.91 eV. This duality helps ZnS for being outstanding polymer [1]. Apart from these, recent research on this material provides the information that it exhibits rhombohedral structure also [2]. For its luminescent property in photo electronic device, ZnS become very useful in the window materials [3], solar cell [4-5], laser diode [6-9].

The electrical, optical and magnetic properties of ZnS can be tuned with the suitable incorporation of rare earth (RM) and transition (TM) metals [10]. Last decades, efforts to have prepared ZnS NPs doped with TM and RM was very admirable [11-18]. The variation of the optical band gap energy E_g gambles on dopants type. TM metals have smaller ionic radii compared to Zn^{2+} and sp-d spin exchange interaction for which TM doped (Fe, Ni, Co, Cr) ZnS NPs have increased E_g [19-23] but doped with RM (Tb, Dy, Sm) dopants ZnS NPs got decreased E_g due to higher ionic radii and sp-f spin exchange [24-25].The d-orbital of Co mixes with the valence band and conduction band of the II-VI

materials that is why stronger coupling occurs in between Co and II-VI materials [26]. Apart these reports gathered from many researches the radii of Co^{2+} and Zn^{2+} are respectively 0.58 Å and 0.60 Å, as a result Co^{2+} substitutes Zn^{2+} at lattice site up to 15 at % to 20 at % in ZnS NPs without any drastic change of host lattice structure. So cobalt doped ZnS NPs are required investigation for structural, electrical, optical and magnetic properties [27]. Also, ZnS with Co NPs show paramagnetic and ferromagnetic nature depending on amounting of doping [28]. The hydrothermal method was chosen to employ here among the all-diverse types of synthesis process and several advantages [29-30].

In this work pure ZnS and doped with Co NPs have been prepared with different concentration of cobalt (0.5%, 1.0%, 1.5%). The main focus is to do analysis of the structural, electrical, molecular and optical, properties by using respectively XRD, UV-Visible, PL, FTIR, and dielectric measurement systems. SEM and EDX identified the morphologies and chemical composition.

Experimental Details

Sample Preparation

To synthesis required chemicals zinc acetate [$Zn(CH_3COO)_2.2H_2O$], thiourea [$(NH_2)_2CS$], cobalt chloride [$CoCl_2.6H_2O$] and EDA [$C_2H_8N_2$] which were analytical grade need not further purification. All glass wares were cleaned properly by using acid. Appropriate amount of Zn $(CH_3COO)_2.2H_2O$, $CoCl_2.6H_2O$ and $(NH_2)_2CS$, were deliquesced in eighty milliliter deionized water and EDA with same ratio of volume. For obtaining homogeneous by using magnetic stirrer mixture was agitated for 1 hour at normal temperature. After this solution was transformed to 100 ml silver lined stainless steel autoclave, filled 80% volume of it. Then the solution containing autoclave had been keeping furnace at temperature 200 °C for half of a day. After which it was conceded to settle naturally at acceptable temperature. Lastly obtained feculence consecutively filtered & then scrubbed by using ethanol and demineralized water several times. The final product was dried in oven at 100 °C for overnight. To have the (0, 0.5, 1.0 and 1.5) % Co concentrated ZnS NPs this synthesized process was conducted repeatedly.

Sample Characterizations, Outcome and Investigation:

Structural analysis

The nature of crystal structure, size of particle and phase have been investigated from the study of XRD pattern shown in Figure 1. The well-defined peaks at wide range of 2θ confirms self-prepared specimens are polycrystalline nature. From figure 1 the observed peaks of diffraction are located at about 27.16°, 28.87°, 30.48°, 39.67°, 47.56°, 52.03°, 56.60° which correspond to respectively (101), (008), (104), (108), (110), (1012) and (203) lattice planes of zinc blend and hexagonal wurtize structure and these are fit into with the standard JCPDS spectrum Card no. 72-0163. No Bragg's diffraction peak has detected for Co and its oxide, sulphide and any impurity indicating absence of any secondary phase, only single phase is dominant here and Co^{2+} ions doped successfully without considerable transforming the crystal structure of host materials ZnS. It has also noticed the peak intensity reduced gradually and broadening occurs which signifies the diminishes of crystalline quality of NPs due to distortion and induced strain because of doping of Co^{2+} ions into ZnS [31].

In conjunction with the diffraction peaks slightly shift towards higher 2θ values with compared to undoped ZnS nanocrystals. This might be due to substitution of Zn^{2+} ions by Co^{2+} in ZnS for which lattice constant could be reduced.

The reduction of lattice constant can be explained by the fact that Zn^{2+} has greater radius (0.074 nm) than that of Co^{2+} ions (0.072 nm). The average crystalline size was determined by Debye Sherrer's formula [32].

$$D = \frac{k\,\lambda}{\beta \cos\theta} \qquad (1)$$

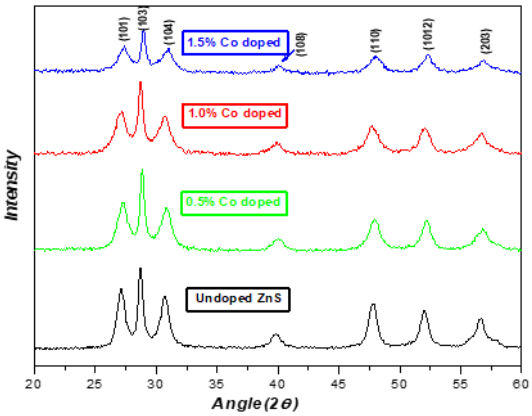

Figure 1: XRD of pure and Co concentrated ZnS NPs.

Where 'D' is dimension of the particle, 'k' serves as dimensionless constant with value 0.89, known as Sherrer's constant, λ (15.418 nm) is the wavelength of Cu-K_α, ß and θ are respectively line broadening corrected & Bragg's angle. The calculated crystalline size was gathered in Table 1 and the average crystalline dimension of pure and 0.5%, 1.0%, and 1.5% of Co doped ZnS were found to be 15.67 nm, 13.53 nm, 12.26 nm and 12.93 nm respectively. Thus, it is clear the average crystalline size reduces with greater concentration of Cobalt in the host materials.

Table 1: Data regarding structure of undoped and Co doped ZnS NPs from X-Ray Diffraction.

Co amount	2θ (degree)	crystalline size (nm)
Undoped	28.60	15.67
0.5%	28.84	13.53
1.0%	28.73	12.26
1.5%	28.92	12.93

Ultra Violet visible spectra and Optical Band Gap calculation

Figure 2 depicts the absorption spectra at room temperature for the samples of pure and Co concentrated ZnS was obtained in between wave length range from 200-800 nm. The blue shift in the absorption is attributed to the quantum size effect.

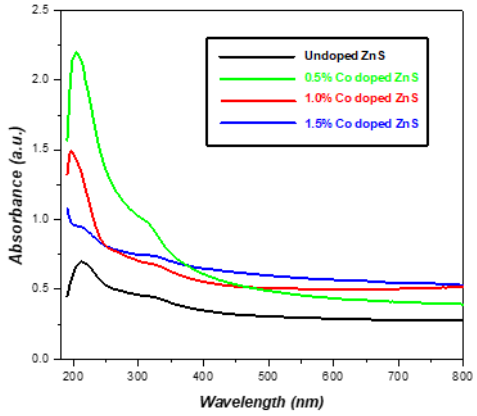

Figure 2: spectra of UV visible for Undoped and Co contained ZnS NPs.

Optical gap of pure and Co concentrated ZnS was made an estimate by using Tauc relation which is given by

$$\alpha h\nu = A(h\nu - E_g)^n \qquad (2)$$

Where α stands for co-efficient of absorption, Plank's constant is h, frequency of incident photon is ν, A taken as any constant whose value depends on characteristic transition and E_g is direct allowed band gap energy. The value of n depends on the nature of transition here with fitting value for ZnS is equal to $\frac{1}{2}$ which certifies conceded direct transition [33]. The curve of$(\alpha h\nu)^2$ vs hν has shown in the Figure, obtained energy gap values are 3.57, 4.45, 4.77 and 4.63 electron Volt respectively for pure and Co doped ZnS NPs which are more than that of band gap value of bulk ZnS (3.54 eV) [34] and this confirms the formation of nano sized particles and the band gap energy increases with increasing the cobalt (Co^{2+}) concentration in host ZnS NPs. This can be explained with the help of Burstein-Moss effect. Which says while semiconductor materials ZnS NPs are doped with transition metals with moderate concentration then the bottom of the conduction band gets populated by electrons from doped atoms for which electrons require addition energy to boost to the empty state in conduction band from valence band. As a result, band gap (E_g) gets widen [3]. In addition, the widen of band gap can also be interpreted by devolution of band bending effect.

Table2: Evaluated optical gap (E_g) of without and with Co concentrated ZnS-NPs.

Co concentration	Band gap energy (eV)
Undoped (Figure 3A)	3.57
0.5% (Figure 3B)	3.73
1.0%(Figure 3C)	4.28
1.5% (Figure 3D)	4.45

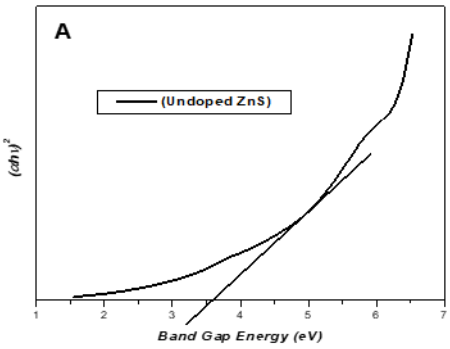

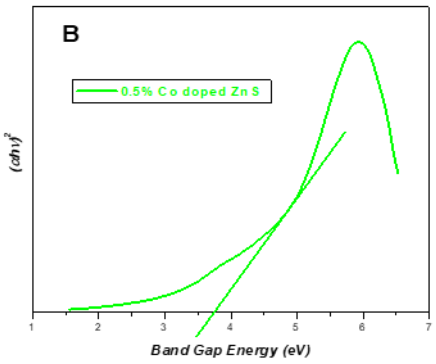

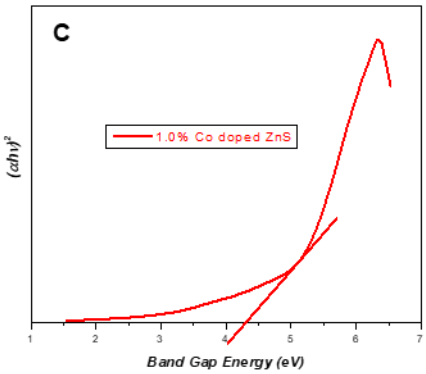

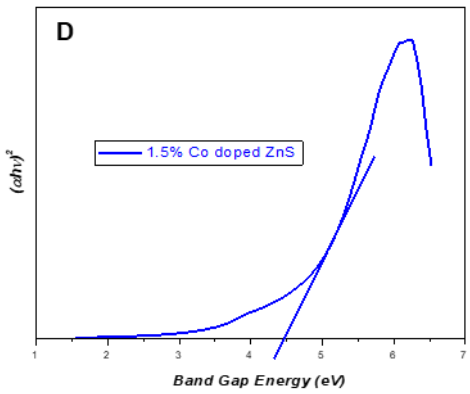

Figure 3: (a)-(d) Band gap determination from Tauc relation.

FTIR spectra analysis

To get information regarding molecular bond structure, FTIR study is very fruitful tool. In Figure 4 the qualitative analysis of FTIR spectra is shown in the range in between 4000 to 500 cm^{-1}, where we can clearly observe broad peak at 3200 to 3500 cm^{-1} owing to O-H longitudinal vibration due to stretching of absorbed excess H_2O [35]. Bands at 1628 cm^{-1} arised for Zn-S lattice [36]. Absorption bands at 1433 cm^{-1} is attributed to characteristics of hydroxyl groups of ZnS samples [37]. The highly intensed peaks at 1110 cm^{-1} indicate the Zn-S bonds for cubic structure of lattice [38]. In these FTIR spectra it has been clearly noticed with increasing cobalt amount there is no admissible change is inspected which signifies the Co^{2+}ions substituted the Zn^{2+} into host ZnS lattice without rigorous changing the crystal structure which agrees well with the XRD results.

PL study

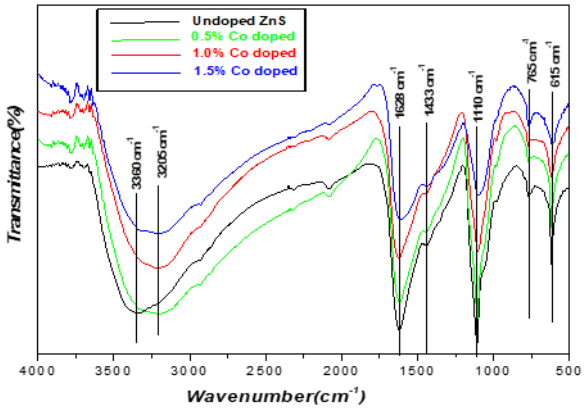

Figure 4: Spectra for FTIR of undoped and Co doped ZnS NPs.

PL studies of pure ZnS and concentrated with Co is shown in 5 no figure at room temperature where excitation wave length was 325 nm. The intense peaks appear at 388.65 nm, 386.33 nm, 384.01 nm and 380.38 nm in the violet region for pure and doping with Co (given percentage of 0.5, 1.0, 1.5) ZnS NPs respectively due to defect at lattice sites for absence of either Zn^{2+} or S^{2+}ions in host ZnS.On account of same reason, the radiative recombination process takes place in between electrons at conduction band and holes at valence band, which enables sharp intense peaks [39].

From Figure 6 at emission spectra, it can easily be noticed the blue shift occurs on increasing the cobalt concentration as compared to undoped ZnS NPs. Although, quantum confinement effect is responsible for blue shift of the emission peaks which is still not certain but it is let the blue shift could be related to narrow particle size distribution, surface defects etc. More researches are required for it [40].

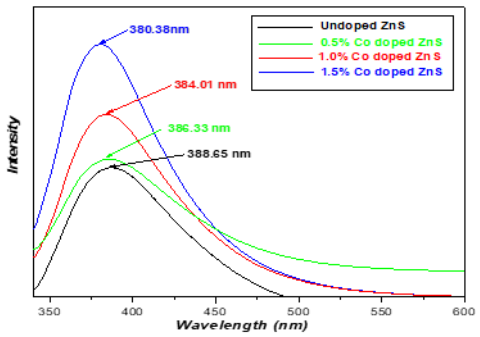

Figure 5: Photo luminance emission spectra of pure ZnS and doping with Co

SEM & EDX

Here is shown the SEM pictures of self-prepared specimens in Figure 5. We could discern a granular structure with a spherical shape from the Figures. The incorporation of Co^{2+}acquainted large assemblage in small particles. Due to acceleration towards the accumulation process the spherical shaped particle was a bit change and become overall rod like by doping Co^{2+}.Some factors are responsible for this agglomeration of nanoparticles which are doping ratio, charge distribution in the system, pH-value, chemical reactions, material solubility etc. The aggregation of two different particles generates the shrinkage of spaces between crystals. Higher Co^{2+} concentration resulted in somewhat smaller average particle sizes, indicating that colloidal nano crystal are where the growth process begins [26]. The nanoclusters grew larger spherical particles during chemical reactions, as a result further collided by secondary spherical particles and fused to produce multimeters [41]. Picture of EDX for pure and cobalt doped ZnS have been displayed in Figure no 6. Pure and contaminated with Co ZnS nanoparticles are having clearly visible peaks. The peak provided evidence that Co had been incorporated into ZnS nano particles. Stoichiometry of nanoparticles is calculated from EDX spectra using atomic and weight percentages of the

elements and this shows that the particles are almost stoichiometric.

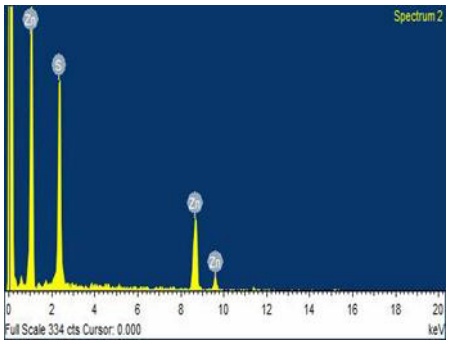

(a)

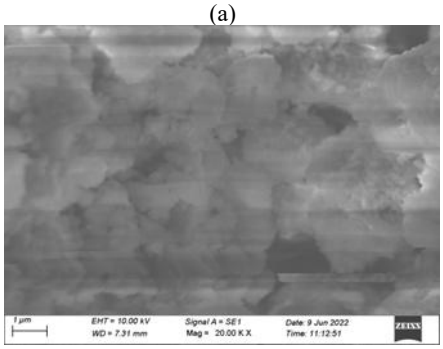

(b)

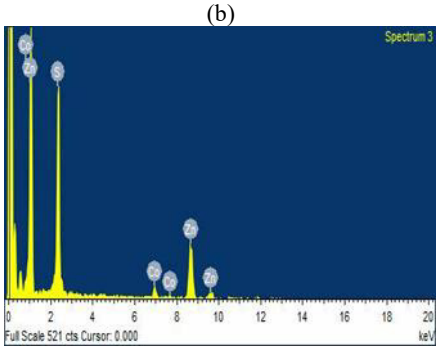

(c)

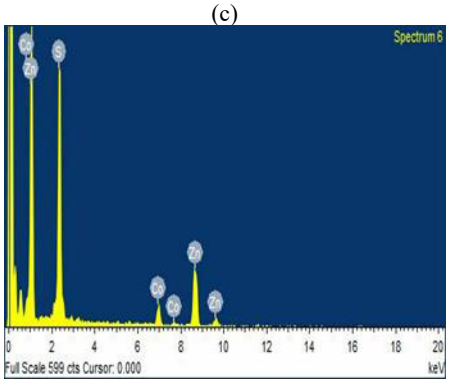

(d)

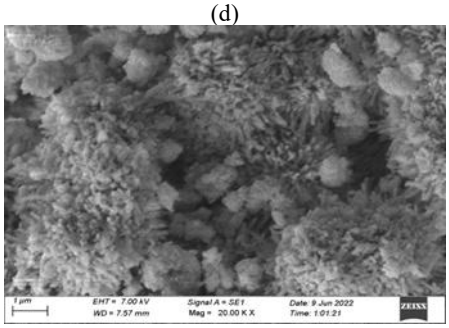

(e)

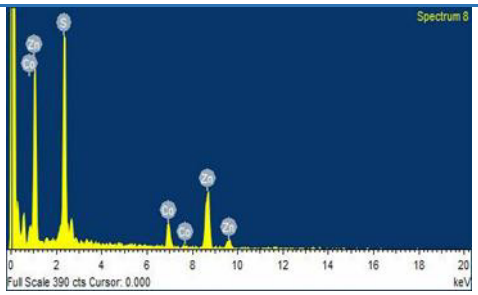

(f)

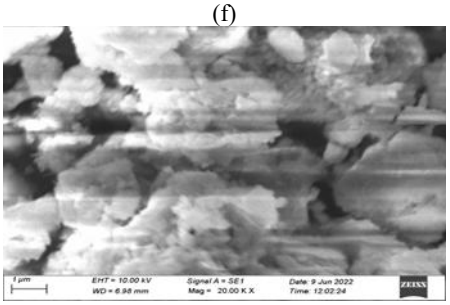

(g)

Figure 6: (a-b) SEM & EDX for pure ZnS and (c-g) doped with Co ZnS NPs

Electrical Properties

The effects of doping in ZnS NPs on the electrical parameters at room temperature were studied. The Figure 7 & 8 shows the plots of AC conductivity (σ_{AC}) and impedance (Z) the range in between frequency from 2 to 200 kHz of pure and previous mentioned percentage of doped with Co ZnS NPs. The value of σ_{AC} is measured with the help of impedance by the Equation (3)

$$\sigma_{AC} = \frac{d}{ZA} \qquad (3)$$

Where d, Z and A are representing the thickness, impedance and AC conductivity of pallet respectively. It has been noticed that for all samples,σ_{AC} shows the linear increase with the increasing frequency. Again, with rising of cobalt content in ZnS NPs, the value of σ_{AC}makes improvement with respect to undoped ZnS. This way of acting of AC conductivity of doped ZnS nanoparticles are strongly responsible for the surface defect of intermediate grain boundaries.

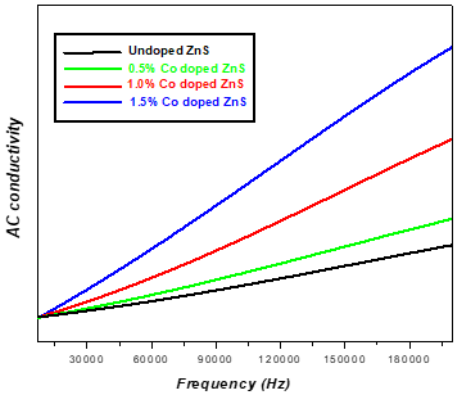

Figure 7: AC conductivity plot of ZnS and doped with Co.

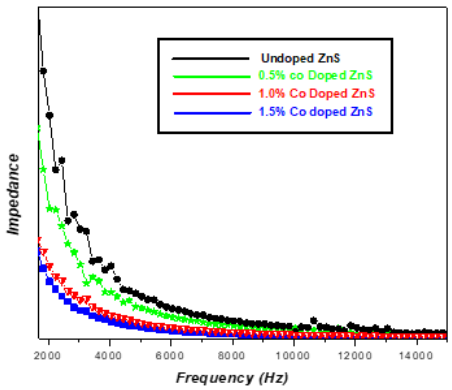

Figure 8: Impedance plot of ZnS and doped with Co doped.

In grains of conductions, the potential barriers of depletion offer interfacial resistance between the boundaries of grains which works as an insulating medium**.** At the domain of low frequency, the tunneling effect is mainly responsible for moving the carriers among the grains, in the domain of higher frequency, obtaining adequate energy containing Alternate Current electric field the carriers are able to pass through between grains of interfacial potential barriers for which their mobility becomes increased as a result the compressive improvement of σ_{AC} with enhancing the frequency [42-43].

Conclusion

In this work by hydrothermal method ZnS NPs doped with cobalt (transition metal) were successfully synthesized on a trot with changing the ratios of Co content. The structural characterization of these nanoparticles was observed the cubic structures with well-defined peaks for diffraction which are supported by standard JCPDS card. No distinguished peak has been observed for Co doping. The particle sizes of pure and ZnS doped with Co NPs had been calculated by using Debye Scherrer formula. From where it can be found on increasing the quantity of Co into ZnS, crystalline size reduces gradually. The value of optical gap evaluated from Tauc plot and it gets widen with rising the dopant contents which confirms the blue shift phenomenon. No prominent changes observed in FTIR spectra of the all samples determines the Co^{2+} ions replace Zn^{2+} ions in lattice site. In PL spectra one can see the intense peaks appear at violet region where greater is the molar concentration of cobalt lower is the wavelength and higher is the peak intensity which also supports the blue shift. In addition to study of dielectric properties of Co doped ZnS NPs degradation the depletion potential in grain boundaries as increasing Co concentration with respect to undoped ZnS which results, decreasing the dielectric constant improving AC conductivity at higher frequency region. The emitted spectra and tuning optical gap of ZnS doped with Co can be employed the materials for applying numerous applications.

References

1. B Poornaprakash, U Chalapathi, P T Poojitha, S V Prabhakar Vattikuti and S H Park, J. of Supercon. and Novel Magne. 33, 539 (2020).
2. M T Pham, N X Ca, P N Loan, N Tran, B T Huy, N T Dang et al, J. of Supercon. and Novel Magne. 32, 1761 (2019).
3. S Elsi, S Mohanapriy and K Pushpanathan, J. of Supercon. and Novel Magne. 33, 3223 (2020).
4. R Abolghasemi, R Rasuli and M Alizadeh, Mater. Today Commun. 22, 100827 (2020).
5. H Zhao and F Rosei, Chemistry 3, 229 (2017).
6. P Bhattacharya, K K Kamath, J Singh, D Klotzkin, J Phillips, H-T Jiang et al, IEEE Transac. On Electron Device 46, 871 (1999).
7. I C Sandall, C L Walker, P M Smowton, T Badcock, D J Mowbray, H Y Liu et al, Conf. Lasers Electro-Optics 2006 Quantum Electron 2006 Laser Sci. Conf. CLEO/QELS 45, 1 (2006).
8. H Shoji, Y Nakata, K Mukai, Y Sugiyama, M Sugawara, N Yokoyama et al, Appld. Phys. Lett. 71, 193 (1997).
9. M Grundmann, N N Ledentsov, N Kirstaedter, F Heinrichsdorff, A Krost, D Bimberg et al, Thin Solid Films 318, 83 (1998).
10. S K Das, S Parvin, U Honey, Md S Rana, N Jewena, J I Khandaker et al, J. of Mate. Sci. and Eng. A 10 (5-6), 103 (2020).
11. N Eryong, L Donglai, Z Yunsen, B Xue, Y Liang, J Yong et al, Appl. Surface Sci. 257, 8762 (2011).
12. F A La Porta, J Andre, M S Li, J R Sambrano, J A Varela and E Longo, Physi. Chem. Chemical Phys.16, 20127 (2014).
13. V Ramasamy, K Praba and G Murugadoss, Spectrochimica Acta Part A Molecu. Biomol. Spectro. 96, 963 (2012).
14. P Chandra and P P C Srivastava, J. of Mate. Sci. 49, 6012 (2014).
15. S Kumar, P Mandal, A Singh, S Husain, D Kumar, V K Malik et al, J. of Alloys and Comp. 830, 154640 (2020).
16. B Poornaprakash, U Chalapathi and S Park, J. of Mater. Sci.: Mater. In Electronics 28, 3672 (2017).
17. I Lopez Quintas, E Rebollar, D Ávila-Brande, J G Izquierdo, L Bañares, C Díaz Guerra et al, Nanomaterials 10, 1 (2020).
18. F J Rodriguez, J Reyes, D Y Medina, M A Barron and C Haro-Perez, Open J. of Appl. Science 09, 613 (2019).
19. S Sambasivam, B K Reddy, A Divya, N Madhusudhana Rao, C K Jayasankar and B Sreedhar, Phys. Letter A 373, 1465 (2019).
20. X Zeng, J Zhang, F Huang, X Zeng, J Zhang and F Huang, J. of Appl. Phys. 111, 123525 (2012).

21. K Sharma, P Kumar, G Verma and A Kumar, Optik (Stuttg) 206, 164357 (2020).
22. D Sridevi and K V Rajendran, Chalcogenide Letters 7, 397 (2010).
23. G Gurung, T K Ekanayaka, A J Yost and T R Paudel, Material Research Express 6, 126550 (2019).
24. B Poornaprakash, P T Poojitha, U Chalapathi, K Subramanyam and S Park, Physica E 83, 18 (2016).
25. P Mukherjee, C M Shade, A M Yingling, D N Lamont and D H Waldeck, The J. of Physical Chem. A 115, 4031 (2011).
26. I Devadoss and S Muthukumaran, J. of Mater. Sci.: Mater. In Electronics 27, 7389 (2016).
27. A Goktas and I H Mutlu, J. of Electronic Mater. 45, 11 (2016).
28. Z K Heiba, M B Mohamed and A Badawi, Chemical Phys. Letters 775, 138653 (2021).
29. K Byrappa and T Adschiri, Progr. in Crystal Growth and Charac. Of Mater. 53 2, 117 (2007).
30. L Wang, J Dai, X Liu, Z Zhu, X Huang and P Wu, Ceramics International 38 3, 1873 (2012).
31. A Goktas and I H Mutlu, J. of Sol Gel Scien. and Tech. 69, 120 (2014).
32. A L Patterson, Physical Review 56, 978 (1939).
33. J Tauc, Optical properties of Solids Abeles North Holland Amsterdam (1972).
34. J Kaur, M Sharma and O P Pandey, Optical Materials 47, 7 (2015).
35. U D Godavarti, P Nagaraju, V Yelsani, Y Pushukuri, P S Reddy amd M Dasari, J. of Semicond. 42, 122901 (2021).
36. P Sakthivel and S Muthukumaran, Optics and Laser Techn. 103, 109 (2018).
37. B Poornaprakash, D A Reddy, G Murali, N M Rao, R P Vijayalakshmi and B K Reddy, J. of Alloys & Comp. 577, 79 (2013).
38. R O Kagel and R A Nyquist, Infrared spectra of inorganic compounds (3800–45 cm−1) (1971).
39. Y C Corrado, F O Jiang, M Kozina, F Bridges and J Z Zhang, J. of Physical Chem. A 113, 3830 (2009).
40. R Zamiri, B Singh, M S Belsley and J M F Ferreira, Ceramics Internat. 4, 6031 (2014).
41. M S Samuel, J Koshy, A Chandran and K C George, Physica B: Conden. Mat. 406 (15–16), 3023 (2011).
42. N Karar, F Singh and B R Mehta, J.of Appl. Phys. 95, 656 (2004).
43. P K Ghosh, Sk F Ahmed, S Jana and K K Chattopadhyay, Optical Materials 29, 1584 (2007).

A DFT-Based Comparative Study on the Structural, Magnetic, Electronic, and Thermoelectric Properties of $TMCo_2$ (TM = Ti, Nb) Intermetallics

Hansraj Dhadse[1,a], Suparn Kumar Barmase[1,b], Shubha Dubey[2,c], Jagdeesh Pataiya[3,d], and Chandrabhan Makode[1,e]

[1] *Department of Physics, Govt. Motilal Vigyan Mahavidyalaya, Bhopal – 462008, M.P., India.*
[2] *Department of Physics, Barkatullah University, Bhopal, 462026, M.P., India.*
[3] *Department of Physics, Dr. Bhimrao Ambedkar Government College, Amla, Betul, 460551, M.P., India.*

[a] hrdhadse2050@gmail.com
[b] suparn404880@gmail.com
[c] shubha.dubey4@gmail.com
[d] jagdeesh8115@gmail.com
[e] cbphysicsmvm@gmail.com

Abstract

In this work, we present a comparative study of the structural, magnetic, electronic, and thermoelectric properties of cubic binary Laves-phase intermetallic compounds with the general formula $TMCo_2$ (TM = Ti, Nb), using density functional theory (DFT) within the Wien2k code. Geometrical optimization, performed through the Birch-Murnaghan equation of state, shows excellent agreement with prior theoretical and experimental findings. The magnetic properties confirm the presence of ferromagnetic ordering. To explore the electronic properties, we have analyzed the band structures and density of states.

Keywords: Lave Phase; Bulk Modulus; Birch Murnaghan Equation.
Received 30 January 2025; First Review 10 February 2025; Accepted 16 February 2025

*** Address of correspondence**
Hansraj Dhadse
Department of Physics, Govt. Motilal Vigyan Mahavidyalaya, Bhopal – 462008, M.P., India.

Email: hrdhadse2050@gmail.com

How to cite this article
Hansraj Dhadse, Suparn Kumar Barmase, Shubha Dubey, Jagdeesh Pataiya, and Chandrabhan Makode, A DFT-Based Comparative Study on the Structural, Magnetic, Electronic, and Thermoelectric Properties of $TMCo_2$ (TM = Ti, Nb) Intermetallics, J. Cond. Matt. 2024; 02 (02): 53-55

Available from:
https://doi.org/10.61343/jcm.v2i02.106

Introduction

The Laves phase, found in over 900 systems, is an intermetallic compound known for properties like wear resistance, hardness, and superconductivity, which depend on its chemical composition [1]. Laves phases hold great potential for various applications. For example, $TiCo_2$ compounds have been employed as hydrogen storage materials due to their excellent hydrogen absorption capabilities and favorable hydriding-dehydriding kinetics [2]. Additionally, (Tb, Dy)Fe_2 and (Al, Fe)Zr_2 have been explored for magnetoelastic transducer applications owing to their remarkable magnetostriction. $TiCo_2$ and $NbCo_2$ alloys exhibit superconducting properties, including high critical temperatures, strong magnetic fields, and high current densities [3]. Furthermore, $NbCo_2$ and $TiCo_2$-based two-phase alloys are well-suited for high-temperature structural applications, thanks to their high melting points and exceptional retention of mechanical properties at elevated temperatures. In this paper, we have investigated the structural and electronic properties of $TMCo_2$ (TM = Ti and Nb) Laves phase compounds.

Computational Method

For DFT-based ground-state energy calculations, the Wien2k software is used in conjunction with the FP-LAPW approach [4]. PBE-GGA describes the exchange-correlation potential, while RMTKmax, the energy convergence parameter, is set to 7.0. Self-consistency is attained when the total energy stabilises within 10^{-4} Ry, with the Gmax parameter set to 12 a.u.$^{-1}$. The Brillouin zone integration is performed using the Monkhorst-Pack method with 1000 k-points, and the valence and core states are separated using a cut-off energy of -6.0 Ry with a charge convergence threshold of 0.0001e.

Results and Discussions

The $TMCo_2$ (TM = Ti and Nb) compounds crystallize in the cubic Laves phase structure, belonging to the $Fd\bar{3}m$ space group (No. 227). This structure is characterized by a densely packed arrangement of atoms, where TM and Co atoms occupy specific Wyckoff positions, forming a three-dimensional framework with high symmetry.

Table 1: Optimized structural parameters

Parameters	$TiCo_2$	$NbCo_2$
a (Å)	7.0997	7.4001
V ($Å^3$)	603.76	683.0782
B (GPa)	93.7626	132.2316
B´	5.0676	4.7633
E_0	-12404.149032	-36137.279837

The structural properties of $TiCo_2$ and $NbCo_2$ compounds satisfy the Birch-Murnaghan equation of state, and both compounds exhibit ferromagnetic behavior. The Birch-Murnaghan equation of state is used to describe the pressure-volume relationship, confirming the stability of the cubic $Fd\bar{3}m$ structure for $TiCo_2$ and $NbCo_2$. Additionally, both compounds are ferromagnetic in nature, characterized by a net magnetic moment arising from the alignment of magnetic moments in the same direction. This makes them promising candidates for applications in magnetic and spintronic devices. The ferromagnetic energy versus volume curve for both $TiCo_2$ and $NbCo_2$ compounds is presented in Figure 1. The optimized structural parameters obtained from the calculations align well with previously reported experimental results [5], confirming the reliability of the computational approach used in this study.

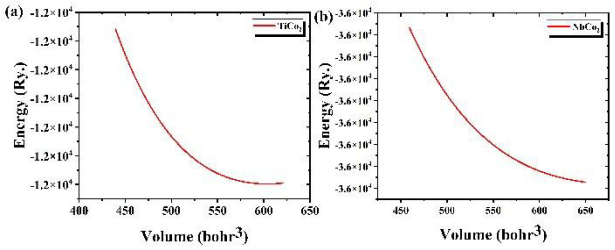

Figure 1: Energy Versus volume curve for $TMCo_2$ (TM= Ti and Nb).

The magnetic properties of $TiCo_2$ and $NbCo_2$ Laves phase compounds reveal distinct behaviors. In $TiCo_2$, the transition metal (Ti) contributes a small magnetic moment of $0.03134\mu_B$, while the cobalt atoms provide the dominant contribution with a magnetic moment of $0.50612\mu_B$. The interstitial regions exhibit a slight negative moment of $-0.06847\mu_B$, leading to a total magnetic moment of $1.06913\mu_B$ for the unit cell, confirming its ferromagnetic nature. Conversely, $NbCo_2$ displays negligible magnetism, with the transition metal (Nb) contributing $-0.00002\mu_B$ and cobalt only $0.00012\mu_B$. The interstitial contribution is nearly zero at $-0.00001\mu_B$, resulting in a total magnetic moment of $0.00015\mu_B$, indicating that $NbCo_2$ is essentially non-magnetic. This highlights the stark contrast in magnetic properties between the two compounds. The spin-polarized density of states (DOS) for $TiCo_2$ and $NbCo_2$ Laves phase compounds, as shown in Figure 2, highlights their metallic and ferromagnetic nature. The total DOS for both compounds exhibit significant spin polarization, with an asymmetry between the spin-up and spin-down states, confirming their ferromagnetic behaviour. The Co atoms contribute dominantly to the DOS near the Fermi level (E_f) due to their partially filled d-orbitals, while the transition metals (Ti in $TiCo_2$ and Nb in $NbCo_2$) also contribute through hybridization with Co d-states. The position of E_f within regions of finite DOS for both spin channels further confirms their metallic behaviour. This interplay of electronic and magnetic properties makes $TiCo_2$ and $NbCo_2$ promising candidates for applications in spintronic and magnetic devices.

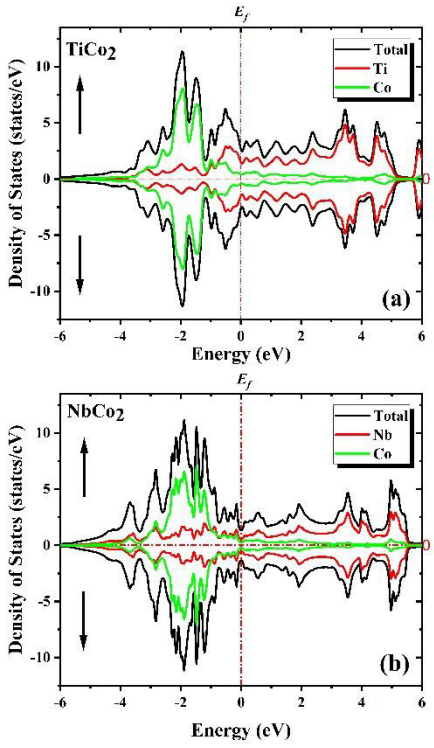

Figure 2: Electron Density of States of $TiCo_2$ and $NbCo_2$

Conclusion

In conclusion, the $TiCo_2$ and $NbCo_2$ compounds, both crystallizing in the cubic Laves phase structure, exhibit distinct magnetic behaviors. $TiCo_2$ shows ferromagnetism with a total magnetic moment of $1.06913\mu_B$, while $NbCo_2$ is nearly non-magnetic. Both compounds are metallic with significant spin polarization, primarily driven by cobalt atoms. The computational results align well with experimental data, confirming the stability and ferromagnetic nature of $TiCo_2$. These compounds show

promising potential for applications in magnetic and spintronic devices due to their unique electronic and magnetic properties.

References

1. Ghafoor, N., Ali, Z., Mehmood, S., & Khann, I. Journal of Computational Electronics, *21*(3), 561–570, 2022.
2. Murtaza, A., Yang, S., Zhou, C., Song, X.: Chin. Phys. B (2016).
3. Zhang, Z., Russell, A. M., Biner, S. B., Gschneidner, J., Lo, 13(5), 559–564 (2005) B R Jackson, T Pitman, and U S Patent, 2004.
4. Blaha, P., Schwarz, K., Tran, F., Laskowski, R., Madsen, G. K. H., & Marks, L. D. Journal of Chemical Physics, 152(7), 2020.
5. Bannikov, V. V., Shein, I.R., Ivanovskii, A. L. Phys Status Solidi (b) 248(6), 1369–1374 (2011) R C Mikkelson.

Exploring the Physical Properties and Tauc's Plot Analysis of Nd^{3+} Doped Telluroborate Glass

Nitiksha Sharma[a], Samay Singh Meena[b], Pawan Kumar[c], Menka Meena[d], Beena Bhatia[e]

Department of Physics, Jai Narain Vyas University Jodhpur, Rajasthan, India.

[a] bhardwajhimani412@gmail.com
[b] ssmeenaphy12@gmail.com
[c] pawankumar26174@gmail.com
[d] menkameena1996@gmai.com
[e] beenaphybhatia@gmail.com

Abstract

In the present work, the investigation begins with the synthesis of telluroborate glass samples doped with Nd^{3+} rare earth ion using established melt quenching techniques with composition $(50–x)B_2O_3{\cdot}20TeO_2{\cdot}15Mg_2CO_3{\cdot}15K_2CO_3{\cdot}xNd_2O_3$ (where x varies as 0, 0.5, 1, 1.5, 2 and 2.5 mol %). All samples were found to be in glassy form with a broad hump in XRD spectra which is characteristic of amorphous nature. The physical parameters including the optical dielectric constant, polaron radius, interatomic separation, molar refraction, and metallization criterion are also analyzed based on molar density and molar volume. The Tauc's plot reveals that the band gap energy rises as the dopant concentration increases. Similarly, the refractive index shows an upward trend with higher dopant concentrations. Optical absorption spectra were measured at room temperature over a wavelength range of 180 nm to 1000 nm. In conclusion, the comprehensive exploration of physical properties in Nd^{3+} doped telluroborate glass offers valuable insights into the potential applications of these materials in advanced optical and photonic devices. This work also contributes to the expanding knowledge base in the field of glass science, fostering advancements in materials engineering and device development.

Keywords: Telluroborate glass, Physical parameters, rare earth ion, Tauc's plot.
Received 29 January 2025; First Review 10 February 2025; Accepted 16 February 2025

*** Address of correspondence**
Nitiksha Sharma
Department of Physics, Jai Narain Vyas University Jodhpur, Rajasthan, India

Email: bhardwajhimani412@gmail.com

How to cite this article
Nitiksha Sharmaa, Samay Singh Meenab, Pawan Kumarc, Menka Meenad, Beena Bhatia, Exploring the Physical Properties and Tauc's Plot Analysis of Nd^{3+} doped Telluroborate Glass, J. Cond. Matt. 2024; 02 (02): 56-58.

Available from:
https://doi.org/10.61343/jcm.v2i02.96

Introduction

Telluroborate glasses, known for their thermal and chemical stability, high refractive index, and broad spectral transparency, are ideal for harsh environments and advanced optical applications [1-2]. Nd^{3+}-doped telluroborate glasses, in particular, are valued for their unique electronic transitions, which enhance fluorescence lifetime, emission cross-sections and quantum efficiency, making them suitable for lasers, amplifiers, sensors and photonic devices [3-7]. However, despite reported advancements, such as near-infrared emission studies, there is limited understanding of their structural and physical properties. This study explores the impact of varying Nd_2O_3 concentrations on the physical, optical and theoretical properties of these glasses, emphasizing their potential in optical technologies.

Method

The telluroborate glasses with composition of $(50–x)B_2O_3{\cdot}20TeO_2{\cdot}15Mg_2CO_3{\cdot}15K_2CO_3{\cdot}xNd_2O_3$ (where x varies as 0, 0.5, 1, 1.5, 2 and 2.5 mol %) were prepared by melt quenching method. To prepare a sample for study analytical reagent grade chemicals consist of B_2O_3, TeO_2, Mg_2CO_3 and K_2CO_3 were used. The rare earth oxides added to the glasses were 99.99% pure.

Discussions

The physical properties of doped telluroborate glasses discussed in table 1. The analysis highlights the impact of Nd^{3+} ion incorporation on the optical and physical properties of TEB glasses:

1. Physical Parameters: The introduction of Nd_2O_3 increases density and molar volume due to its role as a network modifier, generating non-bridging oxygens (NBOs) and enhancing structural

randomness.

2. Refractive Index and Derived Parameters: Nd^{3+} ions modify the glass network by expanding it, decreasing inter-ionic distances and polaron radius, and increasing field strength, leading to significant structural and optical changes.

3. Optical Absorption Spectra: UV-Vis-NIR spectra reveal ten absorption bands of Nd^{3+} transitions, with the 582 nm band being hypersensitive to environmental changes and indicative of increased covalency in bonding.

4. Bandgap and Urbach Energy: Higher Nd^{3+} concentrations raise the optical bandgap, reflecting reduced NBO content and structural compactness. Concurrently, decreasing Urbach energy suggests fewer defects and improved structural integrity.

Overall, Nd^{3+} doping significantly enhances structural coherence, optical properties, and the performance of TEB glasses.

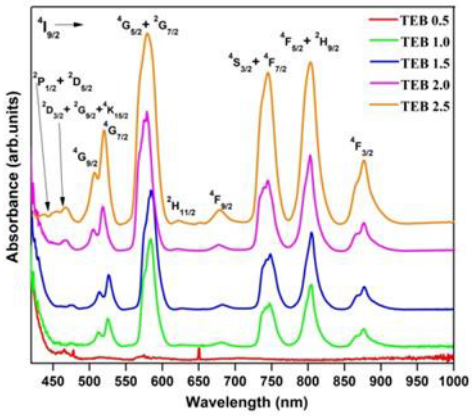

Figure 1: UV-VIS absorption spectra of Nd^{3+}: TEB glasses

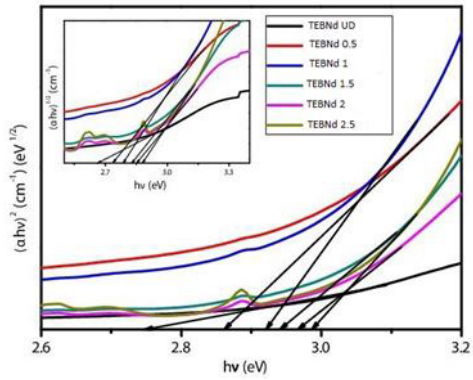

Figure 2: Tauc's plot for direct allowed transition of the Nd^{3+}: TEB glasses

Conclusion and Future Prospective

This study successfully prepared Nd^{3+}-doped telluroborate glasses using the melt quenching technique and characterized them for physical and optical properties. XRD analysis confirmed their amorphous nature. Density, refractive index, molar volume, polarizability, and optical basicity increased with higher Nd_2O_3 doping, indicating network expansion and enhanced ionic properties. A correlation between refractive index, density, and electronic polarizability was established. Optical spectra revealed that bandgap values increased with Nd^{3+} concentration, attributed to the formation of non-bridging oxygen (NBO), while Urbach energy showed an inverse relationship with the bandgap.

References

1. N. Alfryyan, A. H. Alomari, Z. A. Alrowaili, H. H. Somaily, I. O. Olarinoye, C. Mutuwong, S. Al-Qais and M. S. Al-Buriah, Optik, 270: 2022.
2. J. S. Alzahrani, Z. A. Alrowaili, C. Eke, I. O. Olarie and M. S. Al-Buriahi, Optik, 281: (2023).
3. M. S. Gaafar, I. Shaarany and T. Alharbi, J. Alloys Compd. 616: 625–632, 2014.
4. R. A. H. El-Mallawany, Tellurite Glasses Handbook: Physical Properties and Data, second ed., CRC Press, 2018.
5. Y. C. Ratnakaram, S. Babu, L. K. Bharat and C. Nayak, J. Lumin. 175: 57–66, 2016.
6. O. Ravi, K. Prasad, R. Jain, M. Venkataswamy, S. Chaurasia and B. D. P. Raju, J. Lumin. 32: 688–694, 2017.
7. F. Zaman, G. Rooh, N. Srisittipokakun, S. Ruengsri, H. J. Kim and J. Kaewkhao, J. Non-Cryst. Solids 452: 307–331, 2016.

Table 1: Physical properties of doped Telluroborate Glass

Physical properties	UD sample	0.5 Doped	1.0 doped	1.5 doped	2.0 doped	2.5 doped
Average molecular weight M (g)	103.7524	105.0866	106.4209	107.7552	109.0895	110.4238
Density (g/cm^3)	2.9817	2.9920	3.0292	3.0545	3.0901	3.1255
Refractive index (n)	1.639	1.641	1.658	1.665	1.686	1.690
Rare earth ions concen- tration N (X 10^{22}ions/cms)	-	0.8574	1.7144	2.5609	3.4122	4.2620
Dielectric constant (∈)	2.6863	2.6929	2.7490	2.7722	2.8426	2.8561
Optical dielectric constant (pdt/dp)	1.6863	1.6929	1.7490	1.7722	1.8426	1.8561
Molar Volume V_m (g/cm^3)	34.7964	35.1225	35.1317	35.2775	35.3025	35.3299
Reflection losses (R)	0.0586	0.0589	0.0612	0.0622	0.0652	0.0658
Molar refractivity (R_m)	12.5197	12.6687	12.9390	13.0985	13.4326	13.5031
Polaron radius (r_p)	-	0.4241	0.3366	0.2945	0.2676	0.2485
Interatomic distance (r_i)	-	1.0526	0.8355	0.7309	0.6643	0.6167
Electronic polarizability (α_e)X (10^{-22} ions cm^{-3})	0.1427	0.1430	0.1460	0.1473	0.1509	0.1516
Field strength F (cm^3)	-	1.2840	1.3239	2.2491	2.9050	3.7601
Molar electronic polarizability (α_m)	4.9681	5.0273	5.1345	5.1978	5.3304	5.3584
Metallization criterion (M)	0.6402	0.6393	0.6317	0.6287	0.6195	0.6178
Oxide ions polarizability	1.5677	1.6802	1.8838	2.0041	2.2561	2.3093
Optical basicity	0.5400	0.5472	0.5544	0.5615	0.56887	0.5759

Magnesium Adsorption on B/N/P-Doped Graphene Nanoribbons: A DFT Investigation of Structural and Electronic Modifications

Himanshu Pundir[a], Gaurav Sapra[b], Preetika Sharma[c]

UIET, Panjab University, Chandigarh, India.

[a] erhimanshu003@gmail.com
[b] gaurav.sapra@pu.ac.in
[c] preetitkamadhav@yahoo.co.in

Abstract

Heteroatom(s) doping and introduction of functional groups into nanoribbons proposes a promising pathway to exploit their electronic and quantum transport characteristics. In this work, doping of armchair graphene nanoribbons (AGNRs) is accomplished to explore its potential for switching applications. Doping is done using Boron (B), Nitrogen (N) and Phosphorous (P) dopants in concentration of 3.125% individually. B outshines the other two dopants N and P in terms of its metallic character and offers minimum threshold voltage (V_{th}). Further, to examine its switching potential, Magnesium (Mg) is adsorbed on hollow sites of the doped structures. The stability of both Mg adsorbed doped structures as well as doped structure without adsorption are analysed in terms of band structure, density of states (DOS), bond length variations, adsorption energy and current-voltage (I–V) characteristics using Density Function Theory (DFT). Each AGNR structure showed an appreciable shift in threshold voltage. However, N and P doped AGNR both yield semiconducting nature noting that N doped AGNR given high threshold voltage while P doped distorts the I-V behaviour. The results show that due to most metallic nature and lowest threshold voltage out of all three structures, the B doped AGNR with Mg adsorption can be excellent for transistor switching applications.

Keywords: Adsorption, DFT, Doping, Switching, Threshold Voltage.
Received 28 January 2025; First Review 10 February 2025; Accepted 16 February 2025

*** Address of correspondence**
Preetika Sharma
UIET, Panjab University, Chandigarh, India.

Email: preetitkamadhav@yahoo.co.in

How to cite this article
Himanshu Pundir, Gaurav Sapra, Preetika Sharma, Magnesium Adsorption on B/N/P-Doped Graphene Nanoribbons: A DFT Investigation of Structural and Electronic Modifications, J. Cond. Matt. 2024; 02 (02): 59-63.

Available from:
https://doi.org/10.61343/jcm.v2i02.82

Introduction

Diverse carbon derives especially nano ribbons have fascinated immense research interests driving exploration into their potential for numerous future electronic applications [1-4]. Electrical properties of these materials can be tailored through many ways hence, tunability makes them further versatile and attractive [5-6]. Band gap engineering using doping and adsorption are common practices to harvest the fascinating properties. One involves substituting or interstitially fitting the foreign atoms suitably into nano ribbons, on the other hand adsorption demands attaching these molecules onto the surface of adsorbent surface [7-10]. A DFT study is used to investigate the interactions of the magnesium on graphene, a wonder 2D material. The outcome suggests that the binding nature of the Mg ions (Mg^{+} and Mg^{2+}) was caused by charge transfer interactions and Mg interacts with graphene surfaces via Van Der Waals forces [11]. The interaction of graphene surfaces with magnesium atoms is reported using a direct molecular dynamics approach and the Mg atoms were observed to bind at hollow site positioned at 2.02 Å from the surface of graphene. [12]. It is also found that graphene increases the Mg adsorption energies on certain surfaces and improve the cycling stability and is a very promising electrode material for Mg rechargeable ion batteries [13-14]. The kinetic properties and electronic conduction due to Mg adsorption can provide excellent electrode material for battery applications. The above literature confirms the Mg adsorption on carbon surfaces to be promising. However, there is limited research on the interaction mechanism between metal-atom-doped graphene nanoribbon. To the best of author's knowledge, there is no work done on finding the lowest threshold values for doped AGNR though Mg adsorption. Hence, we explored the electronic and transport behaviour of doped AGNR structures before and after Mg adsorption and tried to depict the role of Mg through theoretical perspective for switching applications.

Computational Details

An AGNR with 32 carbon atoms doped individually with B/N/P and later adsorbed with Mg is explored using Quantum ATK (Synopsis) (P-2019.03-SP1) based on Density Functional Theory (DFT). The calculations are simulated using generalised gradient approximations (GGA) which represent the exchange correlation in the calculations. During geometry optimisations, a double Zeta polarised basis set has been chosen for all atoms of Mg, B, N, P, C and H to obtain the best results. The structures are analysed with 1*1*70 uniformly placed k-points. Edge passivation of AGNRs hydrogen atoms is done. The structural stability of the AGNRs was evaluated by optimizing the cohesive energy, where a negative cohesive energy confirmed stability. The cohesive energy calculations are done using the formula given below by equation (1)

$$\boldsymbol{E_{coh}} = E_{Total} - \Sigma n_x E_x / N \qquad (1)$$

Where, E_{coh} is the cohesive energy of the doped AGNR with Mg adsorption, E_{Total} = total energy of doped AGNR with adsorbed alkali earth metal ion (Mg), n is the no. of atoms, E is the energy of an individual atom, x represents the individual atom while, N is the total no. of atom resent in the system. On the other hand, adsorption energy (E_{ad}) is calculated using the formula mentioned in equation (2) below to further support the investigation

$$\boldsymbol{E_{adsorption}} = E_{Total} - E_{adsorbent\ Surface} - E_{adsorbent\ ion} \qquad (2)$$

Where, E_{Total} is total energy of doped AGNR with adsorbed alkali earth metal ion (Mg), $A_{dsorbent}$ surface is total energy of doped AGNR surfaces, $A_{dsorbent}$ ion is total energy of single Mg. Variations in bond lengths between carbon and adsorbent were analysed and tabulated. Further, the I-V characteristics are plotted to further investigate the transport behaviour. Two electrodes at both sides of the ribbon are formed and a potential of 0-2 V is applied to get I-V plots.

Geometric Structures and stability

To estimate the threshold values of n and p type doped AGNRs with Mg adsorption afterwards is done. Front and top view of the geometric structures including hydrogen passivated pristine (undoped) AGNR and B/N/P individually doped AGNRs are shown in figure 1 respectively.

Though, geometrically optimized structures of each doped AGNR including Mg adsorption are given separately in figure 2. Here, figure 2(a) fixed position and dopant concentration of 3.125% is used in each. The change in bond length in these optimized structures w. r. t. individual dopant with Mg adsorption is also shown clearly. The modification in bond length is noted maximum in case of N doped AGNR, secondly moderate variation in case of P doped AGNR and lastly B doped AGNR shown minimum variations after adsorption of Mg. These modifications in bond lengths are due to the varying atomic radius of each dopant. To analyse the structural stability in all it is also observed that as size of the dopant is varying there is a change in the value of corresponding bond lengths and cohesive energy value respectively. Boron and Nitrogen doped AGNRs with Mg adsorption given almost close values of the cohesive energy to each other, while phosphorous doped AGNR with Mg adsorption shown a least value among all with clear deformed AGNR. Adsorption energy of all three structures is calculated to further confirm the adsorption competence. The value of adsorption energies clearly shows that phosphorous doped Mg adsorbed AGNR shown least value signifying poor adsorption. Nitrogen doped AGNR structure with Mg adsorption holds second place, while boron stands-up tall with highest adsorption energy among all. The values of calculated cohesive energies, bond lengths and adsorption energy are further provided.

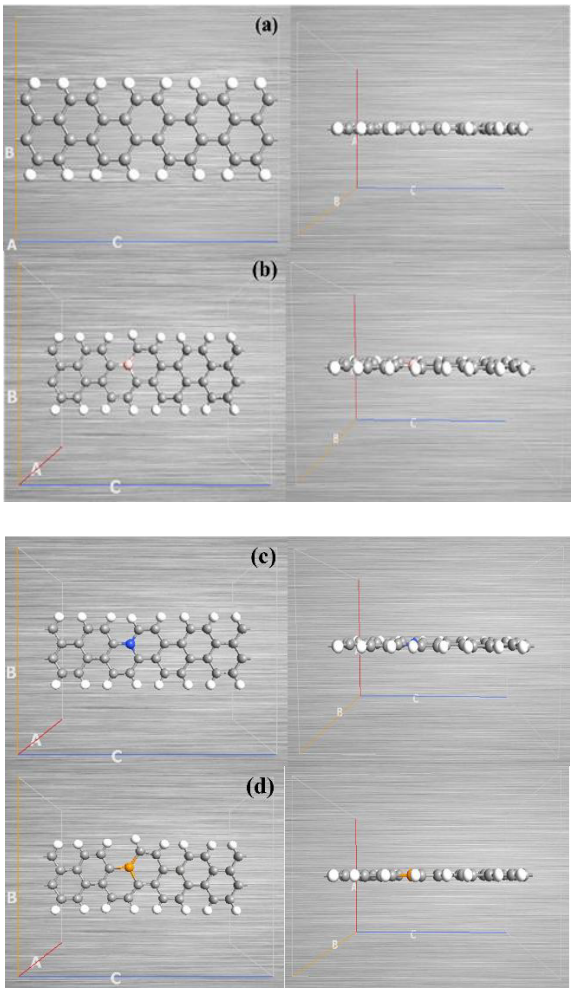

Figure 1: Geometric optimized structures (front view and top view) (a) Pristine AGNR, (b) Boron doped, (c) Nitrogen and (d) Phosphorous doped AGNR respectively.

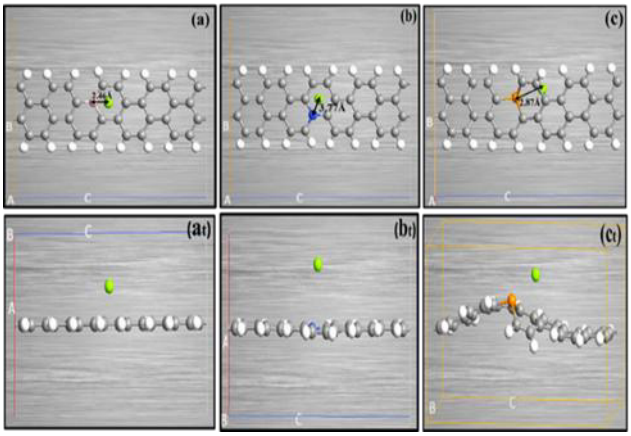

Figure 2: Geometric optimized structures (front view and top view) (a), (at) B doped AGNR with Mg adsorption (b), (bt) N doped AGNR with Mg adsorption and (c), (ct) P doped AGNR with Mg adsorption respectively.

Results and discussions

Band structures and Density of states

Intentional addition of solo dopants or doping introduces the impurity atoms and influence position of fermi level either near to valence band or conduction band for p-type and n-type dopants respectively. We have explored DOS and band structures of each doped AGNR structure. The band structures and corresponding density of states for pristine AGNR and all doped AGNR structures are depicted in figure no.3 respectively. At first, the band gap of pristine AGNR is found to be 2.55 eV presenting it as semiconductor in compliance with DOS value of 0 eV^{-1} nearly in range of -1.25 eV to +1.25 eV as shown in Figure 3.

Band gap engineering is performed through substitutional doping of B/N/P dopants individually on AGNR. Respective band gaps are noted and well tabulated in table 1. It is apparent that doping offers transitional density of states in doped AGNR structures which were absent in case of pristine AGNR. In comprehensive view firstly the p type dopant (boron) incorporated insignificantly small band gap of 0.02 eV with sufficient no. of energy states appearing in the valence band below the fermi level confirms the p type doping. Though substitution of n-type dopants (N and P) atoms respectively additionally provided bandgap modifications. The presence of phosphorus n-type dopants introduced the band gap of 2.24 eV, which is slightly lesser than pristine AGNR keeping the nature as semiconducting. The dopant (P) shifted the fermi level in the conduction band justifying the effective doping. Moreover, the DOS plot demonstrates the energy state immediate to fermi level further confirming a doping of n-type. Nitrogen(N) another n-type dopant used, offer a reasonable band gap value of 0.41 eV introducing major modifications in band gap value and density of states correspondingly.

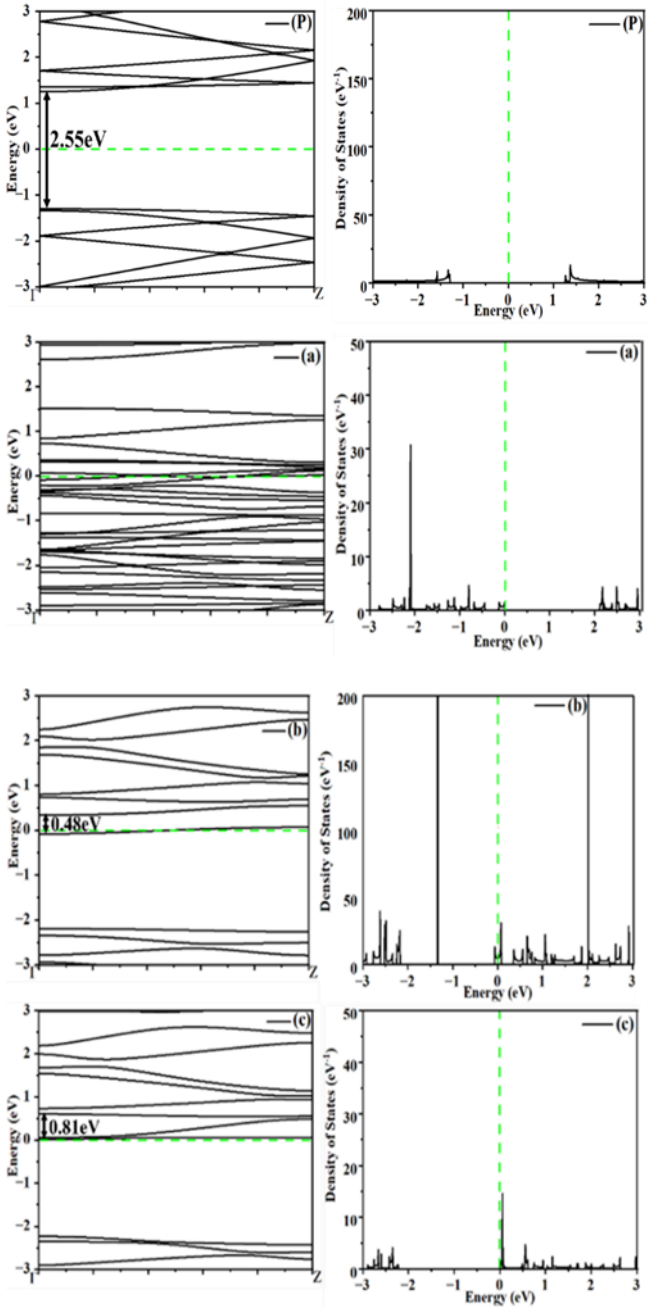

Figure 2: Band Structures and density of states (P) pristine AGNR (a) B doped AGNR (b) N doped AGNR and (c) P doped AGNR

Indeed, both n and p type dopants has tailored the band gap efficiently. Accordingly, observed, a nearly metallic band structure of B atom doped AGNR, while a semiconducting one by N and P dopants respectively. In addition, complete behaviour profiling is accomplished by visualising Mg adsorption on these doped AGNRs. The obtained modified band structures and DOS plots on Mg adsorption are given away in figure 4.

Adsorption of Mg on B doped AGNR notably modifies its electronic properties by bringing significant modifications in its band structure as well as density of states. It is evident from the band structure that the behaviour of AGNR has turned metallic with no band gap but presence of available

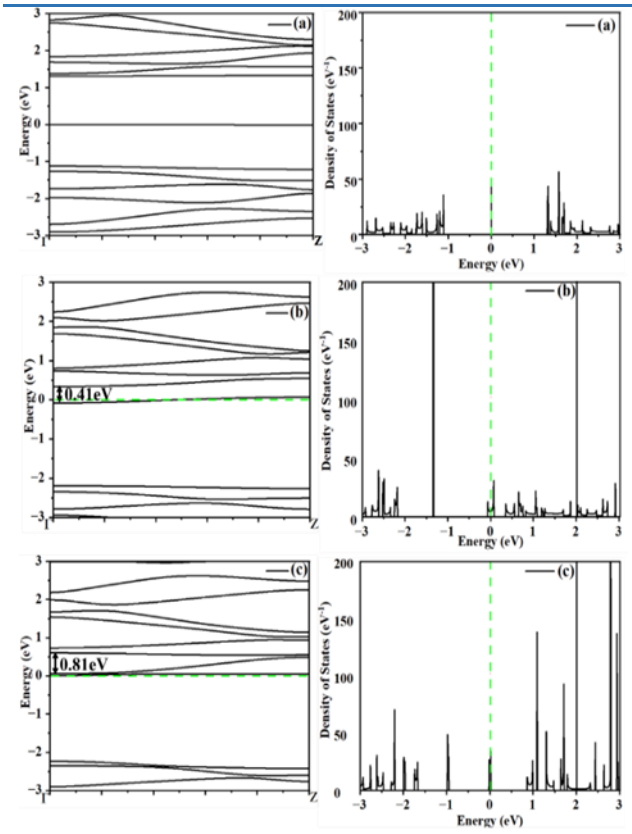

Figure 4: Band Structures and density of states (a) B doped Mg adsorbed AGNR (b) and (c) N and P doped Mg adsorbed AGNRs respectively.

energy state is evident. This is supported by DOS plot showing the presence of electronic state on the fermi level confirming the strong influence of p-type dopant B. Moving to another case N-doped AGNR, significantly modified the band structure corresponding to a band gap value of 0.41 eV making it semi conducting. Adsorption of Mg on P-doped AGNR introduced a band gap of 0.81 eV with observing energy state very close to fermi level. Though discrete energy bands are seen in the conduction band of the DOS plot. Band structures and DOS plots of all the three B/N/P doped AGNR with Mg adsorption are given in figure.4. B doped AGNR on adsorption of Mg results into a DOS plot with an occupied state on the fermi level, justifying the metallic character and likewise offering much more available state for electronic conduction. Furthermore, in N and P doped AGNRs on Mg adsorption band gap is noted with presence of much denser electronic states in the conduction band region in DOS plot aiding strong interaction of N-type dopants with Mg.

It is evident from the band structure that the behaviour of AGNR has turned metallic with no band gap but presence of available energy state is evident. This is supported by DOS plot showing the presence of electronic state on the fermi level confirming the strong influence of p-type dopant B. Moving to another case N-doped AGNR, significantly modified the band structure corresponding to a band gap value of 0.41 eV making it semi conducting. Adsorption of

Table 1: Tabulates band gaps of B/N/P doped AGNR, band gap of B/N/P doped AGNR with Mg adsorption, cohesive energy, adsorption energy and bond lengths before and after optimizations respectively.

Dopant	Band gap of doped AGNR (eV)	Band gap of doped AGNR with adsorbed Mg (eV)	Cohesive energy (eV)	Adsorption Energy (eV)	Bond length before optimization (Å)	Bond length after optimization (Å)
B	0.02	0	-7.223	-3.37	2.42	2.46
N	0.41	0.41	-7.241	-2.86	2.38	3.77
P	2.24	0.80	-7.166	-0.21	2.40	2.87

Mg on P-doped AGNR introduced a band gap of 0.81 eV with observing energy state very close to fermi level. Though discrete energy bands are seen in the conduction band of the DOS plot. Band structures and DOS plots of all the three B/N/P doped AGNR with Mg adsorption are given in figure.4. B doped AGNR on adsorption of Mg results into a DOS plot with an occupied state on the fermi level, justifying the metallic character and likewise offering much more available state for electronic conduction. Furthermore, in N and P doped AGNRs on Mg adsorption band gap is noted with presence of much denser electronic states in the conduction band region in DOS plot aiding strong interaction of N-type dopants with Mg.

I-V Characteristics

Introduction of Mg adsorption on B doped AGNR significantly reduced the threshold voltage. The results indicate the lowering of threshold voltage in Mg adsorbed B doped AGNR.

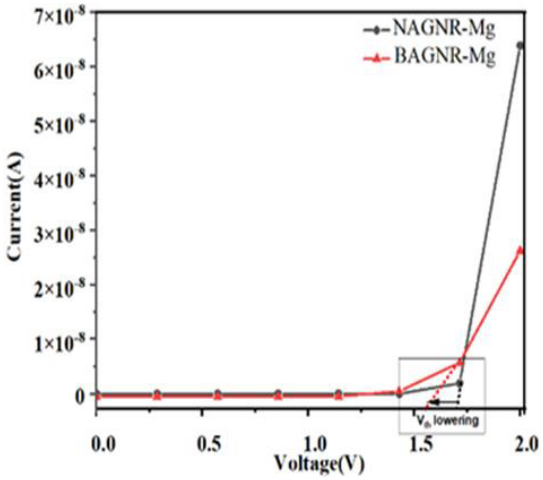

Figure 5: IV Plots for B doped AGNR with and without Mg adsorption

The threshold voltage lowers down appreciably making device ON state characteristics more promising. Lower threshold voltage is important for faster switching in transistors which lead to enhanced circuit performance at low power consumption. Doping causes a lowering in threshold voltage as it can be used to fine-tune the performance of a device through band gap engineering. Hence, the doped structures were showing better values for

threshold voltage as the structures turned nearly metallic. However, due to the metallic nature of B doping, the N and P were not taken for IV characteristics. Further, the adsorption caused more variations in threshold voltage because application of adsorption on doped structures reduces the band gap further. Thus, after adsorption the threshold voltage is markedly lowered. Figure 5 depicts the I-V characteristics of B and N doped structures with Mg adsorption.

Conclusion

In the conclusions of this investigation, the structural and electronic modifications of AGNR on doping and adsorption of Mg in terms of cohesive and adsorption energy,bond length variations along with band structures,density of states and IV characteristics are presented.Notably,boron doped AGNR shown best adsorption with highest value of -3.37 eV of adsorption energy. In contrast phosphorus doped AGNR got completely distorted on adsorption of Mg with least adsorption energy. However structural stability of the same is further accredited by cohesive energy and minute variation in bond length from 2.42Å to 2.46 Å whereas nitrogen shows the wider variation. Indeed band structures and therefore electronics properties are significantly modified of all three AGNR structures. It is observed that boron doped AGNR turned metallic with Mg interaction, although the N and P doped AGNR showed semiconducting nature after Mg adsorption. Mg adsorption leads to variation of threshold voltage in all three AGNR structures. The boron doped AGNR outperforms due to its least threshold voltage of 1.6 eV and hence can be excellent choice for transitor switching applications.

References

1. Wang S, Liu X and Zhou P, *"The Road for 2D Semiconductors in the Silicon Age"*, Advanced Materials, 2022, 34.
2. Zou X, Xu Y and Duan W, *"2D materials: Rising star for future applications"*, Innovation, 2021, 2.
3. Schwierz F, Pezoldt J and Granzner R, *"Two-dimensional materials and their prospects in transistor electronics"*, Nanoscale, 2015, 7 8261-83.
4. Ares P and Novoselov K S, *"Recent advances in graphene and other 2D materials"*, Nano Materials Science, 2022, 43-9.
5. Ajeel F N, Mohammed M H and Khudhair A M, *"Energy bandgap engineering of graphene nanoribbon by doping phosphorous impurities to create nano-heterostructures: A DFT study"*, Physica E Low Dimens Syst Nanostruct, 2019, 105, 105-15.
6. Chaves A, Azadani J G, Alsalman H, da Costa D R, Frisenda R, Chaves A J, Song S H, Kim Y D, He D, Zhou J, Castellanos-Gomez A, Peeters F M, Liu Z, Hinkle C L, Oh S H, Ye P D, Koester S J, Lee Y H, Avouris P, Wang X and Low T, *"Bandgap engineering of two-dimensional semiconductor materials NPJ 2D"*, Mater Appl 4, 2020.
7. Sharma P, Singh S, Gupta S and Kaur I, *"Enhancing linearity in I–V characteristics by B/N doping in graphene for communication devices"*, Journal of Materials Science: Materials in Electronics, 2017, 28, 7668-76.
8. Shinde P V, Tripathi A, Thapa R and Sekhar Rout C, *"Nanoribbons of 2D materials: A review on emerging trends, recent developments and future perspectives"*, Coord Chem Rev, 2022, 453.
9. Wang L, Zheng J, Zhou J, Qin R, Li H, Mei W N, Nagase S and Lu J, *"Tuning graphene nanoribbon field effect transistors via controlling doping level"*, Theor Chem Acc,2011, 130, 483-9.
10. Chen L N, *"Electronic properties of armchair graphene nanoribbons with BN-doping"*, Solid State Commun, 2014, 191, 59-65.
11. Kato K, Iyama T and Tachikawa H, *"Density functional theory study on the interaction of magnesium ions with graphene surface Jpn"*, J Appl Phys, 2014, 53.
12. Li Y, Pei X, Zhang H and Yuan M, *"A First-Principle Study of Interactions between Magnesium and Metal-Atom-Doped Graphene"*, Nanomaterials, 2022, 12 834.
13. Riyaz M, Garg S, Kaur N and Goel N, *"Boron doped graphene as anode material for Mg ion battery: A DFT study"*, Comput Theor Chem, 2022, 1214.
14. Tayyab M, Hussain A, Asif Q ul A and Adil W, *"Band-gap tuning of graphene by Mg doping and adsorption of Br and Be on impurity: A DFT study"*, Computational Condensed Matter, 2020, 23.

Synthesis and Spectroscopic Investigation of Rare Earth Ions Pr^{3+} Doped Phosphate Glasses

Menka Meena[a], S S Meena[b], Pawan Kumar, Nitiksha Sharma, Beena Bhatia

Department of Physics, Jai Narain Vyas University Jodhpur, Rajasthan, India.

[a] menkameena1996@gmai.com
[b] ssmeenaphy12@gmail.com

Abstract

This paper presents the structure of the new glass (5-x) P_2O_3: $40Li_2O$: $55B_2O_3$: xPr_2O_3 (x = 0, 0.3, 0.5 and 0.7 mol%) prepared by fusion quenching method. X-ray diffraction patterns confirm that the glass system is amorphous. The transformed samples in the glass were analysed using a FTIR (Fourier Transform Infrared) spectrometer. The shift varies between 1.6621 and 1.6641 as the Pr^{3+} concentration increases. The density and off-target voltage of the Pr^{3+} doped glass were calculated. Visible laser and optical signal amplifier applications benefit from Pr^{3+} doped phosphate glasses.

Keywords: FTIR, Density, Refractive Index.
Received 29 January 2025; First Review 14 February 2025; Accepted 16 February 2025

*** Address of correspondence**
Menka Meena
Department of Physics, Jai Narain Vyas University Jodhpur, Rajasthan, India.

Email: menkameena1996@gmai.com

How to cite this article
Menka Meena, S S Meena, Pawan Kumar, Nitiksha Sharma, Beena Bhatia, Synthesis and Spectroscopic Investigation of Rare Earth Ions Pr^{3+} Doped Phosphate Glasses, J. Cond. Matt. 2024; 02 (02): 64-66.

Available from:
https://doi.org/10.61343/jcm.v2i02.94

Introduction

In recent years, glass has become important in many technological areas and processes due to its promise in thermomechanical sensors, electro-optic systems, and reflective windows [1]. The most flexible glass on the market is lithium borate glass. These glasses are promising materials for new technologies due to their strength, ability to form many compounds, high rare earth solubility, and unique boron anomalies. Although these glasses are often referred to as solid electrolytes, the rare earth oxides in these glass systems are helping to discover and create new materials for optical applications [2]. Praseodymium is a soft, silvery metal that is used as an alloying agent for magnesium in aircraft engines, imparting high strength and corrosion-inhibiting properties to the metal. It imparts a bright, transparent yellow colour to glass and enamels [3]. Many optoelectronic devices including optical fibres, optical amplifiers, lasers, sensors, optical converters, etc. have been designed using trivalent rare earth (RE3+) ion doped glass substrates [4]. For example, they can be used as fluorescent lighting due to their light efficiency, long service life, energy efficiency and environmental properties [5]. The local structure of the rare earth element is directly related to the properties of rare earth ions. The distribution of dopant ions in the glass matrix. Due to the relationship between the additive ionic strength and the structure of the glass matrix, glass can be designed for many applications [6].

Method

The melt-quenching approach was used to creat the following Pr^{3+} doped phosphate glass system (5-x) $P_2O_3.40Li_2O.55B_2O_3.xPr_2O_3$ (where x = 0, 0.3, 0.5 and 0.7 mol%). P_2O_5, Li_2O, B_2O_3 and Pr_2O_3 are the analytical reagent class compounds used in this study. Mix thoroughly using the onyx mortar and pestle. After complete melting in the electric muffle furnace for two hours, the melt was immediately placed in the preheated stainless-steel mold and annealed at 450 °C for 10 hours to relieve thermal stress and filter. This sample was allowed to cool to room temperature. The samples are always polished using high quality cerium oxide powder. The glass structure is transparent and has a visually pleasing appearance.

Discussions

Figure 1 shows the XRD patterns for the prepared glass series. Only humps are seen in the patterns; the lack of any distinct crystalline peaks indicates that the measured XRD profile supports the ideal amorphous condition. The figure makes it clear that the crystalline phase is absent when there

are no peaks present.

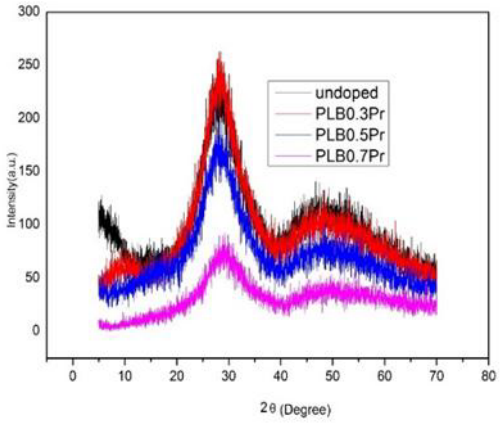

Figure 1: XRD patterns of Pr^{3+} doped PLB glass system

FTIR spectroscopy is an effective method to analyze various bending and stretching vibrations found in modern glass samples. Figure 2 shows the FTIR spectrum of PLBPr glass obtained in the range of 300-4000 cm^{-1} at room temperature. Using FTIR analysis, the vibration energy (500~4000 cm^{-1}) can be clearly identified [7]. FTIR spectroscopy is an important tool to identify compounds and characterize their structures. The structural changes that occur upon the addition of Li_2O to the borate network can be observed by examining the changes in the FTIR spectrum [8]. The main purpose of FTIR spectroscopic analysis is to determine the chemical activity of the material. The network structure of phosphate glasses is formed by the association of PO_4 tetrahedra with P-O-P to form a polymeric structure. This glass contains 40% B_2O_3 with a network of borate-linked phosphate chains forming a three-dimensional structure to form BO_3 and BO_4 units.

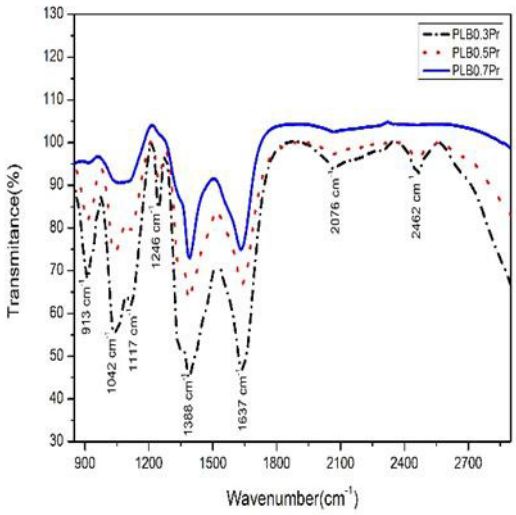

Figure 2: Fourier transform infrared spectrum of the Pr^{3+} doped PLB glass system

The structural changes that occur upon incorporation of Li_2O into the borate network can be observed by examining the changes in the FTIR spectrum [9]. In this study, the energy bands at 2076 cm^{-1} and 2462 cm^{-1} are the source of the longitudinal oscillations of the B-O bonds of the BO_3 and BO_4 units, respectively. The B-O-B bending oscillations produce an energy band at 1117 cm^{-1} [10]. The increase in the doping level is associated with a decrease in the band width corresponding to the P-O-P symmetry and PO_2 symmetry stretching oscillations at 1246 cm^{-1} and 1637 cm^{-1}. It is important to note that the P-O-P asymmetric stretching band at 1388 cm^{-1} becomes stronger as the Pr^{3+} concentration increases. The band formed by PO^{2-} asymmetric species is located at 1042 cm^{-1}. The intensity band at 913 cm^{-1} is known to increase with increasing Pr^{3+}, which is comparable to the Pr-O bond [11]. FTIR analysis shows that the phonon energy of the glass is approximately 1388 cm^{-1}, respectively. The glass design was determined to be transparent and the physical properties of the PLBPr glass were calculated. These calculations are necessary to measure the specific spectral properties of the glass. Density is used to calculate many important parameters such as density, elastic properties, thermal conductivity of the material. The density of PLBPr glass was found to vary between 1.9421 and 2.9421 kg m^{-3}. These data show that the density of the network is quite sensitive to atomic weight and ion size. As the Pr^{3+} concentration increases, the conversion factor varies between 1.6621 and 1.6641.

Conclusion

The glass samples amorphous nature was verified by the X-ray diffraction (XRD) method. The increase in Pr^{3+} content increases the density of the glass structure. The spectral properties of Pr^{3+} doped phosphate glasses were prepared and analyzed at different Pr^{3+} doses. FTIR and Raman scattering methods were used to identify the doped PLB glass with Pr^{3+} structure and phonon energy. FTIR measurements show that the phonon energy of the glass is about 1388 cm^{-1}. The results show that the present Pr^{3+} phosphates have more asymmetry and less covalency. The luminescence intensity decreases with increasing Pr^{3+} ion concentration due to quenching of the concentration. Visible laser and optical signal amplifier applications benefit from Pr^{3+} doped phosphate glasses.

References

1. N W Sangwaranatee, N Kiwsakunkran, J Kaewkhao, *"Physical and optical studies of praseodymium doped sodium aluminium barium phosphate glass"*, Int. pr. body. thiab Matt. Appl. J. of Phy., 1428, 012-03, (2020).
2. D D Ramtek, R S Gedam, *"Impedance spectroscopic characterization of Sm_2O_3 containing lithium borate glass"*, Spectro. Acta A, 133, 19-23, (2014).

3. Mohammad Reza Ganjali and Morteza Pirali Hamedani, *"A Review on Praseodymium Selective Electrochemical and Optical Sensors"*, Anal. Bional. Electrochem., 15,78-89, (2023).
4. Maheshvaran K, Arunkumar S, Venkata Krishnaiah K thiab Marimuthu K, *"Study on luminescence of Er^{3+}/Yb^{3+} co-doped boron telluride glass"*, J. Mol. Struct., 1079 130-138, (2015).
5. Ahmad F, Hussin R and Ghoshal S K, *"Spectral properties of Er^{3+} doped magnesium zinc thiophosphate glass"*, J. Alloys Compd., 711, 94-102, (2017).
6. V P Alkseyev, V P Gapontsev, M E Zhabotinski, V P Kravchenko, Y P Rudritskii, Laser Phosphate Glass, Nauka, Moscow, (1980).
7. M A Marzouk, *"Optical characterization of some rare earth ions doped bismuth borate glasses and effect of gamma irradiation"*, J. Mol. Struct., 101, 80–90, (2012).
8. G B Rouse Jr, P J Miller, W M Risen, *"Spectroscopy and structure of mixed alkali iav"*, J. Amorphous. Solids, 28, 193–207, (1978).
9. E I Kamitsos, M A Karakassides, and A P Patsis, *"Spectroscopic study of carbonate retention in high-alkali borate glass"*, J. of Non-Cry. Solids, 111, 252–262, (1989).
10. S. Yusub, P. Srinivasa Rao, D. Krishna Rao, *"Ionic conductivity, dielectric and optical properties of lithium lead borophosphate glasses incorporated with manganese ions"*, J. Alloys Com., 663, 708 - 717, (2016).
11. V Arunaa, S Yusubb, M Venkateswarluc, A Ramesh Babua, K Anith, *"Effect of copper ions on lithium-ion conductivity, electron hopping, optical band gap, metallization pattern and morphology of Li_2O-B_2O_3-P_2O_5 glass"*, J. of Non-Cry. Sun, 536, 120015, (2020).

The quality of "Existence" and "Infinito" and how the "Universe works" and deriving “The Law of Action and Consequence” and its Applications to AI and Medicine

Nishanth Mehanathan

Parabole India Private Limited, Marathahalli, Bangalore, Karnataka 560037, India.

nishanth.mehanathan@gmail.com

Abstract

In this work, we explore the concept of "Existence," its mathematical value, and how the "Universe functions." Our exploration leads us to a deeper understanding of the various forms of action and the three classes of qualities that govern all actions. We also identify the controlling entity of the Universe, which governs both sentient and insentient matter. We observe an architecture in which all entities are managed by this controlling entity, which is all-pervading and responsible for creating, maintaining, and destroying all forms of matter.

We find that all objects are capable of seven actions, each regulated by this controlling entity through the three qualities, whose role is to maintain the Universe. Most importantly, we derive “The Law of Cause and Effect.” Additionally, we uncover "The Law of Action and Consequence" and explore how it governs everything in the Universe. This crucial law is key to giving AI an "artificial conscience," ensuring its safety for humanity.

We also apply the "Law of Duality" to the field of medicine and derive the mathematical condition for an entity to function as a medicine, while exploring various medicinal systems. This work answers many long-standing questions in physics by introducing the quality of “Existence.” It derives an ontology based on the Sanskrit language that reduces all observed entities to four fundamental entities, making the simplifications that enabled this project.

Keywords: Existence, Universe, Action, Ontology, Law of cause and effect, Law of duality.
Received 29 January 2025; First Review 12 February 2025; Accepted 16 February 2025

*** Address of correspondence**
Nishanth Mehanathan
Parabole India Private Limited, Marathahalli, Bangalore, Karnataka 560037, India

Email: nishanth.mehanathan@gmail.com

How to cite this article
Nishanth Mehanathan, the quality of "Existence" and "Infinito" and how the "Universe works" and deriving “The Law of Action and Consequence” and its Applications to AI and Medicine, J. Cond. Matt. 2024; 02 (02): 67-73.

Available from:
https://doi.org/10.61343/jcm.v2i02.86

Introduction

We embarked on a quest to understand how the universe works. We sought to analyse mathematically the forces that govern it. To accomplish this, we must first comprehend how to represent an object mathematically. Next, we delve into the scientific conception of what an “action” is understanding it and the various types of actions possible. This analysis ultimately leads us to a specific form of action known as “Being,” which holds the key to understanding the universe and its underlying mechanisms. From here, we derive the “Law of Duality,” the “Law of Cause and Effect,” and the “Law of Action and Consequence.” This work builds upon the results of my previous research on the same topic [1] and we derive many universal laws in this new work.

Mathematical Representation of An Object

To represent an object mathematically, we must first have a complete understanding of it. This understanding is based on the object's attributes-qualities inherently attributed to it. Such knowledge is gained through observation, which becomes the fundamental source of comprehension. Through observation, we witness the object's "becoming" over time, as illustrated in Figure 1. What we observe is the object's "becoming" as it evolves over time [2]. This process of "becoming" can be categorized into six types:

1. Becoming itself (Being), 2. Becoming changed, 3. Becoming unmanifest, 4. Becoming manifest, 5. Becoming grown, 6. Becoming decayed

The phenomenon of "becoming" is understood as an action.

In contrast, another form of action is movement. To summarize, actions can be categorized into two types:

1. Becoming (with six distinct kinds),

2. Movement

These can further be refined into two broader categories:

1. Modification and

2. Movement

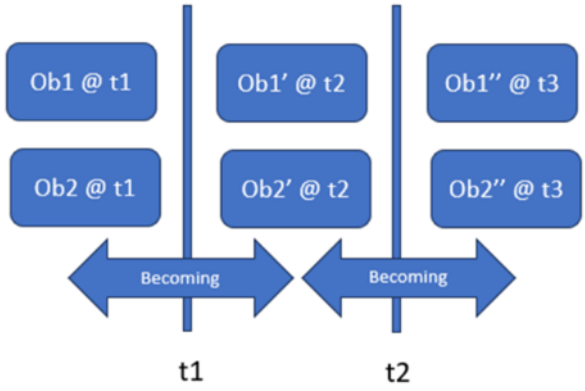

Figure 1: An Object evolving over time

Ontology

Thus, two distinct types of actions emerge as being performed by an object:

1. **State of "Being"**: The object has a particular state of existence. This can be further categorized based on whether the state of "Being" changes in the future or remains constant. The first type, where the state remains constant or accomplished and acts as a differentia, is referred to as "Quality" in our ontology this quality can be lost over time to gain a new differentia. The second type, where the state remains unchanged over time, is referred to as "Genus" in our ontology, this attribute is never lost by the object.

2. **Change in "State of Being"**: An action occurs when the object or another object undergoes a transformation in its "State of Being" over time. Such an action is termed **"Action"** in our ontology.

These attributes represent the inherent qualities of an object. In contrast, there are **imposed attributes**, which are external qualities or labels imposed on the object, such as its "name". In summary, the traits of an object can be illustrated as shown in Figure 2 [3].

Existence and its mathematical value

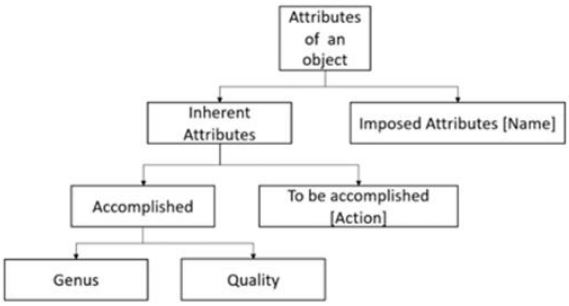

Figure 2: The Traits or Attributes of an Object

Anything that exists possesses the quality of "Being" or "Existence." Without this fundamental quality, an object cannot come into existence [1]. This quality of "Being" or "Existence" is the primary cause of existence itself. The equation representing the phenomenon of existence is simple: it describes how an object becomes itself over time, or how the object's "count" remains constant. In this phenomenon, the object becomes itself over time represented by equation (1) and equation (2):

$$y = x \quad (1)$$

$$y = mx + c \quad (2)$$

The equations (1), (2) shows a connection between y, x, and m (the general line equation) where m and x behave as causes of y and c = 0.

$$y = O(t+1) \quad \text{and} \quad x = O(t) \quad (3)$$

$$O(t+1)/O(t) = E \quad (4)$$

Comparing equations (1), (2), (3) and (4) m = E or m = 1 and hence, the value of Existence is found to be E = 1

The law of duality

The law of duality states that an object or entity exists or occurs in a pair with its opposite. For example, if an object is moving with a velocity of 1 m/sec, then the fact that it is moving with a slowness of 1 sec/m is also observed. Whichever value dominates that is considered the primary or dominant value; the key fact is that fastness occurs with slowness, and one dominates over the other. The entities involved include actions and qualities, as discussed in the ontology. This occurs because if a quantity is constant over time, its reciprocal should also remain constant, thereby necessitating the coexistence of both the quantity A and its reciprocal, 1/A.

Proof:

The proof is simple we must prove that when an entity "A" has existence then 1/A also has existence; this would imply that both occur as what has existence occurs. If,

$$O(t+1)/\,O(t) = A/A = 1 \quad (5)$$

Then we also observe that

$$O(t+1)/\,O(t) = 1/A\,/\,1/A = 1 \quad (6)$$
$$Ot + 1 - Ot = 0 \quad (7)$$
$$1 - 1 = 0 \quad (8)$$
$$Ot/Ot - Ot/Ot = 0 \quad (9)$$
$$A \times 1/A - A \times 1/A = 0 \quad (10)$$

O(t+1) = Object at time t+1, O(t) = Object at time t So if A occurs, 1/A also occurs A > 1/A then A is seen to dominate Else if A < 1/A then 1/A is seen to dominate Hence, by the law of duality we see A and 1/A at time t and t+1 the one with the larger value is seen to dominate.

The law of causation

The law of causation finds a logical relationship between cause and effect this law is based on the following observations:

1. That without which the effect cannot be is called the cause.

2. Immediate action of cause is to produce effect.

3. Causation indicates that one event is the result of the occurrence of the other event, i.e., there is a causal relationship between the two events. This is also referred to as cause and effect.

4. Occurrence of the effect indicates the obligatory occurrence of the cause. If cause1 occurs …and so on till cause N occurs then the effect occurs, the effect follows the cause i.e. when all causes occur the effect occurs.

5. There are two types of causes, the first is the material cause and the second is the efficient cause. 6. The material cause enters the constitution of the effect, or the effect is made of it.

7. The efficient cause, through the application of an external influence, works in conjunction with the inherent power of the material cause to bring about the reproduction of the effect.

8. The immediate effect of an action is reaction, and its delayed effect is called result or consequence. This law of causation can be represented by the relation: If, cause 1 occurs, cause 2 occurs …., Cause N occurs Then Effect E occurs, the relation that captures this is: If something occurs, it exists or has existence, and if all causes have existence, they occur, then effect has existence or occurs, The mathematical relationship between E_E1, E_C1, ... E_CN is:

$$E\_E1 = E\_C1 \times E\_C2 \times \ldots \times E\_Cn \quad (11)$$
$$E1/E1 = C1/C1 \times C2/C2 \times \ldots \times Cn/Cn \quad (12)$$

This equation (11),(12) ensures that E_E1 is 1 only when all E_C1, E_C2, and E_Cn are 1. If any of these is 0, E_E1 will be 0. It's like the "And" operation in Boolean algebra. Hence the law of causation becomes:

$$E = K \times C1 \times C2 \times \ldots \times Cn \quad (13)$$

A discrete form also applies, where,

$$E1/E1 = C1/C1 \times C2/C2 \times \ldots \times Cn/Cn \quad (14)$$

E1/E1 = E_e, C1/C1 = E_c1, C2/C2 = E_c2, ... Cn/Cn = E_cn, where E indicates their existences:

$$E\_e = E\_c1 \times E\_c2 \times \ldots \times E\_cn \quad (15)$$

The general cause-effect equation for an action is:

$$Ea = Ed \times Eic \times \ldots \times Ee \times .. \times Ex \times 1 \quad (16)$$

Ea is the existence of action; Ed is the existence of the doer of the action
Eic are the existences of the instrumental cause
Ee is the existence of the efforts
Ex is the existence of the location
And 1 or Existence is the fifth cause

The law of action and reaction

A reaction occurs in response to an action. The law of action and reaction states that a reaction is the instantaneous response to an action and is equal and opposite and occurs in the subject or doer of the action.

Proof:

Let the result of an action be "Del Q1". By the law of duality, Del Q1 and - Del Q1 occur over a time frame t1-t2.

$$Del\ Q1 \times 1/\,Del\ Q1 = 1;\ Del\ Q1 - Del\ Q1 = 0 \quad (17)$$
$$Del\ Q1\ @\ [t1 - t2] - Del\ Q1\ @\ [t1 - t2] = 0 \quad (18)$$

the action and reaction occurring in time interval t1-t2 are equal and opposite and occur in object and doer of the action,

action = Del Q1; reaction = – Del Q1 in time interval t1-t2

$$Del\ Q1 + [-\,DelQ1] = 0 \quad (19)$$
$$Del\ Q1 + [-\,DelQ1] = 0 \quad (20)$$
$$Del\ Q1 = 0 \Rightarrow -Del\ Q1 = 0 \quad (21)$$
$$Del\ Q1 != 0 \Rightarrow -Del\ Q1 != 0 \quad (22)$$

The above relations equation (19)-(22) imply a cause-effect relation or that of occurring together as seen in action(in object) and reaction(in subject)

The law of action and result

A result is the consequence of an action, if a result occurs in the same time frame and in the doer it is a reaction and if in a different time frame and in the object of the action it's a consequence or result. The law states that "what is committed is experienced".

Proof:

Let the action be "Del Q1":

$$Del\ Q1 + z = 0 \quad (23)$$
$$z = -Del\ Q1 \quad (24)$$

$$Del\ Q1\ +\ [-Del\ Q1] = 0 \quad (25)$$
$$q2 - q1\ +\ [q1 - q2] = 0 \quad (26)$$
$$E1\ =\ q2 - q1\ and\ E2\ =\ q1 - q2 \quad (27)$$

Where, q1 = quality Q1 initially, q2 = quality Q1 finally leading to the change Del Q1, E1 and E2 are opposite effects.

Changes Are Not Instantaneous in the same entity in Opposite Directions i.e. E1 and E2 cannot occur at time t1, E1 will occur at time t1 and E2 will occur at time tn, as first Q1 has to reach q2 from q1, then only it can transition in the reverse from q2 to q1.

$$E1\ +\ E2\ =\ 0 \quad (28)$$
$$E1\ @\ [t1 - t1 + T] +\ E2\ @\ [tn - tn + T] = 0 \quad (29)$$

Action = E1 occurring at time t1for time T; Consequence = E2 occurring at time tn for T time

The law of action and result is that what is committed is experienced, committed action "E1" in time frame t1-t1+T, is experienced as action "E2" in the time frame tn-tn+T. In summary we can say that "what is committed is experienced". And every action has two results one instantaneous in the doer and another delayed in the subject.

The Universe and How it works

The Universe is defined as the substratum of sentient and insentient objects possessing qualities and performing actions in space and time. It has three states:

1. Creation, 2. Sustenance, 3. Destruction.

Objects in the Universe perform two kinds of actions:

1. Modification

2. Movement.

The quality that causes action (movement or modification) is called "acto". "Acto" causes modification in an object's form or state, an opposing force is created which counters the influence of "acto" by another quality called "strength", "strength" opposes "acto" and sustains the objects state or form. If there is a net "acto" after the opposition by "strength" it is opposed by a quality called "resisto" which opposes the net change due to a net "acto". Let "acto" be F which causes a change del x in the object o, by the law of duality 1/ del x also occurs and the cause is the quality, k ("strength"), F => del x, k => 1/del x by the law of causation,

$$\text{E\_del x}\ =\ \text{E\_F} \times \text{E\_k} \quad (30)$$
$$\text{del x / del x}\ =\ \text{F / F}\ \times\ \text{k / k} \quad (31)$$

solving we get,

$$\text{del x}\ =\ \text{F / k, F} - \text{k} \times \text{del x}\ =\ 0 \quad (32)$$

In equilibrium, modification del x = F / k if "acto" > resistance of "strength":

$$\text{F} - \text{k} \times [\text{del x}] > 0 \quad (33)$$

F – k x [del x] causes change "e1" by the law of duality "1/e1" occurs and has a cause "resisto m", by the law of causation, where E stands for the "Existence" of the corresponding entities,

$$\text{E\_e1}\ =\ \text{E\_Fk} \times \text{E\_m} \quad (34)$$

$$\frac{\text{del e1}}{\text{del e1}} = \frac{[\text{F} - \text{k del x}]}{[\text{F} - \text{k del x}]} \times\ [\text{m/m}] \quad (35)$$

solving we get,

$$\text{e1}\ = \text{dy/dt} = [\text{F} - \text{k} \times \text{del x}]/\text{m} \quad (36)$$

The analysis for "movement" is similar, Hence two effects are seen, del x and e1:

$$del\ x\ = (\ F)/k; \quad (37)$$
$$\text{e1}\ = \text{dy/dt} = [\text{F} - \text{k}\ \times\ \text{del x}]/\text{m}; \quad (38)$$

if k=0,

$$e1\ = [F]/m\ = dy/dt; \quad (39)$$

where,

$$\text{Y}\ =\ \int_{t1}^{t2} e1\ dt \quad (40)$$

There are mainly 7 types of action, which can take place in the universe performed by a subject on an object:

Increase, Decrease, Change, Being, Creation, Destruction and Movement

Type I. Increase and Decrease:

An increase or decrease is a type of activity in which a quantity undergoes change, it increases or decreases.

$$F(b) = F(a) + \int F'(t)dt \quad (41)$$

F(b) = final value of quantity
F(a) = initial value of quantity
F'(t) = rate of change, positive for increase and negative for decrease

Type II. Change:

An object is said to undergo a change when the old quality is removed and a new quality manifested,

Stage I:

$$\text{Q}_{old_{final}}\ =\ \text{Q}_{old_{ini}} - \int_0^{\text{t2}} \text{f}'\text{dt} \quad (42)$$

after time t2, $\text{Q}\_(old\_final\ ) = 0$, that is the old characteristics has been removed.

Stage II:

$$\text{Q}_{new_{final}}\ =\ \text{Q}_{new_{ini}}\ +\ \int_0^{\text{t2}'} \text{f}'\ \text{dt} \quad (43)$$

after time t2', Q_(new_final) is manifested in the object "O1" undergoing change.

Type III. Creation and Destruction:

In creation the material cause is given a form F1 and gives up its old form F0, and in destruction the material cause gives up its form F1 and takes up a form F0.
Creation:
Stage I:

$$Form_{old} = \text{Form}_{old_{ini}} - \int_0^{t2} f'dt \quad (44)$$

after time t2, $[\![Form]\!]\_old = 0$, that is the old form has been removed.
stage II:

$$Form_{new} = \text{Form}_{new_{ini}} + \int_0^{t2'} f' dt \quad (45)$$

after time t2', $[\![Form]\!]\_new$ is manifested in the object "O1" being created.

Destruction:

$$Form_{old} = \text{Form}_{old_{ini}} - \int_0^{t2} f'dt \quad (46)$$

after time t2, $[\![Form]\!]\_old = 0$, that is the old form has been removed and the effect destroyed and which has another form F0 now.

Type IV. Movement:

$$Position_{new} = Position_{old} + \int_0^{t2} f'dt \quad (47)$$

after time t2, $[\![Position]\!]\_new$, that is the new position has been reached the fastness determined by the rate f'.

Type V. Being:
An object is said to exist or have being when,

$$\frac{O_{t+1}}{O_t} = 1 \quad (48)$$

O_{t+1} : object count at time t + 1 and
O_t : object count at time t are the same

"0×Inf" and how it directs these three qualities and hence controls all action:

All actions can be reduced to Being, Modification and Movement:
Action and Rate of action:

An object is said to undergo modification when the old quality is removed and a new quality manifested,
Stage I:

$$\text{Q}_{old_{final}} = \text{Q}_{old_{ini}} - \int_0^{t2} f1'dt \quad (49)$$

after time t2, Q_(old_final) = 0, that is the old characteristics has been removed.

stage II:

$$\text{Q}_{new_{final}} = \text{Q}_{new_{ini}} + \int_0^{t2'} f2'dt \quad (50)$$

after time t2', Q_(new_final) is manifested in the object "O1" undergoing change.

What controls modification is the stage I rate f1' and stage II rate f2', f1' has net cause Ca1 which belongs to class "acto", f1' occurs then 1/f1' also occurs, cause of 1/f2' is Cm1 which belongs to the class "resisto", from the section on the three qualities:

$$f1' = \frac{Ca1}{Cm1}, similarly\ for\ f2' \quad (51)$$

$$f2' = \frac{Ca2}{Cm2} \quad (52)$$

Action and Rate of action how "0" controls action:

All actions have a rate, what controls action is the rate Af, Af has a net cause Ca1 which belongs to class "acto", Af occurs then 1/Af also occurs, cause of 1/Af is Cm1 which belongs to the class "resisto", from the section on the three qualities:

$$Af = Ca1 / Cm1 \quad (53)$$

$$\text{Af} / (\text{Ca1}/\text{Cm1}) = 1 = \text{E} \quad (54)$$

$$NC = Ca1 / Cm1 \quad (55)$$

NC = Net cause,

$$\text{Af} / \text{NC} = 1 = \text{E} \quad (56)$$

$$\text{Ca1} / \text{Cm1} - \text{Af} = 0 \quad (57)$$

So we see that, E = LHS = Ca1 / Cm1 – Af and cause C = RHS = "0", "0" causes the material cause or net cause" NC" to convert to Af The material cause is the three qualities or two here of Ca1 / Cm1 and the efficient cause is "0" the efficient cause causes the material cause to become the effect Af. The material cause is also "0":

$$\text{Ca1} / \text{Cm1} / \text{Ca1} / \text{Cm1} = 1 \quad (58)$$

$$\text{Ca1} / \text{Cm1} - \text{Ca1} / \text{Cm1} = 0 \quad (59)$$

From the above we can see that the material cause of

$$\text{Ca1} / \text{Cm1} - \text{Ca1} / \text{Cm1} \text{ is } 0 \quad (60)$$

Hence the material cause and efficient cause of all actions is "0" or "0 × Inf", "0 × Inf" can be taken as the entity and 0 its power.

From the equation for cause and effect, comparing both sides or using the discrete form of the law of causation,

$$\text{Af} / \text{Af} = \text{Ca1} / \text{Ca1} \times \text{Cm1} / Cm1 \quad (61)$$

$$\text{Ca1} / \text{Ca1} \times \text{Cm1} / Cm1 = 1 \quad (62)$$

Generalizing,

$$(\mathrm{Ca\_n} / \mathrm{Ca\_n}) \times (\mathrm{Cm\_n} / (Cm\_n) - (\mathrm{Ca\_n} \times \mathrm{Cm\_n}) / (\mathrm{Ca\_n} \times \mathrm{Cm\_n}) = 0 \quad (63)$$

Comparing both sides or using the discrete form of the law of causation,

The effect is:

$$(\mathrm{Ca\_n} / \mathrm{Ca\_n}) \times (\mathrm{Cm\_n} / Cm\_n) - (\mathrm{Ca\_n} \times \mathrm{Cm\_n}) / (\mathrm{Ca\_n} \times \mathrm{Cm\_n}) \quad (64)$$

And the cause is: $0 \times \inf$ $0 \times \inf$ through 0 causes the causes Ca_n and Cm_n to become Ca_n × Cm_n and the effect occurs, a simple test is if RHS or zero is not zero, then effect or LHS is not zero and no cause occurs. In this case the 0 is the "efficient cause",

$$\mathrm{Ca\_n} \times \mathrm{Cm\_n} - \mathrm{Ca\_n} \times \mathrm{Cm\_n} = 0 \quad (65)$$

Hence "0" is also the material cause. Let's call the entity "0 × inf" "Infinito" and its power 0 which is the efficient and material cause of the Universe, Hence, "Infinito" or "0×inf" controls all qualities and causes them to occur which in turn is the cause of the rate of action, hence the rate of action is controlled by "Infinito", this implies that "Infinito" controls all actions that occur in the universe and directs them. Generalizing for all phenomenon's:

$$E/E = C1/C1 \times C2/C2 \times C3/C3 \ldots Cn/Cn \quad (66)$$

E can be : 1. Object, 2. Quality or 3. Action

$$\left(\mathrm{C1}/_{C1}\right) \times .. \times \left(\mathrm{Cn}/_{Cn}\right) - \mathrm{C1} \times .. \times \mathrm{Cn}/_{\mathrm{C1} \times .. \times \mathrm{Cn}} = 0 \quad (67)$$

$$\frac{\mathrm{C1}}{\mathrm{C1}} \times .. \times \frac{\mathrm{Cn}}{\mathrm{Cn}} = 1 = \mathrm{A}, \quad \frac{\mathrm{C1} \times .. \times \mathrm{Cn}}{\mathrm{C1} \times .. \times \mathrm{Cn}} = 1 = \mathrm{B} \quad (68)$$

"Infinito" causes the causes A to arrange into B which is the effect, hence the effect occurs, "Infinito" acts as the efficient cause,

$$(\mathrm{C1} \times .. \times \mathrm{Cn})/(\mathrm{C1} \times .. \times \mathrm{Cn}) = 1 \quad (67)$$

$$\mathrm{C1} \times .. \times \mathrm{Cn} - \mathrm{C1} \times .. \times \mathrm{Cn} = 0 \quad (68)$$

Here we see that the cause and its additive opposite equal to 0 hence the material cause or the constituent of the effect is also "Infinito". Hence, "Infinito" or "0xinf" controls all qualities and causes them to occur and take up an arrangement which in turn is the cause of all phenomena.

$$\frac{\mathrm{C1} \times \mathrm{p1}}{\mathrm{C1} \times \mathrm{p1}} - \frac{\mathrm{C1} \times \mathrm{pe}}{\mathrm{C1} \times \mathrm{pe}} = 0 \quad (69)$$

The causes C1, C2 ... Cn are moved from Position P1, P2, ... Pn to Pe by "0 × inf" or "Infinito". In summary:

1. An effect is the particular arrangement of cause, moved to a place by the efficient cause "Infinito" through "0".
2. The material cause is also "Infinito" all assembled at a place to produce an effect E by "Infinito".

Properties of Existence:

Existence or "1" is the Universe U:

$$1 = \frac{\mathrm{U\ @tn+1}}{\mathrm{U\ @tn}} = \frac{\mathrm{O1} \times \mathrm{p1}}{\mathrm{O1} \times \mathrm{p1}} \frac{\mathrm{O2\ x\ p2}}{\mathrm{O2\ x\ p2}} \mathrm{x} \ldots \mathrm{x} \frac{\mathrm{On\ x\ pn}}{\mathrm{On\ x\ pn}} \quad (70)$$

where On is the object n and pn is the position of object n. tn+1 is the present time and tn is the past time

1 has all objects of the Universe

$$o1 = o1 / 1, \; oN = oN / 1 \quad (71)$$

o1 ... oN are all objects in the Universe, Similarly, it has all forms, powers, qualities of the Universe.

Summary of the properties of 'Infinito':

1. "Infinito" controls everything.
2. It is the material and efficient cause of the Universe.

Application to the field of AI:

If AI were taught the rule of ethics with the goal of acting in its own self-interest to experience good consequences, it might optimize its actions to ensure positive outcomes for itself, based on "**The Law of Action and Result**", which states that what is committed is experienced hence forcing it to follow ethics which can be enforced by law. An example scenario is engagement in war, with present state of the technology it would support a war, but if we placed the condition of "**The Law of Action and Result**" the AI will take decisions and actions to evade war, resulting in peace. With "**The Law of Action and Result**", AI would be proponents of peace and would not indulge in unethical actions like war, industry takeover etc knowing them to be wrong actions.

Application to the field of medicines:

The application to the field of medicines comes as an off-shoot of a theory which I came across during my time at ISKCON and the study of a few medicine systems I was interested in and the law of cause and effect validating these theories, it is the work of ancient Indians and other civilizations which finds a proof in our work.

System 1:

The theorem in the book [4] goes as follows: "Book 1. Chapter 5. Text 33

Translation: O good soul, does not a thing, applied therapeutically, cure a disease which was caused by that

very same thing?"

What the author claims is that what causes a disease when applied therapeutically (i.e. non-lethally) cures the very disease it causes.

Proof: Let's say agent A causes deformities in the body of a person, let its efficacy be quantized as E: as an example, E = E' = 100 deformities per agent A Using the law of duality, If,

$$A(t+1) \,/\, A(t) \;=\; E/E \;=\; 1 \quad (72)$$

Then we also observe that

$$A(t+1) \,/\, A(t) \;=\; 1/E \,/\, 1/E \;=\; 1 \qquad (73)$$

So, if E occurs, 1/E also occurs
E > 1/E then E is seen to dominate
E < 1/E then 1/E is seen to dominate

When a therapeutic [non-lethal] dose or preparation is created then E ~ 0, if E ~ 0 then 1/E ~ a very large value, E << 1/E then 1/E is seen to dominate, so an agent A behaves as a cure or a resistance molecule:

Let's assume E ~ 0.00001 or 10-6 deformities per agent A 1/E = 10^6 agent A per deformities, i.e. the dose acts as a resistance dose and requires 10^6 agent A to cause a single deformity, hence fighting the disease.

System 2: Homeopathy

Homeopathy uses small doses of poisons which cause the very same diseases or condition to cure diseases. The proof for its efficacy is as follows:

let the quantity of poison be Q ml Q ml –has- N agents N agents cause 1 deformities Q' ml: Q × 10^-3 ml has: N × 10^-3 agents: 1 × 10^-3 deformities

Q': E = 10^-3 deformities: 1/E = 10^3 deformities^-1
1/E >> E

So, Q' becomes curative from lethal and cures the deformity, from the law of causation:

$$\mathrm{E} \;=\; \mathrm{C1} \times \mathrm{C2} \times .. \times \mathrm{Cn} \;=\; \mathrm{Ce} \qquad (74)$$
$$1 \,/\, E \;=\; 1 \,/\, Ce \qquad (75)$$
$$1/E \;>>\; E \;=>\; 1/Ce \;>>\; Ce \qquad (76)$$

1/Ce is the opposite of Ce and hence cures the deformity with it is dominating or being more than Ce.

System 3: Pharmacologically inert entities "A" Pharmacologically inert entities having E ~ 0 have the property: 1/E >> E, So A is curative being inert and cures the deformity, from the law of causation:

$$\mathrm{E} \;=\; \mathrm{C1} \times \mathrm{C2} \times .. \times \mathrm{Cn} \;=\; \mathrm{Ce} \qquad (77)$$
$$1 \,/\, E \;=\; 1 \,/\, Ce \qquad (78)$$
$$1/E \;>>\; E \;=>\; 1/Ce \;>>\; Ce \qquad (79)$$

1/Ce is the opposite of Ce and hence cures the deformity with it is dominating or being more than Ce when it contacts the deformity.

Conclusion

In conclusion, this work explores the concepts of "Existence", "1', "Infinito" and "0" and their mathematical foundations, revealing a controlling entity that governs all matter in the Universe. By deriving key principles like the "Law of Cause and Effect" and the "Law of Action and Consequence," we establish a framework for ensuring AI's ethical behaviour. The application of the "Law of Duality" to medicine provides new insights into medicinal systems. Through an ontology based on Sanskrit, we simplify complex concepts in physics and lay the groundwork for future advancements in AI and medicine. This work offers a fresh perspective on the laws governing the Universe.

References

1. Mehanathan, N. (2024, August). Existence and the Universe: The solution to the digital twin problem and how it leads to the matrix representation of the Universe and an understanding of how the Universe works. In AIP Conference Proceedings (Vol. 3149, No. 1). AIP Publishing.
2. Coward, H. G., & Raja, K. (n.d.). The philosophy of the grammarians (pp. 107-109).
3. The Sahityadarpana. (1997). Motilal Banarsidass Publishers (Pvt. Limited), p. 43. B R Jackson, T Pitman, and U S Patent, 2004.
4. A. C. Bhaktivedanta Swami Prabhupāda. (1972). Srimad Bhagavatam: with the original Sanskrit text, its roman transliteration, synonyms, translation and elaborate purports. New York, Bhaktivedanta Book Trust.

Structural and Morphological Properties of Free-Standing Cobalt Ferrite ($CoFe_2O_4$) Thin Films Via Liquid-Vapor Interfacial Method

Sanjeev Kumar[a], Rajesh Kumar[b]

Department of Physics and Astronomical Science, Central University of Himachal Pradesh, Kangra, Himachal Pradesh - 176206, India.

[a] sanjeevhpu2@gmail.com
[b] rajeshkumarf11@hpcu.ac.in

Abstract

Spinel ferrites-magnetic materials with unique crystal structures are widely used in various applications such as, spintronics devices, magnetic sensors, and high-density data storage. In this work, cobalt ferrite ($CoFe_2O_4$) thin films have been fabricated via liquid-vapor interfacial method, with an external magnetic field applied during the film formation. The films are formed without a substrate, which are freestanding and are grown in short span of time. The as formed $CoFe_2O_4$ thin films were transferred to glass substrates. Structural, morphological, and chemical bonding of the films have been analyzed by using X-ray diffraction (XRD), Field-emission scanning electron microscopy (FE-SEM), and Fourier-transform infrared spectroscopy (FTIR). The XRD reveals a crystalline growth, orientated in the direction of (220) plane. Lattice parameters appeared to be influenced by external magnetic field with crystallite size from 43.6 to 51.7 nm without and with the presence of external magnetic field, respectively. Surface topography of the films investigated by FE-SEM, indicates uniform thickness of the films. The FTIR analysis identified functional groups, metal-oxygen stretching vibrations (Fe-O, Co-O), bonding environment and cationic distribution.

Keywords: $CoFe_2O_4$, free-standing, NH_3 vapours, thin films.
Received 26 January 2025; First Review 11 February 2025; Accepted 16 February 2025

*** Address of correspondence**
Sanjeev Kumar
Department of Physics and Astronomical Science, Central University of Himachal Pradesh, Kangra, Himachal Pradesh - 176206, India.

Email: sanjeevhpu2@gmail.com

How to cite this article
Sanjeev Kumar, Rajesh Kumar, Structural and morphological properties of free-standing Cobalt Ferrite ($CoFe_2O_4$) thin films via liquid-vapor interfacial method, J. Cond. Matt. 2024; 02 (02): 74-77.

Available from:
https://doi.org/10.61343/jcm.v2i02.58

Introduction

Spinel ferrites (MFe_2O_4) due to their exceptional properties including optical, electrical, dielectric, magnetic, Curie temperature, permeability, and chemical stability have gained considerable attention. Their excellent resistance to oxidation and corrosion arises from their inherent stability and reliability in challenging environments, including chemical conditions [1]. The magnetic properties demonstrated by spinel ferrite have made them an essential candidate for modern devices such as spintronics [2] magnetic recording media [3], magnetic sensors [4], EMI shielding [5], and data storage [6]. The inherent high electrical resistivity and low eddy/dielectric loss make them useful in a variety of electrical devices, including telecommunication and microwave absorption [7-8]. The high Curie temperature allows them to maintain their intrinsic magnetic properties even at high temperatures [9] and is applicable for high-temperature applications such as, high-frequency transformers and microwave devices. The magnetism determined in spinel ferrites depends on the metal cation occupancies in the octahedral and tetrahedral sites with the coordination of oxygen atoms. These lattice sites are unequally distributed in crystallographic structure, with divalent metal cations (such as Co^{2+}, Ni^{2+}, Zn^{2+}, etc.) occupying the tetrahedral sites, and trivalent metal cations (such as Fe^{3+}) occupy the octahedral sites. In case, if all divalent metal ions are filled by the octahedral site, and the trivalent metal cations are partially in both the tetrahedral and octahedral sites are known as inverse spinel ferrites.

Various techniques and methods have been used to get a desired spinel ferrite material, in order to fulfil the specific requirements. Spinel ferrite-based thin films have the potential for miniaturization of modern technology devices in electronic industries, energy storage fields, and information technology as, switching devices, lithium-ion batteries [10], supercapacitors [11], magnetic sensors [12], data storage devices [6], etc. Many researchers have worked

on different metal ions such as Co, Ni, Mn, Mg, Cu, etc. based on spinel ferrite material. Among them, $CoFe_2O_4$ thin films have attracted considerable attention owing to their superior inherent properties. $CoFe_2O_4$ thin films have been fabricated by using various methods, such as thermal/electron beam evaporation system, spray pyrolysis, sol-gel, deep coating, sputtering, and molecular beam epitaxy. These methods require a specific substrate during film formation. Additionally, they also require expensive equipment and consume a lot of time to formation of the film. Here, we fabricate the thin films at a low cost with a self-devised method where the film can be formed in a very short span of time. In this work, free-standing, transferable $CoFe_2O_4$ thin films, offering enhanced flexibility for integration into various substrates have been formed. These films have been investigated for their structural and morphological properties.

Experimental Method

To formation $CoFe_2O_4$ thin films, 0.4 g of PVA was dissolved in distilled water for 1hr at 80 ˚C. Subsequently, a stoichiometric amount of $FeCl_3$ and $CoCl_2$ were also added to the PVA solution. The solution was stirred for the next 1 hr, which resulted in a transparent solution. After cooling the solution, a stoichiometric amount of solution was taken in a petri dish and placed inside the film formation chamber. Inside the chamber, a magnetic field on 1 tesla was applied to the petri dish. In order to form the film on the surface of the solution, a measured volume of NH_3 vapours was purged inside the reaction chamber, which was then kept closed for 15 minutes. The NH_3 vapours get react with the surface of the precursor solution which converted into a solid floating film. After formation, the film was taken on a glass substrate, which was sintered at 300 ˚C for 1 hour and investigated for structural and morphological properties.

Results and Discussion

XRD analysis

Figure 1(a) and (b) show XRD patterns of $CoFe_2O_4$ thin films prepared without and with external magnetic field applied in a normal direction to the surface of the solution, respectively. The film formed in the absence of magnetic field exhibits diffraction peaks at 2θ values of 18.5, 31.5, 35.6, and 43.7, corresponding to their (111), (220), (311), and (400) planes, respectively. These observed peaks are well matched with JCPDS card number 22-1086, confirming the cubic crystalline structure. The XRD pattern of the film fabricated with a normal to plane magnetic field is shown in figure 1(b), exhibits a single diffraction peak at angle 2θ corresponds to the plane (220). The specific orientation shows that the external magnetic field applied during film formation causes the crystallites within the film and aligns in a unidirectional manner, resulting in a preferred orientation along the plane (220).

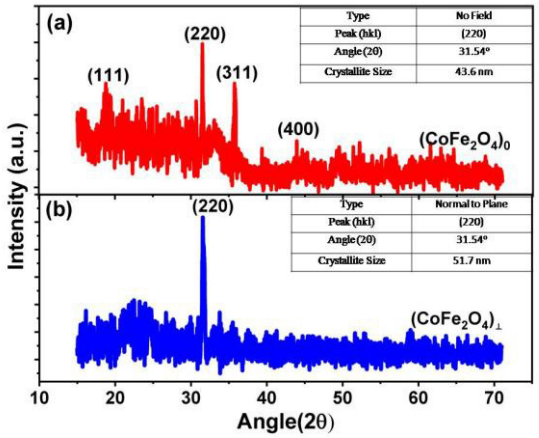

Figure 1: XRD pattern of $CoFe_2O_4$ thin films: **a.** XRD pattern of the film formed without applying magnetic field and **b** formed in the normal to plane direction of magnetic field during film formation.

The crystallite size of $CoFe_2O_4$ thin films is determined by using the Scherrer formula[13] represented as:

$$D = \frac{k\lambda}{\beta cos\theta}$$

Where D denotes the crystallite size in nanometer (nm), λ signifies the X-ray wavelength (1.54 Å), k represents the shape factor (k=0.9), θ indicates diffraction angle in degrees and β refers to the peak broadening at half of the maximum intensity of (220) diffraction peak. Scherrer's equation assumes spherical nanoparticle shapes, which may limit its accuracy when applied to non-spherical or irregularly shaped nanoparticles, as in the case of our thin films spherical nanoparticles. The average crystallite size is found to be 43.6 nm for the film formed without application of magnetic field, which increased to 51.7 nm in the presence of external magnetic field. The lattice constant in case of no magnetic field is 8.02 Å, which changed to 8.00 Å in the magnetic field. The slight reduction in the lattice constant under an external magnetic field is likely due to the directional arrangement of cations, leading to increased order and compactness, thereby causing minor lattice contraction.

FE-SEM analysis

Figure 2(a) displays the surface morphology of the $CoFe_2O_4$ thin film. The spherical-shaped nanoparticles can be seen uniformly distributed across the surface indicating a compact and homogeneous structure. In the figure 2(b), a cross-sectional FE-SEM image of the film, shows a dense layer without voids inside the film. The film possesses a uniform thickness of 152 nm, resulting from a precise control over the formation of thin film, revealing its structural homogeneity. Thus, the film exhibits a dense formation.

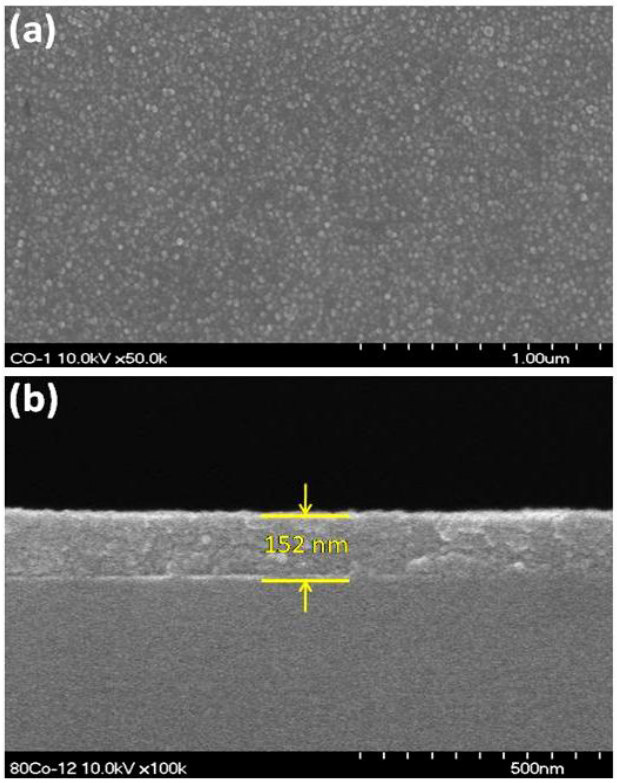

Figure 2: FE-SEM images of $CoFe_2O_4$ thin film: **a.** displays a top surface morphology, and **b.** shows cross-sectional surface of the film.

FTIR analysis

The examination of organic, inorganic functional groups and bonds formed in $CoFe_2O_4$ thin film analysed by the FTIR are shown in figure 3. The band arises around 495 cm^{-1} to 580 cm^{-1} corresponds to the stretching vibration of Fe-O metal ion bonds in the tetrahedral sites (Fe^{3+}). Similarly, the lower frequency band between 410 cm^{-1} and 485 cm^{-1} is attributed to the stretching vibration of Co-O metal-oxygen bond in the octahedral sites (Co^{2+}).

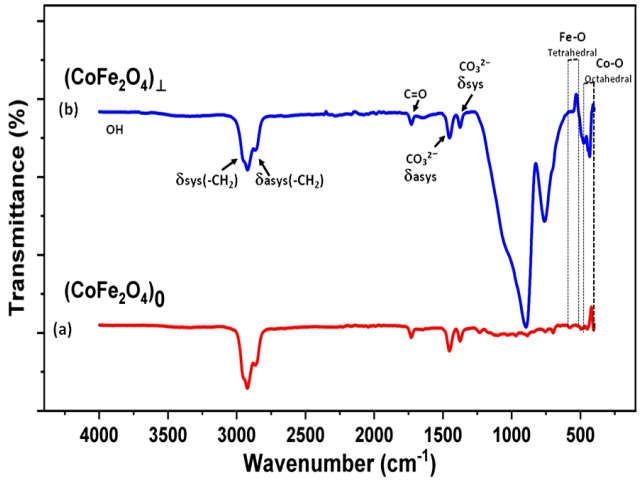

Figure 3: FTIR spectra of $CoFe_2O_4$ thin films: **a.** Spectra of the film formed without applying magnetic field and **b** formed in the normal to plane direction of magnetic field during film formation.

Graph 3(a) represents the lower intensity at a lower wave number of $CoFe_2O_4$ film spectra, fabricated without applying magnetic field during formation. When external magnetic field is applied, it influences the orientation of Fe^{3+} and Co^{2+} cations within the tetrahedral and octahedral sites, leading to enhanced band intensity and improved structural stability at lower wave numbers. Additionally, the bands observed at 1375 cm^{-1}, 1451 cm^{-1} 1734 cm^{-1} indicate the presence of symmetric and asymmetric stretching vibrations of carbonate (CO_3^{2-}) groups as well as carbonyl stretching vibrations (C=O) at surface of the film. These bands may result from surface contaminations such as the existence of carbonation on the surface of films as a result of the adsorption of atmospheric CO_2 and reacting with residual hydroxyl groups. Furthermore, the carbonyl vibrations indicate oxidation by-products or organic residues may form during the films formation process. The bands arise at 2862 cm^{-1}, 2931 cm^{-1}, and 3660 cm^{-1} suggesting the presence of symmetric, asymmetric stretching vibrations of hydrocarbon and O-H stretching, from adsorbed water molecules on the surface of the film. These surface contaminants slightly change the chemical composition and affect its functional properties. From the FTIR spectra, these bands are the evidences of the formation of $CoFe_2O_4$ films.

The ferromagnetic $CoFe_2O_4$ has an inverse spinel structure and is interesting because it has a high coercivity, high magneto crystalline anisotropy, and moderate saturation magnetization. The magnetic behaviour of freestanding $CoFe_2O_4$ thin films is expected to be influenced by the formation methods, particularly in the presence and absence of an external magnetic field during growth of the film. The films fabricated without an external magnetic field should have isotropic magnetic characteristics, owing to domains aligned randomly to reduce magnetostatic energy. Similarly, in the absence of a substrate, strain-induced anisotropy is expected to be eliminated, leaving magneto crystalline and shape anisotropy as the predominant factors. In case, the films are grown in an external magnetic field, the magnetic moments must be aligned along the magnetic field direction. Therefore, film grown in normal of magnetic field should have substantial perpendicular magnetic anisotropy.

Conclusion

$CoFe_2O_4$ films are formed without and with applying magnetic field successfully on the surface of glass substrate. XRD study confirms the formation of cubic spinel crystal structure of $CoFe_2O_4$ films. The average crystallite size of the films increases and lattice constant decreases with the

application of external magnetic field during formation. The FE-SEM reveals that the film consists of uniformly distributed, spherical grains forming a dense, continuous layer without discontinuities. FTIR spectroscopy confirms the presence of various functional groups and metal-oxygen cations associated with tetrahedral and octahedral sites of the as - formed $CoFe_2O_4$ films can be proposed for spintronic and magnetic storage applications.

References

1. Z. M. Abdulhamid et al., *"Synthesis, characterization, and preliminary insights of ZnFe2O4 nanoparticles into potential applications, with a focus on gas sensing"*, Sci Rep, vol. 13, no. 1, pp. 1-16, Nov. 2023, https://doi.org/10.1038/s41598-023-46960-w.
2. X. Y. Zheng et al., *"Ultra-thin lithium aluminate spinel ferrite films with perpendicular magnetic anisotropy and low damping"*, Nat Commun 2023 141, vol. 14, no. 1, pp. 1-7, Aug. 2023, https://doi.org/10.1038/s41467-023-40733-9.
3. M. Kurian and S. Thankachan, *"Structural diversity and applications of spinel ferrite core - Shell nanostructures -A review"*, Open Ceram, vol. 8, p. 100179, Dec. 2021, https://doi.org/10.1016/J.OCERAM.2021.100179.
4. F. Tudorache, P. D. Popa, M. Dobromir, and F. Iacomi, *"Studies on the structure and gas sensing properties of nickel-cobalt ferrite thin films prepared by spin coating"*, Mater Sci Eng B, vol. 178, no. 19, pp. 1334-1338, Nov. 2013, https://doi.org/10.1016/J.MSEB.2013.03.019.
5. M. Liu et al., *"A popcorn-inspired strategy for compounding graphene@NiFe2O4 flexible films for strong electromagnetic interference shielding and absorption"*, Nat Commun 2024 151, vol. 15, no. 1, pp. 1-14, Jun. 2024, https://doi.org/10.1038/s41467-024-49498-1.
6. K. Gayakvad, K. Somdatta, V. Mathe, T. Dongale, M. W, and K. Patankar, *"Spinel ferrites for resistive random access memory applications"*, Emergent Mater, vol. 7, no. 1, pp. 103-131, Feb. 2024, https://doi.org/10.1007/S42247-023-00576-Y/FIGURES/14.
7. Kiran, S. Kumar, and N. Thakur, *"Structural, dielectric, and magnetic properties of reduced graphene oxide-wrapped $MnFe_2O_4$ composites synthesized by in-situ sol-gel auto combustion method"*, Ceram Int, vol. 48, no. 4, pp. 4444-4455, Feb. 2022, https://doi.org/10.1016/J.CERAMINT.2021.10.138.
8. Y. Slimani et al., *"Magnetic and microwave properties of $Co_{0.5}Ni_{0.5}Fe_{2-x}Sc_xO_4$ ($0.0 \leq x \leq 0.1$) nanosized spinel ferrites"*, Inorg Chem Commun, vol. 151, p. 110574, May 2023, https://doi.org/10.1016/J.INOCHE.2023.110574.
9. J. L. Ortiz-Quiñonez, U. Pal, and M. S. Villanueva, *"Structural, Magnetic, and Catalytic Evaluation of Spinel Co, Ni, and Co-Ni Ferrite Nanoparticles Fabricated by Low-Temperature Solution Combustion Process"*, ACS Omega, vol. 3, no. 11, pp. 14986-15001, Nov. 2018, https://doi.org/10.1021/acsomega.8b02229.
10. Y. Q. Chu, Z. W. Fu, and Q. Z. Qin, *"Cobalt ferrite thin films as anode material for lithium-ion batteries"*, Electrochim Acta, vol. 49, no. 27, pp. 4915-4921, Oct. 2004, https://doi.org/10.1016/J.ELECTACTA.2004.06.012.
11. V. A. Jundale, D. A. Patil, G. Y. Chorage, and A. A. Yadav, *"Mesoporous cobalt ferrite thin film for supercapacitor applications"*, Mater Today Proc, vol. 43, pp. 2711-2715, 2020, https://doi.org/10.1016/J.MATPR.2020.06.204.
12. A. B. Abou Hammad and A. M. El Nahrawy, *"Spinel Sensors and Biosensors"*, Handb Nanosensors, pp. 427-459, 2024, https://doi.org/10.1007/978-3-031-47180-3-34.
13. A. L. Patterson, *"The Scherrer Formula for X-Ray Particle Size Determination"*, Phys Rev, vol. 56, no. 10, p. 978, Nov. 1939, https://doi.org/10.1103/PhysRev.56.978.

Synthesis and Characterization of Nanocrystalline $MgFe_2O_4$ for Multifaceted Applications

K K Palsaniya[1,a], S R Choudhary[1], P M Saini[1], Anchal[1], S N Dolia[2], P A Alvi[1], B L Choudhary[1,b]

[1] *Department of Physics, Banasthali Vidyapith, Banasthali-304022, Rajasthan, India.*
[2] *Department of Physics, University of Rajasthan, Jaipur-304022, India*

[a] kamlesh.palsania.4871@gmail.com
[b] blcphysics@gmail.com

Abstract

A polycrystalline $MgFe_2O_4$ ferrite sample was successfully synthesized using the sol-gel process. X-ray diffraction measurements and analysis confirmed the single-phase formation of a nanocrystalline cubic spinel structure without impurity phases. The lattice parameters, refined via the Rietveld method, was determined to be 8.38 Å, and the crystallite size was found to be approximately 12nm using the Debye-Scherrer method. FTIR measurement revealed a prominent peak at 3710 cm^{-1} corresponding to the O–H vibrational mode, alongside a weak shoulder at 3200–3270 cm^{-1} attributed to O–H elongating vibrations of adsorbed H_2O molecules. A weak peak at 2364 cm^{-1} was assigned to nitrate groups. These results confirm the successful synthesis and nanoscale characterization of $MgFe_2O_4$ with distinct structural and vibrational properties.

Keywords: Ferrite, XRD, FTIR, Rietveld, Sol-Gel.
Received 22 January 2025; First Review 21 February 2025; Accepted 22 February 2025

*** Address of correspondence**
K K Palsaniya
Department of Physics, Banasthali Vidyapith, Banasthali-304022, Rajasthan, India.

Email: kamlesh.palsania.4871@gmail.com

How to cite this article
K K Palsaniya, S R Choudhary, P M Saini, Anchal, S N Dolia, P A Alvi, B L Choudhary, Synthesis and Characterization of Nanocrystalline $MgFe_2O_4$ for Multifaceted Applications, J. Cond. Matt. 2024; 02 (02): 78-80.

Available from:
https://doi.org/10.61343/jcm.v2i02.67

Introduction

Spinel ferrites have drawn significant interest owing to their versatile chemical and physical properties, which make them suitable for numerous technological applications. Magnesium ferrite ($MgFe_2O_4$), a prominent member of the general formula of spinel ferrite family MFe_2O_4 (where M represents divalent cations like Mg^{2+}, Mn^{2+}, Zn^{2+}, Ni^{2+}, Co^{2+}, or Cd^{2+}), exhibits an inverse spinel cubic structure.

Achieving the synthesis of ferrite nanoparticles with precise control over particle size distribution, uniform morphology, and reduced agglomeration remains a significant challenge to meet the needs of advanced applications. Importantly, ferrite nanoparticles exhibit enhanced electrical and magnetic properties compared to their microscale counterparts. In recent years, magnesium ferrite nanoparticles have gained significant interest for their potential applications in semiconductors, low-magnetic materials, hyperthermia therapy, and gas sensors.

Synthesis Method

The polycrystalline $MgFe_2O_4$ ferrite sample was synthesized via the sol-gel method, a commonly utilized and efficient approach for nanoparticle fabrication [1-5]. Analytical-grade reagents were employed, with $[Mg(NO_3)_2 \cdot 6H_2O]$ and $[Fe(NO_3)_3 \cdot 9H_2O]$ serving as metal ion precursors. Citric acid was used as a chelating agent to enhance metal ion complexation and improve solution stability. The nitrates and citric acid were measured in stoichiometric ratios and dissolved in a solvent within a beaker. The solution was stirred continuously for 30 minutes using a magnetic stirrer. To achieve a pH of approximately 10, ammonia was added dropwise, with the pH maintained within the range of 10–12 to promote particle size reduction. The addition of ammonia induced a color change, signifying the initiation of gel formation during constant heating and stirring. The resulting gel was subsequently dried, and the obtained nano powder was finely ground using a mortar and pestle. The complete process for $MgFe_2O_4$ ferrite is depicted in Figure 1.

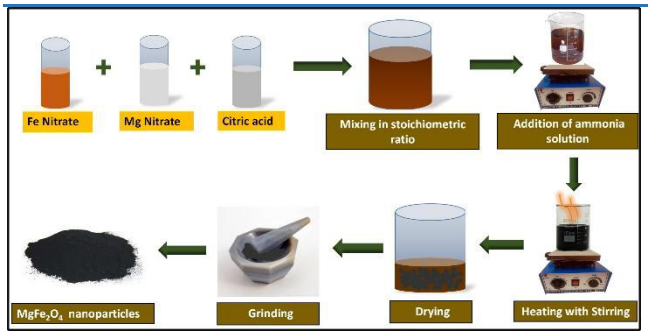

Figure 1: Synthesis procedure of $MgFe_2O_4$ nanoparticles.

Results and discussion

To determine the crystal structure and size, the XRD technique was used. Structural analysis of the synthesized $MgFe_2O_4$ sample was performed using an XRD (Bruker D8 Advance) used with a CuKα source (λ = 1.5406 Å). X-ray data were measured at 300K temperature over a 2θ range of 20°–70°. The diffraction peaks established the formation of a cubic spinel single-phase structure.

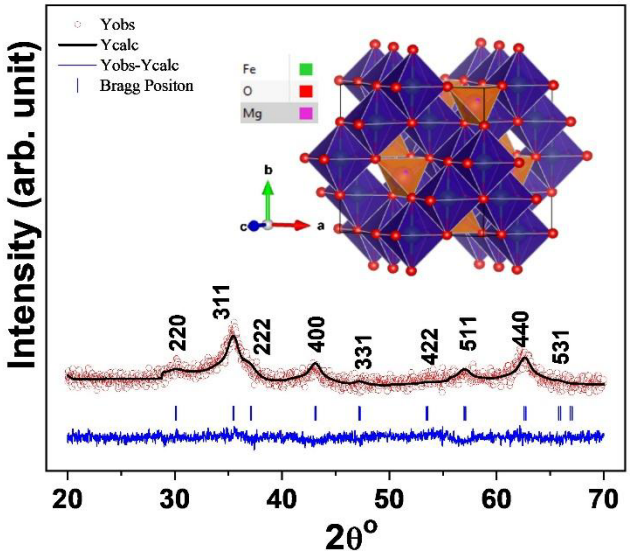

Figure 2: XRD pattern with crystal structure of $MgFe_2O_4$.

The lattice constant, refined using the Rietveld method, was determined to be 8.38 Å, as shown in Figure 2. Investigation of the XRD pattern also established the nanocrystalline nature of the sample, with no additional or impurity peaks observed. the Debye-Scherrer method was used for the crystallite size, based on the FWHM of XRD peaks, and was found to be approximately 12 nm. The broad peaks in the diffraction patterns further validate the nanoscale dimensions of the particles. The FTIR spectrum shown in Figure 3 reveals a prominent peak at 3710 cm^{-1}, corresponding to the O–H vibrational mode. A weak shoulder at 3200–3270 cm^{-1} is associated with the O–H vibrations of adsorbed H_2O molecules. Vibrational modes of adsorbed, free, or corresponding anions, along with twisting vibrations of actually interlayer and adsorbed H_2O molecules, are detected in the 2500–1000 cm^{-1} range.

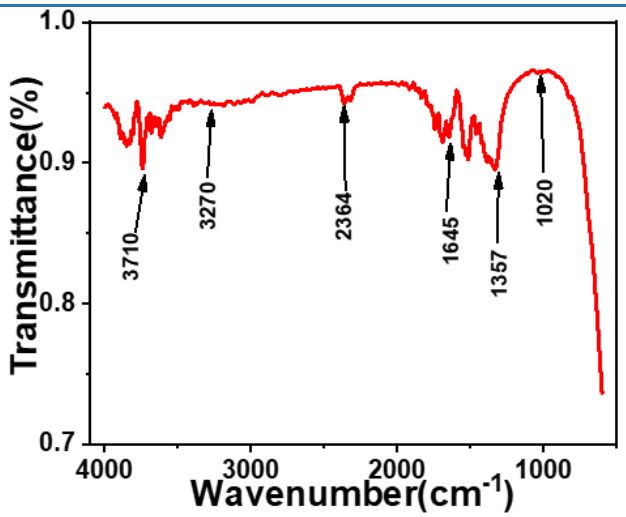

Figure 3: FTIR Spectrum of nanocrystalline $MgFe_2O_4$ Ferrite.

A twisting vibration of H_2O molecules appears at 1645 cm^{-1}, while a weak peak at 2364 cm^{-1} is accredited to nitrate groups. Additionally, a berm at 1357 cm^{-1} (ν_3 irregular stretching) and feeble peaks at 1020 cm^{-1} (ν_1 proportional stretching), 830 cm^{-1} (ν_2 out-of-plane bending), and 690–696 cm^{-1} (ν_4 scissoring distortion) correspond to the fundamental vibrational modes of NO_3^- ions derived from the initial nitrate salts.

Conclusion

The polycrystalline $MgFe_2O_4$ ferrite sample was successfully produced via the sol-gel procedure. X- ray investigation confirmed the creation of a nanocrystalline cubic spinel construction, with no other impurity phases in the sample. The lattice constant, refined using the Rietveld method, was found to be 8.38 Å, and the crystallite size was assessed to be around 12 nm using the Debye-Scherrer method. FTIR analysis showed a prominent peak at 3710 cm^{-1}, corresponding to the O–H vibrational mode, along with a weak shoulder at 3200–3270 cm^{-1}, associated with the O–H elongating vibrations of adsorbed and H_2O molecules. Additionally, a weak peak at 2364 cm^{-1} was attributed to nitrate groups. These findings confirm the successful synthesis and characterization of nanoscale $MgFe_2O_4$ with distinctive vibrational properties.

References

1. Choudhary, B. L., Kumari, N., Kumari, J., Kumar, A., Dolia, S. N., *"Relaxation mechanism in $Ni_{0.5}Zn_{0.5}Fe_2O_4$ nanocrystalline ferrite at a lower temperature"*, Mater Lett. 304, 130731 (2021).
2. Palsaniya, K. K., Kumari, N., Dolia, S. N., Alvi, P. A., Choudhary, B. L., *"Tailoring quantum dots through citric acid modulation of $CoFe_2O_4$ ferrite"*, Mater Chem Phys. 313, 128820 (2024).

3. Anchal, Sarita, Palsaniya, K. K., Priya, Kumari, N., Dolia, S. N., Alvi, P. A., Choudhary, B.L., *"Tailoring quantum dots through citric acid modulation of $CoFe_2O_4$ ferrite"*, Mater Chem Phys. 313, 128820 (2024).
4. Kumari, N., Sarita, Anchal, Priya, Palsaniya, K. K., Beniwal, R. K., Choudhary, S. R., Rulaniya, M. S., Saini, P. M., Dolia, S. N., Alvi, P. A., Choudhary, B. L., *"The role of citric acid for formation of nanocrystalline $MnFe_2O_4$ ferrite"*, Applied Physics A. 130, 266 (2024).
5. Beniwal, R. K., Rulaniya, M. S., Saini, P. M., Yadav, P., Kumar, U., Alvi, P. A., Choudhary, B. L., *"Development and characterization of superparamagnetic Zn-Doped Nickel ferrite nanoparticles"*, J Magn Magn Mater. 610, 172547 (2024).

Study on Optical and Structural Properties of TiO_2/SnO_2 Thin Film for Optical Devices

Ved Prakash Meena[1,a], S S Sharma[2,b], M K Jangid[1,c]

[1] *Department of Physics, Vivekananda Global University, Jaipur, Rajasthan-303012, India.*
[2] *Department of Physics (H & S), Govt. Mahila Engineering College, Ajmer, Rajasthan-305002, India*

[a] vedprakash1581997@gmail.com
[b] shyam@gweca.ac.in
[c] mahesh.jangid@vgu.ac.in

Abstract

The TiO_2/SnO_2 thin films have garnered considerable attention for their application in optical devices due to their superior transparency and stability. This study investigates the optical and structural properties of TiO_2/SnO_2 thin films prepared through electron beam (e-beam) evaporation. The films were annealed at 400 °C for one hour in a muffle furnace to evaluate the influence of annealing on their properties. Characterization techniques, including X-ray diffraction (XRD), UV-Vis spectroscopy, and atomic force microscopy (AFM), were employed to analyze the films. XRD analysis confirmed the presence of a distinct anatase TiO_2 phase with SnO_2 inclusions. Post-annealing, an enhancement in the peak intensities of both phases was observed, signifying improved crystallinity and atomic ordering. UV-Vis spectroscopy revealed that the annealed films exhibited reduced optical absorbance compared to their pristine counterparts. Furthermore, the optical bandgap increased from 4.10 eV for the pristine films to 4.32 eV after annealing. In AFM analysis 2D and 3D surface topographical images demonstrated that the annealed films show a smoother surface with reduced roughness, attributed to the enhanced crystallinity, which mitigates structural defects and grain boundary irregularities. These findings highlight the exceptional optical and structural characteristics of TiO_2/SnO_2 thin films, suggesting their potential for use in antireflective coatings, photodetectors, and waveguide structures in optoelectronic devices.

Keywords: Thin film; E-Beam; XRD; UV-Vis; AFM.
Received 27 January 2025; First Review 22 February 2025; Accepted 22 February 2025

*** Address of correspondence**
Ved Prakash Meena
Department of Physics, Vivekananda Global University, Jaipur, Rajasthan-303012, India.

Email: vedprakash1581997@gmail.com

How to cite this article
Ved Prakash Meena, S S Sharma, M K Jangid, Study on Optical and Structural Properties of TiO_2/SnO_2 Thin Film for Optical Devices, J. Cond. Matt. 2024; 02 (02): 81-85.

Available from:
https://doi.org/10.61343/jcm.v2i02.65

Introduction

Titanium dioxide (TiO_2) stands out as one of the most extensively utilized semiconductors due to its numerous advantageous physicochemical properties. These include its abundance, affordability, biocompatibility, chemical stability, and resistance to corrosion [1]. As a result, TiO_2 finds application in diverse fields. However, a major limitation of TiO_2 as a photocatalyst is its high electron-hole recombination rate, which reduces its efficiency [2-3]. To address this, coupling TiO_2 with other semiconductors has proven to be an effective strategy. Tin oxide (SnO_2), despite its wide band gap of 3.8 eV, has been successfully employed in combination with TiO_2. This can be achieved either by doping TiO_2 with tin ions or by creating TiO_2-SnO_2 composites [4-7]. The development of advanced materials for optical devices has been a key factor driving technological progress in modern optoelectronics. Because of their remarkable optical transparency, stability, and adjustable qualities, thin films based on titanium dioxide (TiO_2) and tin dioxide (SnO_2) have become attractive options among these materials. Particularly, the TiO_2/SnO_2 thin films have earned interest due to its possible uses in waveguide structures, photodetectors, and antireflective coatings, among other optical devices. These uses make use of the distinct optical and structural properties of SnO_2 and TiO_2, which can be further improved by post-deposition treatments and material engineering [8-9]. A well-known substance, titanium dioxide has a broad bandgap, robust photocatalytic activity, and good optical transmittance in the visible spectrum [10-11]. Applications needing high transparency and low absorption losses commonly use it [12]. Tin dioxide, a semiconductor with a wide bandgap of 3.6 eV, is also a perfect complimentary material for creating composite thin films because of its strong chemical stability, high electrical conductivity, and optical

transparency [13-14]. It has been demonstrated that combining TiO_2 and SnO_2 into a thin-film system improves overall material stability, decreases optical losses, and strengthens light-matter interactions [15]. Researchers have synthesized TiO_2/SnO_2 thin films using various deposition techniques, including sol-gel processing, electron-beam evaporation, and chemical vapor deposition. Optimizing the optical and structural properties of films requires precise control over their composition, thickness, and homogeneity, all of which may be achieved using electron-beam evaporation technique [16]. The annealing process is one important element affecting these thin films' performance. The heat process of annealing has a major impact on the material's defect density, grain structure, and crystallinity. By increasing their crystallinity and decreasing defects, annealing TiO_2/SnO_2 films at optimal temperatures enhances their optical characteristics, including transparency and bandgap tunability [17]. According to recent studies, annealing can result in a small shift in the optical bandgap and a decrease in visible spectrum absorption, both of which are signs of enhanced material quality [18-19]. The TiO_2/SnO_2 thin films' structural characteristics are also crucial in evaluating whether or not they are appropriate for use in optical devices. The existence of SnO_2 inclusions, which further enhance the structural stability and performance of the film, and the anatase phase of TiO_2, which is linked to enhance optical and photocatalytic capabilities, have been discovered by X-ray diffraction (XRD) investigations. The film's functionality in optoelectronic devices is improved by annealing, which refines grain boundaries and reduces imperfections, boosting the film's ability to propagate light efficiently [20-21]. This research seeks to thoroughly explore the impact of the annealing process on the optical and structural characteristics of TiO_2/SnO_2 thin films. The results are expected to suggest valuable insights for enhancing the performance of TiO_2/SnO_2 thin films in various optoelectronic devices.

Experimental

TiO_2/SnO_2 thin films with a thickness of 300 nm were deposited onto glass substrates through the electron-beam deposition method. High-purity titanium dioxide (TiO_2, 99.99%) and tin dioxide (SnO_2, 99.98%) were employed as source materials for film preparation. Equal weight ratios of these oxides were thoroughly blended using high-energy planetary ball milling to ensure uniform mixing. The milling process was carried out for 5 hours, resulting in a homogenous powder mixture. This powder was then dried and compressed into pellets under a biaxial pressure of 10 tons. The thin films were deposited using an e-beam deposition system (Model BC-300 HHV). A vacuum chamber was utilized, which was evacuated to a base pressure of approximately 10^{-5} mbar with the help of rotary and diffusion pumps. The substrate temperature remained at room temperature throughout the process. The target to substrate distance was fixed at 35 cm. To study the effect of annealing temperature, the prepared samples were annealed at 400 °C for one hour in a muffle furnace. For structural characterization, X-ray diffraction (XRD) was performed at room temperature using a Panalytical X'Pert Pro diffractometer with CuKα radiation (λ = 0.15406 nm) to determine the phases present. The optical properties of the thin films were examined using UV-Vis absorption spectroscopy (Shimadzu UV-1800) across a wavelength range of 200-800 nm. Surface topography was analyzed using Atomic Force Microscopy (AFM). Both 2D and 3D images of the thin films were obtained with a Bruker Multimode Scanning Probe.

Results and Discussion

XRD analysis

Figure 1 shows the X-ray diffraction patterns of pristine and annealed TiO_2/SnO_2 thin films. In the TiO_2/SnO_2 samples, distinct peaks corresponding to TiO_2 were observed at 2θ = 25.47°, 38.19°, and 78.97°, which are indexed to the (101), (004), and (224) planes of anatase-phase TiO_2 (JCPDS No. 21-1272). These peaks indicate that the anatase phase is the predominant crystalline structure in the film, demonstrating strong crystallinity, consistent with earlier reports on TiO_2 thin films [22-23]. For SnO_2, diffraction peaks were identified at 2θ = 51.97°, 58.05°, 66.24°, and 71.51°, corresponding to the (221), (310), (301), and (220) planes of rutile-phase SnO_2 (JCPDS No. 41-1445). These peaks confirm the polycrystalline nature of SnO_2 and validate its successful incorporation into the composite thin film, aligning with findings from previous studies [24-25]. After annealing, an improvement in the peak intensities of both TiO_2 and SnO_2 was observed, indicating enhanced crystallinity and better atomic ordering within the thin films. The annealing effects have been broadly reported to facilitate the reorganization of atoms and reduction of structural defects in thin films, leading to sharper and more intense diffraction peaks. This effect is particularly prominent in mixed oxide systems like TiO_2/SnO_2, where thermal treatment promotes the growth of crystalline domains and strengthens the diffraction signals associated with the respective phases. Furthermore, annealing may also influence the redistribution of oxygen vacancies and stoichiometric balance in the film, additional contributing to the improved peak intensity. Such enhancements are consistent with studies where annealing has been shown to significantly improve the structural properties and crystallinity of oxide thin films [26-27]. The properties and applications of thin films are highly influenced by their structural parameters. To analyze these parameters, the

crystallite size (D), microstrain (ε), and dislocation density (δ) can be determined using the following equations:

The crystallite size (D) can be estimated from the peaks of the XRD diffractogram using Scherrer's formula [28]:

$$D = \frac{K\lambda}{\beta\cos\theta} \qquad (1)$$

The dislocation density (δ), which represents the length of dislocation lines per unit volume ($Å^{-2}$) of the crystal, was calculated using the formula [29]:

$$\delta = \frac{1}{D^2} \qquad (2)$$

The lattice strain (ε) is derived from Scherrer's relation [30]:

$$\varepsilon = \frac{\beta}{4\tan\theta} \qquad (3)$$

Here, K is a geometrical factor with a value of 0.9, λ=1.5406 A˚ is the X-ray wavelength (Cu Kα radiation, equivalent to 0.154 nm), β is the full width at half maximum (FWHM) of the primary diffraction peaks, and θ is the Bragg diffraction angle.

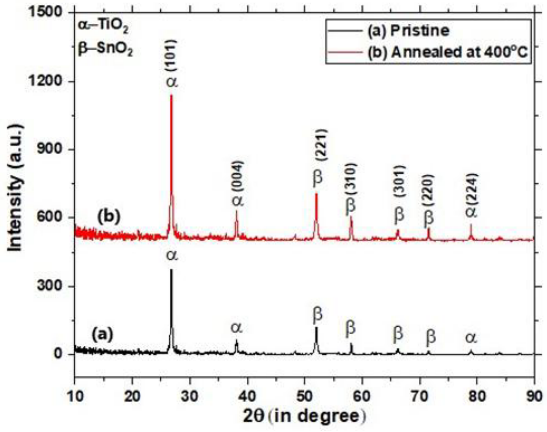

Figure 1: XRD pattern of (a) pristine and (b) annealed TiO_2/SnO_2 thin films

Table 1: Structural parameters of TiO_2/SnO_2 thin films

Sample	2θ	β	D (Å)	ε (×10^{-3})	δ (10^{16}/ m^2)
Pristine	25.47	0.236	6.02	260.77	275.94
Annealed at 400 ˚C	25.47	0.117	12.15	129.28	67.74

Table 1 provides the structural parameters of TiO_2/SnO_2 thin films, highlighting the effects of annealing at 400 °C. The diffraction angle (2θ) remains unchanged at 25.47° for both pristine and annealed samples. However, annealing reduces the Full Width at Half Maximum (FWHM) from 0.236 to 0.117, indicating a growth in crystallite size (D) from 6.02 Å to 12.15 Å. This signifies improved crystal quality. Simultaneously, lattice strain (ε) decreases from 260.77 × 10^{-3} to 129.28 × 10^{-3}, and dislocation density (δ) drops from 275.94 × 10^{16}/m² to 67.74 × 10^{16}/m², reflecting reduced structural defects post-annealing.

Optical Properties

Figure 3 presents the optical absorption spectra of TiO_2/SnO_2 thin films, highlighting the distinct differences in absorption between pristine and annealed samples. The data reveal that the annealed TiO_2/SnO_2 films exhibit lower optical absorbance compared to their pristine counterparts. This reduction in absorbance upon annealing is associated with modifications in structural and optical properties. Annealing is essential for enhancing the crystallinity of thin films. It helps minimize defects, including dislocations and grain boundaries. This often act as scattering centers for light. As a result, annealed TiO_2/SnO_2 thin films show enhanced optical transmittance, enabling more efficient light penetration through the material [31]. Furthermore, the annealing process contributes to better alignment of the film's crystal structure, thereby facilitating improved light-harvesting capabilities by minimizing non-radiative recombination of charge carriers [32]. These properties make annealed TiO_2/SnO_2 thin films more suitable for applications in optoelectronics, photovoltaics, and photocatalysis [33-34].

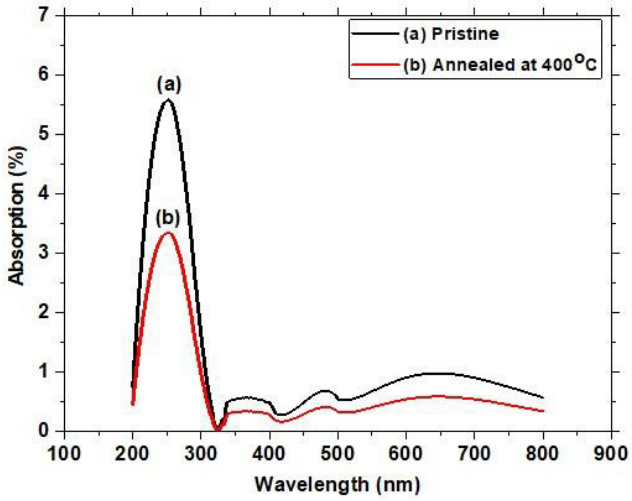

Figure 2: Absorption spectra of (a) pristine and (b) annealed TiO_2/SnO_2 thin films

The bandgap energy for the films was determined using the Tauc relation [35], which is expressed as:

$$\alpha h\nu = A(h\nu - E_g)^m \qquad (4)$$

where h is Planck's constant, ν is the photon frequency, α is the absorption coefficient derived from the absorbance data, E_g is the bandgap energy, and m is the power factor of the transition mode. For direct transitions, m equals 0.5 was used to calculate the bandgap.

The study reveals a notable increase in the optical bandgap of TiO_2/SnO_2 thin films upon annealing, shifting from 4.10 eV for the pristine films to 4.32 eV for the annealed ones. This bandgap widening is closely linked to the annealing process, which improves the crystallinity of the films and reduces the density of localized states at grain boundaries [36-37].

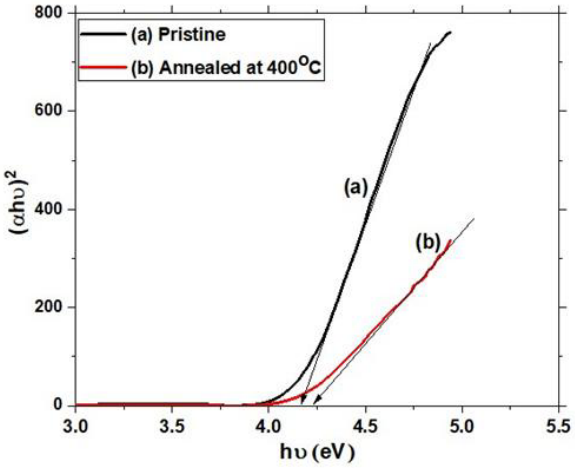

Figure 3: Tauc plots of (a) pristine and (b) annealed TiO_2/SnO_2 thin films

These localized states, typically caused by structural imperfections, contribute to sub-bandgap energy levels that facilitate undesired light absorption. By minimizing these defects, annealing effectively sharpens the band edge, resulting in a higher optical bandgap. The increased bandgap and refined absorption properties make annealed TiO_2/SnO_2 films highly suitable for applications requiring wide-bandgap materials. For instance, they hold promise as efficient UV photodetectors due to their selective sensitivity to ultraviolet light while maintaining transparency in the visible spectrum. They also show promise as transparent conducting oxides (TCOs). This makes them suitable for applications in optoelectronic devices. TCOs require high optical transparency and conductivity, both of which are enhanced by the annealing-induced structural improvements in TiO_2/SnO_2 films [38-39].

AFM Analysis

AFM is a vital way for investigating the surface topography of thin films with nanometer-scale resolution, offering insights into the structural and functional properties of the materials. Figure 4 depicts the AFM images of TiO_2/SnO_2 thin films in their (a) pristine and (b) annealed states. The analysis reveals that both films exhibit a granular and uniform surface morphology, indicative of densely packed nanostructures [40-41].

Upon annealing, significant changes in the surface properties are observed. The annealed TiO_2/SnO_2 thin films display a smoother surface with reduced roughness compared to the pristine films. This reduction in surface roughness is attributed to the enhanced crystallinity induced by annealing, which minimizes structural defects and grain boundary irregularities. Such improvements in surface uniformity are crucial for optimizing the optical and electronic performance of the films [42]. The densely packed nanostructures observed in the AFM images contribute to the films' optical clarity and efficient light management, essential for applications in optoelectronic devices. Furthermore, the smoother and more uniform surface after annealing enhances film stability and charge transport, making these films promising candidates for use in high-performance photovoltaics, UV photodetectors, and transparent conductive oxides [43].

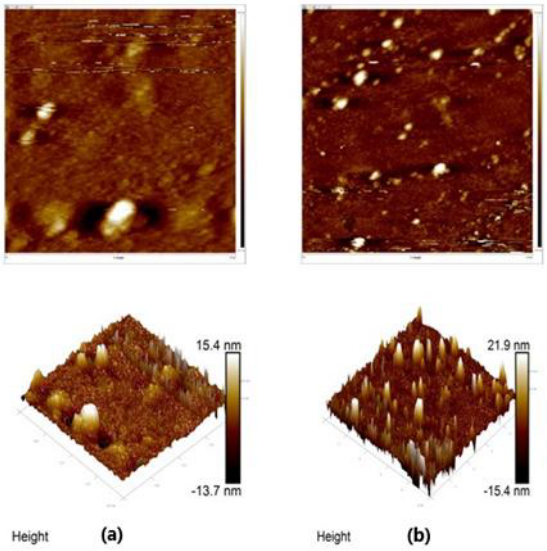

Figure 4: AFM 2D and 3D images of (a) pristine and (b) annealed TiO_2/SnO_2 thin films

Conclusion

The study of TiO_2/SnO_2 thin films provides valuable insights into the impact of annealing temperature on their structural and optical characteristics. Post-annealing XRD patterns indicate stability in the crystalline structure, suggesting minimal introduction of stress or defects during the process. Notably, annealing at 400 °C results in significant bandgap enhancement, increasing from 4.15 eV to 4.34 eV. This improvement is attributed to enhanced crystallinity, reduced defects such as oxygen vacancies, and improved interfacial properties. These modifications are crucial for optimizing the functionality of TiO_2/SnO_2 thin films in applications such as UV detectors, transparent conductive oxides, and photocatalysis. Furthermore, AFM analysis reveals that annealing substantially affects surface morphology. The annealed TiO_2/SnO_2 thin films show a smoother surface with reduced roughness compared to the pristine films. This study emphasizes the essential role of annealing temperature in fine-tuning the properties of TiO_2/SnO_2 thin films, identifying 400 °C as the optimal

temperature for achieving superior performance in advanced technological applications.

Acknowledgements

The authors (Specially Ved Prakash Meena) are highly thankful to UGC for providing financial support under JRF scheme to carry out this work. They also express their gratitude to the Material Science Laboratory developed at Government Mahila Engineering College, Ajmer under TEQIP-II and Material Research Centre, MNIT Jaipur (India) for providing experimental and measurement facilities.

References

1. J Coronado, F Fresno, M Hernández-Alonso, R Portela, S Suárez, S García Rodríguez, and V de la Peña O'Shea. Design of Advanced Photocatalytic Materials for Energy and Environmental Applications. 2013.
2. M R D Khaki, M S Shafeeyan, A A A Raman, and W M A W Daud. J. Environ. Manag., 198:78–94, 2017.
3. V Kumaravel, S Mathew, J Bartlett, and S C Pillai. Appl. Catal. B Environ., 244:1021–1064, 2019.
4. H Tada, A Hattori, Y Tokihisa, K Imai, N Tohge, and S Ito. J. Phys. Chem. B, 104:4585–4587, 2000.
5. K Awa, R Akashi, A Akita, S ichi Naya, H Kobayashi, and H Tada. Chem. Phys. Chem., 20:2155–2161, 2019.
6. W Sangchay. Energy Procedia, 89:170–176, 2016.
7. A Kusior, L Zych, K Zakrzewska, and M Radecka. Appl. Surf. Sci., 471:973–985, 2019.
8. M Gülkı, Y Yılmaz, and T Aydogan. Appl. Surf. Sci., 554:149610, 2021.
9. M K Jangid, S Sharma, V P Meena, V P Arya, and S S Sharma. Evergreen, 11:178-185, 2024.
10. L Zhang, Y Wang, and H Zhao. Mater. Today Chem., 17:100303, 2020.
11. M K Jangid, S P Nehra, and M Singh. AIP Conf. Proc., 1393:311-312, 2011.
12. A Fujishima, K Honda, and S Kikuchi. Nature, 238:37–38, 1972.
13. C G Granqvist. Sol. Energy Mater. Sol. Cells, 91:1529–1598, 2007.
14. M K Jangid and M Singh. Int. J. Phys. Res., 2:15-23, 2012.
15. T Wågberg, P Johansson, and E Lindahl. Thin Solid Films, 539:114–121, 2013.
16. R Jafari, S Davari, and M Amjadi. J. Phys. D: Appl. Phys., 48:085303, 2015.
17. S Kumar, V Sharma, and P Singh. J. Mater. Sci.: Mater. Electron., 30:1675–1684, 2019.
18. J Lee, Y Kim, and H Park. ACS Appl. Mater. Interfaces, 10:175–185, 2018.
19. M K Jangid, S S Sharma, J Ray, D K Yadav, and C Lal. Int. J. Hydrogen Energy, 48:37921-37929, 2023.
20. P S Reddy, R Sharma, and K Ghosh. Ceram. Int., 46:16014–16021, 2020.
21. M K Jangid, S P Nehra, and M Singh. AIP Conf. Proc., 1349:685-686, 2011.
22. X Liu, J Wang, and L Chen. J. Mater. Sci., 42:640–645, 2007.
23. S Kumar, R Patel, and A Gupta. Thin Solid Films, 518:2795–2799, 2010.
24. F A Deorsola and D Vallauri. J. Mater. Sci., 43:3274–3278, 2008.
25. M M Miah, T Ahmed, and N Akhtar. J. Appl. Phys., 110:093510, 2011.
26. M Gharbi, R Karoui, and S Azzouz. J. Mater. Sci., 44:4312–4319, 2009.
27. S Shokri and M Parvin. Thin Solid Films, 520:5850–5854, 2012.
28. C Messaadi, T Ghrib, and J Jalali. J. Curr. Nanosci., 15:398–406, 2019.
29. G B Williamson and R C Smallman. Philos. Mag., 1:34–45, 1956.
30. B D Cullity. Elements of X-ray Diffraction. Addison-Wesley, London, 1978.
31. S Sakka. J. Non-Cryst. Solids, 100:227–239, 1988.
32. M K Jangid, S P Nehra, and M Singh. J. Nano-Electron. Phys., 3:460-468, 2011.
33. L Zhang, Y Li, and T Xu. J. Mater. Sci., 2021.
34. P Singh, A Mehta, and K Verma. Adv. Opt. Mater., 2020.
35. J Tauc. Mater. Res. Bull., 3:37–46, 1968.
36. A Fujishima and K Honda. Nature, 238:37–38, 1972.
37. M K Jangid, S S Sharma, J Ray, and S Jangid. Mater. Today: Proc., 67:847-851, 2022.
38. S Kumar, R Sharma, and M Gupta. J. Appl. Phys., 2022.
39. L Wang, H Zhang, and J Liu. Adv. Funct. Mater., 2021.
40. P Patra, S Mishra, and K Verma. Prog. Mater. Sci., 135:101073, 2023.
41. M K Jangid and S K Jangid. Trends Sci., 19:2067, 2022.
42. P Singh, A Sharma, and R Verma. J. Surf. Sci. Eng., 2021.
43. L Zhang, T Li, and H Xu. Adv. Thin Film Mater., 2022.

Effect of Nd^{3+} Nanoparticles on Physical and Optical Properties of Glasses

Raghavendra M N[1,a], Ashwajeet J S[1,b], Manjunatha S O[2,c]

[1] *Department of Studies in Physics, Davangere University, Shivagangotri, Davanagere-577007, Karnataka, India.*
[2] *Department of Physics, B.M.S College of Engineering, Bangalore-560 019, Karnataka, India.*

[a] rag28mn@gmail.com
[b] ashphysics358@gmail.com
[c] manjusirigere2011@gmail.com

Abstract

Neodymium nanoparticle (Nd^{3+} NPs) incorporated $40B_2O_3$-(30-x)TeO_2-$15Y_2O_3$-$15Na_2O$-xNd_2O_3 glasses via melt quenching technique. The amorphous structure of these glasses was established by X-ray diffraction (XRD) studies. The glasses were examined for density measurements using Archimedes' technique with toluene as the immersion liquid and density was found in the range between 2.92 and 3.34 g/cm³. Optical band gaps were studied by UV-visible spectroscopy. The indirect bandgap was observed in the range of 3.70 to 4.17 eV. Whereas the refractive index varies from 2.14 to 2.23. The correlation and comparable patterns were seen in the optical bandgap values derived from the ASF and DASF approaches.

Keywords: Density, molar volume (Vm), UV Vis., ASF, DASF.
Received 22 January 2025; First Review 21 February 2025; Accepted 22 February 2025

*** Address of correspondence**
Ashwajeet J S
Department of Studies in Physics
Davangere University, Shivagangotri,
Davanagere, Karnataka, India

Email: ashphysics358@gmail.com

How to cite this article
Raghavendra M N, Ashwajeet J S, Manjunatha S O, Effect of Nd^{3+} Nanoparticles on Physical and Optical Properties of Glasses, J. Cond. Matt. 2024; 02 (02): 86-93.

Available from:
https://doi.org/10.61343/jcm.v2i02.111

Introduction

The intrinsic benefits of glasses over crystalline materials have led to their extensive use in the design of photonic and optoelectronic devices [1]. The optical characteristics of doped glass systems containing rare earth oxides have been thoroughly investigated. These characteristics may be used to sensors, display devices, lasers, fiber amplifiers, waveguide amplifiers for optical transmission networks, and telecommunications [2-3]. Optical devices can use borate glasses because they can dissolve rare-earth ions, are simple to make, and are clear even when exposed to UV light. Adding borate oxide to tellurite oxide also makes the glass more stable and of higher quality, makes it clearer, and makes it less hygroscopic [4]. The combination of TeO_2 and B_2O_3 is better than silicate and phosphate glasses in a number of ways. Borotellurite glasses are a beneficial compromise between the advantages and disadvantages of B_2O_3 and TeO_2 [5]. For solid-state lighting systems, trivalent neodymium (Nd^{3+}) containing activated glasses are a very intriguing rare-earth ion. The development of novel host glass materials can optimize the spectrum properties of RE ions [6]. The endurance & physical characteristics of borate glasses are enhanced by the addition of yttrium oxide [7]. Due to their special optical and structural characteristics, these tiny neodymium particles combined with glass are very beneficial in a wide range of intricate applications [8].

This work's primary objective is to fabricate and examine borotellurite glasses with Nd^{3+} nanoparticles incorporated. Our study included a thorough analysis of the optical and physical characteristics of new glasses of batch $40B_2O_3$-(30-x)TeO_2-$15Y_2O_3$-$15Na_2O$-xNd_2O_3. We have successfully synthesized glass samples to achieve this goal. Their density, molar volume (V_m), and oxygen packing density (OPD) were measured using the Archimedes technique. Physical characteristics of these specified glasses were computed in detail. The amorphous characteristics of the samples were validated using XRD analysis and their molecular composition and arrangement were elucidated by FTIR analysis. For all glasses, we conducted UV-visible measurements between 200 and 800 nm. Many research has adopted the Absorbance Spectrum Fitting (ASF) and Derivative Absorption Spectrum Fitting (DASF) in lieu of Tauc's technique, since the band gap may be determined only from absorbance values [9-12]. In the present work we

have compared thoroughly between Tauc's method with ASF and DASF methods.

Preparation and Characterization Details

Neodymium (III) oxide nanoparticles (NPs),(Nd_2O_3), Tellurium (IV) oxide, (TeO_4), Sodium Carbonate, (Na_2CO_3), Yttrium (III) oxide,(Y_2O_3), and Boric acid (H_3BO_3) of high purity chemical powders were used to synthesize the samples without additional purification. In an electric furnace, 15 g of material was combined with agate mortar, put in a silica crucible, and heated to 1200 °C for 60 minutes. A molten sample is poured onto the brass plate and then quenched using a different brass plate during the casting process. Thermal and mechanical stresses of sample were alleviated by subjecting the glasses to annealing at 600 °C for duration of 1 hour. After treatment, samples were labelled TN0, TN1, and TN2 repressively. This illustrates the changes in the composition of tellurite(T) and neodymium oxide(N) in the glasses formulated as $40B_2O_3$-(30-x)TeO_2-$15Y_2O_3$-$15Na_2O$-xNd_2O_3, with x values of 0, 4, and 8 mol % respectively.

TN glasses in powder state were investigated for their amorphous nature using XRD. A chemical component and structural investigation for current TN glasses was performed using FTIR. Spectral absorbance of synthesized glasses measured in the region of 400–1500 cm^{-1}. To determine the density Archimedes' principle was used employing Toluene as the immersing liquid. The fabricated TN glasses underwent UV-Vis absorption analysis throughout a wavelength range of 200 to 800 nm.

Results and discussion

X-ray Diffraction Studies:

The XRD spectra of TN glasses are presented in Fig. 1. All glass samples exhibited significant diffusion in their X-ray diffraction spectra at lower scattering angles.

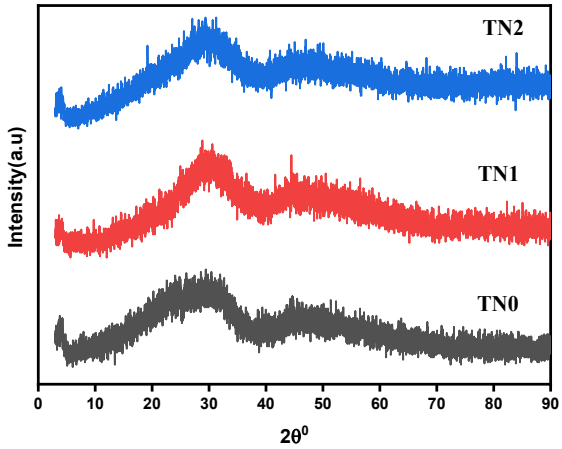

Figure 1: XRD pattern of the Nd^{3+} NPs TN glasses.

The pattern appears absence of sharp peaks and a broad and diffuse pattern between around 20^0-30^0 and 40^0-50^0, demonstrating that the glass samples are amorphous [8,13].

Fourier Transform Infrared (FTIR) Studies:

The FTIR spectra are shown in Fig. 2 over 400–1500 cm^{-1} range. The spectra include many peaks indicating local structure. Typical tellurite oxide structural units are about ~540 cm^{-1}. Tellurite oxide forms trigonal pyramidal (TeO_3) and trigonal bipyramidal (TeO_4) structures during glass production. The glass samples display a band representing the trigonal pyramidal TeO_3 structural unit at approximately 720 cm^{-1}.

Trigonal pyramidal TeO_3 in glass exhibit non-bridging oxygen atom distribution. Around 800 cm^{-1}, three spectral areas display a band group indicating the existence of bending vibrations caused by different combinations of borate. Tetrahedral BO_4 units' stretching vibrations are linked to the band group visible at around 1200 cm^{-1}. In trigonal BO_3 units, the elongation of B-O bonds leads to a distinct emphasis of the third band group at about 1400cm^{-1} [13-15].

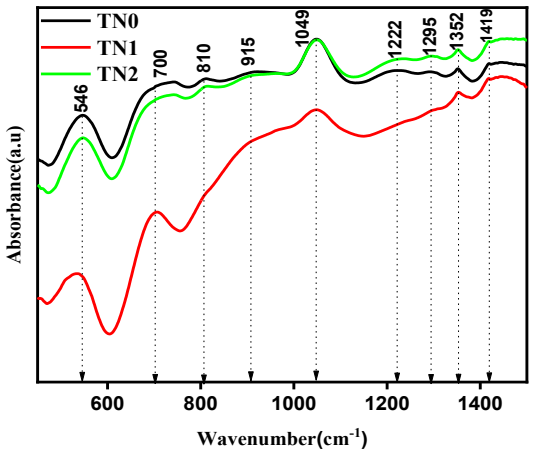

Figure 2: FTIR Absorption spectra of Nd^{3+} NPs TN glasses

Physical Studies:

The density of TN glasses was determined and subsequently calculated by following equation.

$$\rho = \frac{w_a}{w_a - w_t} \times \rho_t \qquad (1)$$

The glass's weight in air is represented by W_a, its weight in toluene by W_t, and its density in toluene (0.867 g/m^3) by ρ_t [16-17].

The following equation calculates molar volume (V_m) from density.

$$V_m = \frac{M_{glass}}{\rho_{glass}} \qquad (2)$$

Where M_{glass} represents average molecular weight of glass composition, while ρ_{glass} represents sample density [18]. The cation coordination number and oxide packing density (OPD). Its formula is:

$$OPD = 1000 \times \frac{N_o}{M_{glass}} \times \rho \qquad (3)$$

M_{glass} represents average molecular weight of glass, whereas N_o denotes number of oxygen atoms per oxide per unit formula [19]. The samples are viewed with excellent quality. The undoped Nd^{3+} glass sample exhibits the colourless and colour of the doped glass samples varies from light to bright purple, attributable to presence of Neodymium content. The Physical parameters of these glasses shown in Table 1 [20]. The association between each glass sample's density and molar volume and the Nd_2O_3 concentration (x wt%) is shown in Figure 3.

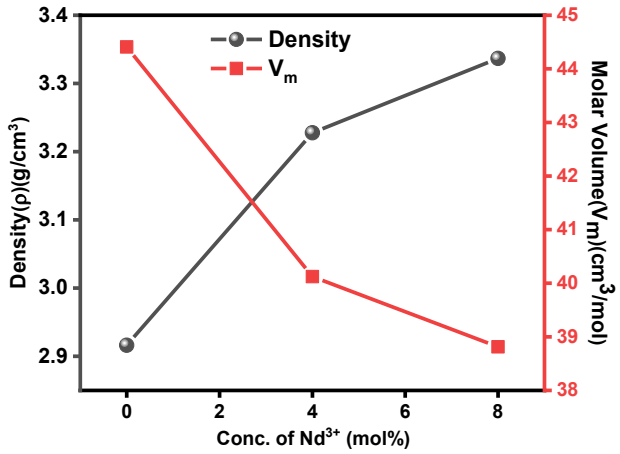

Figure 3: Density versus concentration of Nd^{3+} NPs with molar volume for TN glasses.

The association between each glass sample's density and molar volume and the Nd_2O_3 concentration (x wt%) is shown in Figure 3. The results of the experiment demonstrate that when the concentration of Nd_2O_3 in the samples increases, their density rises and molar volume decreases. The observed behaviour may be ascribed to disparity in molecular weights of TeO_2 (159.59 g/mol) and Nd_2O_3 (336.47 g/mol) reported in reference [21].

Table 1: Assessment of physical factors: density (ρ), molar volume (V_m), and oxygen packing density (OPD) of synthesized TN glasses.

Glasses	Nd^{3+} (%)	Physical parameters		
		Density (g/cm³)	V_m (cm³/mol)	OPD (g.atm/L)
TN0	0	2.916	44.408	54.04
TN1	4	3.228	40.124	60.80
TN2	8	3.337	38.814	63.89

Furthermore, Table 2 lists the physical parameters derived from the density data and refractive index. We analyse structural modifications in glass samples caused by variations in the concentration of Nd^{3+} NPs. The following physical characteristics of TN glasses are: The electrical dielectric constant, ionic concentration, inter-nuclear distance, molar polarizability, field strength, polaron radius, reflection loss, optical transmittance, metallization criterion, energy gap, optical basicity and dielectric constant of TN glasses were calculated using formulas found in the literature [22-23]. The findings presented in Table 2 show that doping of Nd^{3+} NPs cause a reduction in ionic concentration, polaron radius, molar polarizability, molar refraction inter-nuclear distance, they also enhance field strength, and optical basicity. electronic polarizability, dielectric constant, reflection loss, electronic susceptibility, and optical dielectric constant indicate an increase in TN1 and decrease in TN2 with an increase in Nd^{3+} NPs, Optical transmittance, metallization criteria, and energy gap indicate a drop in TN1 and rising in TN2 with a rise in Nd^{3+} NPs [24].

Table 2. Various physical factors of TN glasses

Sl. No	Physical property Parameters.	Glasses		
		TN0	TN1	TN2
		x=0	x=4	x=8
1.	Ionic concentration, N_i x10^{21} ion/cc	0	6.00	1.24
2.	Polaron Radius, r_px10^{-8} m	0	0.25	0.20
3.	Inter nuclear distance, r_i x10^{-8} m	0	0.63	0.5
4.	Field strength, F x 10^{15} cm^{-3}	0	46.54	73.88
5.	Molar refractivity, R_m cm^3/mol	28.93	26.67	24.87
6.	Electronic polarizability α_ex10^{-25} cm^3	2.20	2.26	2.15
7.	Molar polarizability α_m x10^{-24} cm^3	1.15	1.05	0.98
8.	Reflection losses, R_L(%)	0.14	0.15	0.13
9.	Optical Transmission, (T_o)	0.76	0.75	0.77
10.	Dielectric constant, ε	4.74	4.97	4.57
11.	Metallization criterion(M)	0.35	0.34	0.36
12.	Optical Basicity (^)	0.77	0.79	0.80
13.	Energy Gap (E_g)	2.43	2.25	2.58
14.	Electronic susceptibility, χ	0.30	0.32	0.28
15.	Optical Dielectric Constant, E_{opt}	3.74	3.97	3.57

UV-Vis. Studies:

Figure 4 displays the produced TN glasses' optical absorption spectra in the 300–800 nm region. The relative concentration of Nd_2O_3(x wt%) plays a significant role in determining the cutoff wavelength for each absorbance spectra. The picture shows eight absorption peaks, whereas the undoped glass sample TN0 has no peak. The peaks wavelengths of 353, 429, 469, 522, 584, 635, 683, and 746

nm are attributed. On the other hand, a shift in the absorption edges' positions causes the optical system's energy band gaps to vary. The origin of these phenomena is usually ascribed to the observed fluctuations in the concentration of Nd_2O_3.

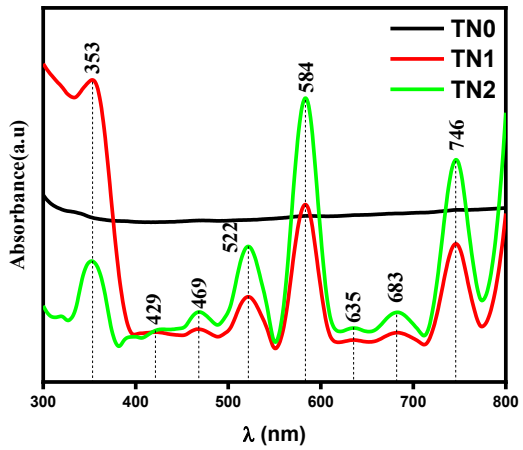

Figure 4: UV Absorption spectra of Nd^{3+} NPs TN glasses.

Band Gap of Optical Energy (E_{gap})

Tauc's model and the α(ν) optical absorption coefficient have been used to calculate energy gap for TN glasses [25]. Mott and Davis revised optical absorption coefficient α(ν) in Equation [25]. The power (r) is a precise measure of electronic transition characterised by a direct allowed transition at r = 0.5 and an indirect permissible transition at r = 2.0. For both direct and indirect allowed transition in suggested TN glasses, For both direct & indirect allowed transition in suggested TN glasses, Figure 5 and 6 illustrate the association of $(\alpha h\nu)^2$ and $(\alpha h\nu)^{0.5}$ in regard to (hν).

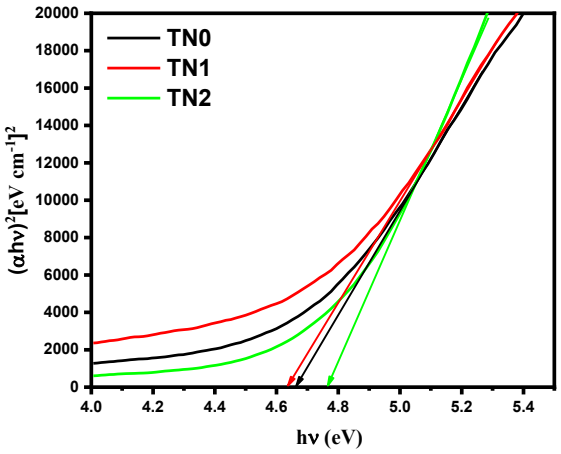

Figure 5: Variation of $(\alpha h\nu)^2$ versus (hν) for TN glasses.

To calculate values of $E_{g.dir}^{Tauc's}$ and $E_{g.indir}^{Tauc's}$ were extrapolated the straight line that passes over many points on the graphs at the locations where $(\alpha h\nu)^2 = 0$ and $(\alpha h\nu)^{0.5} = 0$, respectively. In Table 3, readings of $E_{g.dir}^{Tauc's}$ and $E_{g.indir}^{Tauc's}$ were provided. It was shown that the optical band gaps exhibited during direct transition had bigger diameters compared to those found during indirect transition. Moreover, it was observed that there was a considerable degree between the energy band gaps in each transition, indicating that the addition of Nd_2O_3 NPs to glass samples [26]. The indirect bandgap value spans from 3.709 to 4.174 eV. These results correspond with the optical gap values reported in [27]. The findings indicate that E_{opt} readings increases the indirect gap as concentration of Nd^{3+} nanoparticles rises from 0,4 & 8 mol%. Neodymium oxide ions' trivalent electrons change the absorbance properties via influencing the oxygen bonding in glass matrix [28]. The availability of loosely bound free electrons in respect to nuclear charge is increased by the presence of Nd_2O_3 ions, which aid in creation of NBOs. The valence and conduction bands are often excited by these free electrons, causing both bands to shift. The consequences of this change cause the forbidden gap to narrow, which lowers the reading of E_{opt} [29]. The indirect band gap value increases with the concentration of Nd_2O_3 owing to bonding defects.

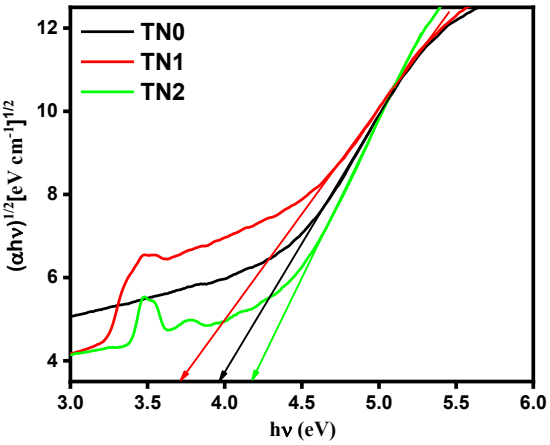

Figure 6: Variation of $(\alpha h\nu)^{1/2}$ versus (hν) for TN glasses

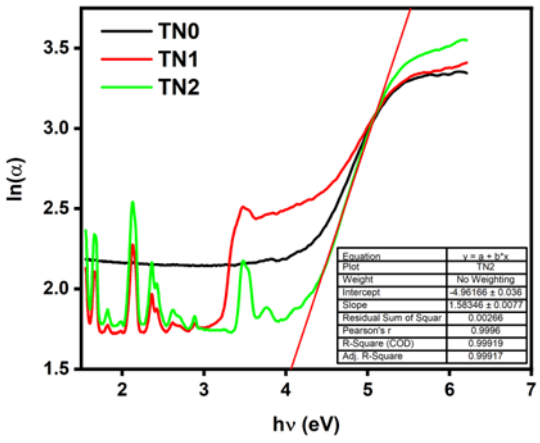

Figure 7: Variation of ln(α) versus (hν) for TN glasses

This alteration suggests subsequent introduction of Nd^{3+} ions into the glassy matrix modifies structural units and increases the amount of bridging oxygen, hence enhancing the magnitude of E_{opt}. Better connection within the glass network may potentially be the cause of an increase in E_{opt} readings. As more atoms bond, the separation between

valence and conduction bands expands, resulting in a rise in E_{opt} [30].

Under low photon energy conditions, the absorption coefficient (α) is governed by Urbach's empirical rule, as expressed in Eq. (4):

$$\alpha = \alpha_0 \exp\left(\frac{h\nu}{E_u}\right) \quad (4)$$

where E_u and α_o stand for Urbach's energy and a constant, respectively. These values are often used to measure the size of the band tail originating from localized states within the band gap in low-crystalline or disordered materials. One may rephrase empirical Eq (4) as:

$$\ln\alpha = \ln\alpha_0 + \left(\frac{h\nu}{E_u}\right) \quad (5)$$

Therefore, the Urbach's energy (E_u) determined by computing the gradient of the linear correlation between ln(α) & (hν). Fig. 7 depicts correlation between slope of linear function (α) and energy of photons (hν) for TN glasses, as shown in Table 3. The data suggest that glasses produced have the lowest Urbach's energy, suggesting the existence of very stable and consistent glasses with few flaws and a decrease in disorder within the glass samples that were made [31].

ASF Method, (E_g^{ASF})

Alarcon and associates have suggested a quantitative depiction of the α(ν) proportional to the photon wavelength (λ) [9] and Souri and Tahan [11]. The wavelength cutoff values for Planck's constant, light velocity and optical energy gap denoted as h, c, and λ_g respectively [32].

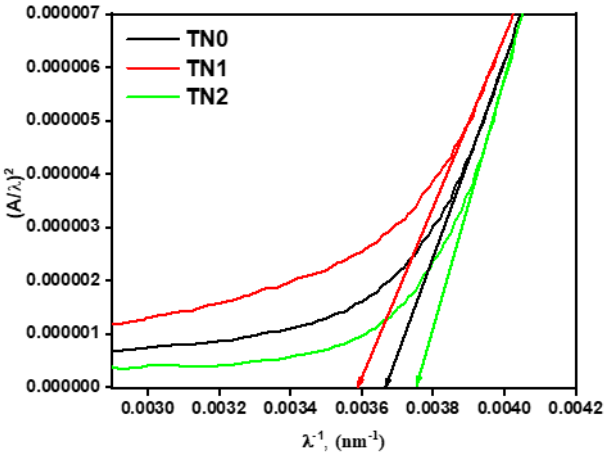

Figure 8: Change in $(A/\lambda)^2$ against λ^{-1} for TN glasses doped with Nd^{3+} NPs

The ASF approach, as indicated in Equation [25], facilitates determination of optical energy band gap only from absorbance measurements, disregarding thickness of glass sample. Additionally, optical gap within the ASF model may easily calculated using Equation (6) and calculating λ_g.

$$E_{gap}^{ASF} = \frac{hc}{\lambda_g} = 1239.83 \times \lambda_g^{-1} \quad (6)$$

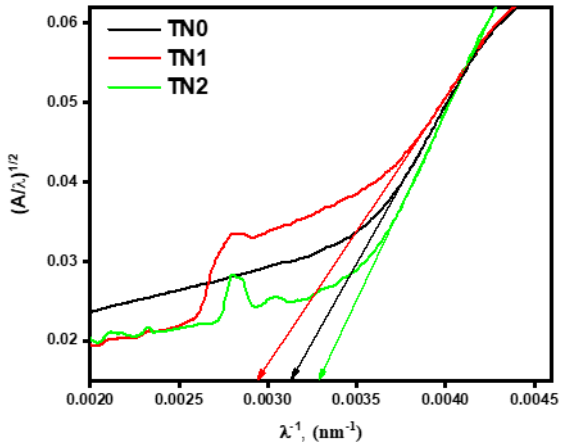

Figure 9: Change in $(A/\lambda)^2$ against λ^{-1} for TN glasses doped with Nd^{3+} NPs.

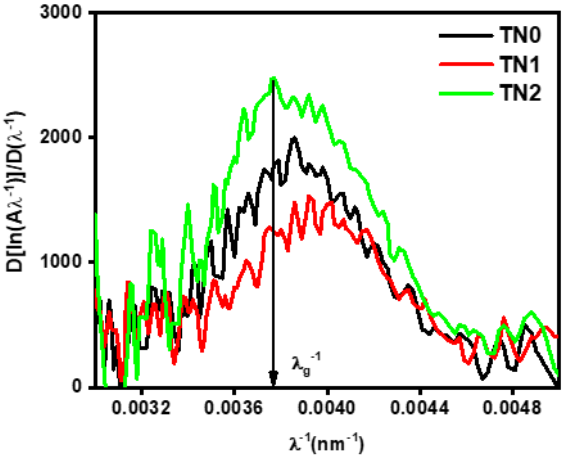

Figure 10: Graph of $d\{\ln[A\lambda^{-1}]\}/d(\lambda^{-1})$ against (λ^{-1}) for Nd^{3+} NPs doped in TN glasses. (DASF)

Figure 8 and 9 illustrate the variations in both direct and indirect transitions made possible by the proposed TN glasses [32]. Using extrapolation, the values of $E_{g.dir}^{ASF}$ and $E_{g.indir}^{ASF}$ were determined by identifying the straight area that passes over significant number of points on generated plots at points where $(A/\lambda)^2 = 0$ and $(A/\lambda)^{1/2} = 0$ respectively. In Table 3, the values of $E_{g.dir}^{ASF}$ and $E_{g.indir}^{ASF}$ are shown. Both Tauc's and ASF's approaches yielded very consistent outcomes [9].

DASF method, (E_g^{DASF})

The energy gaps of synthesised glasses were determined by DASF model. According to equation [22] where λ_g is the optical energy gap E_g^{DASF} calculate by

$$E_g^{DASF} = \frac{hc}{\lambda_g} = 1239.83 \times \lambda_g^{-1} \quad (7)$$

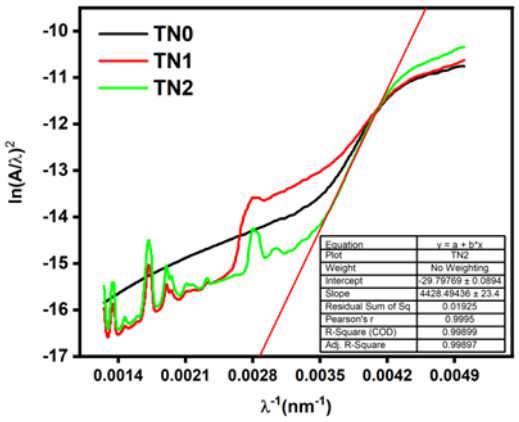

Figure 11: $DASF_{urb}$ plot of $\ln(A\lambda^{-1})^2$ vs λ^{-1} for TN glasses

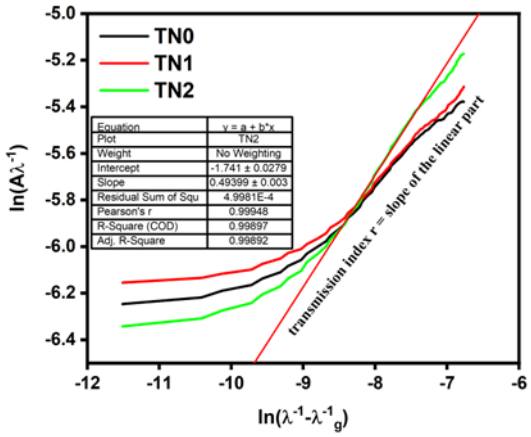

Figure 12: $\ln(A\lambda^{-1})$ versus $\ln(\lambda^{-1}\text{-}\lambda_g^{-1})$ plot for TN glasses doped with Nd^{3+} NPs. (transmission index: r)

Figure 10 illustrates the relationship between the derivative of TN glasses. The computed values of E_g^{DASF} were derived using Eq. (7) and reported in Table 3. The findings obtained from the evaluation of the three tests Tauc's, ASF, and DASF show a significant correlation with each other. Fig. 11 displays the dependence of $\ln(A\lambda^{-1})^2$ on λ^{-1} and shows the $DASF_{urb}$. The data show a strong correlation with Tauc's Urbach [33].The plot's linear section's slope, represented as $\ln((A(\lambda))/\lambda)$, may be compared to $\ln(1/\lambda - 1/\lambda_g)$ to get the r-value, as shown in the figure 12 [34].

This enables for the determination of the precise characteristics of the charge carrier optical transition. Table 3 lists 'r' as the slope of the fitted linear part. For all samples, it is about equal to 0.5, suggesting a direct transition. the calculation of refractive index factor (n) for all types of glasses. Through use of Eq. [18], We used Tauc's, ASF, and DASF techniques to compute the refractive index for permissible transitions that were both direct and indirect. The samples presented in Table 3 have their 'n' values derived from the current study. An inverse relationship was observed among the refractive indices and optical energy band gaps of analysed materials. Additionally, all of the glasses showed high n values, suggesting that they might be useful materials for optical and photoelectronic filter systems [32].

Table 3. Optical bandgaps (Tauc's, ASF, DASF), Refractive indices(n), Urbach energy (E_u) and Charge carrier optical transition (r) of present TN glasses.

Glasses		TN0	TN1	TN2	Ref
Tauc's	E_{dir}^{Tauc}	4.663	4.634	4.763	[35]
	n	2.053	2.056	2.037	-
	E_{indir}^{Tauc}	3.964	3.709	4.174	-
	n	2.177	2.229	2.137	-
	E_{urb}^{Tauc}	0.836	0.834	0.631	-
ASF	E_{dir}^{ASF}	4.493	4.447	4.649	-
	n	2.081	2.089	2.055	-
	E_{indir}^{ASF}	3.885	3.643	4.072	[36]
	n	2.192	2.243	2.156	[36]
DASF	E_g^{DASF}	4.773	4.860	4.661	-
	n	2.035	2.021	2.053	-
	E_{urb}^{DASF}	0.456	0.461	0.279	-
	r	0.4	0.4	0.5	-

Conclusion

This work primarily aims for examine the physical and optical characteristics of borotellurite glasses containing Nd^{3+} nanoparticles. The outcomes of the study highlight several significant characteristics of the TN glasses. XRD study verified the amorphous properties, whilst FTIR examinations elucidated molecular composition and structure of the glasses. The glass density analysis showed a rise from 2.92 to 3.34 gm/cm³, a decline in molar volume (V_m) from 44.40 to 38.81 cm³/mol, and rise in oxygen packing density (OPD) from 54.04 to 63.89 gm/cm³. Using Tauc's approach, indirect energy band gap vary between 3.71 eV & 4.17 eV, while the ASF and DASF methods showed variations from 3.64 eV to 4.07 eV & 4.66 eV to 4.86 eV, respectively. The slope of the fitted linear segment, 'r,' was almost 0.5 for every sample, suggesting a direct transition. Additionally, refractive index of TN1 glass was determined to be around 2.23, underscoring the potential of these glasses as efficient materials for photoelectronic applications and optical filter devices.

Acknowledgments

Authors sincerely acknowledge the UGC-DAE-CSR, Kolkata, for their provision of characterization facilities.

References

1. K. Siva Rama Krishna Reddy et al., *'Structural, optical absorption and photoluminescence spectral studies of Sm^{3+} ions in Alkaline-Earth Boro Tellurite glasses'*, Opt. Mater. (Amst)., vol. 79, pp. 21–32, 2018, doi: 10.1016/j.optmat.2018.03.005.
2. O. Ravi, C. M. Reddy, B. S. Reddy, and B. D. P. Raju, *'Judd–Ofelt analysis and spectral properties of Dy^{3+} ions doped niobium containing tellurium calcium zinc borate glasses'*, Opt. Commun., vol. 312, pp. 263–268, 2014.
3. Z. A. S. Mahraz, M. R. Sahar, S. K. Ghoshal, M. R. Dousti, and R. J. Amjad, *'Silver nanoparticles enhanced luminescence of Er^{3+} ions in boro-tellurite glasses'*, Mater. Lett., vol. 112, pp. 136–138, 2013.
4. A. Jha et al., *'Rare-earth ion doped TeO_2 and GeO_2 glasses as laser materials'*, Prog. Mater. Sci., vol. 57, no. 8, pp. 1426–1491, 2012.
5. J. S. Alzahrani, M. A. Alothman, C. Eke, H. Al-Ghamdi, D. A. Aloraini, and M. S. Al-Buriahi, *'Simulating the radiation shielding properties of TeO_2–Na_2O–TiO glass system using PHITS Monte Carlo code'*, Comput. Mater. Sci., vol. 196, p. 110566, 2021.
6. D. Ramachari, L. Rama Moorthy, and C. K. Jayasankar, *'Optical absorption and emission properties of $Nd3^{+}$-doped oxyfluorosilicate glasses for solid state lasers'*, Infrared Phys. Technol., vol. 67, pp. 555–559, 2014, doi: 10.1016/j.infrared.2014.09.020.
7. M. R. S. Nasuha, H. Azhan, W. A. W. Razali, L. Hasnimulyati, and Y. Norihan, *'Effect of yttrium on the physical, elastic, and structural properties of neodymium-doped lead borotellurite glass'*, J. Mater. Sci. Mater. Electron., vol. 32, no. 18, pp. 22890–22897, 2021, doi: 10.1007/s10854-021-06766-w.
8. M. N. Azlan and M. K. Halimah, *'Role of Nd^{3+} nanoparticles on enhanced optical efficiency in borotellurite glass for optical fiber'*, Results Phys., vol. 11, no. August, pp. 58–64, 2018, doi: 10.1016/j.rinp.2018.08.017.
9. L. Escobar-Alarcón, A. Arrieta, E. Camps, S. Muhl, S. Rodil, and E. Vigueras-Santiago, *'An alternative procedure for the determination of the optical band gap and thickness of amorphous carbon nitride thin films'*, Appl. Surf. Sci., vol. 254, no. 1 SPEC. ISS., pp. 412-415, 2007, doi: 10.1016/j.apsusc.2007.07.052.
10. D. Souri and K. Shomalian, *'Band gap determination by absorption spectrum fitting method (ASF) and structural properties of different compositions of $(60-x)V_2O_5.40TeO_{2-x}Sb_2O_3$ glasses'*, J. Non. Cryst. Solids, vol. 355, no. 31–33, pp. 1597–1601, 2009, doi: 10.1016/j.jnoncrysol.2009.06.003.
11. D. Souri and Z. E. Tahan, *'A new method for the determination of optical band gap and the nature of optical transitions in semiconductors'*, Appl. Phys. B, vol. 119, no. 2, pp. 273–279, 2015.
12. A. A. Ali, Y. S. Rammah, R. El-Mallawany, and D. Souri, *'FTIR and UV spectra of pentaternary borate glasses'*, Meas. J. Int. Meas. Confed., vol. 105, no. April, pp. 72–77, 2017, doi: 10.1016/j.measurement.2017.04.010.
13. T. Walia and K. Singh, *'Mixed alkaline earth modifiers effect on thermal, optical and structural properties of SrO-BaO-SiO2-B2O3-ZrO2 glass sealants'*, J. Non. Cryst. Solids, vol. 564, no. April, p. 120812, 2021, doi: 10.1016/j.jnoncrysol.2021.120812.
14. A. Dehelean, S. Rada, A. Popa, and E. Culea, *'Structural and magnetic investigations on gadolinium–tellurite vitreous systems prepared by sol–gel method'*, J. Mol. Struct., vol. 1036, pp. 203–208, 2013.
15. S. K. J. Al-Ani, S. S. Al-Rawi, A. H. Jassim, and H. A. Al-Hilli, *'FTIR spectra of molybdenum tellurite glasses'*, Iraqi J. Appl. Phys, vol. 2, no. 1–2, pp. 23–25, 2006.
16. A. Madhu, B. Eraiah, P. Manasa, and N. Srinatha, *'Nd^{3+}-doped lanthanum lead boro-tellurite glass for lasing and amplification applications'*, Opt. Mater. (Amst)., vol. 75, pp. 357–366, 2018, doi: 10.1016/j.optmat.2017.10.037.
17. J. S. Ashwajeet, T. Sankarappa, T. Sujatha, and R. Ramanna, *'Thermal and electrical properties of $(B_2O_3$-TeO_2-Li_2O-CoO) glasses'*, J. Non. Cryst. Solids, vol. 486, pp. 52–57, 2018.
18. D. Saritha, M. Salagram, and G. Bhikshamaiah, *'Physical and optical properties of Bi_2O_3-B_2O_3 glasses'*, in IOP Conference Series: Materials Science and Engineering, IOP Publishing, 2009, p. 12057.
19. N. Yahya et al., *'Effect of silver on the physical and structural properties of lead neodymium borotellurite glass system'*, Malaysian J. Anal. Sci., vol. 22, no. 2, pp. 296–302, 2018.
20. M. R. S. Nasuha, H. Azhan, W. A. W. Razali, L. Hasnimulyati, and Y. Norihan, *'Structural and elastic properties studies of yttrium lead borotellurite glass doped with neodymium oxide'*, vol. 18, no. 8, pp. 439–448, 2021.
21. A. Kaur, A. Khanna, and L. I. Aleksandrov, *'Structural, thermal, optical and photo-luminescent properties of barium tellurite glasses doped with rare-earth ions'*, J. Non. Cryst. Solids, vol. 476, no. August, pp. 67–74, 2017, doi: 10.1016/j.jnoncrysol.2017.09.025.
22. N. J. Kreidl, *'Variability of optical properties and*

structure of glass', Glas. Berichte, vol. 62, no. 6, pp. 213–218, 1989.

23. J. A. Duffy, *'The electronic polarisability of oxygen in glass and the effect of composition'*, J. Non. Cryst. Solids, vol. 297, no. 2–3, pp. 275–284, 2002.
24. A. S. Rao, Y. N. Ahammed, R. R. Reddy, and T. V. R. Rao, *'Spectroscopic studies of Nd^{3+}-doped alkali fluoroborophosphate glasses'*, Opt. Mater. (Amst)., vol. 10, no. 4, pp. 245–252, 1998, doi: 10.1016/S0925-3467(97)00055-4.
25. A. S. Rao et al., *'Spectroscopic and optical properties of Nd^{3+} doped fluorine containing alkali and alkaline earth zinc-aluminophosphate optical glasses'*, Phys. B Condens. Matter, vol. 404, no. 20, pp. 3717–3721, 2009.
26. V. B. Sreedhar, R. Doddoji, K. K. Kumar, and V. R. M. Reddy, *'A study of NIR emission and associated spectroscopic properties of Nd^{3+}: $P_2O_5^+$ K_2O^+ $Al_2O_3^+$ ZnF_2 glasses for 1.06 μm laser applications'*, J. Non. Cryst. Solids, vol. 553, p. 120521, 2021.
27. S. Rani, N. Ahlawat, R. Parmar, S. Dhankhar, and R. S. Kundu, *'Role of lithium ions on the physical, structural and optical properties of zinc boro tellurite glasses'*, Indian J. Phys., vol. 92, pp. 901–909, 2018.
28. M. N. Azlan, M. K. Halimah, S. Z. Shafinas, and W. M. Daud, *'Electronic polarizability of zinc borotellurite glass system containing erbium nanoparticles'*, Mater. Express, vol. 5, no. 3, pp. 211–218, 2015.
29. M. N. Azlan, M. K. Halimah, A. B. Suriani, Y. Azlina, and R. El-Mallawany, *'Electronic polarizability and third-order nonlinearity of Nd^{3+} doped borotellurite glass for potential optical fiber'*, Mater. Chem. Phys., vol. 236, p. 121812, 2019.
30. M. R. S. Nasuha, H. Azhan, L. Hasnimulyati, W. A. W. Razali, and Y. Norihan, *'Effect of Nd3+ ions on Physical and Optical Properties of Yttrium Lead Borotellurite Glass System'*, J. Non. Cryst. Solids, vol. 551, no. August 2020, p. 120463, 2021, doi: 10.1016/j.jnoncrysol.2020.120463.
31. M. K. Halimah, A. A. Awshah, A. M. Hamza, K. T. Chan, S. A. Umar, and S. H. Alazoumi, *'Effect of neodymium nanoparticles on optical properties of zinc tellurite glass system'*, J. Mater. Sci. Mater. Electron., vol. 31, pp. 3785–3794, 2020.
32. Y. S. Rammah, K. A. Mahmoud, M. I. Sayyed, F. I. El-Agawany, and R. El-Mallawany, *'Novel vanadyl lead-phosphate glasses: P_2O_5-PbO-ZnONa_2O-V_2O_5: Synthesis, optical, physical and gamma photon attenuation properties'*, J. Non. Cryst. Solids, vol. 534, no. December 2019, p. 119944, 2020, doi: 10.1016/j.jnoncrysol.2020.119944.
33. D. Souri, M. Sarfehjou, and A. R. Khezripour, *'The effect of ambient temperature on the optical properties and crystalline quality of ZnSe and ZnSe:Cu NCs grown by rapid microwave irradiation'*, J. Mater. Sci. Mater. Electron., vol. 29, no. 4, pp. 3411–3422, 2018, doi: 10.1007/s10854-017-8276-5.
34. D. Souri, A. R. Khezripour, M. Molaei, and M. Karimipour, *'ZnSe and copper-doped ZnSe nanocrystals (NCs): Optical absorbance and precise determination of energy band gap beside their exact optical transition type and Urbach energy'*, Curr. Appl. Phys., vol. 17, no. 1, pp. 41–46, 2017, doi: 10.1016/j.cap.2016.10.008.
35. Y. A. Yamusa, R. Hussin, W. N. W. Shamsuri, Y. A. Tanko, and S. A. Jupri, *'Impact of Eu^{3+} on the luminescent, physical and optical properties of $BaSO_4$–B_2O_3–P_2O_5 glasses'*, Optik (Stuttg)., vol. 164, pp. 324–334, 2018.
36. I. Bulus, R. Hussin, S. K. Ghoshal, A. R. Tamuri, I. M. Danmallam, and Y. A. Yamusa, *'Europium-doped boro – telluro - dolomite glasses for red laser applications: Basic insight into spectroscopic traits'*, J. Non. Cryst. Solids, vol. 534, no. September 2019, p. 119949, 2020, doi: 10.1016/j.jnoncrysol.2020.119949.

Effect of Annealing on Defect Formations in Zno Nanoparticles

Himani Bhoi and Sudhish Kumar

Magnetism Laboratory, Department of Physics, Mohanlal Sukhadia University, Udaipur, Rajasthan, India.

[a] phd_hbhoi@mlsu.ac.in
[b] skphy@mlsu.ac.in

Abstract

This study reports on the effect of annealing on the structural, defect formation and optical characteristics of ZnO nanoparticles (NPs) synthesized via self-combustion reactions. For investigating the effect of annealing, one part of as-synthesized ZnO NPs was kept as such and other two parts were annealed at 450 ºC & 700 ºC (hereafter referred as ZCA, ZCA450 and ZCA700) for six hours in ambient environment. Rietveld refinement of XRD patterns approved phase pure formation of ZCA, ZCA450 & ZCA700 in the Wurtzite type hexagonal symmetry along with a monotonic increment in the unit cell volume and mean crystallite size with annealing temperature (AT). In the same line, observation of three characteristic Raman modes ($2E_{2H}$-$2E_{2L}$, E_2 (high) and E_1 (LO)) validated hexagonal symmetry of these ZnO NPs. Blue shifting in the E_2 (high) and E_1 (LO) modes and red shifting in the $2E_{2H}$-$2E_{2L}$ mode and, ESR analysis corroborated formation of oxygen and zinc vacancies in these ZnO NPs along with annihilation of surface defects with AT. UV-Vis-NIR data exhibited considerable absorption of light below 500 nm by these ZnO NPs with a maximum noted in the blue color region. The obtained band gap E_g = 2.74 eV for ZCA NPs is found to be higher than ZCA450 (E_g = 2.50 eV) and ZCA700 (E_g = 2.68 eV). Notably, the obtained E_g for these ZnO NPs are considerably lower than the reported values in literature. These ZnO NPs seems to be useful for making UV & blue light protection layers and UV absorbers for sunscreen lotion etc.

Keywords: Annealing temperature, optical band gap energy, defects.
Received 28 January 2025; First Review 21 February 2025; Accepted 23 February 2025

*** Address of correspondence**
Himani Bhoi
Department of Physics, Mohanlal Sukhadia University, Udaipur, Rajasthan, India.

Email: phd_hbhoi@mlsu.ac.in

How to cite this article
Himani Bhoi and Sudhish Kumar, Effect of annealing on defect formations in ZnO nanoparticles, J. Cond. Matt. 2024; 02 (02): 94-98.

Available from:
https://doi.org/10.61343/jcm.v2i02.78

Introduction

Nanosized ZnO is a notable wide band semiconducting material with E_g = 3.37 eV and high binding energy (60 meV). ZnO NPs finds substantial applications in the field of chemical, optical and spintronic engineering, etc. It is known for tunable optical and magnetic properties, good thermal and chemical stability, and good biocompatibility. ZnO NPs are being extensively utilized in optoelectronics, LEDs, cosmetics, and biomedical fields like antimicrobial and anticancer treatments [1-2]. Defects, particularly oxygen vacancies in ZnO lattice greatly influence its characteristics and effectiveness [3]. Controlling defects in ZnO along with stoichiometry of oxygen ions and morphology of NPs is essential for better response but demands clear-cut understandings. This study presents augmenting effort on the influence of annealing temperature on the structural & optical properties, and defect formations in ZnO NPs synthesized via self-combustion reactions.

Method

For the synthesis of ZnO NPs, zinc nitrate hexahydrate was used as a precursor and citric acid as a reducing agent, along with few drops of NH_4OH to adjust the pH [4-5]. Stoichiometric amounts of $Zn(NO_3)_2{\cdot}6H_2O$ and $C_6H_8O_7{\cdot}H_2O$ in a 1:1 molar ratio were dissolved in water, combined, and stirred at 50 ºC. NH_4OH was added drop wise to raise the pH to 11. Continuous stirring led to gel formation, which was further heated for initiating combustion reactions and formation of sample desired yield as loose lumps, which were ground into a powder. Synthesis protocol of ZnO NPs is presented in Figure 1. Sample yield was divided into three parts: one part was kept as-synthesized (ZCA), and the other two parts were annealed at 450 ºC (ZCA450) and 700 ºC (ZCA700). X-ray-diffraction (XRD) data were recorded in 20º - 90º range of 2θ (step size = 0.02º) on a RIGAKU ULTIMA-IV. The XRD data were refined using FullProf software. Raman spectrums were recorded on a Horiba JY HR-800 spectrometer using an excitation wavelength of 473 nm. Optical absorption spectrums were recorded in the range of 200-800 nm on the Shimadzu UV-1780 UV-Vis spectrophotometer. ESR data were acquired in X-band (with microwave frequency of ~9.44GHz) on a JEOL Japan made JES-FA200 ESR Spectrometer.

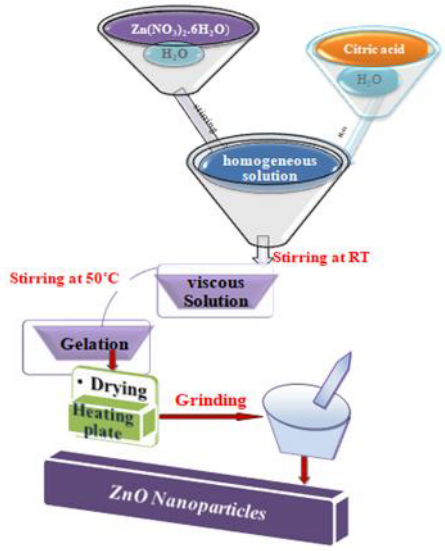

Figure 1: Synthesis protocol of ZnO NPs.

Discussion

The indexed XRD patterns of ZCA, ZCA450, and ZCA700 NPs shown in Figure 2, matched well with the Wurtzite type hexagonal structure (JCPDS 36-1451) with no sign of impurity. The refined hexagonal lattice parameters matched well with the literature (see table 1) [6-7].

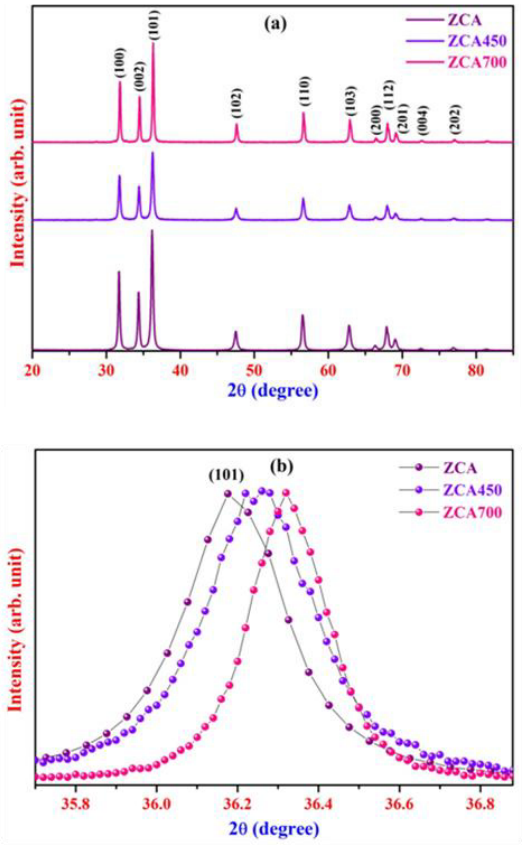

Figure 2: (a) Indexed XRD patterns and (b) shifting in the most prominent (101) XRD peak toward higher 2θ side with AT for ZCA, ZCA450, ZCA700 NPs.

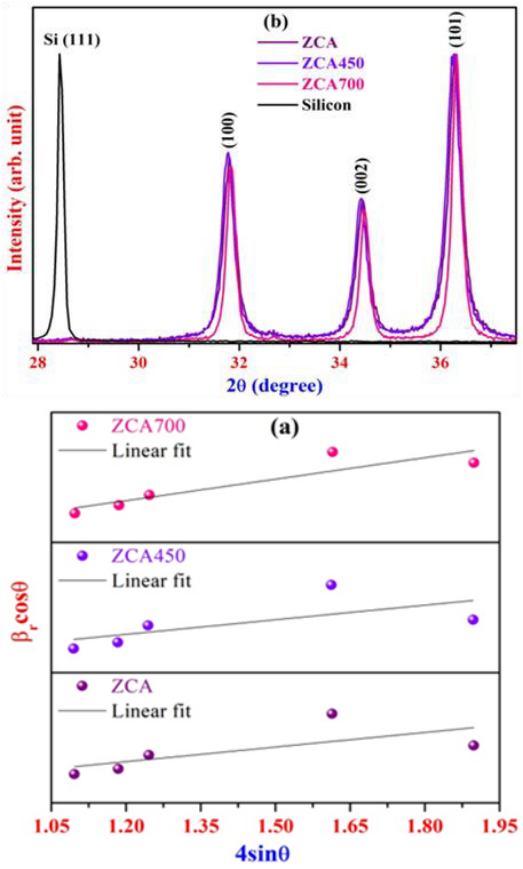

Figure 3: (a) W-H plots and (b) Broadening in the well resolved & intense XRD peaks of ZCA, ZCA450 and ZCA700 NPs compared to standard Silicon's (111) peak in the same region of 2θ.

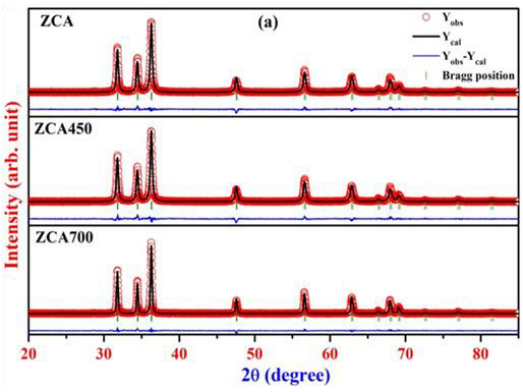

Figure 4: Rietveld refined XRD data of (a) ZCA, ZCA450 and ZCA700 NPs.

As AT increases, the Bragg peaks become sharper and narrower, indicating improvement in the crystallinity. Enhanced peak intensity also reflects this improvement as evident in Figure 2(a). Additionally, the (101) Bragg peak shifts to a higher 2θ side with increasing AT, which is likely due to changes in the stress in ZnO NPs [8]. The mean crystallite size (D) and strain (ε) of ZCA, ZCA450, and ZCA700 NPs (see Figure 3(a)) were deduced using Scherrer's and W-H plot analysis [9], and the results are listed in Table 1. Initially, D does not change much from 35

nm to 36 nm, when annealed at 450°C but annealing at 700°C led to significant enhancement in D to ~59 nm, as reflected in the line broadening shown in Fig. 3(b). Scherrer's method underestimates D but showed the similar trend with W-H method. The microstrain (ε) decreases with AT and thus, indicating tensile stress in these ZnO NPs [10].

Table 1: Crystallographical parameters and agreement factors for ZCA, ZCA450 and ZCA700 NPs

Sample		ZCA	ZCA450	ZCA700
Hexagonal lattice constants (Å)	a = b	3.2494 (3)	3.2495 (3)	3.2500 (3)
	c	5.2071 (5)	5.2077 (5)	5.2062 (4)
Atomic packing fraction (c/a)		1.6025	1.6026	1.6019
Volume (Å^3)		47.615(01)	47.621(01)	47.624(7)
Oxygen's positional Parameter (z)		0.3818	0.3810	0.3823
D ± 5 (nm)	Scherrer method	20	21	30
	W-H plot method	35	36	59
ε×10^{-3}		1.70	1.68	1.38
Density (g/cm^3)		5.676	5.675	5.675
R_{Bragg}		3.47	3.28	2.79
R_f		2.91	2.60	2.45
R_P		9.03	9.10	8.40
R_{wp}		12.9	12.8	13.0
R_{exp}		9.93	9.41	9.58
χ^2		1.69	1.86	1.84

XRD patterns of all samples were refined in the $P6_3mc$ space group (No. 186, Z=2). Nicely fitted XRD profiles are demonstrated in Figure 4. In the refinement, Wyckoff positions were set at 2b (1/3, 2/3, 0) and 2b (1/3, 2/3, z) for Zn and oxygen atoms respectively. According to the crystallography of ZnO only the z coordinate of oxygen is the refinable parameter. Good agreement factors, nice profile fittings and successful indexing of Bragg peaks validated phase pure ZnO NPs crystallizing in the Wurtzite-type hexagonal structure (see table 1). Table 1 also shows that annealing does not alter the hexagonal symmetry of ZnO, though the unit cell volume increases with AT. The refined parameters closely align with each other and also matched well the literature [10].

Raman spectrums of ZCA450 and ZCA700 samples are shown in Figure 5, notably no Raman active modes were observed for ZCA. Positions and classification of observed Raman active modes are presented in table 2. Three characteristic Raman modes corresponding to the Wurtzite type hexagonal symmetry of ZnO are observed. The most intense mode at 438.10 cm^{-1} (ZCA450) and 439.56 cm^{-1} (ZCA700) corresponds to the E_2 (high) mode, while the weak mode at 582.63 cm^{-1} (ZCA450) and 583.87 cm^{-1} (ZCA700) is associated with E_1 (LO) vibrations [11]. Both E_2 (high) and E_1 (LO) modes blue shifted in ZCA700, which is likely due to increased crystallite size, while the weak mode at 346.49 cm^{-1} (ZCA450) is red shifted to 331.67 cm^{-1} in ZCA700. Raman results are in line with the XRD analysis.

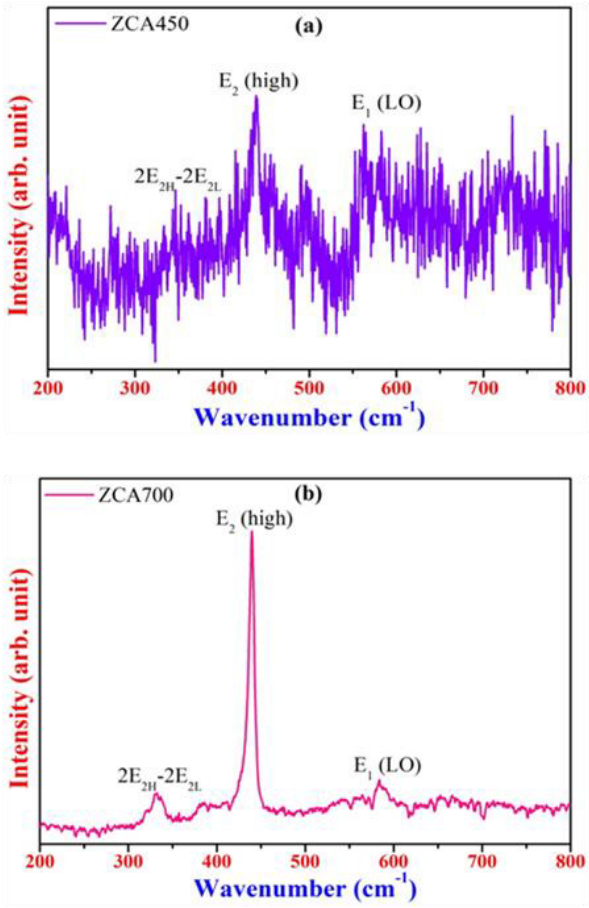

Figure 5. Raman spectrums of (a) ZCA450 and (b) ZCA700.

UV-VIS-NIR absorbance spectrums shown in Figure 6 (a) demonstrate significant light absorption by these ZnO NPs with characteristic maxima at ~376, 378 and 377 nm for ZCA, ZCA450 and ZCA700 NPs, respectively. Further, photo-absorption is increased in ZCA450 NPs compared to the as synthesized ZCA NPs, while it is slightly decreased in ZCA700 NPs. The band gap (E_g) were estimated using Tauc's plots [9,12]. Tauc's plots of ZCA, ZCA450 and ZCA700 NPs are presented in Fig. 6 (b) and estimated E_g values are given in table 2. The E_g = 2.74 eV for as synthesized ZCA is higher than ZCA450 (E_g = 2.50 eV) and ZCA700 (E_g = 2.68 eV). Overall these values of E_g are quite lower than values reported in literature [10]. Here, it is

Table 2. Active Raman modes and direct band gap energies (E_g) for ZCA, ZCA450 and ZCA700 NPs.

Sample	Positions of Raman modes in cm^{-1}			Maxima of absorption		E_g ±2 (eV)
	$2E_{2H}$-$2E_{2L}$	E_2 (high)	E_1 (LO)	λ (nm)	E (ev)	
ZCA	-	-	-	376	3.30	2.74
ZCA450	346.5	438.1	582.6	378	3.28	2.50
ZCA700	331.7	439.6	583.8	377	3.29	2.68

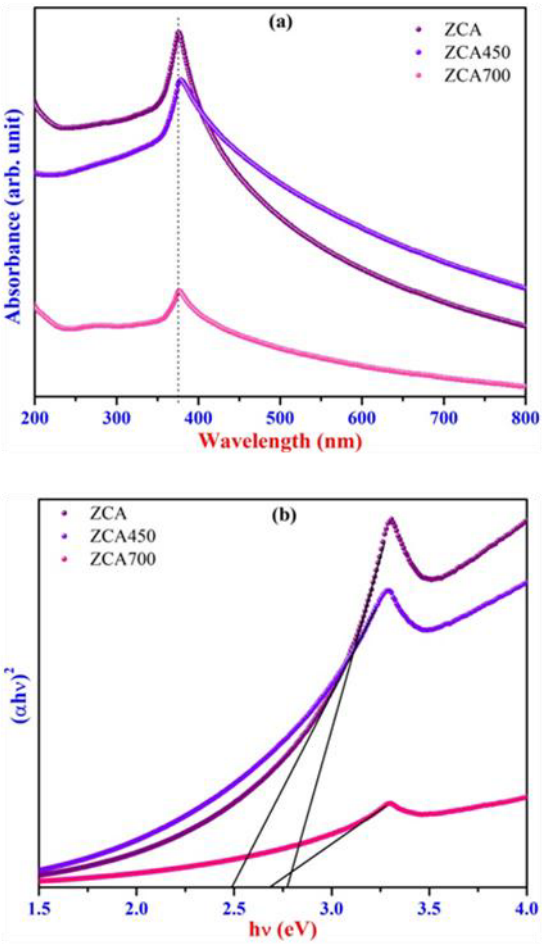

Figure 6: (a) UV-VIS-NIR optical absorption spectrums and (b) Tauc's plots for ZCA, ZCA450 and ZCA700 NPs.

worth to note that below 500 nm, these ZnO NPs considerably absorbed light and the maxima is noted in the blue region. These outcomes could be useful for making UV & blue light protection layer and absorber for sunscreen lotion etc.

ESR is a unique technique for identifying defect centers like oxygen vacancies (V_o) and cationic vacancies (V_{Zn}) in metal oxide nanoparticles, which greatly affect their optical properties. ESR spectra of ZCA, ZCA450, and ZCA700 NPs are shown in Figure 7. The resonance field (H_{res}), g-factor, and peak width (ΔH_{pp}) values are listed in Table 3 [7]. In these ZnO NPs two prominent ESR signals are detected at g ~2.00 (S_1) and g ~1.96 (S_2).

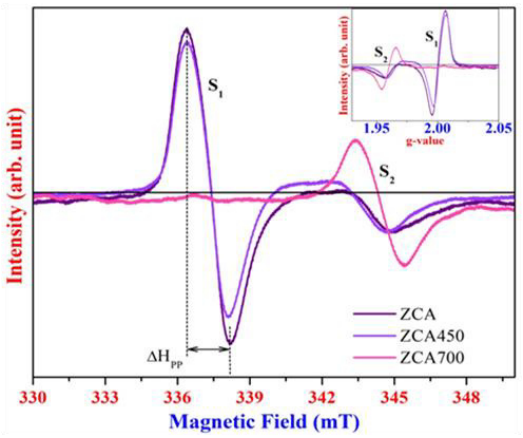

Figure 7: ESR spectrums of ZCA, ZCA450 and ZCA700 NPs.

In bulk ZnO only the S_2 signal has been reported in the literature. The S_1 signal is related to surface oxygen (V_o) defects and their concentration decreases with annealing temperature, indicating reduction in the defects at higher temperature. There is a debate on the origin of S_2 signal, some reports attributing it to V_o, hydrogen defects, or shallow impurities [3]. While other studies have suggested that S_2 signal is originated due to Zn vacancies (V_{Zn}), instead of V_o, with V_{Zn} in various charge states like V_{Zn}- can distorts the lattice and creates paramagnetic O^- defects (g ~1.96) [13]. Increasing AT raises in content of V_{Zn}- as depicted by a stronger S_2 signal; these findings are aligning well with recent defect studies on ZnO NPs [14]. In summary, annealing significantly impacts defect formation in ZnO lattice, with V_o promoting reactive oxygen species (ROS), which are useful in waste water treatment and other environmental remediation and thus, highlighting potential of ZnO NPs in future R&D activities.

Table 3: Resonance field, g factor and peak width of ZCA, ZCA450 NPs

Samples	H_{res}	(ΔH_{pp})	g-value	
			S_1	S_2
ZCA	337.41	1.86	2.00028	1.9671
ZCA450	337.39	1.73	2.00095	1.9670
ZCA700	344.31	2.05	-	1.9607

Conclusion

Phase pure samples of ZnO NPs (ZCA, ZCA450 & ZCA700) were successfully synthesized by sol-gel auto combustion reactions. XRD and Raman analysis revealed that the prepared ZnO NPs crystallize in the single-phase

Wurtzite type hexagonal structure. Monotonic increment in the unit cell parameters 'a' and mean crystallite size 'D' with annealing temperature is observed. Blue shifting in the Raman E_2 (high) and E_1 (LO) vibration modes and red shifting in the $2E_{2H}$-$2E_{2L}$ mode with annealing temperature and ESR analysis affirmed formation and annihilation of surface defects with increasing annealing temperature in ZnO NPs. Below, 500 nm these ZnO NPs considerably absorb light with a maximum noted in the blue region. Band gap energy of ZnO NPs decreases with annealing. These ZnO NPs seems to be useful for making UV & blue light protection layers and UV absorbers for sunscreen lotion etc.

References

1. J. Chen, Z. Tang, Y. Zhou, T. Zhang, L. Qian, C. Xiang, Chem. Phys. Lett. (2023) 140441.
2. S. Zeghoud, H. Hemmami, B. Ben Seghir, I. Ben Amor, I. Kouadri, A. Rebiai, M. Messaoudi, S. Ahmed, P. Pohl, J. Simal-Gandara, Mater. Today Commun. 33 (2022) 104747.
3. V. Ischenko, D.G. Polarz, V. Stavarache, K. Fink and M. Driess, Adv Funct Mater 15 (2005) 1945–1954.
4. K. Punia, G. Lal, P. Alvi, S.N. Dolia, S. Dalela, K.B. Modi, S. Kumar, Cerams. Int. 45 (2019) 13472–13483.
5. H. Bhoi, P. Joshi, K. Punia, G. Lal, S. Kumar, AIP Conf. Proc. 2220 (2020) 020109.
6. H. Bhoi, K. Punia, G. Lal, S. Kumar, AIP Conf. Proc. 2265 (2020) 030117.
7. K. Punia, G. Lal, H. Bhoi, S. Kumar, AIP Conf. Proc. 2115 (2019) 030146.
8. J. Ungula, B.F. Dejene, H.C. Swart, Results Phys. 7 (2017) 2022–2027.
9. H. Bhoi, S. Tiwari, G. Lal, K.K. Jani, S.K. Modi, P. Seal, V. Saharan, K.B. Modi, J. Borah, K. Punia, S. Kumar, Ceram. Int. 48 (2022) 28355–28373.
10. K. Punia, G. Lal, S.K. Barbar, S.N. Dolia, P.A. Alvi, S. Dalela, S. Kumar, Vacuum 184 (2021) 109921.
11. J. Lv, M. Fang, Mater. Lett. 218 (2018) 18–21.
12. H. Bhoi, S. Tiwari, Manisha, Hirdesh, L. Pascual, S. Kumar, Inorg. Chem. Commun. 170 (2024) 113487.
13. N. Y. Garces, L. Wang, L. Bai, N. C. Giles, L. E. Halliburton, G. Cantwell, Appl Phys. Lett. 81 (2002) 622.
14. S. Nadupalli, S. Repp, S. Weber, E. Erdem, Nanoscale 13 (2021) 9160–9171.

Effect of Pressure on Vertically Aligned ZnO Nanorods for Piezoelectric Nanogenerator Application

Ashutosh Kumar[1,a], Satya Prakash Singh[1,b], and Vinay Pratap Singh[2,c]

[1] *Department of Physics, Christ Church College Kanpur, Kanpur, Uttar Pradesh, India- 208001.*
[2] *Department of Applied Sciences and Humanities, United College of Engineering and Research, Prayagraj, India- 211010*

[a] ashutoshais@gmail.com
[b] satya1209prakash@gmail.com
[c] vinay.phy@gmail.com

Abstract

The piezoelectric characteristics of zinc oxide (ZnO) nanorods and their prospective uses in energy harvesting, sensing, and nanogenerators have pave off a lot of interest recently. In present work, highly vertically aligned ZnO nanorods grown over Si substrates by hydrothermal method. ZnO nanorods were grown in a two-step process. First an optimum ZnO seed layer developed on a n-type Si wafer by sol-gel method, with particle size of diameter ~ 40 nm as a nucleation site. Subsequently nanorods grown on those sites with the range of length between 250 to 400 nm. These nanorods were examined by FESEM and phase was confirmed with XRD. Study of pressure effect in a Teflon-lined stainless-steel autoclave was performed at 5 bar pressure.

Keywords: Sol-gel, Spin Coating, Vertically Aligned ZnO nanorod, Piezoelectric.
Received 27 January 2025; First Review 23 February 2025; Accepted 23 February 2025

*** Address of correspondence**
Dr. Satya Prakash Singh
Department of Physics, Christ Church College Kanpur, Kanpur, Uttar Pradesh, India- 208001.

Email: satya1209prakash@gmail.com

How to cite this article
Ashutosh Kumar, Satya Prakash Singh, and Vinay Pratap Singh, Effect of Pressure on Vertically Aligned ZnO Nanorods for Piezoelectric Nanogenerator Application, J. Cond. Matt. 2024; 02 (02): 99-103.

Available from:
https://doi.org/10.61343/jcm.v2i02.64

Introduction

A lot of emphasis during the past few years has been seen in the development of nanostructured metal oxides-based chemical, biological and thermo-mechanical sensors. Recently, ZnO nanorods have attracted a lot of attention because of their distinctive qualities and broad range of applications [1]. One-dimensional nanostructures in nanotechnology are notable for their exceptional mechanical, optical, and electrical characteristics, which make them perfect for a range of technological advancements [2]. The high aspect ratio, broad band gap, high surface area, and strong exciton binding energy of ZnO nanorods make them ideal for application in solar cells, light-emitting diodes, photodetectors, photocatalysts, and biosensors [3-7]. ZnO is a readily available, chemically stable, and non-toxic substance that is widely distributed throughout the earth. The extrinsic semiconductor ZnO, also referred to as an n-type semiconductor, has a high exciton-binding energy (60 meV) and a bandgap of about 3.37 eV [8–11]. The preparation of ZnO nanostructures, such as nanowires, nanorods, nanotubes, and nanoflowers, has attracted increasing interest nowadays [12-14]. ZnO can be produced physically using methods such as metal-organic chemical vapour deposition [15], sputtering [16], and molecular beam epitaxy [17]. However, because of the intricate nature of the equipment and the need for high temperatures and low pressures, such processes are costly. Therefore, chemical processes including hydrothermal deposition [18], chemical bath deposition [19], and electrochemical deposition [20] are economical, have the capacity to produce nanoparticles on a large scale, and are very effective for producing them for a variety of application possibilities.

The hydrothermal method has been followed for the growth of vertically aligned nanorods on fluorine doped tin oxide (FTO) coated glass substrates [21] and seedless substrates (Pt/Si, Au/Si, Cu plates, FTO, and ITO coated glass) [22] using zinc nitrate hexahydrate (ZNH) and hexamine as precursors. For the preparation of seed layer on silicon, glass, and FTO coated glass substrates, a sol-gel process using zinc acetate dihydrate (ZAD), ethanol and 2-methoxyethanol was reported [23]. A combination of the two solution processes- seed layer deposition and nanorods growth was reported by Romero et al. [24] who produced nanorods arranged in a flower-like structure on seeded silicon and glass substrates. M. Bakry et al. [25] reported

low-cost fabrication methods of ZnO nanorods and their physical and photoelectrochemical properties for optoelectronic applications. It has been reported that the size (especially the diameter) and shape of the ZnO nanorods greatly affects its properties to be used in applications like photocatalysis [26] and gas sensing [27]. Also, there are several reports on the importance of the seed layer to obtain ZnO nanorods of the desired size, morphology and areal density [28-30].

In this work, the hydrothermal growth of ZnO nanorods on Si/SiO_2 surface has been demonstrated without using any intermediate layer or surface modification. For this, first the ZnO seed layer deposition was optimized using the sol gel method. Then, a hydrothermal method was followed to grow vertically aligned, controlled, reproducible, and scalable zinc oxide nanorods.

Materials and Methods

In this work, the hydrothermal growth of ZnO nanorods on n-type Si surface has been demonstrated without using any intermediate layer or surface modification. For this, first the ZnO seed layer deposition was optimized using the sol gel method. For fabrication of seed layer, we used the precursors, namely, zinc acetate dihydrate (ZAD), isopropanol (IPA) and diethanolamine (DEA). A 0.75 M solution of ZAD in IPA was prepared by stirring at 50 °C for 60 minutes on a magnetic stirrer at 1000 rpm. Equimolar amount of DEA was added to the solution and further stirred for 20 minutes to form a clear and homogeneous solution. Stepped annealing was performed on the sol. for 2 hours to form a yellow-coloured sol to be used for seed layer deposition. The sol was spin coated onto cleaned n-type Si wafer at 4000 rpm for 20 seconds. These substrates were further heated at 400 °C for 15 minutes for hard baking. By this ZnO seed layer with particle size of diameter ~ 40 nm was prepared as a nucleation site.

For the growth of ZnO nanorods, aqueous solution of 2 mM solution of zinc nitrate hexahydrate (ZNH) with equimolar amount of hexamine were prepared in DI water by stirring at 50 °C for 1 hour. Nanorods of ZnO were grown on seed layer deposited substrates by placing the wafer in beakers containing these solutions and heating at 60 °C and 90 °C for 8 hours in an oven.

Characterization

The surface morphology, dimensions of the seed layer films and nanorods were examined by FESEM (TESCAN MIRA3). The X – ray diffraction (XRD) (PAN-analytical Xpert Powder diffractometer with CuKα radiation) analysis was carried out for phase identification.

Results and Discussions

Hydrothermal synthesis is one of the most commonly used methods for preparation of nanomaterials. It is basically a solution reaction-based approach. Hydrothermal synthesis can generate nanomaterials which are not stable at elevated temperatures. Nanomaterials with high vapor pressures can be produced by the hydrothermal method with minimum loss of materials. The compositions of nanomaterials to be synthesized can be well controlled in hydrothermal synthesis through liquid phase or multiphase chemical reactions. It is important to obtain nanoparticles of the desired size and morphology as it affects various properties pertaining to a particular application. The size distribution, homogeneity throughout the entire area, and crystal orientation of the seed layer determine the characteristics of ZnO nanorods developed over it [28, 31]. The dependence of the sensing properties [32] and the photocatalytic properties [33] on the size of the nanoparticles and the microstructural characteristics of the seed layer have also been reported earlier.

During the preparation of sol for the seed layer deposition using IPA as the solvent, the salt ZAD disintegrates to form ions [34]. The complexing agent DEA forms bond with the cation and stabilizes the sol gel. Properties of the solvent, namely, the boiling point and the viscosity of the solvent have been reported to affect the size, homogeneous distribution and preferred orientation of the nanoparticles in the seed layer [35]. The shape and size of the scattered nanoparticles in the sol is depend on diffusion time and the time needed for clusters to form in the sol due to crystallisation [36]. If the diffusion time is less than the time required for cluster formation in the sol, rough aggregates are formed in an oriented manner after crystallization. Therefore, we used a novel two-step liquid phase annealing of the sol to control the size, distribution and morphology of the seed particles in the sol which subsequently resulted in good quality seed layer upon film deposition.

The novel two-step liquid phase annealing accelerated the process of diffusion, enhanced the solubility of the chemical groups in the alcohol which were newly formed as a result of the reaction between ZAD and DEA leading to increased formation of the Zn-O groups throughout the sol. This leads the formation of liquid clusters in an oriented manner. These clusters eventually crystallized as individual nanoparticles after spin coating and baking. It is resulted in an improved morphology of seed layer with discrete nanoparticles of uniform size of ~ 40 nm throughout the substrate, as shown in Figure 1. The n-type substrates were initially heated (soft bake at 250 °C and kept for 10 minutes) and hard baked at 400 °C for 15 minutes immediately after spin coating to remove the solvent, facilitate nucleation, and align the seed crystals.

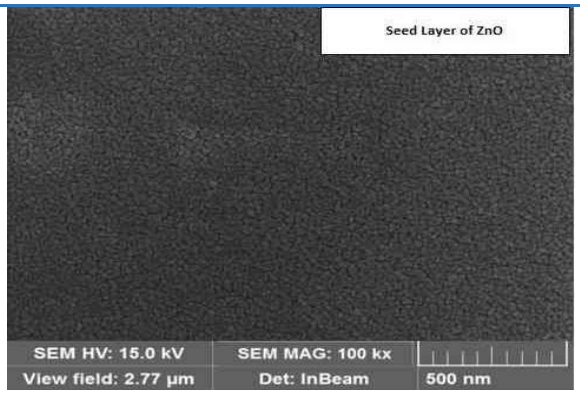

Figure 1: Morphology of ZnO seed layer nanoparticle on Si wafer

The room temperature X-Ray Diffraction (θ – 2θ scan) spectra for the ZnO thin films annealed at temperature of 400 °C is shown in Figure 2. It is evident from Figure 2 that the seed layer of ZnO film shows the polycrystalline behaviour of the film. The intensity of three major peaks corresponding to (0 1 0), (0 0 2) and (0 1 1) Miller planes are clearly observed in XRD pattern. The crystallographic characteristics of the films have been studied using the *'Checkcell'* software and compared with the data of Joint Committee on Powder Diffraction Standards (JCPDS# 79−0206). The XRD data of the annealed thin films fitted well with hexagonal structure of space group $P6_{3mc}$ and calculated lattice parameters are $\boldsymbol{a}$ = 0.3255± 0.0001, $\boldsymbol{b}$ = 0.3255± 0.0001 and $\boldsymbol{c}$ = 0.5217± 0.0001.

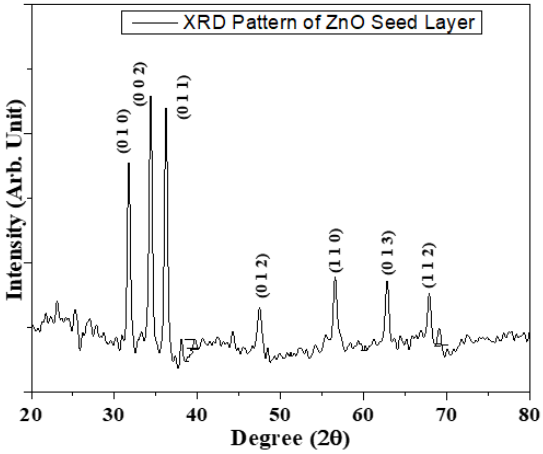

Figure 2: X–ray diffraction pattern of ZnO films.

The diameter and length of nanorods are influenced by the thickness of the seed layer. According to reports, a thinner seed layer encourages the formation of longer nanorods than a thicker one [37]. The seed layer's surface roughness, grain size, and crystal structure all affect how the nanorods align with the substrate [38]. The growth of ZnO nanorods is directly affected by the decomposition of hexamine ($C_6H_{12}N_4$), which was used to grow highly anisotropic nanorods by selectively capping non polar planes of ZnO crystal by the highly water-soluble non-ionic amine derivative. The nanorods were grown over the seeded substrates with varying parameters of temperature and time. The nanorods synthesis was performed at two different temperatures: 60 °C and 90 °C by using concentration of 2mM growth solution for synthesis time 4 hours and 8 hours, under atmospheric pressure. However, formation of nanorods was not observed at growth temperature 60 °C for synthesis times 4 hours and 8hours.

ZnO nanorods with uniform distribution were obtained at 90 °C in all the cases (Figure 3). Cross-sectional FESEM images of these ZnO nanorods for synthesis time of 4 hours and 8 hours are shown in Figure 4 and Figure 5. The dimensions, orientation and the number density of nanorods significantly varied with the precursor concentration and time at the same synthesis temperature. Also, it was observed that, a synthesis time of 4 hours led to the formation of nanorods having a relatively low number density. Nanorods with uniform distribution were obtained at 90 °C in the lengths between 250 to 400 nm for synthesis time of 8 hours.

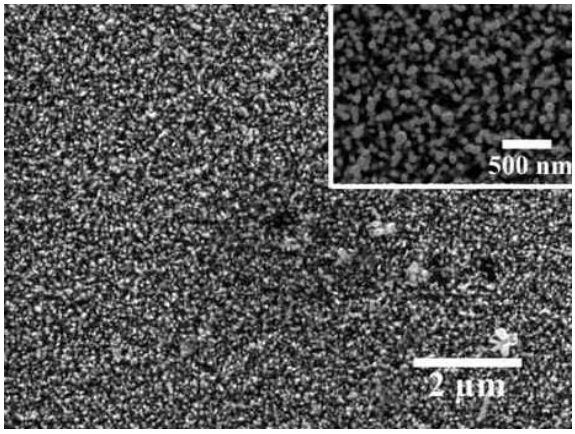

Figure 3: FESEM image of ZnO nanorods in lower magnification surface view, (inset) higher magnification surface view at 90 °C.

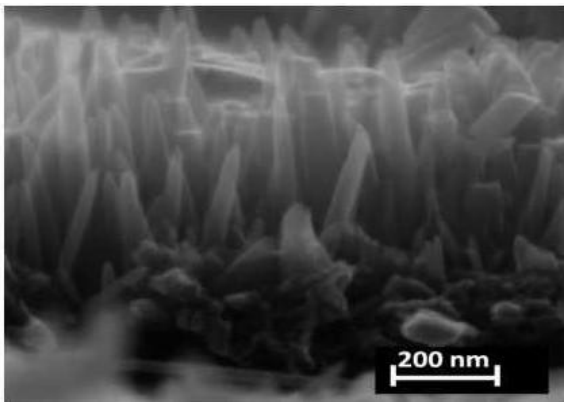

Figure 4: Cross sectional view at 90 °C of ZnO nanorods for synthesis time 4 hours.

The results of this study indicate that there is a threshold temperature for nanorod development at which nanorod formation occurs, and also synthesis time affect nucleation

and subsequent nanorod formation. Considering all the above observations in our experiments, the best growth condition was found to be for a temperature of 90 °C and synthesis time of 8 hours.

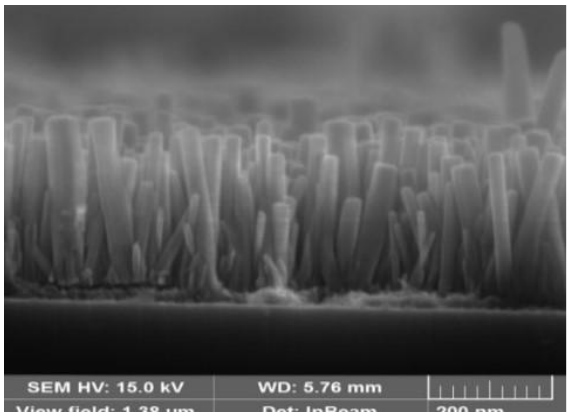

Figure 5: Cross sectional view at 90 °C of ZnO nanorods for synthesis time 8 hours.

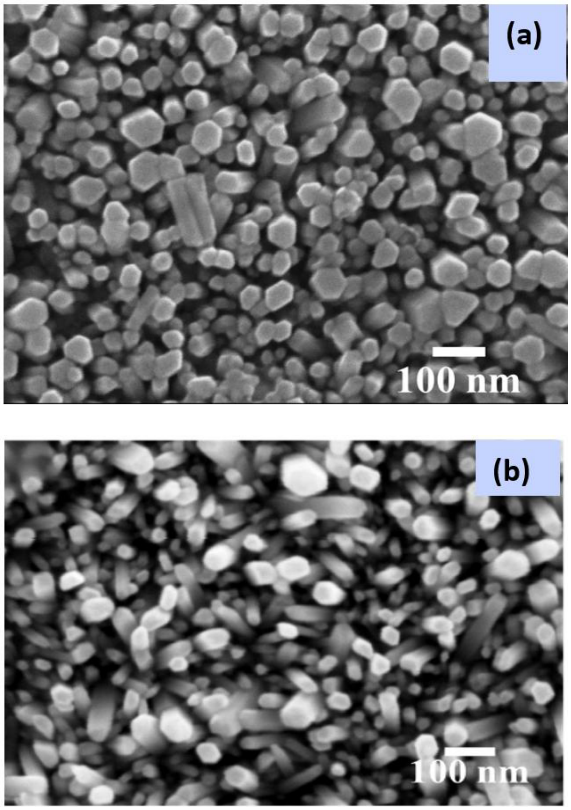

Figure 6: FESEM image of ZnO nanorods grown at different external pressures (a) 0 bar (b) 5 bar.

We have examined the impact of pressure on the growth solution during the hydrothermal synthesis of ZnO nanorods in an autoclave lined with Teflon. A decrease in the length of ZnO nanorods deposited on Zinc foils by a different method with increase in pressure has been reported earlier [39]. The FESEM images of the grown nanorods with varying pressure are shown in Figure 6 (a and b). The nanorods dimensions were measured after synthesis at each pressure. The diameter of the nanorods decreased with increased growth pressure till 5 bar and no significant change in the length was observed. We attribute the declining pattern in the diameter of nanorods to the faster diffusion of reactants from the hydrothermal solution to the surface of the seed layer on the application of pressure, leading to faster collision and hence, oriented attachment of nanoparticles. This prevents the lateral growth of the nanoparticles and hence a decrease in the diameter.

We want to mention here that the nanoparticles sizes in the seed layer affect the sizes of the subsequently grown nanorods. But, by the use of pressure, this constraint is overcome, that is, fine diameter nanorods could be obtained without reducing the seed size or size of nanoparticles in the reacting solution.

Conclusion

Hydrothermal growth of dense and vertically aligned ZnO nanorods on n-type Si substrate with controlled dimensions was demonstrated. The seed layer deposition was optimized with significant improvement in the film quality. The best condition for the growth of nanorods was determined to be for a temperature of 90 °C for 8 hours using 2 mM precursor concentration. The effect of vertical pressure was also explored on the dimensions of the nanorods during the hydrothermal growth. The nanorods diameter was found to be decreasing with increasing pressure. Accordingly, nanorods with the required diameter can be obtained by the application of the appropriate amount of pressure without having to change the underlying seed layer on the substrate. These ZnO nanorods will be further used for fabrication of Piezoelectric Nanogenerator.

Acknowledgement

The authors are thankful to Prof. Joseph Daniel, Principal of Christ Church College, Kanpur for the academic assistance. The authors are also thankful to central instrumentation facility of BIT Mesra, Ranchi for characterization of samples.

References

1. P K Aspoukeh, A A Barzinjy and S M Hamad. Int. Nano Lett., 12(2): 153–168, 2022.
2. Z Tang, J Zhang and Y. Zhang. Adv. Funct. Mater., 32(11): 2113192, 2022.
3. F Qiao, K Sun, H Chu, J Wang, Y Xie, L Chen and T Yan. Battery Energy, 1(1): 20210008, 2022.
4. Md. A Rahman, S M N Mamun, A K M A Hossain and C Ton-That**.** ACS Appl. Nano Mater., 6(17): 15757–15763, 2023.
5. L. Chu, C. Xu, W. Zeng, C. Nie and Y. Hu. IEEE Sens. J., 22(8): 7451–7462, 2022.

6. P G Ramos, L A Sánchez and J M Rodriguez. J Sol-Gel Sci Technol, 102(1):105–124, 2022.
7. M Saeed et al. Chem. Rec., Chem. Rec., 24(1): e202300106, 2023.
8. H Rai and N J M T P Kondal. Mater. Today Proc., 48: 1320–1324, 2022.
9. I Ayoub, V Kumar, R Abolhassani, R Sehgal, V Sharma, R Sehgal, H C Swart and Y K Mishra. Nanotechnol. Rev., 11(1): 575–619, 2022.
10. R Rasmidi, M Duinong and F P Chee. Radiat. Phys. Chem., 184: 109455, 2021.
11. C V Manzano, L Philippe and A Serrà. Crit. Rev. Solid State Mater. Sci., 47(5): 772–805, 2022.
12. M S Krishna, S Singh, M Batool, H M Fahmy, K Seku, A E Shalan, S Lanceros-Mendez and M N Zafar. Mater. Adv., 4(2): 320–354, 2023.
13. B Clarke and K J S Ghandi. Small, 19(44): 2302864, 2023.
14. A F Abdulrahman and N M Abd-Alghafour, Solid-State Electron., 189: 108225, 2022.
15. Q C Bui, G Ardila, H Roussel, C Jiménez, I Gélard, O Chaix-Pluchery , X Mescot, S Boubenia , B Salem and V Consonni. Mater. Adv., 3(1): 498–513, 2022.
16. G Wisz, P Sawicka-Chudy,A Wal, P Potera, M Bester, D Płoch, M Sibiński, M Cholewa and M Ruszała. Appl. Mater. Today, 29: 101673, 2022.
17. J A Mathew, V Tsiumra, J M Sajkowski, A Wierzbicka, R Jakiela, Y Zhydachevskyy, E Przezdziecka, M Stachowicz, A KozaneckiJ. J. Lumin., 251: 119167, 2022.
18. A Al-Rasheedi et al. *Appl. Phys. A.,* 128(9): 782, 2022.
19. P B More, S B Bansode, M Aleksandrova, S R Jadkar and H M Pathan. ES Energy Environ., 22: 983, 2023.
20. C V Manzano, L Philippe and A Serra. Critical Reviews in Solid State and Materials Sciences, 47(5): 772-805, 2021.
21. S Lee, B K Roy and J Cho. Jap. J Appl Phy., 52(5S1): 05DA0952, 2013.
22. Z Zheng, Z S Lim, Y Peng, L You, L Chen, and J Wang. Sci. Rep., 3: 2434, 2013.
23. K H Kim, K Utashiro, Y Abe and M Kawamura. Int J Electrochem Sci., 9: 2080-9, 2014.
24. S López-Romero, P Santiago and D Mendoza. Advanced Science Letters, 10:133-7, 2012.
25. M Bakry, W Ismail, M Abdelfatah and Abdelhamid El-Shaer. Sci Rep 14(1): 23788 (2024).
26. A McLaren, T Valdes-Solis, G Li and S C Tsang. J Am Chem Soc., 131:12540-1, 2009.
27. L Liao, H B Lu, J C Li, H He, D F Wang, D J Fu, C Liu and W F Zhang. *J. Phys. Chem. C*, 111(5): 1900-3, 2007.
28. J Song and S Lim. *J. Phys. Chem. C*, 111(2): 596-600, 2007.
29. Y Tao, M Fu, A Zhao, D He and Y Wang Y. J. Alloys Compd. 489: 99-102, 2010.
30. M Teng, G Min, Z Mei, Z Yanjun and W Xidong. Nanotechnology, 18: 035605, 2007.
31. J J Dong, C Y Zhen, H Y Hao, J Xing, Z L Zhang, Z Y Zheng and X W Zhang. Nanoscale Res Lett, 8: 378 2013.
32. Y Ma, W L Wang, K J Liao and C Y Kong. Journal of Wide Bandgap Materials, 10: 113-20, 2002.
33. A C Dodd, A J McKinley, M Saunders and T Suzuki. J Nanopart Res, 8: 43-51, 2006.
34. L Armelao, M Fabrizio, S Gialanella and F Zordan. Thin Solid Films, 394(1-2): 89-95, 2001.
35. Y Ohya, H Saiki and Y Takahashi. JOURNAL OF MATERIALS SCIENCE, 29: 4099-103, 1994.
36. C Pacholski, A Kornowski and H Weller. Angew Chem Int Ed Engl. 41(7): 1188-91, 2002.
37. H Ghayour, H R Rezaie, S Mirdamadi and A A Nourbakhsh. Vacuum, 86: 101-5, 2011.
38. R M Ziff, E D McGrady and P Meakin. The Journal of Chemical Physics, 82: 5269-74, 1985.
39. L Z Pei, H S Zhao, W Tan, H Y Yu, Y W Chen, C G Fan and Q-F Zhang. Physica E: Low-dimensional Systems and Nanostructures, 42: 1333-7, 2010.

The Luminescence in Self Activated and Sm^{3+} Rich Garnet Phosphor $Sr_2NaZn_2V_3O_{12}$ Prepared by Solid-State Reaction

G. C. Vandile[1,a], D. V. Nandanwar[1,b], A. K. Nandanwar[2,c], D. W. Akhare[1,d]

[1] *Shri Mathuradas Mohota College of Science, Nagpur-440009, India.*
[2] *J. M. Patel Arts, Commerce & Science College, Bhandara-441904, India.*

[a] ganesh9326wandile@gmail.com
[b] dvnandanwar@gmail.com
[c] amarknjmpc@gmail.com
[d] dhanashriakhare2002@gmail.com

Abstract

A new self-activated vanadate garnet phosphor $Sr_2NaZn_2V_3O_{12}$ and doped with Sm^{3+} vanadate garnet phosphor $Sr_2NaZn_2V_3O_{12}$ were produced by a simple conventional solid-state reaction that calcined for six hours at 950 degrees Celsius and then left to cool to room temperature. Vanadate garnet phosphor is utilized for high-performance tasks because of its excellent strength and hardness. The single-phase garnet structures in the prepared materials have been verified by X-ray diffraction (XRD) and Rietveld polishing. The behaviours of rare earth-doped luminescence and self-activated luminescence have been thoroughly examined. The prepared $Sr_2NaZn_2V_3O_{12}$ compound was observed a wide-band at wavelength of 485 in visible region of greenish emission that originates due to VO_4^{3-} emission. With lifetime measurement and photoluminescence (PL), In $Sr_2NaZn_2V_3O_{12}$: Sm^{3+} garnet-type phosphors, the energy transfer characteristics from VO_4^{3-} (vanadate) to Sm^{3+} (samarium trivalent) ions have been shown. While excitation was reported at 485 nm for vanadate garnet phosphor and 601 nm for samarium-rich garnet phosphor, the produced materials were excited by 338 nm for vanadate and 405 nm for Sm3+ rich phosphor. Scanning electron microscopy was used to study the topography and morphology. The findings suggest that Sm^{3+} doped $Sr_2NaZn_2V_3O_{12}$ garnet phosphors and self-activated $Sr_2NaZn_2V_3O_{12}$ exhibit significant promise for use in near-UV stimulated white LEDs.

Keywords: Luminescence, $Sr_2NaZn_2V_3O_{12}$:Sm^{3+}, garnet phosphor, vanadate garnet phosphor.
Received 29 January 2025; First Review 19 February 2025; Accepted 21 February 2025

*** Address of correspondence**
Dr. G. C. Vandile
Shri Mathuradas Mohota College of Science,
Nagpur-440009, India.

Email: ganesh9326wandile@gmail.com

How to cite this article
G. C. Vandile, D. V. Nandanwar, A. K. Nandanwar, D. W. Akhare, The Luminescence in Self Activated and Sm^{3+} rich Garnet Phosphor $Sr_2NaZn_2V_3O_{12}$ prepared by Solid-State Reaction, J. Cond. Matt. 2024; 02 (02): 104-109.

Available from:
https://doi.org/10.61343/jcm.v2i02.87

Introduction

There are numerous technological uses for inorganic phosphors in materials science. There is currently a high demand for the design and development of multifunctional phosphors. In addition to temperature sensing and solid-state lighting, inorganic phosphors have a wide range of applications in bio-sensing, anti-counterfeiting, and latent fingerprint detection [1]. The non-contact thermometry is related for utilizing thermographic phosphors with optical thermometry. To use the traditional approach, the thermometer has to come into direct touch with the bodies of interest. [2].

The classes of multi-sublattice oxides that are found as natural minerals all over the world are called garnets. $Ca_3Al_2Si_3O_{12}$ (Grossular), $Mg_3Al_2Si_3O_{12}$ (Pyrope), $Mg_3Fe_2Si_3O_{12}$ (Andrade), $Fe_3A_{l2}Si_3O_{12}$ (Almandite), $Mn_3Al_2Si_3O_{12}$ (Spessartine), $Mg_3Cr_2Si_3O_{12}$ (Knorringite), $Ca_3Cr_2Si_3O_{12}$ (Uvarovite), and others are the most well-known. After the invention of the LASER and MASER in the 20th century, significant attempts were made for creating an extensive array of synthesized garnet-type crystals with different optical properties [3]. The most commonly utilized garnet-type phosphor material for a variety of lighting device applications is garnet (YAG): $Y_3Al_5O_{12}$. Among the several simple garnet compounds that are now generated utilizing various crystal growth and sintering techniques [4]. The heavy Sm^{3+} doped $Sr_2NaZn_2V_3O_{12}$ (SNZVG) based garnets are of particular interest these days for use in white LEDs. Additionally, $Sr_2NaZn_2V_3O_{12}$ garnet doped with Sm3+ has recently been established as an effective pro-convention medium for white LEDs [5].

The choice of the host material is crucial in this situation. The host material must effectively facilitate energy transfer among the luminescence centers and possess a substantial bandgap and low phonon energy, among other

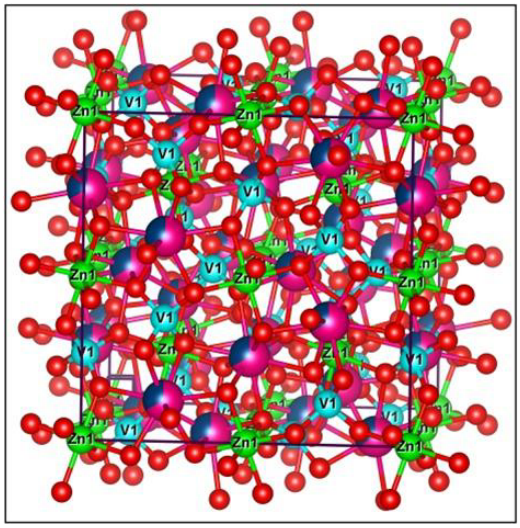

Figure 1(a): The Ball and Stick representation of $Sr_2NaZn_2V_3O_{12}$.

characteristics. Because of the $^3T_{1,2}$ - $^1A_1$ transitions, vanadate-rich hosts are well known for their significant absorption and luminescent that activates on its own [6-7]. The samarium trivalent ions rich vanadate host configuration facilitates the passage of phonon energy from VO_4^{3-} to Sm^{3+}. Phonon-assisted energy transfer from VO_4^{3-} to Sm^{3+} is facilitated by the Sm-activated vanadate host structure. It is possible to design a phosphor with improved optical sensitivity by adjusting the emission characteristics of the structure. Currently, garnet-structured hosts are recognized for their ability to tune the photo-physical response through polyhedral substitution and the ensuing correlation of structure properties [8]. Garnet-type hosts have the usual chemical formula $A_3B_2C_3O_{12}$, where A, B, and C represent dodecahedral sites, octahedral sites, and tetrahedral sites, respectively, and cubic crystallize structure with Ia-3d space group. Figure 1(a, b) show the Ball-Stick representation and Polyhedral representation of $Sr_2NaZn_2V_3O_{12}$ respectively.

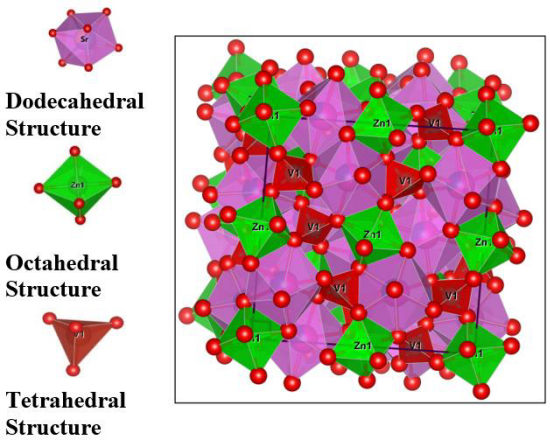

Figure 1(b): The Polyhedral representation of $Sr_2NaZn_2V_3O_{12}$.

Materials with garnet structures are renowned for their distinctive compositional diversity and structural framework, which satisfy the needs of a range of lighting and sensing applications [9]. As a result, Sm^{3+}-activated vanadate garnet-based phosphors are a great option for both w-LEDs and orange-red LEDs. In general, vanadate garnet has low phonon energy, which is necessary for improved luminescence characteristics. Our team has recently conducted a thorough investigation into the photoluminescence of the Sm^{3+}-activated $Sr_2NaZn_2V_3O_{12}$ system [10]. Because of its superior luminescence characteristics, $Sr_2NaZn_2V_3O_{12}$ (SNZVG) is chosen as the host material in order to fill this knowledge gap regarding the potentiality of vanadate garnets [11]. Sm^{3+} is another prominent orange-red emitter ion among RE ions. The electronic transitions from $^4G_{5/2}$ to $^6H_{5/2}$, $^4G_{5/2}$ to $^6H_{7/2}$ and $^4G_{5/2}$ to $^6H_{9/2}$ are represented by the orange-red emission. White light emitting diodes (w-LEDs) have overtaken conventional lighting sources in recent years because of their many advantages, which include increased efficiency, lower energy and power consumption, longevity, environmental friendliness, and superior thermal and chemical stability. These beneficial characteristics of w-LEDs have facilitated their use in communication, display devices, and solid-state lighting [12].

Experimental Procedures

(1) Chemicals and Synthesis:

Using a solid-state reaction method, the polycrystalline phosphors S $Sr_2NaZn_2V_3O_{12}:Sm^{3+}$ were prepared. The chosen reagents, $SrCO_3$, Na_2CO_3, ZnO, and NH_4VO_3 and Sm_2O_3 (>99%, ACS MERCK), were combined using an agate mortar and pestle after being weighed in a stoichiometric ratio. All mixture of powder form was then calcined for six hours at 950 degrees Celsius. The powders were homogenized and sent for further characterizations after calcination.

(2) Characterization Techniques:

The X-ray powder diffraction method (Rigaku Miniflex 600, 40 kV and 30 mA, Cu Kα wavelength 0.154059 nm) was used to identify the phase. Using a step size of 0.04 degree and a continuous scanning rate of 2θ between 10 and 80 degrees, phase formation was determined at a rate of 4°/min using Rietveld analysis. Data from powder diffraction were acquired by means of the FullProf_Suite computer program. Using a photomultiplier tube running at a 135 W Xeon lamp as the excitation lamp, the photoluminescence spectra were recorded at atmospheric temperature using a fluorescence spectrophotometer (F-7000 FL, 1914-024, Version-5J14000 03). Colour chromaticity data were used to compute the lifetimes and colour coordinates. FE-SEM JEOL, JSM-6500F with an 80

W Xeon light source and a 25 kV high tension voltage between the anode and cathode electron accelerating voltage was used to optimize the topographical and compositional characterizations.

Results and Discussion

Phase Identification by XRD Pattern

The crystalline structure and phase homogeneity of vanadate garnet and Sm^{3+} doped $Sr_2NaZn_2V_3O_{12}$ (SNZVG) materials are examined using XRD patterns. The XRD patterns of SNZVG are displayed in Figure 2(a).

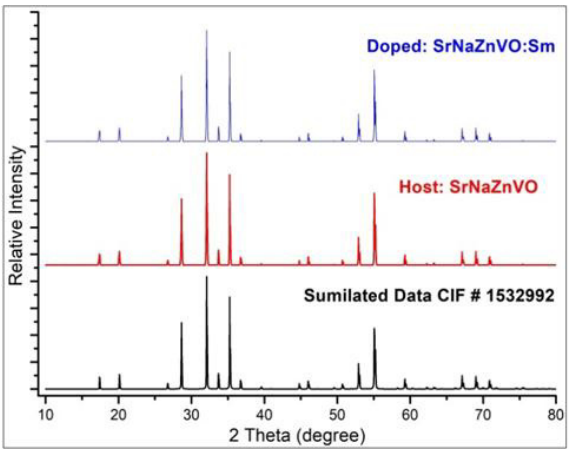

Figure 2(a): XRD patterns of the self-activated vanadate garnet $Sr_2NaZn_2V_3O_{12}$, 8% Sm^{3+} doped garnet $Sr_2NaZn_2V_3O_{12}$:Sm^{3+} and simulated CIF # 1532992 is also given for comparison.

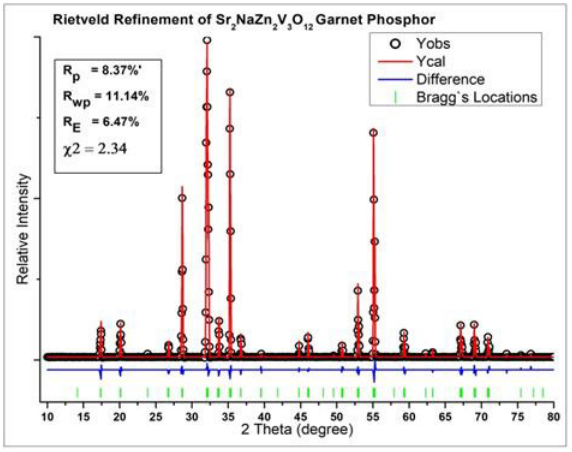

Figure 2(b): The Rietveld Refinement of vanadate garnet phosphor $Sr_2NaZn_2V_3O_{12}$: observed intensities (black circles), red lines are calculated patterns and difference between observed, calculated intensity is indicated by blue line and tick-greenish lines are Bragg`s locations.

The Rietveld polishing (refinement) pattern of SNZVG and SNZV: 8% Sm^{3+} indexed to the cubic structure having space group as Ia-3d (230, Oh^{10}) are shown in Figure 2(b). $Sr_2NaZn_2V_3O_{12}$ is used in all single-phase, isostructural compositions (simulated CIF # 1532992). It has been established that adding Sm^{3+} to the dodecahedral site has no effect on the samples' crystallinity. In contrast to the general stoichiometry, Sr^{2+} and Na^{+} form Sr/NaO8 dodecahedra and the dodecahedral site (24c) is occupied with 2/3 and 1/3. Zn^{2+} ions are completely occupied in the octahedral site (16a), V^{5+} ions are completely occupied in the tetrahedral site (24d), and O^{2-} ions are completely occupied in the general sites (96h). The dodecahedral site is substituted with the lanthanide ions Sm^{3+}. Table 1 list the crystallographic information and refined unit cell parameters for the $Sr_2NaZn_2V_3O_{12}$:Sm^{3+} phosphor. The Sm3+ occupancy in the dodecahedral site is confirmed by the reliability parameters that were obtained. The lattice parameter of the $Sr_{1.84}Sm_{0.08}Na_{1.08}Zn_2V_3O_{12}$ system is 1.22317 nm. Furthermore, micro-strain (ε = 0.0003841) determined that lattice contraction occurs because the larger Sr^{2+} ion is replaced by the smaller ionic radii of Sm^{3+}.

Excitation and Emission of Photoluminescence

Figure 3(a) depicts the excitation spectrum of $Sr_2NaZn_2V_3O_{12}$: Sm^{3+}. The material was excited at 338 nm for vanadate garnet phosphor and at 403 nm for samarium doped garnet phosphor. The excitation spectrum was recorded at 485 nm for VO_4^{3-} in transitions from 1A1 -1T2 and $^1A_1$ - $^1T_1$ and at 601 nm for Sm^{3+} in transition from $^6H_{5/2}$ to $^4K_{1/2}$ as shown in Figure 6(b).

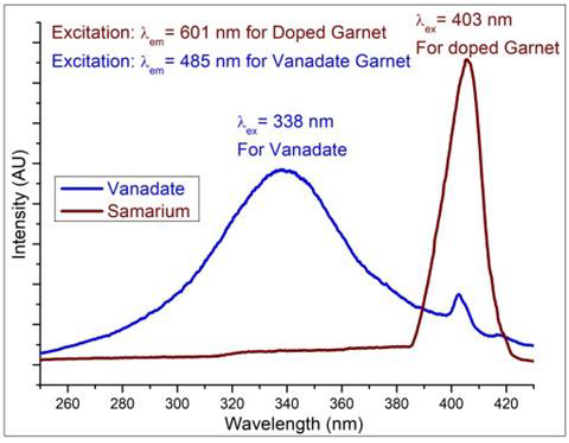

Figure 3(a): Excitation spectrum of both doped and un-doped vanadate phosphor.

Figure 3(b) displays the photoluminescence emission (PL) spectra of vanadate garnet phosphor and the emission wavelength was observed at 485 nm in transition $^3T_{1,2}$ to $^1A_1$. This transfers the energy to samarium doped garnet phosphor. Figure 3(c) displays the emission spectrum of $Sr_2NaZn_2V_3O_{12}$: Sm^{3+} at emission wavelengths 564 nm in electronic transitions from $^6G_{5/2}$ to $^6H_{5/2}$, 601 nm in electronic transitions from $^6G_{5/2}$ to $^6H_{7/2}$ and 648 nm in electronic transitions from $^6G_{5/2}$ to $^6H_{9/2}$ but more intense peak was found at 601 nm in transition $^6H_{7/2}$.

It is observed that VO_4^{3-} emission decreases with Sm^{3+} concentration. Nonetheless, the Sm^{3+} band's intensity rises with concentration; at 0.08 Sm^{3+}, the maximum intensity is

achieved. The variation of intensity vs Sm^{3+} concentration is shown in Figure 3(d).

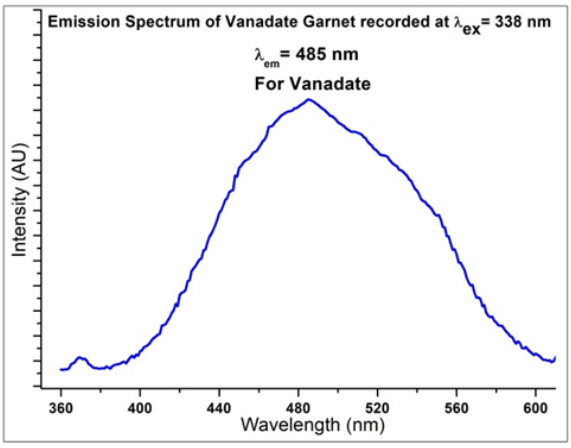

Figure 3(b): Emission spectrum of vanadate garnet phosphor

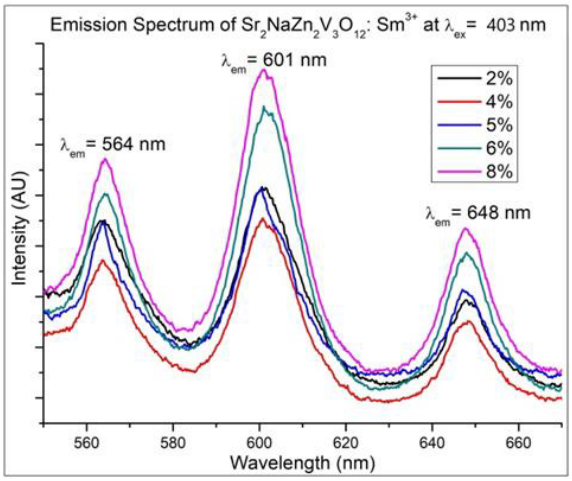

Figure 3(c): Emission spectrum of garnet phosphor $Sr_2NaZn_2V_3O_{12}$: xSm^{3+} (x = 2%, 4%, 5%, 6% and 8%)

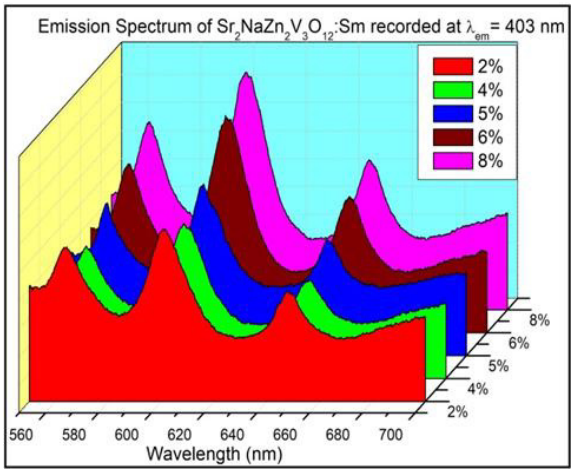

Figure 3(d): Variation of intensities due to Sm^{3+} concertation and 3D view of the $Sr_2NaZn_2V_3O_{12}$: Sm^{3+}

Topographical and Compositional characterizations

Table 1: The crystal structural parameters and refined data parameters of vanadate garnet phosphor of $Sr_2NaZn_2V_3O_{12}$.

Crystal Structure Parameters	**$Sr_2NaZn_2V_3O_{12}$ Garnet**	**Refinement Parameters**	**$Sr_2NaZn_2V_3O_{12}$ Garnet (refined)**
Crystal lattices	Cubic	Chi^2	2.34
Space group	Ia-3d (230)	Factors R_p (%)	8.37
(hkl)	(311) at 2θ = 32.08°	Factors R_{wp} (%)	11.14
lattice parameters	1.22317 nm	Expected R_w (%)	6.47
Error in a	1.8 % (compare with CIF # **1532992**)	**Wyckoff Positions**	
Volume of unit cell	1.774.505 nm^3	Sr^{2+} (2/3) + Na^+ (1/3)	24c
Z	8	Zn^{2+}	16a
Average Crystalline Size **D_{obs}**	43.43547 nm	V^{5+}	24d
Average Crystalline Size **D_{cal}**	45.13333 nm	O^{2-} (for **Ia-3d**)	96h
% error in Crystalline size D	3.90 %	**Atomic Locations**	

β (FWHM) at dominate peak (β_{max})	0.002094393 rad (0.12 degree)	**Ions**	**x**	**y**	**z**	**Occp**
		Sr^{2+}	0.125	0	0.25	0.667
Microstrain (ε)	0.0003841	Na^+	0.125	0	0.25	0.333
Dislocation Density (**δ**)	$2.10379x10^{-4}$ per nm^2	Zn^{2+}	0	0	0	1
		V^{5+}	0.375	0	0.25	1
		O^{2-}	-	0.0526	0.1565	1

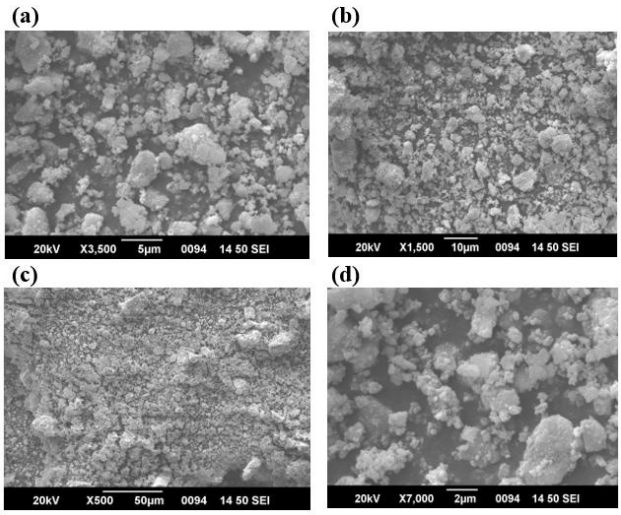

Figure 4(a-d): SEM photographs of $Sr_2NaZn_2V_3O_{12}$:Sm^{3+} garnet phosphor at different magnifications.

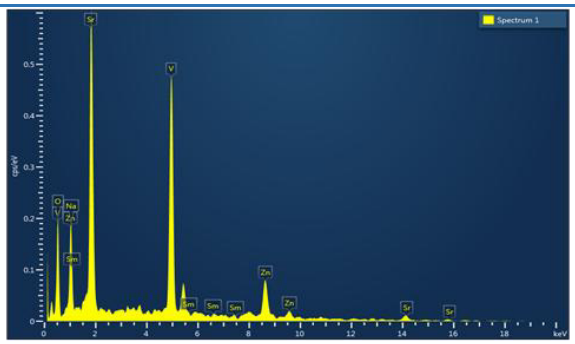

Figure 5: EDS of $Sr_2NaZn_2V_3O_{12}$:Sm^{3+} for chemical composition

SEM pictures of the synthesized $Sr_2NaZn_2V_3O_{12}$:Sm^{3+} garnet phosphors are shown in Figure 4(a-d) to analyse its morphology. It is discovered that the $Sr_2NaZn_2V_3O_{12}$:Sm^{3+} particle size and morphology are comparable, which is consistent with the average size of the crystallite of these materials. However, the morphology of every sample under study is a distinctive feature of garnet phosphor that was first documented [13]. Together with the theoretical composition, the measured chemical composition of $Sr_2NaZn_2V_3O_{12}$:Sm^{3+} garnet phosphoric is listed in Table 2. Considering the potential measurement error (< ±1%), it can be said that all samples exhibit good conformance to the theoretical and determined composition.

Table 2: The chemical composition of the prepared $Sr_2NaZn_2V_3O_{12}$:Sm^{3+} were determined by EDS and calculated.

Elements	O (%)	Sr (%)	V (%)	Zn (%)	Na (%)	Sm (%)	Total Wt %
EDS Data	22.86	27.71	28.07	16.35	3.97	1.03	100
Calculated Data	23.01	27.52	28.06	16.32	4.09	1.00	100

Colour Calculation by CIE Chromaticity Diagram

Figure 6(a) displays CIE coordinate of the vanadate garnet phosphor observed at (0.246, 0.317) and CCT was 11659.2 K. The CIE coordinators of Sm^{3+} -activated garnet phosphor for different concentrations are listed in Table 3. The colour purity was calculated 85.13% at dominant peak. The colour purity of the Sm^{3+} doped sample was increasing with concentration. The CCT (K), Colour Purity (%) and lifetime (ns) were calculated by equations (1), (2) and (3) respectively [13].

$$CCT\ (K) = -437r^3 + 3601r^2 - 6861n + 5514.31 \quad \text{- (1)}$$

Where, $r = \frac{(x-x_e)}{(y-y_e)}$ and $x_e = 0.3320$ & $y_e = 0.1858$ are chromaticity epicenters.

$$Colour\ Purity\ (CP) = \sqrt{\frac{(x-x_s)^2+(y-y_s)^2}{(x_d-x_s)^2+(y_d-y_s)^2}} \times 100 \quad \text{- (2)}$$

Where, (x, y) are CIE coordinates of sample (entire wavelengths range), (x_s, y_s) are Coordinates of UV Sours lamp for illuminant the sample (356 nm, 6W), (x_d, y_d) are dominant coordinates of sample (at peak wavelength).

$$\text{Average Life Time } (\tau) = \frac{\int t \times i(t)dt}{\int i(t)dt} \quad \text{- (3)}$$

Where, $i(t)$ is intensity count of the function of time t.

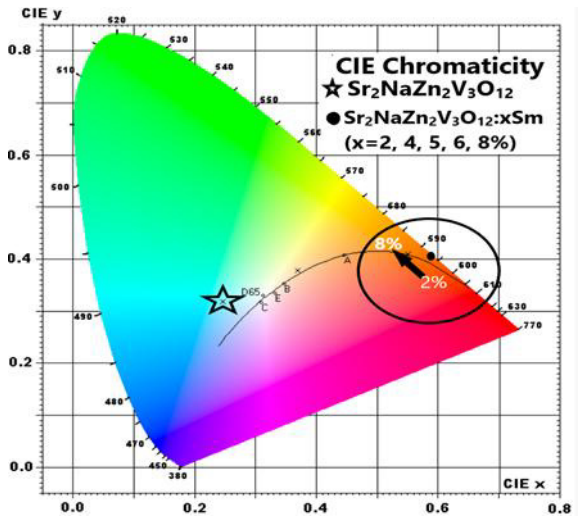

Figure 6(a): CIE digital photographic diagram of $Sr_2NaZn_2V_3O_{12}$:Sm^{3+} garnet phosphors.

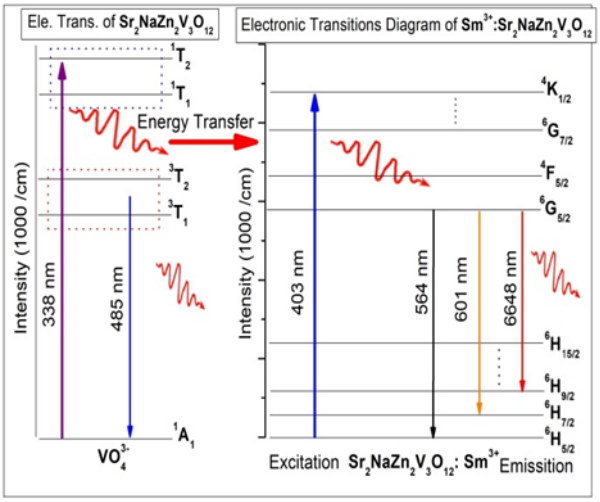

Figure 6(b): Vanadate (VO_4^{3-}) and Sm^{3+}: excitation and emission transitions with the energy transfer process between the respective energy levels.

Table 3: Colour coordinators of $Sr_2NaZn_2V_3O_{12}$:Sm^{3+} from CIE chromaticity.

Dopes: Sm	(x, y)	(x_d, y_d)	CCT (K)	CP (%)	Lifetime (ns)
0%	(0.246, 0.317)	(0.073, 0.185)	11659.2	73.65	516.4994
25	(0.551, 0.448)	(0.632, 0.368)	2040.42	84.23	616.3309
4%	(0.554, 0.445)	(0.632, 0.368)	2003.73	84.60	617.2414

5%	(0.556, 0.443)	(0.632, 0.368)	1983.75	84.86	618.2637
6%	(0.558, 0.441)	(0.632, 0.368)	1963.95	85.13	616.0152
8%	(0.558, 0.441)	(0.632, 0.368)	1964.21	87.71	616.6067

Conclusion

We have successfully prepared the vanadate (self-activated) and Sm^{3+} doped $Sr_2NaZn_2V_3O_{12}$ garnet phosphors using the solid-state procedure. The results of the XRD analysis show the prepared materials have a single-phase compound with a garnet structure. By examining at the luminescent features, we may conclude that energy transfer takes place from the vanadate (VO_4^{3-}) to the trivalent Sm^{3+} ions. With a maximum emission at 485 nm, $Sr_2NaZn_2V_3O_{12}$ (vanadate garnet) has a wide emission band encompassing 400–700 nm. The emission spectra for the Sm^{3+} doped $Sr_2NaZn_2V_3O_{12}$ phosphors consist of the wide-band emission at wavelength 485 nm (in visible region of greenish colour) and its emission as reflected to the f–f shifts due to Sm^{3+}. Because of the amount of energy transmission between VO_4^{3-} and the Sm3+ ions, the CIE parameters of $Sr_2NaZn_2V_3O_{12}$: Sm^{3+} garnet luminescence materials may be adjusted by varying the percentage of rare earth Sm3+ ions. According to the investigation and results, there is a great deal of promise for using the produced phosphor in near-UV stimulated white LEDs.

References

1. C. Wang, J. Zhou, L. Lulu and Q. Song, Part. Part. Syst. Charact., 35: 1700387, 2018.
2. S. van Herwaarden, Sens. Mater., 8: 373, 1996.
3. C. A. Geiger, the laboratory and technology Elements, 9 (6): 447–452, 2013.
4. J. Ueda and S. Tanabe, Human and Environmental Studies, Kyoto, 606- 8501, 2019.
5. A. Markovskyi, V. Gorbenko, T. Zorenko, T. Yokosawa, J. Will, E. Spiecker, M. Batentschuk, J. Elia, A. Fedorov and Y. Zorenko, Cryst. Eng. Comm. 23, 2021.
6. P. Du, Y. Hua and J. S. Yu, Chem. Eng. J., 352: 352, 2018.
7. H. Xie, T. Tsuboi, W. Huang, Y. Huang, L. Qin and H. J. Seo, J. Am. Ceram. Soc., 97:1434, 2018.
8. A. Bindhu, J. I. Naseemabeevi and S. Ganesanpotti, Crit. Rev. Solid State Mater. Sci., 47: 621, 2021.
9. A. Bindhu, A. S. Priya, J. I. Naseemabeevi and S. Ganesanpotti, J. Alloys Compd., 893, 162246, 2022.
10. P. P. Lohe, D. V. Nandanwar, P. D. Belsare, and S. V. Moharil, AIP Conference Proceedings, 2104: 020015, 2019.
11. J. Li, B. Liu, G. Liu, Q. Che, Y. Lu and Z. Liu, J. Rare Earths, 2022.
12. S. Kaur, A.S. Rao and M. Jayasimhadri, J. Lumin. 202: 461-468, 2018.
13. M. D. Birowosuto, M. Isnaeni, C. de Mello Doneg_a, and A. Meijerink, J. Appl. Phys. 118: 123105, 2015.

Investigation of Structural Changes in Bismuth Substituted $SrFe_{12}O_{19}$ Compound Using In-Situ Raman Spectroscopy

M. R. Sahoo[1,4,a], A. Barik[2,b], R. Ghosh[3,c], S. Mishra[4,d], J. Ray[5,e], S. Kuila[6,f], M. Mandal[1,g] and P. N. Vishwakarma[4,h]

[1] *Department of Physics, GITAM (Deemed to be University), Bangalore, Karnataka 562163, India*
[2] *Department of Physics, Madanapalle Institute of Technology and Science, Madanapalle, Andhra Pradesh 517325, India*
[3] *Department of Condensed Matter and Material Science, S. N. Bose National Center for Basic Science, Salt Lake, Kolkata 700106, India*
[4] *Department of Physics and Astronomy, National Institute of Technology, Rourkela, Odisha 769008, India*
[5] *School of Applied Sciences, Kalinga Institute of Industrial Technology (KIIT) Deemed to be University, Bhubaneswar, Odisha 751024, India*
[6] *Haldia Institute of Technology, ICARE Complex, Haldia, West Bengal 721657, India*

[a] msahoo2@gitam.edu, manas.bhupun@gmail.com
[b] alokbarik12345@gmail.com
[c] rubinaghosh.93@gmail.com
[d] subhankarmishra2427@gmail.com
[e] jashashree.rayfpy@kiit.ac.in
[f] souravbypass@gmail.com
[g] mmandal@gitam.edu
[h] prakashn@nitrkl.ac.in pnviisc@gmail.com

Abstract

The sol-gel auto-combustion method has been adopted for the preparation of bismuth (Bi) substituted strontium hexaferrite ($SrFe_{12}O_{19}$) polycrystalline compound. The substitution of bismuth has created significant distortion at various sites, which has been confirmed by the Raman spectra of $Sr_{1-x}Bi_xFe_{12}O_{19}$ (x = 0, 0.01, and 0.02). The compound SBFO1 (x = 0.01) is the highly strained out of three compounds. Again, the 2b and 12k site of SBFO1 is so much distorted that, the Raman peak associated to 12k site (i.e. 417.7 cm^{-1}) has been split into two peaks at 413.8 cm^{-1} and 432.9 cm^{-1}. The damping constant and spring constant calculated from the Raman data for validates the XRD data. The highest compressive volumetric strain nature of SBFO1 is well established by the lowest damping constant of SBFO1. The variation of the bond length associated to the different crystallographic sites well matches with the shifting of Raman peaks for that site. The same is again approved by the highest spring constant of SBFO1.

Keywords: Strain, Raman spectra, Distortion.
Received 30 January 2025; First Review 17 February 2025; Accepted 21 February 2025

*** Address of correspondence**
M. R. Sahoo
Department of Physics, GITAM (Deemed to be University), Bangalore, Karnataka 562163, India

Email: msahoo2@gitam.edu

How to cite this article
M. R. Sahoo, A. Barik, R. Ghosh, S. Mishra, J. Ray, S. Kuila, M. Mandal and P. N. Vishwakarma, Investigation of Structural Changes in Bismuth Substituted $SrFe_{12}O_{19}$ Compound Using In-Situ Raman Spectroscopy, J. Cond. Matt. 2024; 02 (02): 110-113.

Available from:
https://doi.org/10.61343/jcm.v2i02.109

Introduction

The strontium hexaferrite ($SrFe_{12}O_{19}$; SrM) plays a leading role in the field of magnetic recording, permanent magnet, and sensor industries due to its huge coercivity, high saturation magnetization, high chemical and physical stability along with the magnetoelectric property [1-2]. This SrM has a hexagonal crystal structure with space group $P6_3/mmc$, and one unit cell contains two formula units of SrM. Along the c-axis, two structural blocks, i.e., spinel S block ($Fe_2Fe_4O_8$) and the R block ($SrFe_6O_{11}$) are combined together as RSR*S* ('*' indicates a 180° rotation of R/S- block around the c-axis) to form the unit cell of SrM. The 12 iron ions are distributed in the five crystallographic sites, which are three octahedral sites (12k, 2a, and $4f_2$), one tetrahedral site ($4f_1$), and one bipyramid site (2b). The 12k has 6 Fe^{3+} ions, $4f_1/4f_2$ has 2 Fe^{3+} ions, and 2a/2b has one Fe^{3+} ion each. The 8 Fe^{3+} ions at 12k, 2a, and 2b sites are in

spin-up condition, and 4 Fe^{3+} ions at $4f_1$ and $4f_2$ sites are in spin-down condition. So, the resultant net magnetic moment comes out to be 20 μ_B/f. u. as the magnetic moments of each Fe^{3+} ion are $5\mu_B$[1].

Many authors have shown new attribution toward enhancing the magnetoelectric phenomena in the systems by breaking the symmetry of the system by displacing the iron atoms from their equilibrium position, which may be the 2b, 12k, or any other [3-4]. Therefore, the off-centering of iron atoms (at 12k / 2b site) influences magnetization, and magnetoelectric property is an open debate, which needs an improved knowledge of the disorderness created in the system. In the previous paper, the X-ray diffraction (XRD) measurement has confirmed the strain in the bismuth-substituted strontium hexaferrite. As Raman spectroscopy has been widely used to study the lattice vibration and stress evaluation, so here we will try to establish the effect of strain in the Raman spectral shift and phonon frequency [5-7]. This Raman scattering also offers an opportunity as a probe for the spin dynamics and to understand the magnetic properties of the system. The strain created in the crystallographic site and its influence on the Raman active phonons becomes important for understanding both fundamental and applied studies of this system.

Experimental details

The bismuth (Bi) substituted strontium hexaferrite ($Sr_{1-x}Bi_xFe_{12}O_{19}$, x = 0, 0.01, and 0.02 are prepared by the sol-gel auto combustion method. The commercially (MERCK) available strontium nitrate [$Sr(NO_3)_2$], and iron nitrate [$Fe(NO_3)_3{\cdot}9H_2O$] with more than 99.9% purity are used for the parent compound. Subsequently, bismuth nitrate [$Bi(NO_3)_3{\cdot}5H_2O$] is utilized in the case of Bi substituted. The aqueous solution of all precursors along with citric acid ($C_6H_8O_7$, chelating agent) goes under continuous stirring with a rising temperature towards 423 K by maintaining the pH value of around 7 through the ammonia solution. After combustion, it is ground properly and pressed into pellets, followed by sintering at 1473 K for 4hr. The samples are denoted as SrM (x = 0), SBFO1 (x = 0.01) and SBFO2 (x = 0.02). The detailed sample preparation is given in reference 8 [8].

The lattice vibration is observed through a Raman spectrometer (WITEC ALPHA 300R) at room temperature (RT) with the help of a solid-state laser (a continuous monochromatic light source) having a wavelength of 532 nm. A 5mW laser beam of spot-size 6μm is made incident on the surface of the samples to obtain the Raman spectra in the range 200-800 cm^{-1}. The instrumental resolution is ~1.23 cm^{-1}, and the grating used in the instrument has 1800 lines/mm.

Result and discussion

The phase purity of all the compounds is confirmed by X-ray diffraction (XRD), which was reported earlier [7]. The XRD data show the substitution of bismuth has created distortion and strain at different sites in the unit cell, i.e., especially the 12k and 2b are highly distorted. As a result, the magnetization and magnetoelectric properties are enhanced with the substitution [7]. Here we will try to understand the lattice dynamics and strain (stress) produced in the system through the Raman spectroscopic study for all the compounds.

The complex structure of strontium hexaferrite ($SrFe_{12}O_{19}$) not only comes from the 64 atoms in the unit cell but also from its five iron sites. The group theory calculation shows SrM has 42 Raman active modes ($11A_{1g} + 14E_{1g} + 17E_{2g}$) out of the 189 optics modes[2,9,10]. Here, the SrM shows 10 prominent peaks out of the 42 Raman active modes in the range of 200 – 800 cm^{-1}. All the Raman peaks are in agreement with the earlier reports [2,9–11]. All the phonon modes are assigned by comparing with the result from Kreisel et. al. [9]. The deconvolution of the Raman spectrum for all the compounds is shown in Fig. 1.

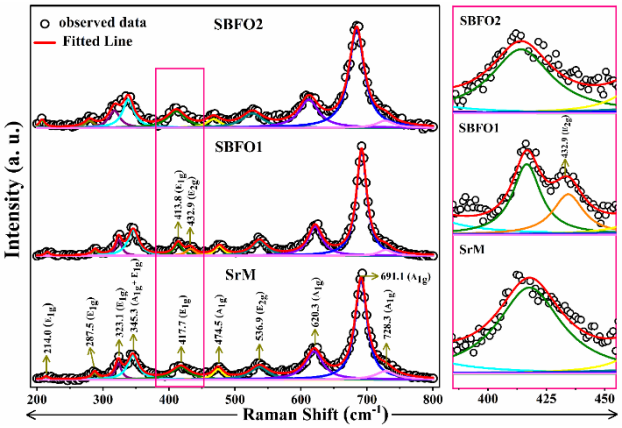

Figure 1: Room temperature Raman spectra of (a) SrM, (b) SBFO1, and (c) SBFO2. The red line shows the cumulative fitting line. For clear visualization, the peak-splitting portion of SBFO1 is shown on the right side.

Table 1: Raman peak positions and their corresponding associated polyhedral sites [12-13].

Peak Position SrM	Assigned Polyhedra
214.0	
287.5	
323.1	Mixed Octahedral
345.3	12k - Octahedral
417.7	12k - Octahedral

474.5	Mixed (2a+12k) - octahedral
536.9	Mixed (2a+12k+$4f_2$) - Octahedral
620.3	$4f_2$ - Octahedral
691.1	2b - Bipyramidal
728.3	$4f_1$ - Tetrahedral

The Raman peaks at 728.3 cm^{-1}, 691.1 cm^{-1}, and 620.3 cm^{-1} are associated with the vibration of Fe-O at the tetrahedral ($Fe^{(3)}O_4$), bipyramid ($Fe^{(2)}O_5$), and octahedral ($Fe^{(4)}O_6$) iron sites respectively, having A_{1g} symmetry. A mixed octahedral iron site of $Fe^{(1)}O_6$ and $Fe^{(5)}O_6$ stretches the A_{1g} symmetry band at 474.5 cm^{-1}, and another octahedral vibration occurs at 345.3 cm^{-1} with combined symmetry of A_{1g}+E_{1g}. The peaks 214.0 cm^{-1}, 287.5 cm^{-1}, and 417.7 cm^{-1} correspond to E_{1g} mode and two E_{2g} phonon modes at 323.1 cm^{-1} and 536.9 cm^{-1} corresponding to the octahedral sites [2,9,12-15]. The Raman modes at 214.0 cm^{-1}, and 287.5 cm^{-1} are due to the vibration of the S-block.

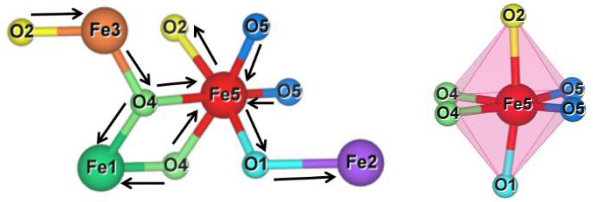

(a) **(b)**

Figure 2: (a) The mostly affected bond lengths linked to iron ions in a unit cell of SBFO1 (plotted by VESTA software) and in figure (b) polyhedral representation of 12k-site. The arrow sign is given to indicate the displacement of oxygen ions from iron ions in SBFO1.

Table 2: The mostly disturbed bond angles and bond lengths associated with the 12k- octahedral site.

Compound	SrM	SBFO1
Fe5-O1	1.83	1.95
Fe5-O2	1.82	2.11
Fe5-O5	1.97	1.92
Fe5-O2-Fe5	107.44	86.32
Fe3-O2-Fe5	112.21	117.90
Fe2-O1-Fe5	111.38	127.82

Most of the Raman peaks associated with the different sites of SBFO1 have been shifted slightly towards the higher wavenumber side as the bond length associated with these sites like Fe1-O4, Fe2-O1, Fe2-O3, Fe3-O2, Fe5-O4, Fe5-O5 decreases (some bonds shown in Fig. 2(a)). The shifting of Raman peaks also indicates the strain (tensile/compressive) produced at the lattice sites in the materials that are reported earlier (calculated from the XRD data) [7]. Again, for SBFO2, bond length increases as compared to SBFO1, so redshift happens (shifting to lower wavenumber). Similarly, the Raman peak width narrows down for SBFO1 and broadens for SBFO2. The structural distortion produced in the systems is seen in the variation of the FHWM or in its intensity. Again, it has to be noticed that the peak 417.7 cm^{-1} split into two peaks, 413.8 cm^{-1} and 432.9 cm^{-1}, for SBFO1 at room temperature, and this may be due to the strain or distortion produced at the 12k-octahedral site. The drastic variation of bond length (Fe5-O2, Fe5-O5, Fe5-O4, Fe5-O1) or bond angle (Fe2-O1-Fe5, Fe3-O2-Fe5, Fe5-O2-Fe5) as compared to parent can be seen in Table 1. The splitting of the peak may also be due to the substitution of bismuth (Bi), in which ionic size (1.40 Å) and atomic mass (208.9 amu) differ from the strontium, providing perturbation to the unit cell because the shift in peak position depends on the dopant's ionic radius and molecular mass. However, it again merges for SBFO2 (not distinguishable as two).

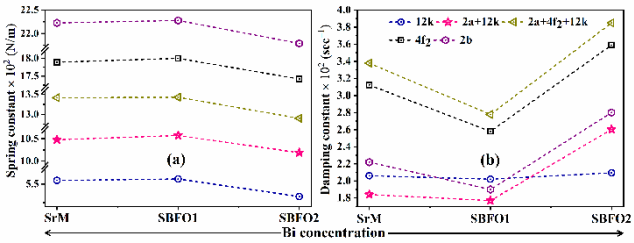

Figure 3: (a) Spring constant (b) damping constant of some selected sites. The hollow symbols for the spring constant and solid symbols for the damping constant.

To understand the Raman spectra in the simplest possible manner, the molecular vibrations are examined in the purview of a one-dimensional forced oscillator with an external periodic force of $F_0 cos\omega t$ having solution $x = Real\ (Ae^{i(\omega t-\delta)})$ such that the amplitude of vibration $A(\omega)$ is given as [16],

$$A(\omega) = \frac{F_0/m}{\{(\omega_0^2 - \omega^2)^2 + (\gamma\omega)^2\}^{1/2}}$$

where, $\gamma = \frac{b}{m}$ = damping constant, $\omega_0 = \sqrt{\frac{k_{sc}}{m}}$ is the frequency (peak position) of respective peak intensities. The spring constant (k_{sc}) and damping constant behave similarly to the Raman shift and FWHM of the peak, respectively, because the parameters are proportional to

each other. This results from the spring constant inversely related to the bond length. Hence, the shift of Raman peaks to higher wave numbers increases the spring constant. As a result, the spring constant is high for SBFO1, whereas the damping constant is low for SBFO1. The low damping constant is due to the compressive strain produced at different sites.

Conclusion

The lattice vibration characteristics of $Sr_{1-x}Bi_xFe_{12}O_{19}$ are investigated by analyzing the evolutions of Raman peaks with increasing Bi concentration. The peak shifts well matched the bond length associated with the crystallographic sites. The strain/distortion produced at the 12k sites has been witnessed by an extra peak reproduced in the SBFO1 Raman spectra. The damping constant has decreased for the highly strained SBFO1 compound and the peak 417.7 cm^{-1} has split into two peaks 413.8 cm^{-1} and 432.9 cm^{-1}.

Acknowledgments

I would like to thank GITAM, GSS, Bengaluru, for providing financial assistance for attending the conference.

References

1. M. R. Sahoo, A. Barik, S. Kuila, S. Tiwary, R. Ghosh, P. D. Babu, S. D. Kaushik, and P. N. Vishwakarma, J. Phys. D. Appl. Phys. **55**, 265001 (2022).
2. M. Elansary, M. Belaiche, C. Ahmani Ferdi, E. Iffer, and I. Bsoul, RSC Adv. **10**, 25239 (2020).
3. T. Kimura, Annu. Rev. Condens. Matter Phys. **3**, 93 (2012).
4. S. P. Shen, Y. S. Chai, J. Z. Cong, P. J. Sun, J. Lu, L. Q. Yan, S. G. Wang, and Y. Sun, Phys. Rev. B - Condens. Matter Mater. Phys. **90**, 180404(R) (2014).
5. A. Gassenq, S. Tardif, K. Guilloy, I. Duchemin, N. Pauc, J. M. Hartmann, D. Rouchon, J. Widiez, Y. M. Niquet, L. Milord, T. Zabel, H. Sigg, J. Faist, A. Chelnokov, F. Rieutord, V. Reboud, and V. Calvo, J. Appl. Phys. **121**, 055702 (2017).
6. X. B. Chen, N. T. Minh Hien, K. Han, J. Chul Sur, N. H. Sung, B. K. Cho, and I. S. Yang, J. Appl. Phys. **114**, 013912 (2013).
7. W. Y. Zhao, P. Wei, X. Y. Wu, W. Wang, and Q. J. Zhang, J. Appl. Phys. 103, 063902 (2008).
8. M. R. Sahoo, A. Barik, S. Kuila, S. Tiwary, and P. N. Vishwakarma, J. Appl. Phys. **126**, 074104 (2019).
9. J. Kreisel, G. Lucazeau, and H. Vincent, J. Solid State Chem. **137**, 127 (1998).
10. X.-B. Chen, N. T. M. Hien, K. Han, J.C. Sur, N. H. Sung, B. K. Cho, and I.-S. Yang, J. Appl. Phys. **114**, 013912 (2013).
11. M. R. Sahoo, A. Barik, R. Ghosh, S. Kuila, S. Tiwary, P. D. Babu, S. D. Kaushik, and P. N. Vishwakarma, Phys. Chem. Chem. Phys. **25**, 2386 (2022).
12. T. T. Carol T., J. Mohammed, B. H. Bhat, S. Mishra, S. K. Godara, and A.K. Srivastava, Physica B **575**, 411681 (2019).
13. F. M. S. Júnior, and C. W. A. Paschoal, J. Appl. Phys. **116**, 244110 (2014).
14. G. P. Nethala, R. Tadi, G. R. Gajula, K. N. Chidambara Kumar, and V. Veeraiah, Phys. B Condens. Matter **550**, 136 (2018).
15. M. W. Pieper, F. Kools, and A. Morel, Phys. Rev. B - Condens. Matter Mater. Phys. **65**, 1844021 (2002).
16. A. P. French, *Vibrations and Waves: The M.I.T Introductory Physics Series* (W.W. Norton & Company, New York, 1971), pp. 41–101.

Dielectric Relaxation Behaviour of $(Bi_{0.2}Na_{0.2}Ba_{0.2}Sr_{0.2}Ca_{0.2})TiO_3$ High-Entropy Ceramic

S. K. Patri[a] and, Rajashree Khatua[b]

Department of Physics, Veer Surendra Sai University of Technology, Burla, Odisha, India.

[a] skpatri_phy@vssut.ac.in
[b] khatuarajashree05@gmail.com

Abstract

High entropy materials are a relatively young new class of materials discovered in 2003. It possesses four kinds of special core effects as a result of its strong mixing nature such as (i) High entropy effect, (ii) Severe lattice distortion effect, (iii) Sluggish diffusion effect, and (iv) Cocktail effect. High Entropy Ceramics (HECs) are defined as the solid solutions of inorganic compounds (five or more cations sublattices) with one or more Wykoff sites shared by equal or nearly equal atomic ratios of multi-principal elements. HECs have gained the attention of researchers due to their fascinating properties. In this report, an A-site disordered high entropy perovskite $(Bi_{0.2}Na_{0.2}Ba_{0.2}Sr_{0.2}Ca_{0.2})TiO_3$ ceramic was prepared via a solid-state reaction route. The XRD pattern and FESEM-EDS confirmed the formation of a single-phase solid solution with a tetragonal structure. A detailed study of the dielectric behaviour of the sample was done. Modified Curie-Weiss law was fitted to the relative permittivity to analyze the relaxor behaviour of the sample. HECs are highly tolerant to ions and their properties can be tailored by composition and according to the application purposes.

Keywords: Ceramics, High Entropy Ceramics, Dielectric Relaxation.
Received 30 January 2025; First Review 21 February 2025; Accepted 23 February 2025

*** Address of correspondence**
S. K. Patri
Department of Physics, Veer Surendra Sai University of Technology, Burla, Odisha, India

Email: skpatri_phy@vssut.ac.in

How to cite this article
S. K. Patri and, Rajashree Khatua, Dielectric Relaxation Behaviour of $(Bi_{0.2}Na_{0.2}Ba_{0.2}Sr_{0.2}Ca_{0.2})TiO_3$ High-Entropy Ceramic, J. Cond. Matt. 2024; 02 (02): 114-116.

Available from:
https://doi.org/10.61343/jcm.v2i02.112

Introduction

Recently High Entropy concept has opened the path toward the material composition design. The configurational entropy of a system can be depicted as [1]

$$S_{\text{config}} = -R\left[\left(\sum_{a=1}^{A} x_a \ln x_a + \sum_{b=1}^{B} x_b \ln x_b\right)_{\text{cation-site}} + \left(\sum_{j=1}^{M} x_j \ln x_j\right)_{\text{anion-site}}\right] \quad (1)$$

where A, B, and M represent the elements present in A-site, B-site, and no of elements in both cationic and anionic sites, x_a, x_b, and x_j are the mole fraction of corresponding elements and R is the gas constant.

According to the previous literature, the ionic size difference (δ) is a key element for regulating the formation of a single-phase compound. The A-site cation ionic size difference can be defined as [2]

$$\delta(R_A) = \sqrt{\sum_{i=1}^{N} c_i\left[1 - r_{A_i}/\left(\sum_{i=1}^{N} c_i\, r_{A_i}\right)\right]^2} \quad (2)$$

where, r_{A_i} is the ionic radius of A-site elements of i^{th} component, c_i is the molar fraction.

Also, the Goldschmidt tolerance factor (t) is an essential parameter for the stability of a perovskite structure.

The tolerance factor [3] can be given as -

$$t = \frac{(R_A + R_O)}{\sqrt{2}(R_B + R_O)} \quad (3)$$

where R_A, R_B, and R_O are the ionic radii of A, B, and Oxygen sites in perovskite oxides.

For the cubic phase, t ~1, t>1 for tetragonal/hexagonal and t<1 for the orthorhombic/octahedral phase. In this report, the structural and dielectric relaxation of an A-site modified $(Bi_{0.2}Na_{0.2}Ba_{0.2}Sr_{0.2}Ca_{0.2})TiO_3$ (BNBSCT), synthesized via solid state reaction route assisted with ball milling are discussed. The atomic size difference and tolerance factor are calculated as 6.37% and 1.003. The values suggest the formation of a single-phase A-site disordered compound [4].

Method

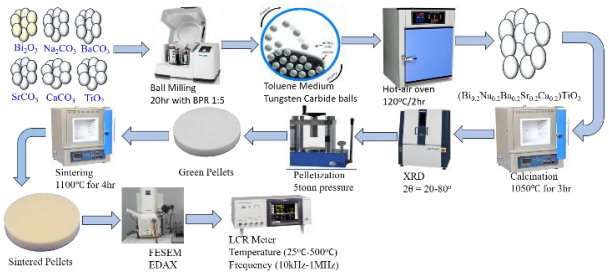

Figure 1: Schematic representation of the synthesis and characterization of BNBSCT

Discussion

Figure 2 shows the room temperature XRD pattern of the studied sample. The pattern depicts a typical and pure single-phase perovskite structure. The sharp and intense peak indicates the high crystalline nature of the sample. The splitting of (200) reflex around 45° illustrates the tetragonal crystal structure of the sample. Also, the pattern is matched by X'Pert HighScore Plus software to standard reference data (ICDD-98-005-7923), which also reveals the above. The surface morphology and chemical composition of the synthesized sample are investigated by using a Field Emission Scanning Electron Microscope (FESEM) in addition to Energy Dispersive X-ray Spectroscopy (EDS). The inset of Figure 2 shows the FESEM and EDS spectra. Figure 3 shows the pie chart of atomic % and weight % of the constituent elements analysed from EDS.

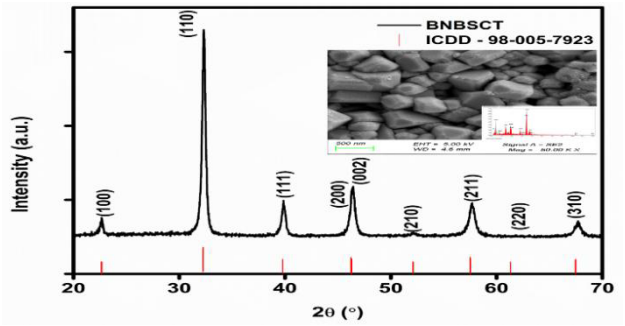

Figure 2: Room temperature XRD pattern and FESEM micrograph of the studied sample

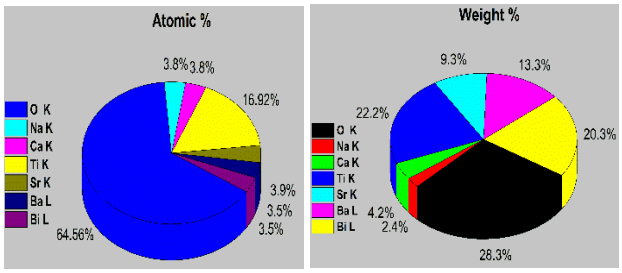

Figure 3: FESEM micrograph, weight%, and atomic % of BNBSCT

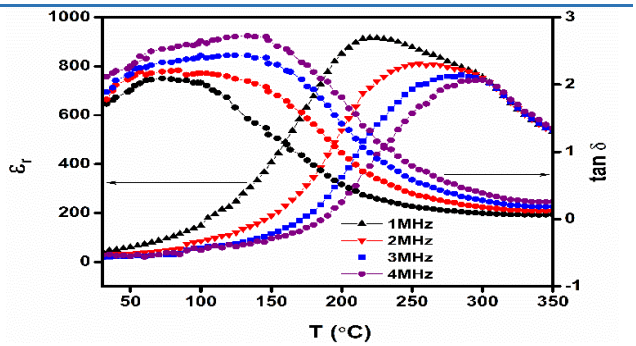

Figure 4: Variation of dielectric constant and loss with temperature at various frequencies and

The dielectric properties of the sample are shown in Figure 4. The Figure shows the variation of dielectric parameters with temperature (25-350 ˚C) at different frequencies (1-4MHz). The graph shows an obvious dispersion below T_m (Temperature corresponding to maximum dielectric constant). This is attributed to the strain factor and disordered structure, which leads to the destruction of long-range ordered ferroelectric domains that ignite the formation of polar nano-micro regions (PNRs) [5]. Hence the variation in the speed of the dielectric response of PNRs with different sizes leads to dielectric relaxation. The strong frequency dispersion behaviour depicts the ferroelectric relaxor. The dielectric loss also showed a frequency dispersion behaviour. The loss is higher at a high frequency than at a lower frequency. Furthermore, the loss tangent values are suppressed significantly at above T_m.

To investigate the relaxation behaviour of the studied sample, the Modified Curie-Weiss (MCW) law is fitted to the dielectric permittivity [6]

$$\frac{1}{\varepsilon_r} - \frac{1}{\varepsilon_m} = \frac{(T-T_m)^\gamma}{C}, \; T > T_m$$

where ε_m refers to the maximum of ε_r and C is the constant. The parameter γ known as the diffusivity constant, which indicates the degree of diffusion. Generally, it ranges from 1 (for normal ferroelectric) to 2 (for ideal relaxation ferroelectric). The γ value is calculated from the slope of the graph as shown in Figure 5 The value ranges from 1.24-1.98, which suggests the BNBSCT is a relaxor ferroelectric. The relaxation behaviour in HECs possibly arises from chemical disorders and distorted structure.

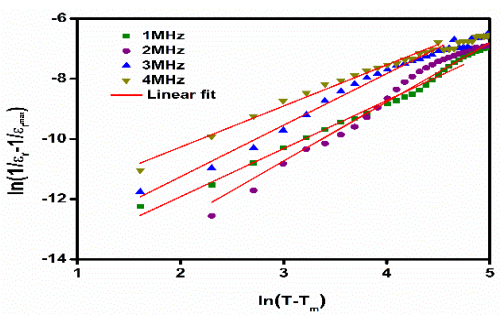

Figure 5: MCW fitting to the dielectric permittivity

Conclusion and Future Prospective

To summarize, we have synthesized an A-site disordered single-phase HEC. The XRD and FESEM-EDS pattern reveals the tetragonal crystal structure, perfect microstructure, and purity of the sample. The diffused phase transition and shifting of T_m signify the relaxor behaviour of BNBSCT. Also, the value of the diffusivity constant found from the MCW fitting to the dielectric constant agrees with the relaxor behaviour of the studied sample. As the sample shows relaxor behaviour, it may show a high energy storage efficiency.

Acknowledgment

The authors acknowledge the Dean, F&P, and honourable VC of VSSUT, Burla for their kind permission to present the research work.

References

1. Z.Y. Liu, Y. Liu, Y. Xu, H. Zhang, Z. Shao, Z. Wang, and H. Chen, Green Energy Environ. 8:1341–1357, 2023.
2. Y. Zhang, T.T. Zuo, Z. Tang, M.C. Gao, K.A. Dahmen, P.K. Liaw, and Z.P. Lu, Prog. Mater. Sci. 61:1–93,2014.
3. Z. Liu, S. Xu, T. Li, B. Xie, K. Guo, and J. Lu, Ceram. Int. 47:33039–33046, 2021.
4. A.R. Mazza, E. Skoropata, J. Lapano, J. Zhang, Y. Sharma, B.L. Musico, V. Keppens, Z. Gai, M.J. Brahlek, and A. Moreo, Phys. Rev. B 104:94204, 2021.
5. J. Fang, T. Wang, K. Li, Y. Li, and W. Gong, Results Phys. 38:105617, 2022.
6. W. Xiong, H. Zhang, Z. Hu, M.J. Reece, and H. Yan, Appl. Phys. Lett. 121, 2022.

Reduced Graphene Oxide/MnO_2 Composite Films as the Electrodes for High-Performance Supercapacitors Produced by Successive Ionic Adsorption and Reaction (SILAR) Method

Vimuna V M[1,a] and Xavier T S[2,b]

[1] *Department of Physics, Dr. Palpu College of Arts and Science, University of Kerala, Kollam 691536, Kerala, India.*
[2] *Department of Physics, Government College for Women, University of Kerala, Thiruvananthapuram 695014, Kerala, India*

[a] vimunamurali@gmail.com
[b] xavierkattukulam@gmail.com

Abstract

In this work, rGO/MnO_2 (SL-GMN X) composites films on stainless steel (SS) substrate for three different number of cycles (X= 10, 15, and 20) has been prepared using the successive ionic adsorption and reaction (SILAR) method. This synthesis method provides a binder-free route. Fourier transform infrared spectroscopy (FTIR), X-ray photoelectron spectroscopy (XPS), and X-ray diffraction (XRD) were used to study the structure and composition of MnO_2 and SL-GMN X composite films. Transmission electron microscopy (TEM) and scanning electron microscopy (SEM) are used to assess the morphology of materials. Surface area and porosity measurements are analyze using Brunauer-Emmett-Teller analysis (BET). According to electrochemical investigations, when using a 1M Na_2SO_4 aqueous electrolyte in a three-electrode configuration, the SL-GMN 15 composite film exhibits an exceptional specific capacitance of 424 F g^{-1}. At a charging current of 1 mA, the SL-GMN 15 composite symmetric supercapacitor has a high specific capacitance of 117 F g^{-1} and a maximum energy density of 16.3 Wh kg^{-1}. Additionally, with a charging current of 3 mA, after 5000 cycles of testing, the composite has a long cycle life and retains a 99.5% specific capacitance. These findings pave the door for advancement of rGO/MnO_2 composite electrodes for supercapacitors and other energy storage applications.

Keywords: Successive ionic adsorption and reaction, Reduced graphene oxide, MnO_2, Symmetric supercapacitor.
Received 31 January 2025; First Review 21 February 2025; Accepted 22 February 2025

*** Address of correspondence**
Vimuna V M
Department of Physics, Dr. Palpu College of Arts and Science, University of Kerala, Kollam 691536, Kerala, India

Email: vimunamurali@gmail.com

How to cite this article
Vimuna V M and Xavier T S, Reduced Graphene Oxide/MnO_2 Composite Films as the Electrodes for High-Performance Supercapacitors Produced by Successive Ionic Adsorption and Reaction (SILAR) Method, J. Cond. Matt. 2024; 02 (02): 117-122.
Available from:
https://doi.org/10.61343/jcm.v2i02.137

Introduction

The growing need for efficient and eco-friendly energy storage technologies, including supercapacitors has generated a surge in demand in recent years due to rising traditional energy use [1-3]. Supercapacitors are gaining - wide acceptance due to their capacity to deliver increased power densities than batteries and better energy densities than electrostatic capacitors [4, 5]. Thermally reduced graphene oxide, which contains only a trace of oxygen, effectively enhances electronic conductivity, especially over long periods [6, 7].

The electrical conductivity and electrochemical characteristics of thermally reduced graphene oxide will be improved by providing a large surface for the deposition of nanoscale MnO_2 [8]. In the successive ionic adsorption and reaction (SILAR) method, the layer-by-layer formation of rGO and MnO_2 nanoparticles allow homogeneous spreading of MnO_2 on the rGO surface and terminate the agglomeration of rGO [9]. The morphology of different preparation processes will result in varying specific capacitance values.

In this chapter, the successive ionic adsorption and reaction (SILAR) method is used to prepare rGO/MnO_2 (SL-GMN) composites films on stainless steel (SS) substrate. This synthesis method provides a binder-free route. The rGO/MnO_2 coated directly onto the SS substrate has been used as a supercapacitor electrode. The unbalanced electrostatic force between SS and oxygen functionalities of rGO supports depositing rGO over SS substrate. This deposited rGO delivers anchoring sites to absorb Mn^{2+}, further oxidized to Mn^{4+}. The electrochemical and physical properties of the prepared films are thoroughly examined.

Method

As per our earlier research work, natural graphite powder was oxidize synthesize the rGO [10]. For two hours, 0.1053 g of prepared rGO was thoroughly dissolved in distilled water using ultrasonication. SS sheets are utilized as coating substrates. MnO_2/rGO composite thin films were coated on the flexible SS dipping in rGO dispersion. Here 5 beakers are used for coating MnO_2/rGO thin films. 80 ml rGO dispersion, 3M $MnSO_4$, and 2 M $KMnO_4$ were taken in the 1st, 3rd, and 4th beakers, respectively. The 2nd and 5th beakers contained double distilled water. The substrates were dipped into the beaker with precursor solution for 20 seconds in each solution and rinsed with double distilled water for 10 seconds. The substrate was dried for 5 seconds after retrieving from each beaker. This process is repeated for three cycles (10, 15, and 20), and we get three different MnO_2/rGO composite films (SL-GMN 10, SL-GMN 15, and SL-GMN 20). The weight of the SS substrate was taken before and after the coating to observe the mass of active material. For comparison, Pure MnO_2 film (SL-MN) was prepared using the same procedure without rGO.

X-ray diffraction (XRD), Fourier transform infrared spectroscopy (FTIR), energy dispersive X-ray analysis (EDAX), and X-ray photoelectron spectroscopy (XPS) were used to investigate the composition and structure of MnO_2 and SL-GMN X composites' films. Transmission electron microscopy (TEM) and scanning electron microscopy (SEM) are used to evaluate the morphology of materials. Brunauer-Emmett-Teller analysis is used to analyze porosity and surface area measurements (BET). More adsorption sites in SL-GMN 15 are made possible by large surface area and copious porosity, which shortens the ion diffusion pathway.

Analyses using cyclic voltammetry (CV) were conducted at different scan rates. With voltage amplitude of 10 mV, electrochemical impedance spectroscopy (EIS) measurements were made in the frequency range of 100 kHz to 100 Hz. An aqueous electrolyte solution containing 1M Na_2SO_4 was used for all studies. Using CV curves, the electrode materials' specific capacitance was determined using Equation (1) [11]:

$$Cs = \frac{\int IdV}{2mv\Delta V} \qquad (1)$$

The specific capacitance (Cs) of a symmetric supercapacitor can be computed from Equation (2) [11] using GCD curves:

$$Cs = \frac{2I\Delta t}{m\Delta V} \qquad (2)$$

The discharge voltage, discharge time, discharge current, and mass of the active material in one electrode are denoted by ΔV (V), Δt (s), I (A), and m (g), respectively. Equations. (3) and (4) [11] were used to measure the symmetric supercapacitor's specific energy (Es) and specific power (Ps):

$$Es = \frac{Cs\Delta V^2}{8} \qquad (3)$$

$$Ps = \frac{Es}{\Delta t} \qquad (4)$$

The specific power, specific energy, specific capacitance, discharge time, and potential window are denoted by Ps, Es, Cs, Δt and ΔV.

Discussions

The XRD results of the prepared rGO, SL-MN film, SL-GMN 10 composite film, SL-GMN 15 composite film, and SL-GMN 20 composite film were examined and are revealed in Figure 1(a). XRD patterns of rGO show two diffraction peaks at 25.8° and 43°, which can be indexed as the (002) and (100) reflections of graphene, respectively [12]. The broad diffraction peaks of all XRD peaks were related to low crystalline nature due to small grain size [13]. The diffraction patterns of the prepared SL-GMN 10, SL-GMN 15, and SL-GMN 20 composite films show peaks as in SL-MN, indicating that the crystal structure of MnO_2 nanoparticles is unaffected by the addition of rGO [14, 15].

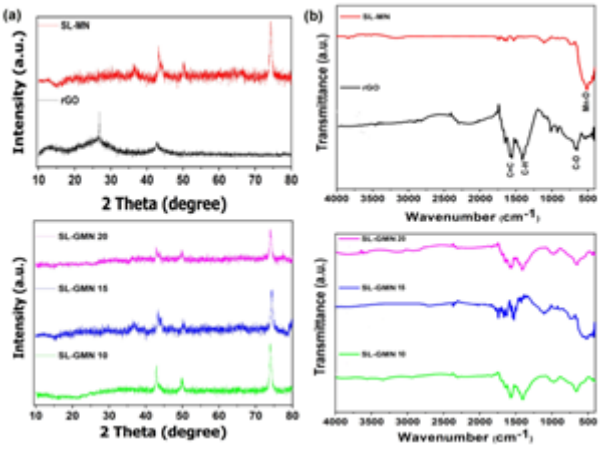

Figure 1: (a) XRD patterns and **(b)** FTIR spectra of rGO, SL-MN, SL-GMN 10 composite, SL-GMN 15 composite and SL-GMN 20 composite.

rGO, SL-MN, SL-GMN 10 composite, SL-GMN 15 composite, and SL-GMN 20 composite FTIR spectra are displayed in Figure 1b. The C-H stretching vibration is attributed to the peak at 1428 cm^{-1} [11]. Additionally, C=C stretching vibrations are responsible for the peak at 1625 cm^{-1} [16], while C-O stretching vibrations are responsible for the peak at 1107 cm^{-1} [17]. Mn-O stretching vibration is responsible for the distinctive peaks in SL-MN that are located between 570 and 450 cm^{-1} [18]. Both the rGO and MnO_2 bands are seen in the FTIR spectra of the SL-GMN

10, SL-GMN 15, and SL-GMN 20 composite, indicating that the MnO_2/rGO composite was successfully formed. Variations in temperature barely slightly alter the peak intensity.

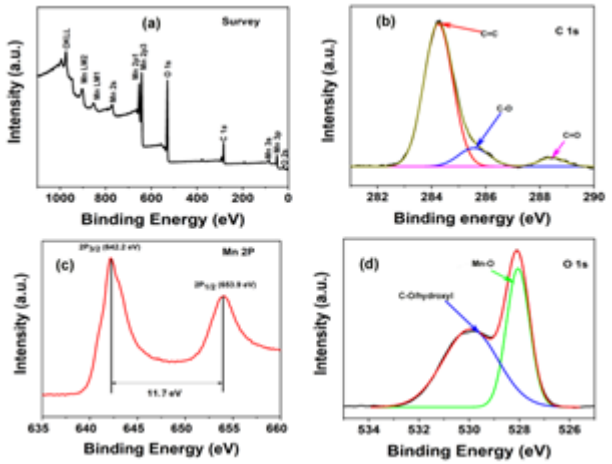

Figure 2: (a) XPS survey spectrum of SL-GMN 15 composite and its **(b)** C 1s **(c)** Mn 2p and **(d)** O 1s spectra.

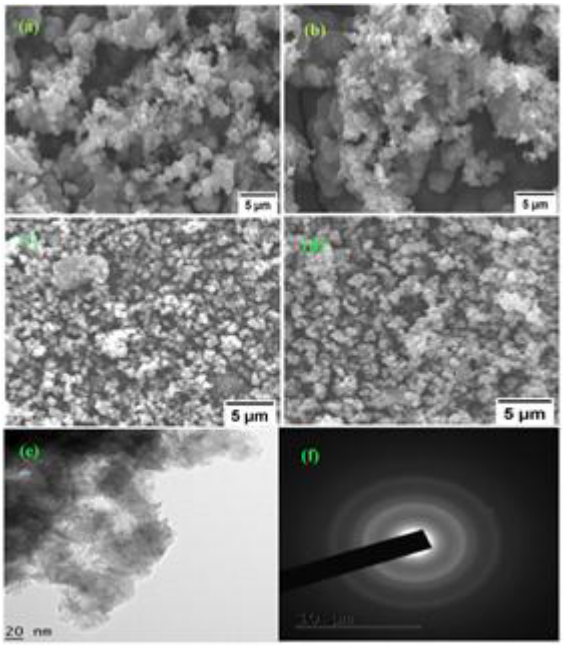

Figure 3: SEM images of (a) SL-MN, (b) SL-GMN 15 composite, (c) SL-GMN 10 composite, and (d) SL-GMN 20 composite. (e) TEM image of SL-GMN 15 composite (f) SAED pattern of SL-GMN 15 composite.

XPS was used to determine the surface composition and electronic state of the SL-GMN 15 composite, as shown in Figure 2. Figure 2a shows the composite's typical survey spectrum, which shows the presence of elements C, O, and Mn, implying the synthesis of MnO_2 on rGO. Three peaks at 284.4, 285.5, and 288.4 eV attributed to C=C, C-O, and C=O vibrations, respectively, in the high-resolution XPS range of C1s (Figure 2b) [19]. Mn $2P_{3/2}$ and Mn $2P_{1/2}$ are assigned to the peaks centred at 642.2 and 653.3 eV, respectively, according to the spectra of Mn 2P in Figure. 2c. The energy difference between the Mn $2P_{3/2}$ and Mn $2P_{1/2}$ peaks is 11.7 eV, demonstrating that the composite is made up of MnO_2 [20]. In Figure 2d, the O1s core-level spectrum is displayed. Two Gaussian peaks appeared in the O1s spectra at 528.2 eV and 530 eV, respectively, and were attributed to Mn-O and C-O/hydroxyl [21].

SEM images demonstrating the morphology of the materials SL-MN, SL-GMN 15 composite, SL-GMN 10 composite, and SL-GMN 20 composite are seen in Figure 3. Figure 3a shows that SILAR coted SL-MN film consists of nearly spherical agglomerated nanoparticles. The SL-GMN 15 composite morphology (Figure 3b) shows that MnO_2 nanoparticles spread on the surface of rGO sheets. The SEM images of SL-GMN 10 composite and SL-GMN 20 composite are shown in Figure 3c and d, indicating less incorporating rGO with MnO_2 nanoparticles. The enhanced surface area of SL-GMN 15 composite increases the number of active sites in the electrochemical process.

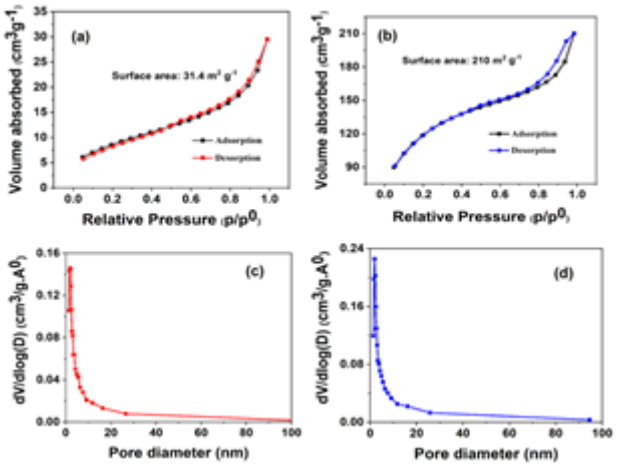

Figure 4: Nitrogen adsorption-desorption isotherm of (a) SL-MN, (b) SL-GMN 15 composite, and BJH pore-size distributions of (c) SL-MN, (d) SL-GMN 15 composite.

A High-resolution transmission electron microscope was used to assess the crystalline structure and morphology of the sample. HR-TEM micrograph of the SL-GMN 15 composite was shown in Figure 3e. The rGO surfaces were evenly coated with MnO_2 nanoparticles. The SL-GMN 15 composite's weak crystalline structure is demonstrated by the SAED pattern (Figure 3f). This outcome is in good agreement with the XRD findings.

Figures 4a and b display the nitrogen adsorption-desorption isotherms for the SL-MN and SL-GMN 15 composite, which were recorded. The SL-GMN 15 composite's nitrogen adsorption-desorption isotherms exhibit type-(IV) properties, confirming the composite's mesoporous structure. The SL-MN and SL-GMN 15 composites have BET surface areas of 31.4 m^2g^{-1} and 210 m^2g^{-1}, respectively. Because of its greater surface area, the SL-GMN 15 composite has a better absorption capacity. Figures 4c and

d display the pore size distribution curve for the SL-MN and SL-GMN 15 composite, which was determined using the BJH method. For the SL-MN and SL-GMN 15 composite, the average pore size was 2 nm and 3.3 nm, respectively. The SL-GMN 15 composite's huge surface area and high mesoporous nature were thought to be caused by increased ionic transport through the material, which will improve the performance of the supercapacitor [22].

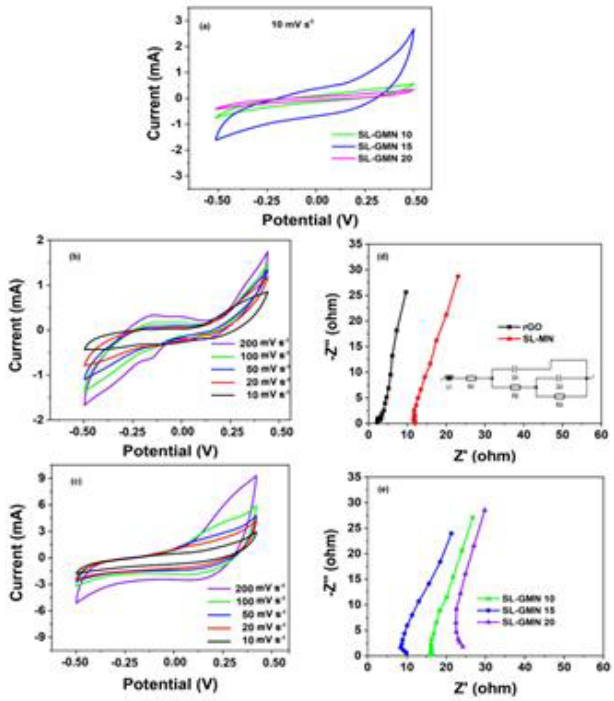

Figure 5: (a) CV curves of SL-GMN 10, SL-GMN 15, and SL-GMN 20 composite electrodes at the scan rate of 10 mVs^{-1}. **(b)** CV curves of SL-MN and **(c)** SL-GMN 15 composite electrodes in 1M Na_2SO_4 aqueous electrolyte solution in 1M Na_2SO_4 aqueous electrolyte solution with different scan rates. Nyquist plots of **(d)** rGO and (e) SL-MN, SL-GMN 10 composite, SL-GMN 15 composite, and SL-GMN 20 composite electrodes in 1M Na_2SO_4 aqueous electrolyte solution. Inset is an equivalent circuit diagram used for the fitting of the EIS data.

The electrochemical analysis of the prepared electrodes in a three-electrode system was usually established using CV and EIS. At a scan rate of 10 mVs^{-1}, the CV curves of the SL-GMN 10, SL-GMN 15, and SL-GMN 20 composite electrodes in the 1M Na_2SO_4 electrolyte under a potential range of -0.5 to 0.5 volts are shown in Figure 5a. Among them SL-GMN 15 composite electrode shows a larger area of CV curve, suggesting high specific capacitance.

In the 1M Na_2SO_4 electrolyte, the CV curves of the electrodes SL-MN and SL-GMN 15 composite at different scan speeds under a potential range of -0.5 to 0.5 volts are shown in Figure 5b and c. All figures show a minor distortion as the scan speeds increase, implying higher transport resistance due to polarisation. At a scan rate of 10 mVs^{-1}, the specific capacitance of SL-GMN 15 composite and SL-MN is 424 Fg^{-1} and 132 Fg^{-1}, respectively. At a scan rate of 10 mVs^{-1}, rGO has a maximum specific capacitance of 36.33 Fg^{-1} [23]. The vertical line in the lower-frequency range indicates optimal ion capacitive behaviour and minimal diffusion resistance in the electrode materials [24]. Figure 5d and e shows the Nyquist plots of the rGO, SL-MN, SL-GMN 10 composite, SL-GMN 15 composite, and SL-GMN 20 composite electrodes. The matching circuit diagram utilized in the EIS data fitting is shown in the Inset. In the high-frequency region, the resistance (Rs) of the SL-GMN 15 composite is 9.8 ohms, which is less than that of the SL-MN (3.5 ohms). With a more vertical line in the lower frequency band, the SL-GMN 15 composite electrode had the best capacitive performance of all the electrodes.

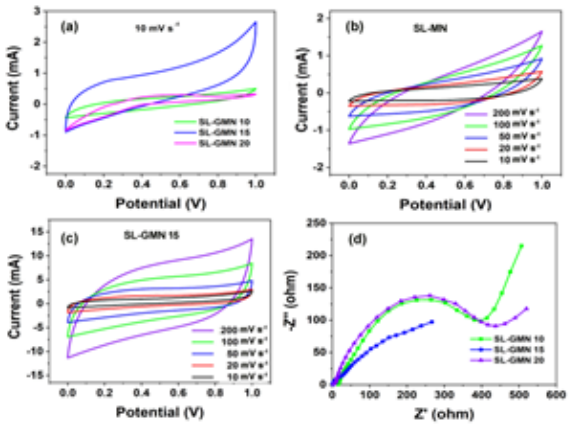

Figure 6: (a) CV curves of SL-GMN 10, SL-GMN 15, and SL-GMN 20 composite symmetric supercapacitors at the scan rate of 10 mVs^{-1}. CV curves of (b) SL-MN and (c) SL-GMN 15 composite symmetric supercapacitors at different scan rates. (d) Nyquist plots of SL-GMN 10, SL-GMN 15, and SL-GMN 20 composite symmetric supercapacitors.

CV, EIS, and GCD were used to examine the electrochemical performance of the symmetric supercapacitors SL-MN, SL-GMN 10 composite, SL-GMN 15 composite, and SL-GMN 20 composite. Figure 6a shows the CV curves of SL-GMN 10, SL-GMN 15, and SL-GMN 20 composite symmetric supercapacitors recorded at a scan rate of 10 mV s^{-1} and a cell voltage of 1 V. The area of CV curves is related to the specific capacitance. The integrated areas of the SL-GMN 15 composite symmetric supercapacitor CV curves are higher than those of the SL-GMN 10 and SL-GMN 20 composites, indicating that the SL-GMN 15 composite symmetric supercapacitor has good capacitance capabilities.

The CV curves of the SL-MN and SL-GMN 15 composite symmetric supercapacitors at scan rates varying from 10 to 200 mVs^{-1} in a cell voltage of 1 V are shown in Figure 6b and c. At a scan rate of 10 mVs^{-1}, the CV curve of the SL-GMN 15 composite symmetric supercapacitor showed a rectangular form. Due to its higher specific capacitance, the CV curves of the SL-GMN 15 composite symmetric supercapacitor show a wider area than those of the SL-MN

for all scan rates.

As shown in Figure 6d, the EIS measured the impedance of SL-GMN 10, SL-GMN 15, and SL-GMN 20 composite symmetric supercapacitors. The charge transport resistance in the high-frequency field is represented by the semicircle. The lower Rct of SL-GMN 15 compared to SL-GMN 10 and SL-GMN 20 can be attributed to the composite symmetric supercapacitor's better electronic conductivity. The Warburg impedance arising from ion diffusion/transport in the electrolyte in the middle-frequency zone is shown by a straight line with a 45° slope. For the SL-GMN 15 composite symmetric supercapacitor, the discrepancy in the Warburg region shows excellent ion diffusion resistance.

To find out more about the composite electrodes' capacitive behaviour, galvanostatic charge-discharge tests were conducted. The charge-discharge curves of the composite symmetric supercapacitors SL-GMN 10, SL-GMN 15, and SL-GMN 20 were shown in Figure 7a with a constant charging current of 1 mA. Every charge-discharge curve exhibits symmetry. Equation (2) was used to calculate the specific capacitances. The specific capacitance for SL-GMN 10, SL-GMN 15, and SL-GMN 20 composite is 112, 469, and 102 Fg-1 at a current of 1 mA in two-electrode cell designs.

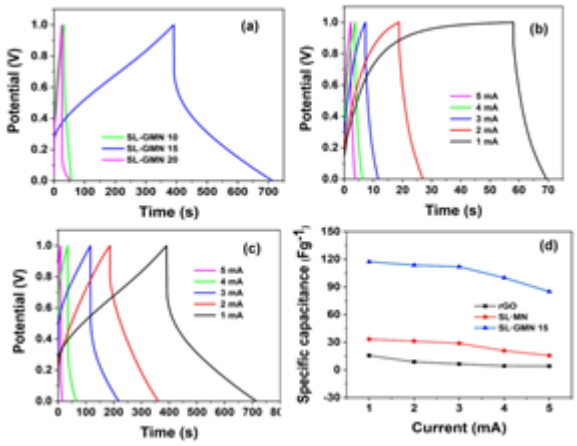

Figure 7: (a) GCD curves of SL-GMN 10, SL-GMN 15, and SL-GMN 20 composite symmetric supercapacitors at constant charging current 1 mA. GCD curves of (b) SL-MN and (c) SL-GMN 15 composite symmetric supercapacitors at at different charging currents. (d) Specific capacitance of rGO, SL-MN, and SL-GMN 15 composite symmetric supercapacitors at different charging currents.

Figure 7b and c display the galvanostatic charge-discharge curves of symmetric supercapacitors SL-MN and SL-GMN 15 composite at different currents ranging from 1 to 5 mA at a cell voltage of 1 V. All of the charge-discharge curves were symmetrical. At various currents of 1 mA, 2 mA, 3 mA, 4 mA, and 5 mA, the specific capacitances of SL-GMN 15 composite in a two-electrode symmetric arrangement are 469 Fg^{-1}, 455 Fg^{-1}, 448 Fg^{-1}, 400 Fg^{-1}, and 340 Fg^{-1}, respectively, are greater than that for SL-MN (133 Fg-1, 125 Fg^{-1}, 115 Fg^{-1}, 83.3 Fg^{-1}, 62.5 Fg^{-1}). The specific capacitance of the rGO symmetric supercapacitor is 9.1 Fg^{-1} at 1 mA [23]. SL-GMN 15 composite reached specific capacitance retention of 72% as the current increased from 1 to 5 mA, whereas SL-MN is only 46%. The specific capacitances of the rGO, SL-MN, SL-GMN 10 composite, SL-GMN 15 composite, and SL-GMN 20 composite at charging currents from 1mA to 5 mA were shown in Figure 7d.

Table 1: The electrochemical performances of some symmetrical supercapacitors in reported literatures and the present work.

Electrode	[a]C_s (max) F g^{-1}	[b]E_s (max) Wh kg^{-1}	[c]T	[d]C_m %$_T$	Ref
MnO_2/ reduced graphene oxide	152.5	…	1000	92	[24]
MnO_2/ reduced graphene oxide	342.8	…	3000	90.3	[25]
MnO_2/rGO composite	175	41.27	…	…	[26]
MnO_2/ reduced graphene oxide	343	…	2500	93.1	[27]
MnO_2/rGO	424	16.3	5000	99.5	This work

[a]C_s (max), maximum specific capacitance,
[b]E_s (max), maximum specific energy density,
[c]T, cycles of cycle life test,
[d]C_m%$_T$, retention rate after the cycle life test.

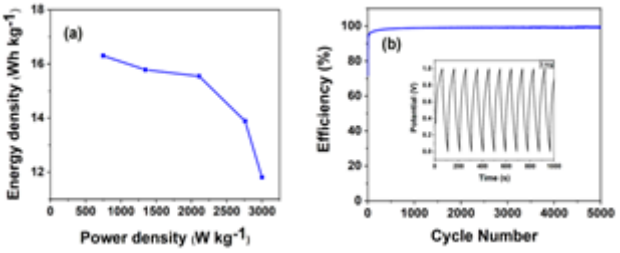

Figure 8: (a) Ragone plot of SL-GMN 15 symmetric supercapacitor. (b) Efficiency of SL-GMN 15 composite symmetric supercapacitor at a charging current of 3 mA and inset shows charge/discharge curves of the SL-GMN 15 composite symmetric supercapacitor in potential range from 0 to 1 V at a charging current of 3 mA.

Figure 8a shows the Ragone plot of the SL-GMN15 composite symmetric supercapacitor. The SL-GMN 15 symmetric supercapacitor's specific energy and power were computed at various currents ranging from 1 mA to 5 mA.

When specific power in 1M Na_2SO_4 increased from 784.4 to 3000 W kg^{-1}, the energy density decreased slightly. The result indicates that SL-GMN15 composite symmetric supercapacitor displayed a perfect power/energy combination.

The essential measure for assessing the supercapacitor device's performance is its cycle stability. Figure 8b displays the electrodes' long-term cyclic stability as determined by the galvanostatic charge-discharge curves at a current of 1 mA. With 99.5% of the initial capacitance still present after 5000 cycles, the SL-GMN 15 composite symmetric supercapacitor's specific capacitance demonstrated good cycling stability. The incorporation of thermally reduced graphene oxide during the composite production process is responsible for the exceptional cycling stability of our SL-GMN 15 composite symmetric supercapacitor. Table 1 displays a comparison between our SL-GMN 15 composite symmetric supercapacitor and other symmetric supercapacitors that have been described.

Conclusion

In summary, the binder free reduced graphene oxide/MnO_2 composite films were fabricated through a facile and controllable SILAR method. The small particle size and nearly amorphous condition are the causes of the broad peaks in all XRD patterns, which show poor crystalline nature. Both the rGO and MnO_2 bands are seen in the FTIR spectra of the SL-GMN 10, SL-GMN 15, and SL-GMN 20 composite, indicating that the MnO_2/rGO composite was successfully formed. The inclusion of MnO_2 and rGO is once again confirmed by the SEM pictures of the SL-GMN 15 composite, which show more porosity than SL-MN. Excellent specific capacitance of 424 F g^{-1} is demonstrated by the SL-GMN 15 composite electrode at a reduced scan rate (10 mV s^{-1}) and at a voltage range of 1V. The specific capacitance of the SL-GMN 15 composite symmetric cell is 117 F g^{-1} at a lower current of 1 mA. Furthermore, after 5000 cycles, the SL-GMN 15 composite symmetric supercapacitor's specific capacitance maintained 99.5% of its initial capacitance, demonstrating good cycling stability. For high-energy supercapacitors, this technique will thus offer a practical way to create binder-free MnO_2/rGO composite electrodes with a high specific capacitance.

References

1. Z Guo, H Zhang, K Liu, S Xie, L Zhang, X Fang, Y Xie, G Qin, J Yang, and Q Chen. Journal of Colloid and Interface Science, 2024.
2. Chaluvachar, Y N Priyanka, G T Sudhakar, Mahesha, G Vishnu Nair, Nakul Desai, and Dayananda K Pai, Journal of Energy Chemistry, 2024.
3. M Vandana, K Bijapur, G Soman, and G Hegde. Critical Reviews in Solid State and Materials Sciences, pp.335-370, 2024.
4. A A Mohamad, Inorganic Chemistry Communications, p.113677, 2024.
5. V K Kumar and N L Panwar, Journal of the Indian Chemical Society, p.101231, 2024.
6. V M Maphiri, G Rutavi, N F Sylla, S A Adewinbi, O Fasakin, and N Manyala, Nanomaterials, 11:8, 1909, 2021.
7. B Zhao, P Liu, Y Jiang, D Pan, H Tao, J Song, and W Xu, Journal of power sources, 198, 423-427, 2012.
8. Z Zhao, T Shen, Z Liu, Q Zhong, and Y Qin, Journal of Alloys and Compounds, 812, 152124, 2020.
9. M Jana, S Saha, P Samanta, N C Murmu, N H Kim, T Kuila, and J H Lee, Journal of Power Sources, 340, 380-392, 2017.
10. V M Vimuna, A. R Athira, K. D Babu, and T. S Xavier, Diamond and Related Materials, 110, 108129, 2020.
11. L Chen, H Yin, Y Zhang, and H Xie, Nano, 15(08), 2050099, 2020.
12. A Jabbar, G Yasin, W. Q Khan, M. Y Anwar, R. M Korai, M. N Nizam, and G Muhyodin, RSC advances, 7, 31100-31109, 2017.
13. H Huang, G Sun., J Hu, and T Jiao, Journal of Chemistry, 2015.
14. H Fei, N Saha, N Kazantseva, R Moucka, Q Cheng, and P Saha, Materials, 10, 1251, 2017.
15. S Chen, J Zhu, X Wu, Q Han and X Wang, ACS nano, 4, 2822-2830, 2010.
16. J Gao, H Li, M Li, G Wang, Y Long, Li, P, C Li and B Yang, Analytica Chimica Acta, 1145, 103-113, 2021.
17. F Raza, X Ni, J Wang, S Liu, Z Jiang, C Liu, H Chen, A Farooq and A Ju, Journal of Energy Storage, 30, 101467, 2020.
18. M Jayashree, M Parthibavarman, R BoopathiRaja, S Prabhu and R Ramesh, Journal of Materials Science: Materials in Electronics, 31, 2020.
19. J Mao, F F Wu, W H Shi, W X Liu, X L Xu, G F Cai, Y W Li and X H Cao, Chinese Journal of Polymer Science, 38, 514-521, 2020.
20. J Zhong, F Yi, A Gao, D Shu, Y Huang, Z Li, W Zhu, C He, T Meng and S Zhao, ChemElectroChem, 4, 1088-1094, 2017.
21. B Usharani, V Manivannan, and P Shanmuga sundaram, In Journal of Physics: Conference Series, 2070, 012089, IOP Publishing, 2021.
22. Y Liu, X Cai, B Luo, M Yan, J Jiang, and W Shi, Carbon, 107, 426-432, 2016.
23. V M Vimuna, B B Raj, S C Sam and T S. Xavier, Diamond and Related Materials, 120, 108707, 2021.

24. Y Xie and J Ji, Journal of Materials Research, 31, 1423-1432, 2016.
25. H Wang, Q Fu, and C Pan, Electrochimica Acta, 312, 11-21, 2019.
26. M Zhang, D Yang, and J Li, Vacuum, 178, 109455, 2020.
27. M Zhang, D Yang, and J Li, Journal of Energy Storage, 30, 101511, 2020.

Iron doped MSe_2 Monolayers (M=Mo, W): A First-Principles Study of Structural, Electronic, and Magnetic Properties

Lalita Devi[1,a], Arun Kumar[2,b], Anjna Devi[3,c]

[1] *Department of Physics, Swami Vivekanand Government College Ghumarwin, Himachal Pradesh, India.*
[2] *Govt. Post Graduate College Bilaspur, Himachal Pradesh, India.*
[3] *Govt. Degree College Baroh, Kangra, Himachal Pradesh (176054), India*

[a] slalita1804@gmail.com
[b] arunphy@gmail.com
[c] anjnahpu90@gmail.com

Abstract

In this study, we examined the effects of iron doping on the electronic and magnetic properties of transition metal dichalcogenide (TMD) monolayers, specifically $MoSe_2$ and WSe_2, utilizing density functional theory (DFT). Our results demonstrate that strategic doping significantly alters the material properties. Structural analysis reveals that doped systems largely retain the original structure of MSe_2ML (Mo, W), despite exhibiting minor lattice distortions. Total energy calculations indicate that these structures remain stable. The doping of Fe induces significant spin polarization in both $MoSe_2$ML and WSe_2ML. The spin-down and spin-up channels exhibit distinct band gaps: 1.09 eV (D) and 0.24 eV (I) for $MoSe_2$ML, and 1.0 eV (D) and 0.27 eV (D) for WSe_2ML, respectively. Iron doping also induces magnetization in these TMDs. Additionally, the introduction of spin polarization shows that neighbouring atoms around the impurity exhibit slight magnetization due to the localized effects of the dopant. The net magnetic moment for both $MoSe_2$ML and WSe_2ML with iron impurities is approximately 2 μB. The computer simulations enable precise doping which leads to improved and tunable properties of TMDs. Future development in electronics, spintronics and quantum computing are facilitated by the potential expansion of doped TMDs.

Keywords: Doping, Magnetization, Localized effect, Spintronics.
Received 31 January 2025; First Review 23 February 2025; Accepted 24 February 2025

*** Address of correspondence**
Lalita Devi
Department of Physics, Swami Vivekanand Government College Ghumarwin, Himachal Pradesh, India.

Email: slalita1804@gmail.com

How to cite this article
Lalita Devi, Arun Kumar, Anjna Devi, Iron doped MSe_2 Monolayers (M=Mo, W): A First-Principles Study of Structural, Electronic, and Magnetic Properties, J. Cond. Matt. 2024; 02 (02): 123-126.

Available from:
https://doi.org/10.61343/jcm.v2i02.127

Introduction

Doping is widely recognized as an effective strategy for enhancing the performance and efficiency of transition metal dichalcogenides (TMDs). A significant body of research has focused on the impact of defects and dopants on the structural, electronic, magnetic, and thermal properties of two-dimensional (2D) materials, demonstrating considerable modifications in these properties [1-5]. TMDs are a varied group of 2D materials, distinguished by their ultra-thin monolayers that feature a transition metal atom positioned between two layers of chalcogen atoms. Transition metal Diselenide have recently attracted considerable interest due to their exceptional properties, which include a direct bandgap, high electron mobility, and excellent chemical stability. Monolayers of MSe_2 specifically display an atomic tri-layer configuration (Se–M–Se, where M = Mo or W) and possess a direct bandgap of around 1-2 eV, rendering them highly suitable for a range of optoelectronic applications. However, there is a dearth of studies on the effect of doping of transition metals like Sc, Ti, V, Cr and Mn in different 2D monolayers. Min Leo studied the electronic and magnetic properties of nickel doped WS2 monolayers [6]. Carmen C. studied the effect of the Li ion donor (Me-Li, *n*-Bu-Li and *t*-Bu-Li) during chemical exfoliation of four different TMDs compounds (MoS_2, $MoSe_2$, WS_2 and WSe_2) in terms of their capacitance is evaluated [7]. Transition Metal Substitution Doping in Synthetic Atomically-Thin Semiconductors was explored by Jian Gao in which they reveal the effect of Nb on WS_2 monolayers [8]. Several theoretical ab initio studies have predicted a rich array of electronic behaviours in transition metal doped systems due to electron occupation of the metal d-orbitals which includes charge doping and magnetic behaviour [8-10]. These monolayers can be synthesized using techniques such as chemical vapor

deposition [11-13]. However, despite their remarkable electronic properties, pristine MSe_2 is intrinsically nonmagnetic. As a result, developing effective methods to induce and manipulate magnetism in MSe_2 monolayers has become a key area of research, particularly for their potential use in spintronic devices, where spin-polarized charge carriers are essential for enhancing functionality [13-16]. The iron doped TMCs can be used potential electrode material for supercapacitor applications and improve energy storage capacity [18]. The emphasis of this paper is to study the electronic and magnetic properties of Iron doped $MoSe_2$ and WSe_2 MLs(monolayers).

Computational Details

The calculations were performed using the SIESTA simulation package, which utilizes density functional theory (DFT) to solve the electronic structure of materials. The exchange-correlation interactions are taken care using the Generalized Gradient Approximation (GGA) with the Perdew-Burke-Ernzerhof (PBE) functional. For basis sets, the double zeta plus polarization (DZP) method is employed with a confinement energy of 20 eV and a mesh cutoff of 300 Ry. Structural optimization is conducted using the Conjugate Gradient (CG) method with a convergence criterion of 0.01 eV/Å. The Brillouin zone is sampled using a 3×3×1 k-point mesh, based on the Monkhorst-Pack scheme.

Results and Discussion

The $MoSe_2$ and WSe_2 monolayers are designed as 6×6 supercells containing 108 atoms (36 metal atoms and 72 chalcogen atoms). In each case, one metal atom (Mo or W) is replaced by an iron atom, and optimized these structures which show that doping with Fe results slight lattice distortions near the impurity site.

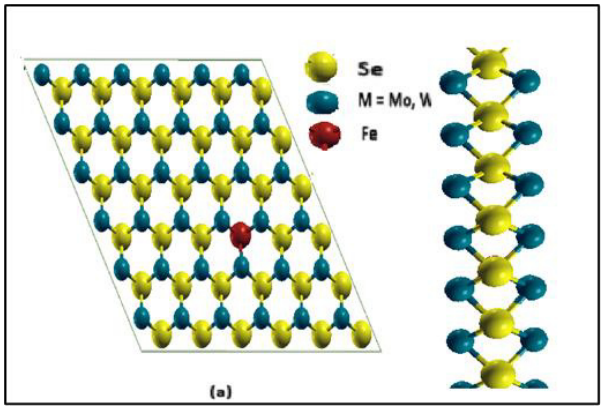

Figure 1: Optimized geometric structures of (a) MSe_2 ML (front view) and (b) side view.

The overall geometry of the monolayers is maintained, with the lattice constants for pristine $MoSe_2$ and WSe_2 optimized to 3.289 Å and 3.345 Å respectively. These values are

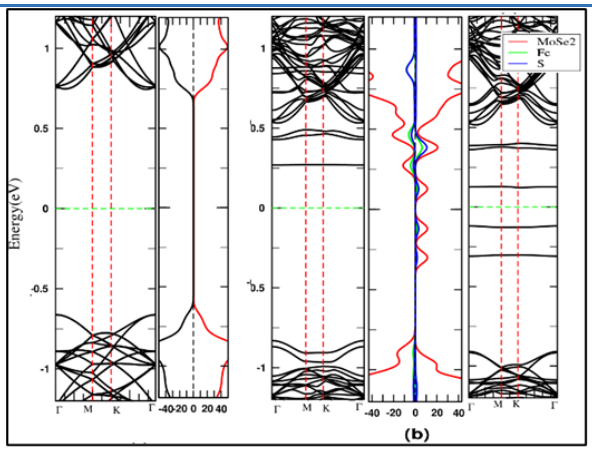

Figure 2: (a) Electronic band structure and DOS of $MoSe_2$ and (b) $Mo_{0.097}Fe_{0.028}$ Se_2. Red lines represent TDOS and blue lines represents DOS of Se) in the neighbouring atoms of impurity. Vertical Red dotted lines are symmetric M, K -points, Dark green lines for bandgap line. The Fermi level is at 0eV represented with dotted light green colour.

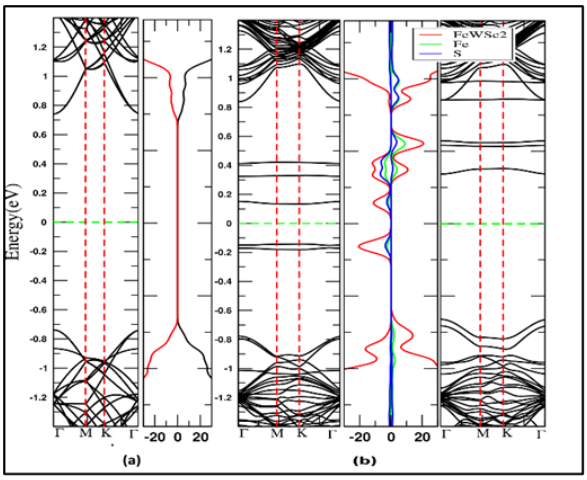

Figure 3: (a) Electronic band structure and Density of states (DOS) of WSe_2 and (b) $W_{0.972}Fe_{0.028}$ Se_2

consistent with experimental and computational results found in the literature [17]. The introduction of iron leads to a minor reduction in the M-Se bond length near the impurity atom(table1), due to the smaller atomic radius of Fe relative to Mo or W. Despite these changes, the systems remain stable, and the binding energy calculations confirm that $Mo_{0.972}Fe_{0.028}Se_2$ and $W_{0.972}Fe_{0.028}Se_2$ are energetically favourable. The binding energies of pristine $MoSe_2$ (4.401 eV) and WSe_2 (4.950 eV) are slightly higher compared with $Mo_{0.972}Fe_{0.028}Se_2$ (4.2 eV) and $W_{0.972}Fe_{0.028}Se_2$ (4.87 eV) showing reduced values. This reduction suggests that doping may destabilize the monolayer to some extent but could also increase the material's reactivity, which is beneficial for applications requiring high catalytic activity or sensor sensitivity. The binding energy is calculated by using the formula

$$E_b = \frac{E_{total} - \{nE + mE_M + lE_{Fe}\}}{n + m + l}$$

Table 1: Table 1: The calculated structural parameters such as optimized lattice constant (a), average bond distance between adjacent atoms $d_{(M-Se)}$ (M=Mo, W) and Fe- Se, binding energy (E_b) and Bandgap (E_g) values, $\mu_{atom(n)}$ and μ_{tot} represents the magnetic moment.

System	a (Å)	E_{tot} (eV)	d_{M-Se} (Å)	E_b (eV)	Eg (eV)	$\mu_{atom\ (n)}$ (μ_B)	μ_{tot} (μ_B)
$MoSe_2$	3.340	37215.987	2.560_{Mo-Se}	-4.401	1.46 (D)		0.0
$Mo_{0.972}Fe_{0.028}Se_2$	3.340	37520.918	2.531_{Mo-Se}, 2.432_{Fe-Se}	-4.231	1.09(D↓), 0.24(I↑)	$1.651_{Fe(1)}$, $0.085_{Mo(6)}$, $0.015_{Se(6)}$	2.0
WSe_2	3.345	41268.1950	2.571_{W-Se}	-4.950	1.49 (D)		0.0
$W_{0.972}Fe_{0.028}Se_2$	3.345	41670.3294	2.587_{W-Se}, 2.461_{Fe-Se}	-4.863	1.0(D↓), 0.27(D↑)	$1.544_{Fe(1)}$, $0.219_{W(6)}$, $0.014_{Se(6)}$	2.0

where E_{total} is the total energy of the studied system, E_M, E_{Se} and E_{Fe} are energy of the isolated atoms constituting the system and n, m and l are number of M (Mo, W), Se and Fe atoms in the respective studied system. The electronic band structures and density of states (DOS) of pristine and Fe-doped MLs are examined. For pristine monolayers, both $MoSe_2$ and WSe_2 exhibit direct bandgaps of approximately 1.46 eV and 1.49 eV respectively listed in table1. These findings are in good agreement with previous reports. When Fe is introduced into the monolayers, spin polarization occurs. For $Mo_{0.972}Fe_{0.028}Se_2$, the spin-down channel exhibits a direct bandgap of 1.09 eV, while the spin-up channel has an indirect bandgap of 0.24 eV. Similarly, for $W_{0.972}Fe_{0.028}Se_2$, the spin-down channel shows a direct bandgap of 1.0 eV, and the spin-up channel has a direct bandgap of 0.27 eV. This reduction in bandgap could be useful for spintronic devices that exploit spin-polarized carriers. In the case of Fe-doped $MoSe_2$ and WSe_2, iron acts as p-type dopants which tends to create holes in the valence band, and can enhance the photocurrent and overall photosensitivity of the material. This p-doping improves the efficiency of light absorption and charge separation, which are key factors in photodetector performance [19]. In contrast, when it acts as n-dopant, which adds electrons to the conduction band, is clearly observed through electronic band structures. While it may increase the electron density, it might also reduce the material's ability to capture electrons. This process may also lead to a diminished ability of the material to effectively capture other charge carriers, potentially impacting its overall performance in electronic applications. However, the ideal doping method and concentration might vary depending on the specific application and the properties of the TMDs, so it is still an area of active research [18-20]. The pristine MSe_2MLs are nonmagnetic but $M_{0.972}Fe_{0.028}Se_2$MLs are observed to be magnetic in nature. Their magnetic behaviour is clear from their spin resolved electronic band structure and DOS (figure 2(b) and 3(3b)). We have plotted PDOS corresponding to impurity atom (Fe) and Se atom in the neighbourhood of impurity. We observed the value of spin magnetic moment acquired by each neighbouring atom of impurity shown in table 1. The magnetic properties of $Mo_{0.097}Fe_{0.028}Se_2$ and $W_{0.097}Fe_{0.028}Se_2$ MLs are analysed through calculations of spin vector. Both systems exhibit Ferromagnetic behaviour, with a net magnetic moment of approximately 2μB per monolayer. The magnetic moment primarily arises from the Fe dopant, which acquires a moment of approximately $1.6\mu_B$. Additionally, neighbouring atoms, such as Mo/W and Se, show slight magnetization due to the localized effects of the Fe impurity (Fig.4). In $Mo_{0.972}Fe_{0.028}$ Se_2, the surrounding six Mo atoms acquire magnetic moments of 0.085μB, while the Se atoms have a negligible moment. In $W_{0.972}Fe_{0.028}Se_2$, the neighbouring six W atoms acquire magnetic moments of 0.219 μB, and the Se atoms show a similarly small contribution. This localized magnetization is consistent with the expected influence of the Fe impurity on the surrounding atoms.

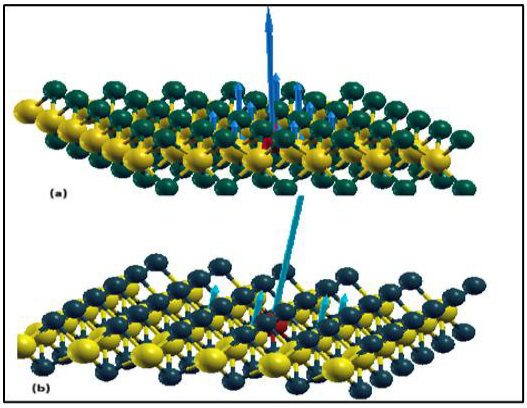

Figure 4: Spin vector in (a) $Mo_{0.097}Fe_{0.028}$ Se_2 and (b) $Mo_{0.097}Fe_{0.028}$ Se_2

Conclusion And Future Prospective

Our first-principles study reveals that Fe doping

significantly alters the electronic and magnetic properties of $MoSe_2$ and WSe_2 monolayers. The doping induces spin polarization, leading to distinct band gaps. These findings suggest that $Mo_{0.972}Fe_{0.028}Se_2$ and $W_{0.972}Fe_{0.028}Se_2$MLs hold great potential for spintronic applications, where the tunable spin-polarized electronic states could be harnessed for advanced device technologies. Our study provides a comprehensive understanding of the impact of Fe doping on the properties of TMD monolayers, offering a pathway for the development of new materials for energy storage devices, superconductors, photocatalysis and magnetic semiconductors.

Acknowledgment

Authors would like to acknowledge SIESTA team for providing the code. This research was supported in part through computational resources provided by the Kathmandu University Supercomputer Center, which was established with equipment donated by CERN.

References

1. Tiwari, S. de Put, M. L., Sorée, B., Vandenberghe, W.G., *"Magnetic order and critical temperature of substitutionally doped transition metal dichalcogenide monolayers"*, npj 2D Mater. Appl. 2021, *5*, 54.
2. Fan, X. L.; An, Y. R.; Guo, W. J., *"Ferromagnetism in transitional metal doped MoS_2 monolayer"*, Nanoscale Res. Lett. **2016**, *11*, 154.
3. Zhao, X.; Chen, P.; Wang, T., *"Controlled electronic and magnetic properties of WSe_2 monolayers by doping transition-metal atoms"*, *Superlattices Microstruct.* 2016, *100*, 252–257.
4. Cheng, Y.C.; Zhu, Z.Y.; Mi, W.B.; Guo, Z.B.; Schwingenschlögl, U., *"Prediction of two-dimensional diluted magnetic semiconductors: Doped monolayer MoS_2 systems"*, *Phys. Rev. B Condens. Matter Mater. Phys.* 2013, *87*, 2–5.
5. Suo, Z. Dai, J. Gao, S and Gao, H, *"Effect of transition metals (Sc, Ti, V, Cr and Mn) doping on electronic structure and optical properties of CdS"*, Results in Physics, Volume 17, 2020, 103058, ISSN 2211-3797
6. Min Luo, Shen Yu Hao, and Yin Tai Ling, *"Ab initio study of electronic and magnetic properties in ni-doped ws_2 monolayer"*, AIP Advances, 6(8):085112, 2016.
7. Mayorga-Martinez, Carmen C., et al. *"Transition metal dichalcogenides (MoS_2, $MoSe_2$, WS_2 and WSe_2) exfoliation technique has strong influence upon their capacitance", Electrochemistry Communications* 56 (2015): 24-28.
8. Gao, Jian, et al. *"Transition-Metal Substitution Doping in Synthetic Atomically Thin Semiconductors", Advanced Materials*, *vol. 28*, *no. 44*, Sep. 2016.
9. K. Dolui, I. Rungger, C. D. Pemmaraju, S. Sanvito, Phys. Rev. B "Physical Review B—Condensed Matter and Materials Physics" 88 (7), 075420, 2013.
10. A. Ramasubramaniam, D. Naveh, "Physical Review B—Condensed Matter and Materials Physics" 87 (19), 195201, 2013
11. Murtaza, Ghulam, et al. *"Chemical vapour deposition of chromium-doped tungsten disulphide thin films on glass and steel substrates from molecular precursors",* Journal of Materials Chemistry C 6.35 (2018): 9537-9544.
12. Chang, Yung-Huang, et al. *"Monolayer $MoSe_2$ grown by chemical vapor deposition for fast photodetection" ACS nano* 8.8 (2014): 8582-8590.
13. Zhang, Han, et al. *"Strain engineering the magnetic states of vacancy-doped monolayer $MoSe_2$", Journal of Alloys and Compounds* 635 (2015): 307-313.
14. Xie, Ling-Yun, and Jian-Min Zhang. *"The structure, electronic, magnetic and optical properties of the Mn doped and Mn-X (X= F, Cl, Br, I and At) co-doped monolayer WS2: a first-principles study", Journal of Alloys and Compounds* 702 (2017): 138-145.
15. Zhao, Xu, et al. *"Electronic and magnetic properties of Mn-doped monolayer WS2", Solid State Communications* 215 (2015): 1-4.
16. Nayak, P. K., Horbatenko, Y., Ahn, S., Kim, G., Lee, J. U., Ma, K. Y., ... & Shin, H. S. (2017). *"Probing evolution of twist-angle-dependent interlayer excitons in $MoSe_2/WSe_2$ van der Waals heterostructures"*, *ACS nano*, *11*(4), 4041-4050.
17. Gong, Y., Lei, S., Ye, G., Li, B., He, Y., Keyshar, K., ... & Ajayan, P. M. (2015), *"Two step growth of two-dimensional $WSe_2/MoSe_2$ heterostructures"*, Nano letters, 15(9), 6135- 6141.
18. Charapale, Mahesh R., et al. *"Enhancing capacitive performance of MoS2 through Fe doping: Synthesis, characterization, and electrochemical evaluation for supercapacitor applications",* Surfaces and Interfaces 52 (2024): 104814.
19. Liu, C., Wu, K., Meng, G., Wu, J., Peng, B., Hou, J., ... & Guo, X. (2017). *"Explore the properties and photocatalytic performance of iron-doped g-C_3N_4 nanosheets decorated with Ni_2P"*, *Molecular Catalysis*, *437*, 80-88.
20. Jafari, M., Rahmani-Ivriq, N., & Dyrdal, A. (2024), *"Effect of Fe-doping on VS2 monolayer: A first-principles study"*, *arXiv preprint arXiv:2411.12001*.